Thermovibrationally-driven Flows and Particle Accumulation in Microgravity Environments

Georgie Crewdson

James Weir Fluids Laboratory
Department of Mechanical and Aerospace Engineering
University of Strathclyde, Glasgow

March 6, 2023

This thesis is the result of the author's original research. It has been composed by the author and has not been previously submitted for examination which has led to the award of a degree.

Abstract

In the present work, thermovibrationally-driven flows and ensuing particle accumulation phenomena are studied in the context of a microgravity environment. The problem is addressed numerically through solution of the governing equations for fluid flow and particle transport (Eulerian-Lagrangian one-way coupled approach). This work follows a logical approach with cases of increasing complexity being analysed as the discussion progresses, in particular, first the properties of this type of fluid flow are investigated in the single-phase (pure fluid) situation considering both two-dimensional (2D) and three-dimensional (3D) geometries. Then the multiphase problem, resulting from the addition of solid particles, is examined. The role played by the direction of the vibrations with respect to the temperature gradient is also investigated. Starting from the situation with concurrent vibrations and temperature difference (parallel case), it is shown that complexity of this situation essentially stems from the properties that are inherited from the corresponding case with steady gravity, i.e., the standard Rayleigh–Bénard convection. The need to overcome a threshold to induce convection from an initial quiescent state, together with the opposite tendency of acceleration to damp fluid motion when its sign is reversed, causes a variety of possible solutions that can display synchronous, non-synchronous, time-periodic, and multi-frequency responses. Moreover, as the constraint of two-dimensionality is removed, the intrinsically three-dimensional nature of the problem and its sensitivity to the thermal boundary conditions can have a remarkable influence on the multiplicity of emerging solutions and the system temporal response even if a geometry as simple as a cubic enclosure is considered. If solid particles are added to the fluid, the hallmark of the phenomena occurring in this case is an endless squeezing and expansion of particle formations along the direction of the temperature gradient. A kaleidoscope of previously unknown solutions is also reported for the situation with vibrations perpendicular to the temperature gradient (perpendicular case) giving emphasis to some still poorly known aspects such as the complex nature of the textural transitions undergone by the time-averaged flow as the Gershuni number is increased. Chaotic states are enabled when larger frequencies of vibration are considered.

When particles are added in these cases, while clusters with a perfect (very regular and stationary) morphology emerge in laminar flow, when thermovibrational flow is chaotic the topology of the structures is relatively irregular and time-dependent. Nevertheless, precise trends and relationships can be established if specific problem 'statistics' are connected to the behaviour of the temporally evolving structures. Finally, cases are considered where the imposed temperature gradient is not unidirectional, i.e. the direction of such a gradient is allowed to change inside the fluid. The relationship between the multiplicity (N) of the loci of particle attraction and the inhomogeneities in the temperature field is studied. It is shown that N can exceed the limit $N = 2$ found in earlier studies and that a zoo of new particle accumulation structures show up, whose ranges of existence depend on the amplitude and frequency of vibrational acceleration, the particle Stokes number, the orientation of vibrations, and the number of inversions in the direction of the temperature gradient. Some experimental activities conducted to support the so-called PARTICLE VIBRATION microgravity experiment are also presented.

Acknowledgements

I would like to take the time to acknowledge all those who have contributed to my Ph.D. experience. This has been an incredible journey both academically and personally.

Firstly, I would like to thank my supervisor Prof. Marcello Lappa who has been incredibly supportive and encouraging throughout my journey, especially in the midst of the pandemic. I thank him for his patience and guidance and for the respect he has show me as a individual and as a researcher. I also would like to thank Dr. Thomas Burel, Dr. Paolo Capobiancci and Dr. Monica Oliveria, for their guidance, support and helpful discussions over the past three years.

It goes without saying that I would not have been able to complete this work without the continuous support and friendship of my dear friend and fellow PhD student Alessio Boaro, who has been at my side through thick and thin. I am also thankful to have been surrounded by the most wonderful colleagues including Kieran, Alessia, Jamie, Phillip and Miguel just to name a few. I would also like to say a huge thank you to my dear friends from the Doctoral Researchers Group and the Strathclyde Doctoral School, namely Atimati, Roberto and Lewis for their friendship and dedication to improve my (and the rest of the PhD cohort at the University) PhD experience.

I would of course like to thank my wonderful partner Jack for his eternal kindness, patience, love and encouragement over the past 7 years.

I cannot begin to thank my family, Johnny, Alison, Ben and Jamma, and Debbie, Rob and Dan and my friends Alice, Alisha and Marisa enough for the love and support they have shown me on this incredible journey.

Last but not least I would like to thank the UK Space Agency and the Dept. Mechanical and Aerospace Engineering of the University of Strathclyde for funding this research and the examiners of this thesis for their time and commitment.

Scientific Contributions

Peer Reviewed Journal Articles

1. Crewdson, G. and Lappa, M., 2021,"The zoo of modes of convection in liquids vibrated along the direction of the temperature gradient", *Fluids*, 6(1), p.30, https://doi.org/10.3390/fluids6010030.

2. Crewdson, G and Lappa, M., 2021, "Thermally-driven flows and turbulence in vibrated liquids", *International Journal of Thermofluids*, 11, 100102, https://doi .org/10.1016/j.ijft.2021.100102.

3. Crewdson, G. and Lappa, M., 2022 "Spatial and temporal evolution of three-dimensional thermovibrational convection in a cubic cavity with various thermal boundary conditions", *Physics of Fluids*, 34, 014108, https://doi.org/10.1063/5.00 78270.

4. Crewdson, G. and Lappa, M., 2022, "An Investigation into the Behavior of Non-Isodense Particles in Chaotic Thermovibrational Flow", *Fluid Dynamics & Materials Processing*, 18(3), 497-510, https://doi.org/10.32604/fdmp.2022.020248.

5. Lappa, M., Burel, T., Kerr, M., Crewdson G., Boaro, A., (...) Hens, S., Lappa, M., Burel, T., Kerr, M. et al., 2022, "Particle Accumulation Structures On Board the International Space Station", *Microgravity Sci. Technol.* 34, 33 . https://doi.org/ 10.1007/s12217-022-09939-2.

6. Crewdson, G., Evans, M. and Lappa, M.,2022, "Two-dimensional solid particle attractors in non-uniformly heated vibrated fluid containers", *Chaos* 32, 103119, https://doi.org/10.1063/5.0104680.

Articles Under Review

1. Crewdson, G. and Lappa, M., "3D Solid Particle Self-assembly in Thermovibrational Flow: The case with Unidirectional Temperature gradient and Concurrent Vibrations", under review for *Physics of Fluids*.

Non-Peer Reviewed Conference Papers

1. Crewdson, G. and Boaro, A.,"Supporting an ISS experiment as PhD students: a case study of the PARTICLE VIBRATION project", 2022, Proceedings of the 4^{th} Symposium on Space Educational Activities, Barcelona, $26^{th} - 29^{th}$ April 2022.

Conference Presentations

1. Crewdson, G. and Lappa, M., 2021, "Control of Small Solid Particles in Heated Fluids Under Vibrations in Space", Strathclyde Doctoral School Multidisciplinary Symposium, Glasgow, $1^{st} - 4^{th}$ June 2021 (Online).

2. Crewdson, G. and Lappa, M., "Preliminary investigation into the behaviour of non-isodense particles in chaotic thermovibrational flow". International Conference on Materials and Energy, $9^{th} - 11^{th}$ June 2021 (Online).

3. Crewdson, G. and Boaro, A., Lappa, M., Kerr, M., "Supporting an ISS experiment as PhD students: a case study of the PARTICLE VIBRATION project",4^{th} Symposium on Space Educational Activities, Barcelona, $26^{th} - 29^{th}$ April 2022.

Research Awards

1. Awarded "Best Presentation" at the International Conference on Materials and Energy, $9^{th} - 11^{th}$ June 2021. (Online).

Contents

List of Figures

List of Tables

List of Symbols

The next list describes several symbols that will be later used within the body of the document.

α	Thermal diffusivity
β	Thermal expansion coefficient
ΔT	Temperature difference
δ	Thickness
ν	Kinematic viscosity
Ω	Non-dimensional angular frequency
ω	Dimensional angular frequency
ρ	Fluid density
τ	Lag
ζ	Kolmogorov length Scale
b	Vibrational Amplitude
g	Gravitational acceleration on Earth
Gs	Gershuni number
Nu	Nusselt Number
P	Non-dimensional period of vibrations

p	Pressure
Pr	Prandtl number
Ra	Rayleigh number
Ra_ω	Vibrational Rayleigh number
T	Temperature
t	Time
u	Velocity component along x
V	Velocity
v	Velocity component along y
w	Velocity component along z

Part I

Background and Theory

Chapter 1

Introduction

1.1 Problem statement, purpose statement and research questions

Problem statement

Today, thermal convection in fluids is at the base of almost all engineering and industrial processes here on earth. As the concepts of long-duration space flight, deep space exploration and the colonisation of other planets become ever more tangible, the problem arises that many fluid dynamic processes humans depend on here on earth, cannot occur in space due to the lack of gravity. Indeed, when multiphase fluid systems are considered, the sedimentation, solidification and other processes that occur on earth due to material density differences, cannot be achieved. This poses an immense challenge to the field of material processing in low gravity environments. Developing better control of fluids and materials in microgravity will be of crucial importance for the future exploration of space. In this regard, of special interest is the elaboration of new contactless strategies for the manipulation of fluid phases, solid phases and related combinations and mixtures.

Purpose statement

The purpose of this research is to explore a specific fluid dynamic mechanism known as thermovibrational convection: a type of thermal convection that occurs in microgravity

when vibrations are applied to a differentially heated body of fluid. In recent years, research in the field of thermovibrational convection has produced promising results in developing the understanding of the behaviour and control of fluids in microgravity.

The goal of this research is to fill the gap associated with the lack of knowledge surrounding the field of thermovibrational convection. More specifically, this work will on the one hand explore new fluid states that can arise when novel combinations of parameters associated with thermovibrational convection are considered and, on the other hand, will explore the effects of this extended range of parameters on particle accumulation phenomena in thermovibrationally driven fluids.

Research questions

The following questions can therefore be posed:

What thermovibrational effects can be achieved in a fluid, when:

- the direction of vibration is changed?
- turbulent thermovibrational convection is considered?
- various sets of thermal boundary conditions are applied to the system?

and,

- How do theses thermovibrational effects modify the behaviour of particle accumulation structures in multiphase systems?

This thesis will build on the current knowledge surrounding multiphase thermovibrational systems, indeed, at the time of writing, an experiment known as PARTICLE VIBRATION has recently been launched into space, to the International Space Station. This experiment sits at the root of the current work and is described in the next section.

1.2 The PARTICLE VIBRATION project

The T-PAOLA Project (Thermovibrationally-driven Particle self-Assembly and Ordering mechanisms in Low grAvity), also know as the PARTICLE VIBRATION project, is a fluid dynamic experiment that was launched to the International Space Station on the 22^{nd} November 2022. The project is a collaboration between the University of Strathclyde, the UK Space Agency, and the European Space Agency and headed by Principal Investigator Dr. Marcello Lappa. The underlying scientific principal of the experiment can be described as follows:

Fluid and solid particles are enclosed in a cavity (i.e. a box) which is vibrated in microgravity conditions (on the International Space Station). When this fluid is subjected to vibrations and is heated from the side or from the bottom, a phenomenon known as thermovibrational convection manifests itself. When small particles (akin to the likes of dust or sand) are added to the fluid, the behaviour of the flow can lead to the accumulation of the particles in specific regions of the container and form well defined structures.

The experiment sent to the ISS is based on numerical studies conducted largely by Dr. Marcello Lappa [1] and the theory on which the experiment is based was already largely in place prior to the beginning of this thesis. This work however aims to investigate (numerically) new flow types (with and without the addition of particles) in order to identify possible mechanism of flow control and, in turn, the control of particle accumulation in fluids in an attempt to answer the aforementioned research questions.

1.3 Thesis scope and structure

This thesis is organised in three parts:

Part.I of this thesis presents firstly in Chapter 2, a review of the existing literature and a discerning of the current level of knowledge in the field. Chapter 3, presents the mathematical models and numerical framework employed for the numerical simulations.

Part.II presents the authors results and findings and is structured as follows: the first three Chapters (Chapters 4, 5 and 6) explore pure thermovibrational flow, without the addition of particles. These three chapters aim to answer the first three research questions:

What thermovibrational effects can be achieved in a fluid, when:

- the direction of the vibration is changed?
- turbulent thermovibrational convection is considered?
- various sets of thermal boundary conditions are applied to the system?

The last three chapters (Chapters 7, 8 and 9), attempt to answer the last research question:

- how do various thermovibrational effects modify the behaviour of particle accumulation structures in multiphase systems?

Finally, Part.III (Chapter 10), provides the reader with the general conclusions of the research carried out in the thesis, and a concise answer the the research questions.

Chapter 2

Literature review

2.1 An introduction to orbiting platforms

The International Space Station (ISS), launched in 1998 is the most recognised platform for microgravity experimentation due to its exhibition of remarkable engineering and international collaboration. However, before diving into an in-depth appraisal of the ISS, it must be noted that many other altered gravity or reduced gravity platforms are available to researchers for scientific experimentation. These platforms vary in g-level, duration, and accessibility and have been continuously evolving since Boeing's KC-135 aircraft was used for microgravity research in the 1960's. The ensuing microgravity platforms include, to name a few; the Apollo module (1964), Skylab (1973), SpaceLab (1974), MIR Space Station (1986) EURECA retractable space module (1992), multiple iterations of drop tower/shafts, sounding rockets and of course, parabolic flights. The most commonly used microgravity platforms in Europe today (excluding the use of the ISS) include, the ZARM drop tower, European Space Agency (ESA) sounding rockets including TEXUS, MASER and MAXUS, and the NoveSpace A310 Zero-G parabolic flight aircraft. Similar platforms have been developed by non-European bodies, however these three types of platforms are sufficient to inform the reader on the scope of modern microgravity research in the context of this literature review.

The advantage of these platforms is that they are extremely accessible due to their relatively low cost. Not only do they host academic research experiments but they are also accessible to students via programs such as the ESA Academy campaigns. The

drawback of these more accessible options is that the microgravity periods available range from 9 seconds (drop tower) to 13 minutes (MAXUS sounding rocket). When designing an experiment for microgravity there is an inevitable trade-off between the *quality* of the microgravity and the time period offered by the platform. For example, the ZARM drop tower located at the University of Bremen in Germany, offers up to 9 seconds of almost pure zero gravity with the residual gravity sitting at one millionth of earth's $9.81 m/s^2$ ($10^{-6}g$), whereas the sounding rocket MAXUS, launched from the Esrange launch site in northern Sweden, offers 13 minutes of $10^{-4}g$. Other constraints such as payload size and free floating options are also to be taken into account depending of the nature of the proposed experiment.

Now that a few examples of microgravity platforms have been discussed, the focus may be shifted onto the host of the T-PAOLA project, the ISS. With the longest available microgravity duration periods, a near zero-g environment and a myriad of experimental facilities, the ISS is the preferred platform for most microgravity experiments. It hosts a multitude of interdisciplinary experiments, these include not only fluid experiments such as flow and heat transfer, solidification and multi-phase flow experiments, but also life science experiments including, biological, chemical, physiological, physical and also experiments external to the station exposed to the radiation of space. Although it is of popular belief that the microgravity environment of the ISS is the same as that of the vacuum of space, this is not entirely true. Only the station's centre of mass is truly in a zero-gravity state, (this centre of mass not being a physical part of the structure). The rest of the station is subject to crew activities, mechanical disturbances due to systems operation and equipment, and external factors such as atmospheric drag, rotational forces and more. These activities and disturbances create vibrations on the ISS known to range from less than $10^{-6}g$ for low-end frequencies and over $10^{-2}g$ for high-end frequencies.

The motivation behind providing such an introduction to microgravity platforms is due to the fact that this thesis will concentrate on the effect of microgravity and its related disturbances (vibrations) on fluid dynamic experiments and buoyancy convection problems in a microgravity environment.

As stated in the introduction (Chap.1), a specific type of buoyancy convection, known as thermovibrational convection, acts as the focal point of this thesis. Before attempting to understand the underlying principals behind thermovibrational flow however, one must be comfortable with the concept of standard buoyancy convection. The next part of this literature review aims to provide the reader with such an understanding.

2.2 An introduction to buoyancy convection

The field of buoyancy convection is a widespread and fruitful field with a high level of applicability across many different industrial and natural processes [2]. From everyday objects and processes such as boiling water in a pan, to highly complex industrial applications and materials processing techniques such as crystal growth [3–6], the understanding of buoyancy convection is at the root of many technological advancements achieved in modern times. In this section, two fundamental types of buoyancy convection are introduced: Hadley flow and Rayleigh-Bénard convection. Although they result in different flow characteristics (due to differences in configuration that will be discussed later on), these two types of convection rely on the same driving force: gravity (the buoyancy force). On earth, when a fluid is heated, the density of the hot fluid will decrease causing it to rise. Similarly, as it cools, the fluid migrates from the top back to the bottom of the pan as a result of the increased density of the colder fluid. Assuming the pan is continuously heated from below, convection currents will arise. Although the reader may easily visualise and relate to this concept, one key component for the advent of buoyancy convection is often taken for granted: the gravity vector. If the gravity vector is removed, and no other forces are applied to the pan (e.g., surface tension forces are ignored), the hot fluid would simply remain at the bottom of the pan. From this, the salient characteristics for the onset of buoyancy convection can be identified: a temperature difference across the fluid and a gravity vector, hence equipping the reader with some key concepts in preparation for the review of both the Hadley Flow and Rayleigh-Bénard convection.

The direction of the temperature gradient with respect to the gravity vector is known to be an essential factor in determining the properties of the flow. This concept applies to both the stability scenario (i.e., the hierarchy of bifurcations undergone by the considered system when the applied temperature difference is increased) and the related patterning behaviour inside the fluid (i.e., flow topology, patters and regimes). The fundamental difference between the two types of convection comes down to the direction of the temperature gradient with respect to the gravity vector. In the case of the Hadley flow, the body force is set perpendicular to the temperature gradient, and in the case of Rayleigh-Bénard convection the body force is set parallel to the temperature gradient. This rigid classification of the direction of the temperature gradient can also be found in companion problems where gravity is replaced by surface-tension effects (that is the scenario where fluid systems posses a free surface, e.g., an interface where a liquid is in contact with an immiscible fluid). In this case, the fluid flow behaves differently according to the angle θ_1 formed by the temperature gradient and the free interface. In particular, $\theta_1 = 0°$ and $90°$ correspond to the so-called thermocapillary and Marangoni–Bénard convection types, respectively. Although investigation into these types of convection is outside the scope of this thesis, it is useful to introduce such concepts in order to highlight the complex yet subtle system configurations than can lead to the onset of thermal convection.

In this work the terms, thermo-gravitational convection and natural convection are synonymous where both terms are used to describe buoyancy convection induced by steady gravity in terrestrial conditions.

Now that the general concept of thermal convection has been introduced, the relevant literature for both the problem of Hadley flow and Rayleigh-Bénard convection can be explored.

2.3 Hadley flow

The first observations of natural convection where made by Hadley in 1735 [7], where he put forward the first theory explaining the behaviour of convection currents on earth known as *trade winds*. The theory suggests that, as the local temperature at the

equator is higher, the air located at that point will heat up and rise due to a decrease in air density. The air will then cool and proceed to circulate towards the (colder) north and south poles, giving rise to atmospheric circulation. Although other factors contribute to this atmospheric circulation such as the moisture content of the air and its compressible nature [8], scientists and engineers (not exclusively pertaining to the field of atmospheric sciences) where quick to adopt a simplified model of the Hadley flow as shown in Fig.2.1 (also known as the differentially heated cavity).

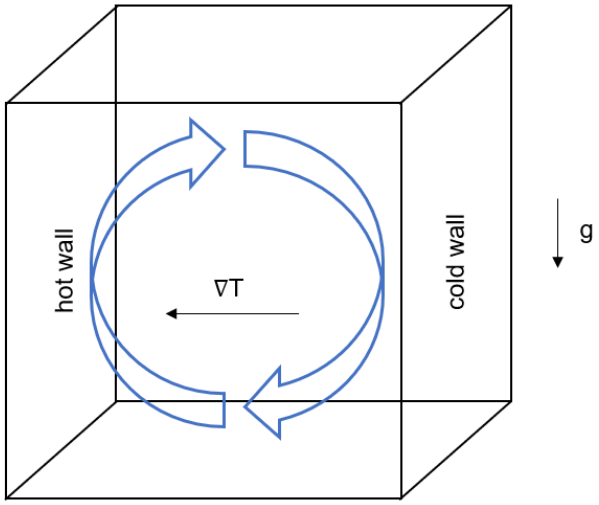

Figure 2.1: Hadley flow configuration

When defining the mathematical model ascribed to the Hadley flow, the main characteristic of said model is that the temperature gradient must be perpendicular to the gravity vector.

This configuration has, over the years, become a benchmark for numerical simulations, due to its simplicity and the high number of intrinsic symmetries (reflectional symmetries with respect to the vertical, horizontal and diagonal directions) that can be obtained and subsequently disrupted. Indeed when this configuration is considered and the flow is unbound by vertical side walls, three distinct types of instabilities can occur within the fluid. These include:

- Two-dimensional transverse rolls

- Stationary longitudinal rolls
- Oscillating longitudinal rolls

Figure.2.2 illustrates the two base types of instabilities that can occur when Hadley flow is considered: transverse rolls and longitudinal rolls. The *oscillating* longitudinal rolls occur when a standing or travelling wave appears in the flow whose presence leads to the flow becoming time-dependent. In the presence of a *standing* wave, the direction of rotation of the rolls is prone to change in time, whereas the existence of a *travelling* wave leads to a time-dependent migration of the axis of the longitudinal rolls in the z direction.

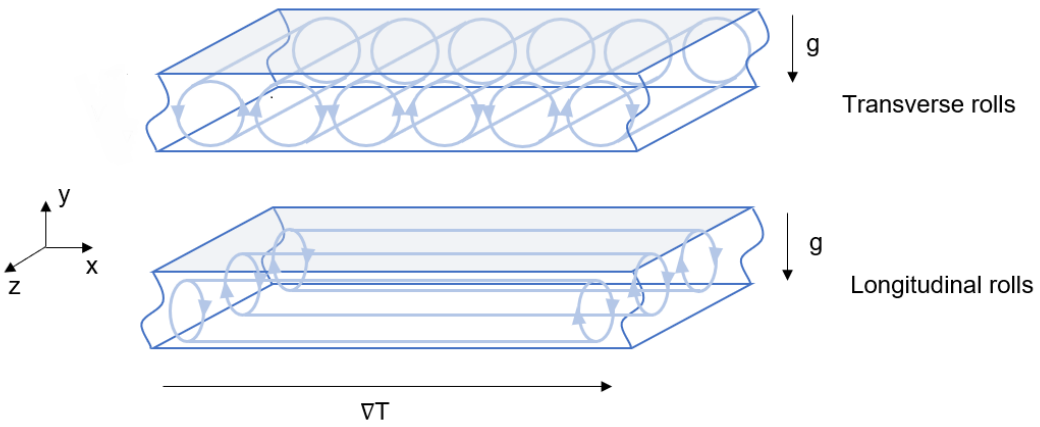

Figure 2.2: Common instability modes; transverse rolls (top) and longitudinal rolls (bottom) that appear when the Hadley type flow is considered

These instability modes were studied in depth by Roux *et al.* [9] and Kuo and Korpela [10], who found that the manifestation of these instabilities depends on the Prandlt number of the fluid, where the Prandtl number is a dimensionless number defined as the ratio of momentum diffusivity, also known as kinematic viscosity (ν in m^2/s) and thermal diffusivity (α in m^2/s) giving: ($Pr = \nu/\alpha$), and the Grashof and wave number of the system, the Grashof number being a non-dimensional number approximating the ratio of buoyancy to viscous force acting on a fluid, defined as:

$$Gr = \frac{\beta_T \Delta T L^3 g}{\nu^2} \tag{2.1}$$

where β_T is the coefficient of thermal expansion (K^{-1}) ΔT is the temperature difference across the system (in K), L is the characteristic length of the cavity (in m) and g is the steady gravity vector (in m/s^2). Finally, the wave number being a scalar quantity representing the spatial frequency of the flow. This introduction of possible instability modes serves the simple purpose of informing the reader of the existence of such modes and their dependence on system parameters.

The question of "boundness" (i.e. a digression from the infinite layer shown in Fig.2.2 to the case where vertical side walls are imposed on the cavity, as shown in 2.1) was largely unknown prior to the works of de Vahl Davis [11] and De Vahl Davis and Jones [12]. These works provided a (2D) solution for the problem of the differentially heated cavity at low Prandtl numbers ($Pr = 0.71$), and a moderated range of Rayleigh numbers ($10^3 < Ra < 10^6$), where the Rayleigh number dictates the "strength" of the convection and is defined as:

$$Ra = \frac{\beta_T \Delta T L^3 g}{\nu \alpha} \tag{2.2}$$

The reader will notice here that the Rayleigh number is simply the product of the Prandtl and the Grashof number.

De Vahl Davis [11] and De Vahl Davis and Jones [12] found that, for the case of a square cavity (i.e., aspect ratio $A = 1$) upon increasing the Rayleigh number (from $Ra = 10^3$ to $Ra = 10^6$), the patterning behaviour of the flow evolved from a singular roll to a state where multiple, symmetrical rolls arise in the cavity space, providing confirmation of the dependence of the stability of the Hadley flow on the Rayleigh number. It can be noted here that, in the case of Hadley flow, convection (i.e. fluid movement) will occur for all non-zero values of ΔT, i.e., when $Ra > 0$.

In the present work, only square cavities are considered, where side walls are imposed on the system, resulting in simple two-dimensional boxes and three-dimensional cubes. Further insight into more specific instability mechanisms will be elaborated upon in Sect.2.8. This section has attempted to provide a brief summary of the literature relating to the Hadley flow. What follows is an introduction to it's sister type of buoyancy convection: Rayleigh Bénard convection.

2.4 Rayleigh-Bérnard convection

Rayleigh-Bénard (RB) convection has enjoyed higher levels of attention when compared to the Hadley flow. In this case the temperature gradient is parallel to the gravity vector. The superposition of a vertical temperature gradient onto an (also vertical) gravity force is a common phenomena in many natural and industrial applications. RB convection is also commonly refereed to as a fluid system "heated from below", and is illustrated in Fig.2.3.

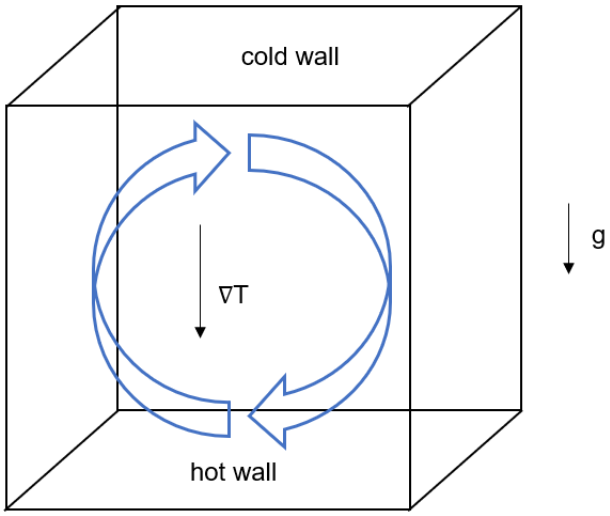

Figure 2.3: Rayleigh-Bénard flow configuration

Unlike the Hadley flow, thermal convection begins in RB problems when a critical value of the Rayleigh number is exceeded (Ra_c). This is due to a competition between the buoyancy forces and viscous forces acting simultaneously on the fluid. The viscosity of the fluid has a stabilising effect and therefore for small temperature gradients (ΔT), the fluid remains at rest. The critical Rayleigh number for the onset of convection for an infinite horizontal layer was found to be $Ra_c = 1708$ by Chandrasekhar in 1961 [13]. This cirtical Rayleigh number is known to depend however on the boundary conditions of the system [14]. If stress-free isothermal horizontal boundaries case considered, $Ra_c = 657$, if no-slip isothermal horizontal boundaries are considered, $Ra_c = 1707$ and finally, if

a stress-free thermally insulated upper and a no-slip isothermal lower boundary are considered, $Ra_c = 669$.

At the onset of convection ($Ra = Ra_c$), when an infinite (non-bounded) fluid layer is considered, straight parallel rolls will arise in the fluid similar to the transverse roll instability discussed in Sect.2.3, as shown in Fig.2.4.

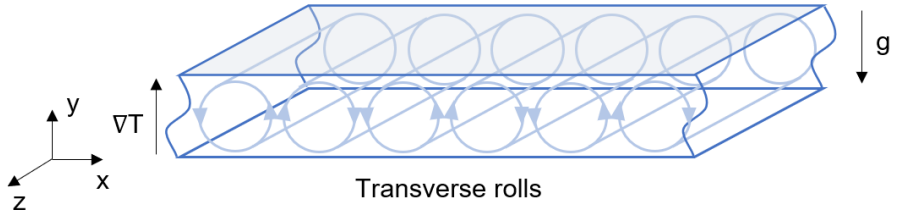

Figure 2.4: Basic rolls appearing for Rayleigh-Bénard convection in a fluid layer heated from below

Upon increasing Ra, the flow is prone to develop many type of instabilities (many more than in the case of Hadley flow) including: the Eckhaus instability, the oscillatory skewed varicose instability, the cross-roll instability, the oscillatory instability with travelling waves, the zig-zag instability, the knot instability and the oscillatory blob instability. These instabilities where coined in works carried out by Busse [15, 16] and constitute in their own right an exciting field of study. Therefore, this short description serves simply to inform the reader, again, on their existence and with the notion that, when RB convection is considered, a multitude of instabilities is possible. These instabilities are again dependent on the Prandtl number, wave number and Rayleigh number of the system.

The analytical solutions found by Busse [15, 16] were also complemented by the work of Davis [17], where the infinite layer problem is replaced with the problem where solid vertical boundaries are imposed on the system. The salient findings of this work are the dependence of the number of rolls on the aspect ratio of the cavity and that, with an increase in the horizontal length of the cavity, comes a decrease in Ra_c.

Numerical simulations of the two-dimensional (2D) bounded RB problem, were carried out chiefly by Goldhirsch [18], who for the first time, observed a multitude of textural transitions in both laminar and turbulent conditions. These textural transitions

where later classified in a clearer way by Mizushima and Mizushima and Adachi [19, 20] and defined as:

- (ss): The symmetric–symmetric mode. This mode is characterized by an even number of rolls along the two coordinate axes. It reduces to a configuration with the central symmetry if the same number (m) of rolls affects both the x and y directions, i.e., $m_x = m_y$.
- (sa): The symmetric–antisymmetric mode. This mode displays symmetry only with respect to the y-axis; accordingly, the flow typically features an odd number of rolls along y and an even number of rolls along the other axis.
- (as): The antisymmetric–symmetric mode. This mode displays symmetry only with respect to the x-axis; accordingly, the flow typically features an odd number of rolls along x and an even number of rolls along the other axis.
- (aa): The antisymmetric–antisymmetric mode. No symmetry is retained in this case, as the number of rolls is odd along both axes (a single column being obtained for $m_y > m_x = 1$)

This classification is summarised in Fig.2.5.

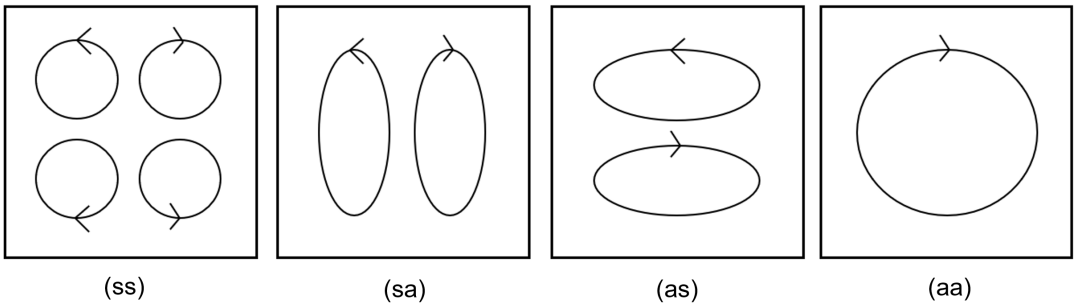

Figure 2.5: Classification of possible symmetries resulting from buoyancy convection in 2D cavities

In this section, the salient characteristics of RB convection have been identified. In the next section, the effects of transition from a 2D to a 3D system in RB convection is discussed.

2.5 Effects of three dimensionality on RB flow

When it comes to carrying out numerical simulations of buoyancy convection driven flows, many authors have limited themselves to considering two-dimensional problems because these provide good insight into the physical response of a system without being overly demanding from a computational point of view. However, when the 3^{rd} dimension is considered, a new degree of freedom is introduced into the system, allowing for more evolved fluid states. Here are reported some key developments in the field of standard buoyancy convection when three dimensionality is employed.

In the case of RB convection, the (2D) works of Mizushima [19, 20] describing the different symmetries and relating transition behaviours in a square cavity heated from below (discussed in Sect.2.4) have been instrumental in providing valuable base information for many studies relating to thermal convection and patterning behaviours. Mizushima later produced a 3D study treating RB convection [21], this time in a parallelepiped cavity, demonstrating that the addition of a third-dimension results in two- and three-dimensional fluid symmetries including planar and toroidal flow fields, shown in Fig.2.6. In addition to Mizushimas works, the case of the cubic cavity subject to steady gravity heated from below has also been treated by Pallarès *et al.* both numerically [22] and experimentally [23]. In their studies seven flow structures were identified, including single roll, two roll and toroidal-type rolls.

Puigjaner *et al.* [24, 25] conducted a stability analysis of this problem and also found that by increasing the strength of convection (i.e. the Rayleigh number), a series of possible steady, stable and unstable patterns emerge resulting in a complex bifurcation diagram. The findings of Puigjaner *et al.* [24, 25] however, are in some cases inconsistent with those of Pallarès *et al.* Some solutions identified by Pallarès *et al.* were not found by Puigjaner *et al.*, in addition, the stability ranges of certain solutions are found to be different when comparing both authors results. Despite these differences, these studies indicate that the study of thermal convection in a 3D square cavity offers a rich playground for researchers due to the extent of possible parametric variations. Other variations such as different heating conditions and driving forces have been ad-

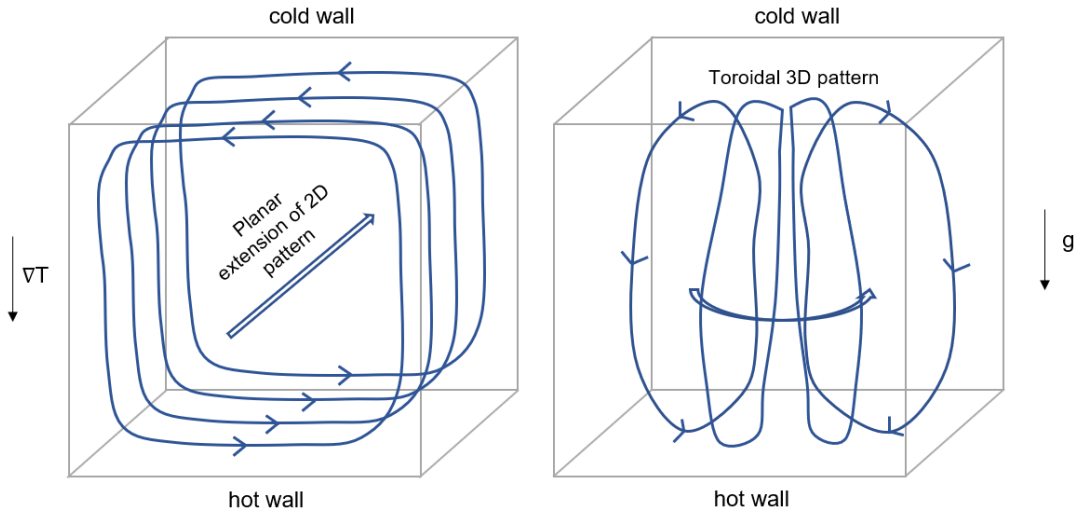

Figure 2.6: Example of a planar extension of a 2D flow pattern (left) and example of a 3D toroidal flow pattern (right)

ditionally investigated by Lappa [26], where RB convection, lateral heating, Marangoni flow (i.e. surface tension driven flow) and mixed driving force configurations have been considered. In this work it is argued that the discrepancies found between Pallarès *et al.* and Puigjaner *et al.* [22–25] can be justified when considering that the transition from one solution to another, upon an increase in Ra, is dependent of the presence of thermal and/or momentum boundary layers, which in turn, depends on the value of Pr, therefore making the comparison of transitional and bifurcation behaviour between cases with different values of Pr ambiguous. This is also acknowledged by Puigjaner *et al.* [25], where it is reported that for the same value of Ra, the Nusselt number (i.e. the ratio of convective to conductive heat transfer at a boundary in a fluid system) varies considerably in the range $0.71 < Pr < 10$ and then tends to an asymptotic value for $Pr > 10$.

In addition to the works discussed above, the work of Gelfgat [27], investigated in more detail the effect of varying the aspect ratio of the cavity and it's effect on Ra_c, when 3D flows are considered. Gelfgat [27] reports on the numerous patterns that occur when the aspect ratio is varied. The similarities between 2D and 3D models are assessed and the conclusion is made that there are several modes of the most dangerous

perturbation which replace each other when A is varied, however, the spectrum of possible perturbations is more complicated in the three-dimensional case.

From this section, it can be seen that the possible solutions associated with RB convection when considering a three dimensional problem become more challenging to predict and interpret than when the (simple) 2D case is considered. None the less, these studies provide a valuable database of knowledge from which can be retrieved general analysis tools when moving to the problem of three dimensional standard buoyancy and thermovibrational convection.

2.6 Influence of thermal boundary conditions on flow behaviour in RB convection

The focus can now be turned to other factors that have shown to contribute to the alteration of flow behaviour in RB convection. One system property that has shown to have significant effects of the onset of convection and system stability is the thermal boundary conditions applied to the non-isothermal walls of the cavity. These are traditionally set either as *perfectly conducting* (where a linear temperature profile is applied along the side walls, where $T = y$) or as *adiabatic* (where no heat transfer into or out of the system occurs along the side walls, where $\dot{Q} = 0$ for $0 < 1 < y$) .

Gershuni and Zhukhovitskii [28] report in early studies, that the thermal conditions applied to the side walls influence the onset of 3D RB convection. For the case of perfectly conducting side walls, the critical Rayleigh number for the onset of convection is found to be higher than for the perfectly insulating case ($Ra_c = 8334$ vs $Ra_c = 2432$ respectively), which shows that systems possessing perfectly conducting side walls are more *stable* than their sister cases possessing adiabatic side walls. Indeed, imposing a linear temperature profile along the side walls sets an additional *obstacle* for the buoyancy force to overcome in order to generate convection.

Moreover, Mizushima [19] revealed that the boundary conditions at the wall can stabilise or destabilise the neutral mode curves (i.e., the curves that represent the passage from one mode to another at Ra_c). Indeed, looking at Fig.2.7, it can be seen that

a slight oscillation is visible in the neutral mode curves (Ra_c vs A) for the case where fully adiabatic walls are considered. This indicates that the inclusion of conducting side walls leads to a smoother transition in system responses when a given parameters is varied (for a given aspect ratio A).

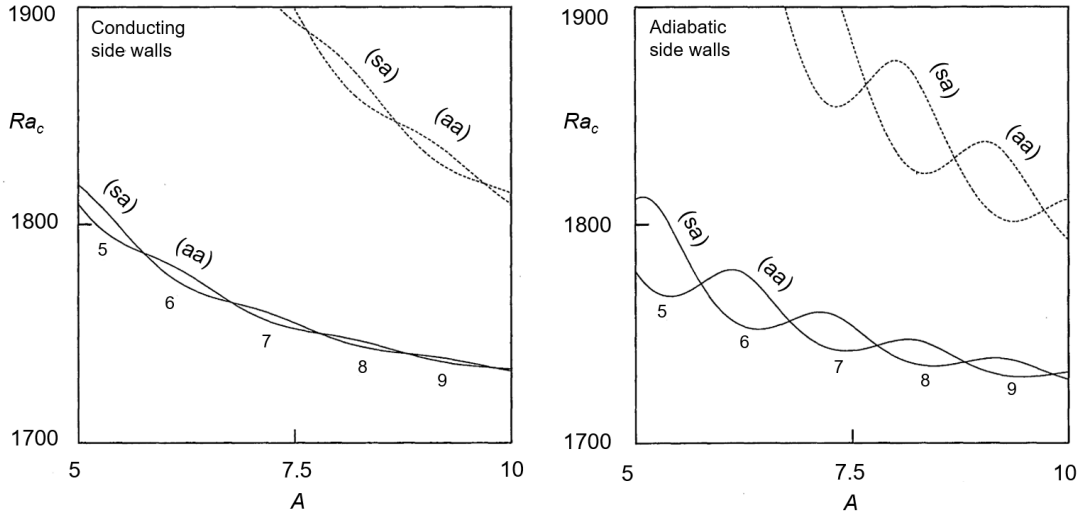

Figure 2.7: Ra_c vs A in standard RB convection the case where the side walls are perfectly conducting (left) and adiabatic (right). The solid and dashed lines show the first mode and the second mode of convections respectively. Figure adapted from [19].

Another study by Mizushima [21] examined the onset of 3D RB convection, and found that the preferred mode at the onset is not always two-dimensional finite rolls with axes parallel to the shorter side which differs from the conclusion derived for the case of perfectly conducting sidewalls by Davis [17] (as aforementioned in Sect.2.4, and illustrated in Fig.2.6). This was found to be due to the different boundary conditions applied to the side walls. In the case of Davis [17], perfectly conducting side walls are considered where as Mizushima [21] considers adiabatic side walls. This comparison, reinforces the idea that the conducting nature of the side walls exhibits a stabilising effect on the flow as less modes are observed in when conducting walls are considered.

The effect of wall conditions on flow structures has also been investigated experimentally by Pallarès *et al.* [23] for high Prandtl numbers (Pr=130) over a range of moderate Rayleigh numbers ($Ra \leq 8 \times 10^4$). Both wall conditions yield similar results

in terms of flow patterns and transitions up to $Ra < 5 \times 10^3$. After that, the flow structures formed differ for both conditions and occur at different values of Ra.

The findings summarised here, lead to the conclusion that the behaviour of a system can vary depending on the choice of thermal boundary conditions at the side walls. This is an important notion when attempting to determine the factors that affect both the onset of convection and the resultant modes and patterning behaviours that occur upon an increase in Ra.

After having taken a look at the spatial instabilities that occur in both Hadley flow and RB convection, the concept of textural transitions can be briefly introduced here. This term is used throughout this work to describe the changes in patterns and flow morphologies when considering both the velocity and temperature field of the fluid.

Having provided the reader with some fundamental knowledge regarding standard buoyancy convection, the chief idea on which this thesis takes root is now introduced: thermovibrational convection.

2.7 Thermovibrational convection

2.7.1 Seminal works

The field of thermovibrational convection has been underway since the 1960's and was pioneered by a number of salient authors whose works and contributions to the field are synthesized below.

The problem of thermovibrational convection introduces an additional degree on freedom (i.e. vibrations) to the classical problem of buoyancy convection, therefore two main types of studies can be carried out from here. Firstly, the problem of terrestrial thermovibrational convection, where vibrations are simply added to the system, and secondly, the case of pure thermovibrational convection where microgravity conditions are assumed (i.e where the vibrations are the only driving force). Figure 2.8 illustrates the different configurations possible when considering thermovibrational flow in a square cavity.

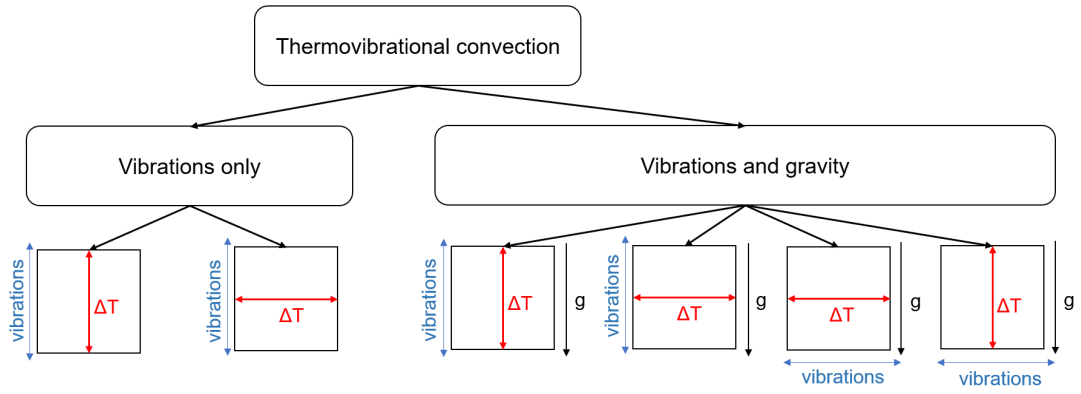

Figure 2.8: Archetype configurations for thermovibrational convection

In addition to these binary problems (where the vibrations, the temperature gradient and the gravity vector are either perpendicular or parallel to one another), other scenarios exist where the angle of vibration (ϕ) is parametrically varied from 0 to 90° with respect to the axis of the thermal gradient.

This section is limited to the consideration of pure thermovibrational convection, as all studies carried out in the scope of this thesis are carried out under the assumption of a microgravity environment. The interested reader is urged to consult the seminal works on thermovibrational flow in terrestrial conditions carried out by Zenkovskaya and Simonenko [29], Geshuni *et al.* [30], Gresho and Sani [31], Biringen and Peltier [32] and Biringen and Danabasoglu [33]. These studies have founded a knowledge base surrounding thermovibrational convection and identified some of the key parameters responsible for the onset of convection, the stability limits and the possible flow patterns adopted by the flow. These key parameters include:

- the direction of the vibrations with respect to the temperature gradient
- the frequency of the vibrations
- the magnitude of the temperature difference
- the shape of the cavity
- the inclusion or exclusion of side boundaries perpendicular to the heated and cooled walls

A key finding that can be reported here before moving to the case where only vibrations are considered is that the works cited above identified an important stabilisation mechanisms in RB type thermovibrational convection: RB convection is mitigated by high frequency vibrations only if they are parallel to gravity.

The concept of thermovibrational flow however was introduced by Gershuni and Zhukhovitskii in 1979 [34] and elaborated upon in further works in 1982 [35]. In these works the static gravity vector is removed and the vibrations become the sole driving force acting on the system. It can be noted here that when thermovibrational convection is considered, the the standard Rayleigh number Ra is replaced by the vibrational Rayleigh number (Ra_ω):

$$Ra_\omega = \frac{b\omega^2\beta_T\Delta T L^3}{\nu\alpha} \tag{2.3}$$

where b is the displacement of the cavity (in m) and ω is the angular frequency (in rad/s).

The notion of instantaneous and time averaged (mean) effects should also be introduced at this stage. The instantaneous effects of thermovibrational flow, are those that can be seen by an observer in real time. Time-averaged effects occur due to the non-linear characteristics of the fluid flow. These two effects are characterised by the aforementioned vibrational Rayleigh number (Ra_ω) and the Gershuni number (Gs) respectively. The Gershuni number is defined as:

$$\begin{aligned} Gs &= \frac{(b\omega\beta_T\Delta T L)^2}{2\nu\alpha} = \frac{(\beta_T\Delta T L)^2}{2\nu\alpha}\left(\frac{g_\omega}{\omega}\right)^2 \\ &= \frac{1}{2Pr}\left(\frac{\beta\gamma}{\omega}\right)^2 = \frac{Pr}{2}\left(\frac{Ra_\omega}{\omega}\right)^2 \end{aligned} \tag{2.4}$$

As the frequency of the vibrations is decreased, the fluctuating flow component tends to become dominant whereas the time-averaged part becomes negligible [36]. In this case Ra_ω is used to characterise the stability boundaries of the flow. While the time-averaged flow scales with Gs, the instantaneous (fluctuating) flow scales with Ra_ω.

One poignant finding in this collection of works , is that by imposing only vibrations onto the system (in the limit of heigh frequency, low amplitude vibrations, also known as *Gershuni's model*), Gershuni and colleagues where able to evaluate the effect of varying the angle of vibration on the flow, without the interference of gravity. The mathematical model used notably in Ref.[35] is shown in Figure 2.9, where the fixed isothermal walls are set at x=0 and x=1, and the angle of vibrations with respect to the temperature gradient (ϕ) is varied (from 0 to 90°) parametrically. The stability boundary (i.e. the value of Gs for which the flow becomes unstable) is reported as a function of (ϕ). In this case, Gershuni and colleagues consider the onset and stability of the time-averaged flow in the framework of a simplified model (potential flow formulation) that assumes infinite frequency and negligible amplitude. In the framework of this approximation, the time-averaged flow is dominant, the fluctuating flow component (difference between effective and time averaged velocity) is negligible.

It is shown that for ϕ=0 (RB type convection) the system is stable for all values of Gs and that the stability limit decreases quasi-proportionally with an increase in ϕ, with the final case of ϕ=90° having a relatively low critical Gershuni number of $Gs = 2129$ [37].

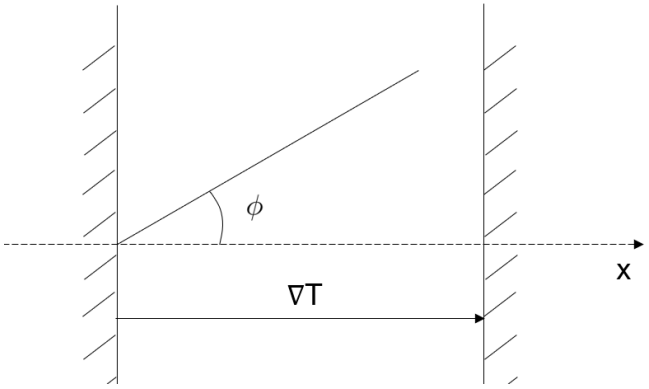

Figure 2.9: Variation of ϕ

Gershuni's work [37] also identifies the patterning behaviour of the flow, where, in the case of $\phi = 90$, two types of flow configurations corresponding to two levels of instability are identified, the first, at the aforementioned critical value of $Gs = 2129$

and the second at $Gs = 2950$. In the first case the fluid is known to develop convective cells where the vertical extension of the individual cells (perpendicular to the x axis in Fig.2.9) is approx. equal to the characteristic length of the cavity. The second instability is described as a two-level cell configuration. This parametric variation of ϕ provides a first interpretation of both the stability limits of Rayleigh-Bénard and Hadley flow type pure thermovibrational convection.

The effect of imposing solid boundaries (i.e a cavity of finite length) is investigated by Gershuni *et al.* [37]. When the vibrations are perpendicular to the temperature gradient (i.e. the Hadley-type flow, as illustrated in Fig.2.10), for the case of the square cavity, mechanical equilibrium is found to be impossible, and convection takes places for all non-zero values of ΔT. This is in keeping with the literature surrounding standard Hadley flow type convection reviewed in Sect.2.3.

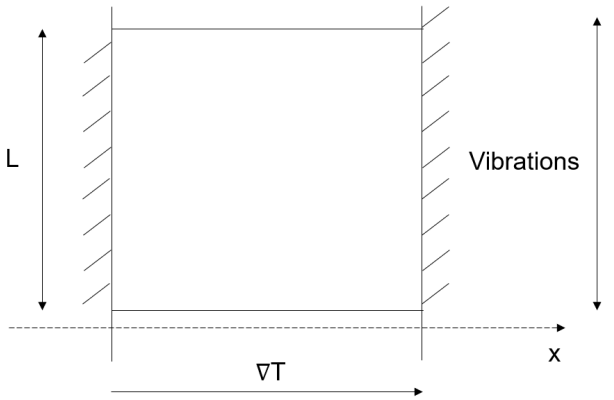

Figure 2.10: Case where vibrations are parallel to the isothermal side walls

The first state, characterized as the *ground state* by Gershuni [37] is the case where four vortices appear (also known as the quaduropolar field). This state occurs for relatively low values of Gs ($Gs < 1.5 \times 10^4$). When Gs is increased beyond this value, a new, three-roll configuration appears (the inversional symmetry pattern), characterised by a central diagonal roll and two corner rolls. These two base states are shown in Fig.2.11.

When L is increased (i.e. the aspect ratio of the cavity is increased) the ground state is still visible for low values of Ra, where the four rolls reside in proximity to the top and bottom solid boundaries and the temperature filed is undisturbed and can

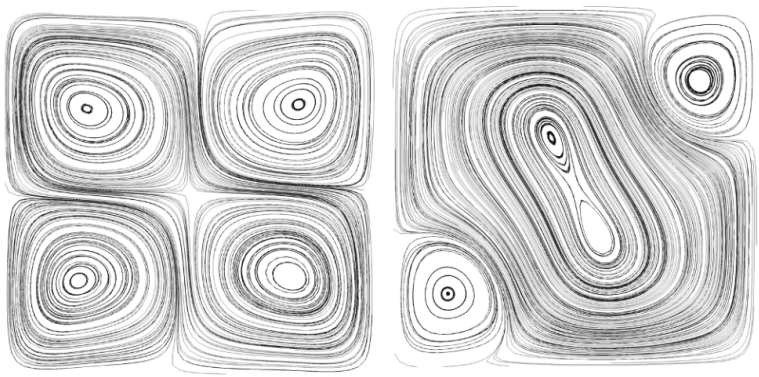

Figure 2.11: The classical transition from the so-called quadrupolar flow field to the inversional symmetry pattern can be seen, as the Gershuni number is increased (from [38])

be assimilated to a linear distribution between the vertical cold and hot plate. It can be noted here that the value of Gs at which the roll-configuration changes to the next metastable state is lower when L is increased. In the case of the infinite layer instability occurs at $Gs = 2129$, resulting in a repetitive cellular pattern across the length of the layer and a significant deviation for the purely diffusive temperature field. This indicates that the metastable ground states identified in this work exist only in a small region of aspect ratios and Gershuni numbers.

Whilst reviewing the literature surrounding pure thermovibrational convection, it was found that only one study exists treating solely the problem of pure thermovibrational convection for the case where vibrations are parallel to the temperature gradient, in a square cavity. Hirata *et al.* [36], investigated the effect of increasing Ra_ω and Ω simultaneously, where Ω is the non dimensional frequency of the vibrations defined as:

$$\Omega = \frac{\omega L^2}{\alpha} \tag{2.5}$$

Where ω is the dimensional angular frequency of the vibrations defined as: $\omega = 2\pi f$ (in rad/s), and f is the frequency (in Hz).

This parametric investigation identified four principal flow regimes. There are split into four possible categories, namely, Synchronous (SY), Subharmonic (SU), Non-periodic (NP), and Stable (ST) solutions. Unfortunately, these authors limited them-

selves to considering values of the vibrational Rayleigh number in the range ($10^4 \leq Ra_\omega \leq 10^5$, the constraint on the upper value being essentially an outcome of the limited computational resources available at that time). The study reports the well-known stabilization of thermovibrational flow when the frequency of vibrations is increased (Simonenko and Zen'kovskaja [29]; Simonenko [39]; Gershuni and Zhukhovitskii [34]; Gershuni *et al.* [35]; Gershuni and Zhukhovitskii [40]). A more in-depth account of the flow characteristics pertaining to these four regimes is given in Chap.4, where the work of Hirata *et al.* [36] is extended to higher values of Ra_ω.

Now that the base concepts of thermovibrational flow have been introduced, the next section explores the relationship between fluid dynamic experiments and the disturbances that occur when considering microgravity platforms.

2.7.2 Applicability to space experiments and orbiting platforms

Whilst the works discussed in Section 2.7.1 originally stemmed from pure scientific curiosity, from the 1970's, the advent of orbiting platforms gave researchers a concrete purpose to continue the investigation into pure thermovibrational flow. The first crewed orbiting platform, Salyut 1, was launched by Russia in 1971, followed by a series of launches under the Salyut project ending with Salyut 7 in 1991. The launches of Skylab (by the Americans) in 1973, Mir (by the Russians) in 1986 and the International Space Station (ISS) in 1998 (an international collaboration including USA, Europe, Japan, Russia, and Canada) solidified the continuous presence of humans in space and subsequently the possibility for microgravity experiments. Researchers however quickly found out that the microgravity environment offered by the platforms was plagued with small vibrations known as g-jitters. This becomes problematic when considering that fluid dynamic processes are can be drastically influenced by (even small) perturbations.

Indeed, as early as 1975, Spradley [41] *et al.* confirms analytically, that for a closed differentially heated cavity (Hadley flow type thermovibrational convection), g-jitter type vibrations can cause important changes in the flow structure and the temperature distribution of the fluid, conjecturing that the most vulnerable processes to g-jitter disturbances would include crystal growth and separation procedures. They also found

that g-jitter type vibrations can be decomposed into an oscillatory part and a mean part and can lead to two types of flow: an instantaneous flow and a mean flow where the mean flow is more deterministic of the fluid response both in terms of heat transfer and in terms of flow field.

The oscillatory velocity and temperature fields with zero time-averaged values generated by g-jitters, are investigated by Kamotani *et al.* [42] (1981), who considered vibrations of similar characteristics to those produced by g-jitters to assess the effect of the 'real' orbiting platform environment on a buoyancy convection experiment and material processing (for the Hadley type configuration). At this point in time, it is well established that the most disruptive case, in terms of convection, is the cases where vibrations are perpendicular to the flow (as has been discussed in the previous section).

In 1994 Nelson [43] published an extensive review on the state of knowledge (at the time) of g-jitters where she presents an extraordinarily detailed characterisation of the different types and sources of g-jitters and the implication of these on buoyancy convection experiments and materials processing. She identifies three predominant types of disturbances: *quasisteady*, *oscillatory* and *transient* disturbances. Quasisteady disturbances, occur due to external forces on the spacecraft, for example aerodynamic drag, Coriolis accelerations and solar radiation pressure. Oscillatory disturbances occur mostly due to crew activities and operation of machinery. Lastly, transient disturbances, occur due to space vehicle manoeuvres and crew motions. An example of this type of disturbance can be seen in Fig.2.12.

The signal captured by Dunbar *et al.* [44] (shown in Fig.2.12) on the orbiting platform Space Shuttle Columbia is just one example of the oscillatory disturbances caused by crew activities. These oscillatory disturbances are the most dangerous when considering fluid dynamic experiments as these sinusoidal or quasi-sinusoidal forces induce thermovibrational flow in fluid experiments designed to sit in an undisturbed microgravity environment.

Although the signal used as an example in Fig.2.12 shows a relatively low frequency, most oscillatory frequencies are high frequency ones as reported by Nelson [43]. Monti and Savino [45, 46], tackled this problem where they evaluated the tolerability limits for

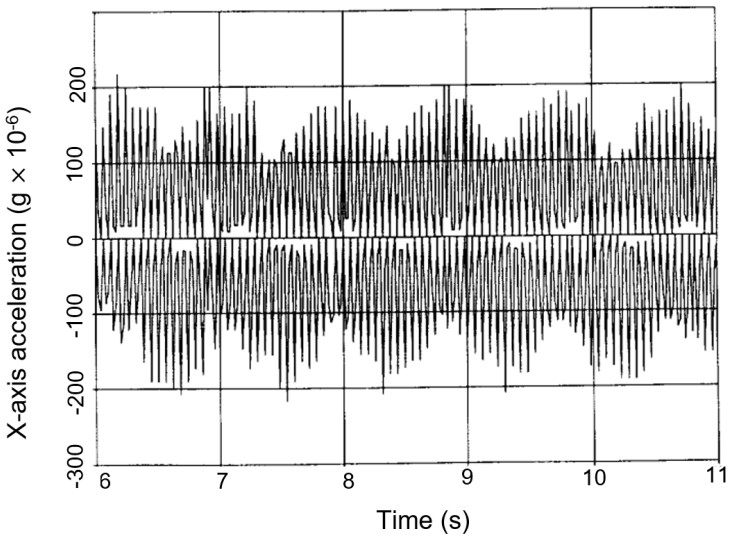

Figure 2.12: Oscillatory disturbance on the microgravity environment of the Space Shuttle Columbia due to a crew member walking on the treadmill, adapted from [44]

fluid dynamic and material science experiments experiments when high frequency, low amplitude vibrations are imposed onto a differentially heated cavity. They found that convective flow patters appear in the streamlines of the flow, where the quadrupolar field and the inversional symmetry patterns observed by Gershuni and colleagues [34, 35] are obtained. Shortly after this, Monti *et al.* [47] confirm that thermovibrational effects induced by high frequency oscillatory disturbances imposed perpendicular to the temperature gradient are the most disruptive, producing the maximum disturbances of the temperature fields. These works take into account the g-jitter scenarios on the International Space Station as this is the current platform used for long duration microgravity experiments. In these works, the presence of g-jitters is seen as detrimental and efforts are made to evaluate when the ARIS (Active Rack Isolation System) is needed when considering a fluid dynamic or materials processing experiment, which allows researchers to attenuate the effect of g-jitters.

At this point the reader may be wondering why the T-PAOLA experiment, does not simply take advantage of the already existing g-jitter present on the ISS in order to induce thermovibrational flow. Why is the science team imposing a set range of frequencies and amplitudes onto the fluid cells? The answer is that the high frequency,

low amplitude vibrational regimes that occur on the ISS encapsulate only a very narrow range of the map of non-dimensional parameters associated with thermovibrational convection. The aim of the project is to push the boundaries of current knowledge and explore a more comprehensive region of the map of these parameters.

From Sect.2.2 to 2.7, buoyancy convection, including the classic Hadley flow and RB type convection has been introduced. The concept that varying the parameters of a system (2D vs 3D, choice of thermal boundary conditions, etc.) can influence the response of said system has also been introduced, as has the fundamental concept of thermovibrational flow an its applicability to space-based fluid dynamic research. In the previous sections, much of the referenced literature deals with the case where convection occurs, however, the regime of the flow is classified as laminar. In the scope of this thesis, one aim is to explore scenarios where thermovibrational flow becomes chaotic. Therefore, the next section provides the reader with the relevant concepts surrounding the transition to chaos in buoyancy convection problems.

2.8 An insight into chaos in fluids and related transition mechanisms

2.8.1 Turbulence and chaos

Despite their technical connotations, both the words *Turbulence* and *Chaos* have found there way into our everyday lives and are used to describe many common scenarios. At first glance, the words may seem like synonyms, however the following differentiation can be made: it is true that all turbulent flows are chaotic, however, not all chaotic flows are turbulent. *Turbulence* is onset by specific, organised parameters in a fluid system and is identifiable namely by a lack of periodicity. For Newtonian fluids, turbulence is observed most commonly in open systems such as water through a pipe or air over a tennis ball, and is instrumental in many industrial applications reliant on mixing flows where the onset of turbulence depends primarily on the Reynolds number of the flow. Turbulence also occurs in closed systems (i.e no inlet or outlet), where the primary driving force is the buoyancy force due the temperature gradient coupled with the

gravity force (or vibrations in the case of thermovibrationally driven flow, as described in Sects.2.2 to 2.7). For example, in terrestrial conditions, turbulent flow both in the case of Hadley flow and Rayleigh-Bénard convection is achieved only when a given temperature difference is exceeded or when the Rayleigh number reaches a critical value. In this work, the terms turbulence and chaos are therefore used interchangeably as the only type of chaos considered here is turbulence. The definition of chaos and the specific mechanisms that fluid dynamic systems undergo before becoming chaotic are discussed in the following sections, attention is paid to introduce salient works dealing with chaos in thermal flows.

2.8.2 Transitions to chaos in buoyancy convection

Edward Lorenz, sensitivity to initial conditions and strange attractors

One of the first characterisation of chaos in a dynamical systems was carried out by Edward Lorenz in 1963 [48]. In this work the hydrodynamics of weather patterns are considered. Lorenz expressed a closed hydrodynamical system of finite collection of molecules, where the governing laws can be expressed finite set of ordinary differential equations, finally developing a simplified mathematical model for atmospheric convection as follows:

$$\frac{dx}{dt} = \sigma(y - x) \tag{2.6}$$

$$\frac{dy}{dt} = x(\rho - z) - y \tag{2.7}$$

$$\frac{dz}{dt} = xy - \beta z \tag{2.8}$$

This simplification is made possible by considering a two dimensional uniformly heated fluid layer from below where the rate of change of three quantities with respect to time are evaluated whereby, x is proportional to the rate of convection, y to the horizontal temperature variation, and z to the vertical temperature variation. The constants σ, ρ , and β are system parameters proportional to the Prandtl number, the Rayleigh number, and the physical dimensions of the layer itself and are real positive

integers. In Lorenz's work the values of σ, ρ, and β are taken as: σ=10, ρ=28 and β=8/3. By setting these initial conditions, so called *attractors* emerge.

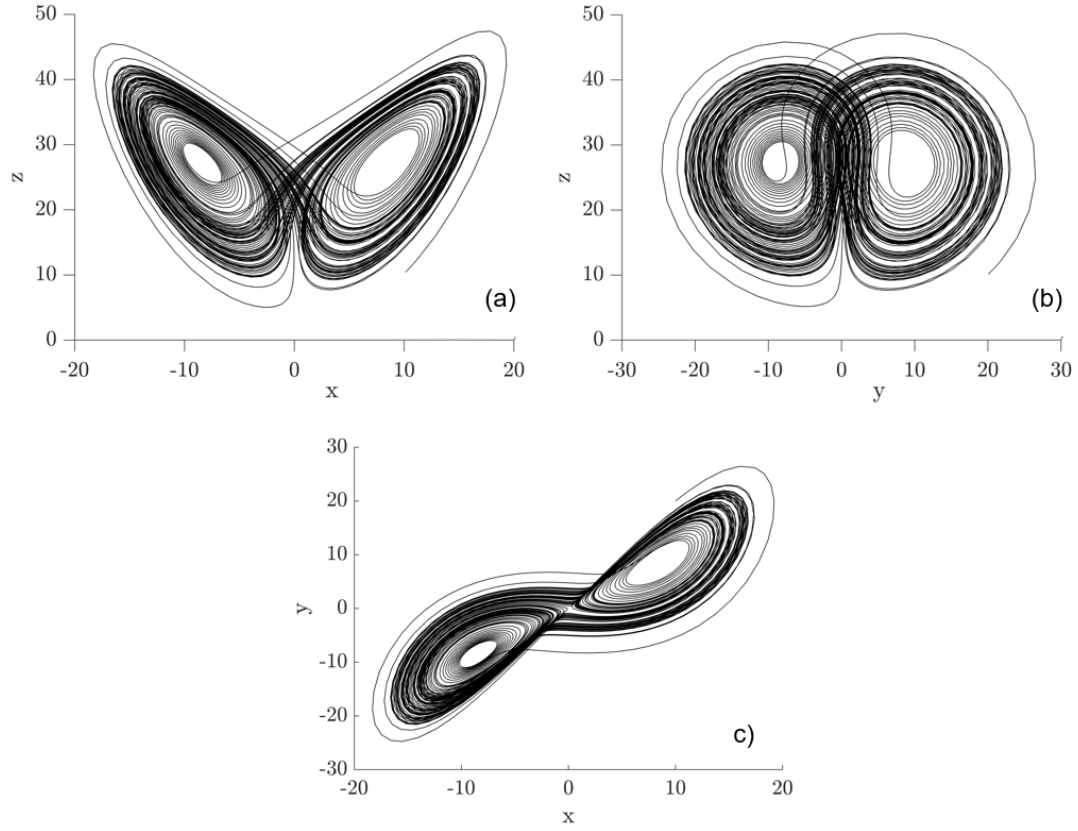

Figure 2.13: Lorenz attractor for σ=10, ρ=28 and β=8/3 on the interval [0, 100]

Looking at the attractor shown in Fig.2.13, each point of the attractor represents a possible solution to the set of Eqs.2.6-2.8. The attractor shows that these equations are therefore deterministic, implying that although many solutions exist, no solutions outside the attractor are possible for a given set of initial conditions. This introduces well the concept of sensitivity to initial conditions (SIC). If the values of σ, ρ and β are changed a new attractor will emerge. Indeed this SIC was solidified when Lorenz was working on a similar problem involving 12 variables related to the characteristic of a flow. When continuing his numerical work, one variable was rounded-off of at three decimal places when the original value boasted a precision off six decimal places. The difference in results compared to the original behaviour of the system due to this round-

off error was catalyst to Lorenz's understanding of the effect of initial conditions. This concept is popularly known as the butterfly effect, where if a butterfly bats its wings in one location, a tornado could emerge as a result in a different location due to the propagation of small changes.

Having introduced the concept of an 'attractor' here, it is necessary to devote a few lines to it's definition. An attractor exists in the *phase space* of a system. Where the phase space is the space of variables that specify the state of the system. In a review, Grebogi *et al.* [49] provide a straightforward example of the attractor of a damped pendulum. Considering the 2D phase-space, where the distance travelled by the pendulum in represented by the x axis and the y axis represents the pendulum velocity $\frac{dx}{dt}$, the final solution to the system will be at the origin of the phase space (0,0) as no external forces are applied to the pendulum, therefore it will end-up at rest. This means that the resulting set is of dimension zero as only one solution exists as $t \to \infty$, if the pendulum was periodical driven, the final set would be of dimension 1, characterised by the systems limit cycle. When considering non-linear dynamical systems however, fractal sets of solutions emerge, leading to complex attractors such as the aforementioned Lorenz attractor. In this case it is referred to as a *strange attractor*.

From this section, a few important concepts have been introduced. Firstly, the concept that chaos in fluid system is characterised by non-periodicity and therefore is very difficult to predict, however these systems are deterministic and therefore not random. Secondly, it has been shown that that the behaviour of the system depend largely on the specific initial conditions. Finally it has been shown that chaotic systems can be represented by a strange attractor in the phase space diagram. Now that these fundamental concepts have been introduced the mechanisms by which a system becomes chaotic are presented below.

2.8.3 Routes to chaos in closed systems

The classical mechanism to chaos in flows follows the intuitive path of: steady $\to$ periodic $\to$ quasi-periodic $\to$ turbulent, as demonstrated by Paolucci and Chenworth [50], Goldhirsh [18] and Villermeaux [51]. Indeed upon an increase in control parameter

(typically the Rayleigh number), the flow becomes time dependent and a self-sustained periodic behaviour occurs, this periodic behaviour becomes quasi-periodic as more energy is imparted into the system, ultimately resulting in a chaotic flow. This periodicity is evaluated by sampling a characteristic variable of the flow such as a temperature or velocity probe and monitoring its evolution over time. This temporal signal can then be convected into a frequency spectrum using a Fast Fourier Transform (FFT). From here the frequency spectrum (Discrete Fourier Transform (DFT) or the power density spectrum (PDS)) can be obtained and used to evaluate the regime of the flow, where the DFT shows the amplitude and phase of each harmonic component of the signal and the PSD shows the power distribution over the different signal frequencies.

In the quest for a global understanding for stability limits and flow characterisation in fluid systems, and more specifically in buoyancy convection, authors have dedicated their time to investigate particular mechanisms that lead to chaotic behaviours.

A collection of studies undertaken by Ruelle, Takens and Newhouse [52–54] examined the evolution of a fluid flow when the control parameters (i.e the Rayleigh number) is increased in thermally driven flows. Indeed, it is known that as a fluid is thermally excited, the flow can become time-dependent i.e. the flow assumes a periodic behaviour, even in the absence of forced vibrations. The *Ruelle-Takens-Newhouse scenario* dictates that when three unrelated frequencies appear in the frequency spectrum of the flow, it is deemed chaotic. Another route to chaos is the *Feigenbaum scenario*. This scenario occurs when an infinite number of period-doubling bifurcations occur in the frequency spectrum. The last transitional mechanism to be brought to the readers attention is the *Manneville-Pomeau scenario*, which dictates that a flow can enter an intermittency regime, when the flow can be stable for a period of time and spontaneously enter a unstable chaotic regime, and then revert back to a stable oscillatory regime [55].

These tools are essential in characterising transition mechanisms and are not mutually exclusive, meaning that systems can undergo any number of transitional mechanisms resulting in chaos. For example, the works of Guzman and Amon [56] and Blondeaux and Vittori [57] provide excellent examples of possible transition to chaos. They found that upon an increase in control parameter the flow undergoes a Feigen-

baum scenario resulting in a series of period locking phenomena, in turn resulting in a Ruelle-Takens-Newhouse scenario.

In the frame work of thermovibrational flow, the works of Lizée and Alexander [58] where the first to examine transition to chaos in thermovibrational flow. They found that, chaos occurs (for relatively low values of Ra_ω) through a sequence of bifurcations characteristic of the Feigenbaum scenario. Where, upon an increase in Ra_ω the first additional frequency to appear is $\Omega/2$ where Ω is the forcing frequency. The authors also found a Pomeau-Manneville intermittency near the limits of of the unstable region, hence demonstrating that the transition mechanisms identified in standard buoyancy convection also take place in thermovibrational flow.

In this section, fundamental concepts surrounding chaotic flows and transition mechanisms in buoyancy and thermovibrational convection have been introduced. These concepts will be instrumental in characterising flow regimes and responses in the results section of this thesis (Part.II).

The next section is dedicated to the introduction of the different phase types considered in this work. Indeed, although thermovibrational flow is fascinating in it's own right, the T-PAOLA project is based on the concept of "multiphase" thermovibrational convection. In order to tackle this problem, some concepts underpinning multiphase flows must first be introduced.

2.9 An introduction to multiphase flows and particle dynamics

The field of multiphase flows is one that spans many disciplines, and a review of the origins of, and advances in multiphase studies would be unrealistic in the framework of this thesis. In order to keep this section concise and to the point, the salient topics touched upon in this thesis are elaborated upon appropriately. This includes some general descriptions of fluid systems and flow types, important characteristic parameters of the dilute phase (i.e. the particles) and recent advances in particle accumulation in thermal flows, and more specificity in the context of thermovibrational flow.

2.9.1 Flow types and dilute vs dense flows

Before entering into a discussion about the specific classification of flow types, it is worth introducing the terminology used to describe multiphase flows.

- *Multiphase* refers to the presence of two *or more* phases in a system. This can take the form of many configurations, the most common being: liquid-solid, liquid-gas, liquid-liquid and flows including all three phases liquid-solid-gas flows.
- A *continuous phase* is the phase that is represented as a continuum, whereby mass can pass from one point to another whilst staying in the medium. For example, a cavity filled with liquid and gas, both phases considered are continuous.
- A *dispersed phase* represents the phase that is separated by the continuous phase. For example particles of sand or gas bubbles in liquid are considered to be the dispersed phase and are surrounded at all times by the continuous phase.

Now that this vocabulary has been introduced, a description of *dilute* versus *dense* flows can be provided. A *dilute* system is one where the fluid influences entirely the motion of the particles and the particles have little to no effect on the fluid. This is due to the fact that a small quantity of particles is present in the system. This also means that particles are far enough away from each other to neglect any effects of particle collisions. Quantitatively, a flow is classified as dilute if $\alpha_d < 0.001$, where α_d is the volume faction of the dispensed phase defined as [59]:

$$\alpha_d = \frac{V_p N_p}{V_f} \tag{2.9}$$

where V_p is the volume of one particle, V_f is the volume of fluid and N_p is the number of particles in the system. Following the definition of dilute flows, for dense flows $0.001 < \alpha_d$. Dense flow can also be separated into two sub-categories including collision-dominated and contact-dominated (summarised in Table 2.1). In the case of collision dominated flow $0.001 < \alpha_d < 0.1$ and for contact dominated flows $\alpha_d < 0.1$.

In this thesis, when multiphase thermovibrational flow is considered, studies will be conducted only on dilute systems. This is due to the fact that a dilute system is

Table 2.1: Characterisation of dilute and dense flow in terms of volume fraction (α_d)

Dilute flow	**Dense flow**	
	Collision-dominated	Contact-dominated
$\alpha_d < 0.001$	$0.001 < \alpha_d < 0.1$	$\alpha_d > 0.1$

considered for the experiment to be conducted under the T-PAOLA framework and also because the modelling of the flow becomes inherently more complicated when particle collisions and back (coupled) influences are considered.

2.9.2 Particle accumulation in fluids

One of the deterministic factors in the behaviour of multiphase flow is not only the type of flow considered (i.e., dense or dilute), but also the properties of the particles themselves. These properties include the particle Stokes number (St), defined as:

$$St = \frac{2}{9}\frac{R_p^2}{L^2} \tag{2.10}$$

where R_p is the radius of the particle and L is the characteristic length of the cavity [59].

Another deterministic factor of the response of the multiphase system is the density of the particle with respect to the fluid, denoted by ξ and defined as:

$$\xi = \rho_p/\rho_f \tag{2.11}$$

This density ratio is an important factor as, in the presence of gravity, the particles will rise or fall in the fluid depending on the value of ξ. If $\xi > 1$, the particles will tend to fall to the bottom and when $\xi < 1$ the particles will tend to rise to the top of the fluid.

Haller and Sapsis [60] and Sapsis and Haller [61, 62] found that owing to the finite size (St) and mass (ξ) of particles, which drives a mismatch between their velocity and that of the carrier flow, the mathematical (and physical) properties of these two kinematic vector fields are essentially different. While the fluid velocity obeys a divergence-

free condition (which implies the fluid volume is conserved), the total volume of particles is not bound to this mathematical restriction. As a result, no requirement for the volume occupied by a certain number of particles to be conserved exists and, accordingly, the spacing among them can vary in time while they are transported inside the fluid. It is by virtue of this simple principle or concept that 'sinks' for particles can exist in the physical space, i.e. specific loci where particles can cluster (also known as "attractors", as previously described in Sect.2.8).

In the context of thermal flows, Yarin *et al.* [63], first investigated the distribution of particles suspended in convective flows in differentially heated cavities, where small density differences are investigated. They found that when the fluid pattern takes on a uni-cellular roll (as described in Sect.2.3), or upon an increase in Ra a parallel set of cellular rolls, when a single particle in inserted into the fluid, it will follow a circular trajectory normal to the circulation plane. Secondly, they found that when the density of the particles ξ is varied below and above $\xi = 1$, the particles accumulate more towards the cold or hot side of the cavity respectfully. This was later also confirmed for moderate values of Ra by Gereltbyamba and Lee [64] and higher values of Ra by Puragliesi *et al.* [65] and Patocka [66].

As the value of Ra is increased and turbulent convection is achieved, inertial particles accumulate in the inner or outer regions of the eddies produced in the flow, depending on the value of ξ. This phenomena is known as preferential concentration. Maxey *et al.* [67] demonstrated that the effect of inertia causes light particles to accumulate in areas of strong vorticity and heavy particles to accumulate in areas of high strain-rate (i.e. the centre and the outer region of the eddies respectively). This was also confirmed by Squires and Eaton [68].

Works treating the accumulation of particles in turbulent flow, was extended by Fallon and Rogers [69] to include the microgravity scenario. When analysing the behaviour of solid particles in air (where the onset of turbulence is induced by forced convection, i.e. fans). They observed experimentally that for $\xi > 1$ strings of particles collect in the high strain rate regions, in agreement with Maxey *et al.* [67] and Squires and Eaton [68].

This subsection has introduced some key concepts relating to particle accumulation in fluids, however, the principal on which the T-PAOLA experiment bases itself on is particle accumulation in thermovibrational convection. It will come to no surprise to the reader that the complex dynamics of thermovibrational convection detailed in Sect.2.7, leads to more involved particle accumulation phenomena, to which the next section is dedicated.

2.9.3 Particle accumulation in thermovibrational convection

The first seminal work on particle accumulation in thermovibrational convection was undertaken by Lappa [1], where particles are dispersed in a differentially heated square cavity and subject to vibrations, all in microgravity conditions. The main findings of this work is that both the properties of the thermovibrational system (Ra_ω, Ω, ϕ and γ), and the properties of the particles (St and ξ) contribute to the formation and destruction of particle accumulation structures (PAS) in the fluid. The configuration considered by Lappa [1] is shown in 2.14.

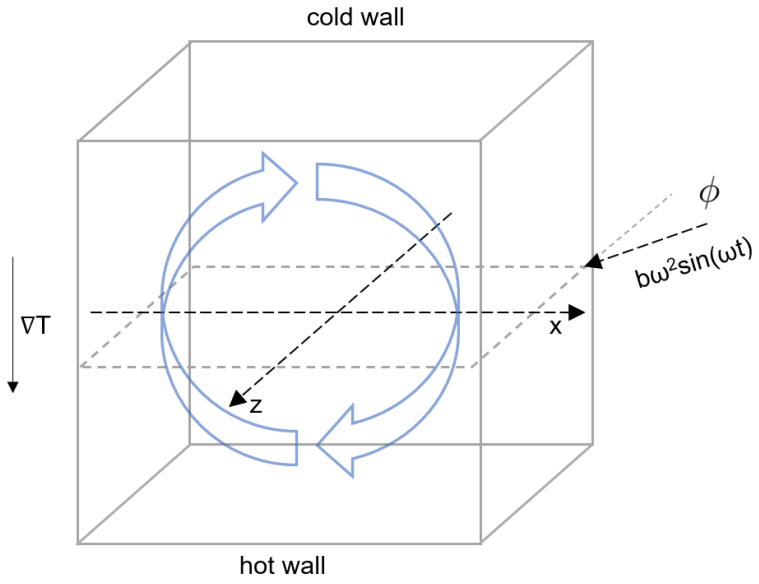

Figure 2.14: Illustration of the variation of ϕ from $\phi = 0$ when the vibrations are aligned with the x axis and $\phi = \pi/2$ when aligned with the z axis

A new non-dimensional parameter γ is introduced, where γ is the non-dimensional amplitude of the acceleration from the vibrations defined as:

$$\gamma = \frac{\omega L^2}{\alpha} \tag{2.12}$$

Starting from the case where the particles are uniformly distributed in the cavity, the structures form gradually over time due to the combined effects of the convective motion of the fluid induced by thermovibrational effects, the particle properties and the effect of the fixed walls perpendicular to the vibrations. Fig.2.15 shows the most celebrated and recognised PAS in the field of thermovibrational convection.

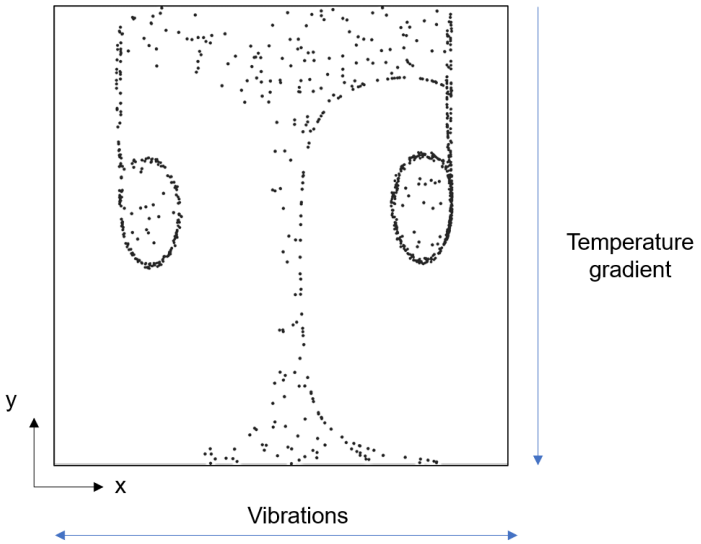

Figure 2.15: Tree like PAS obtainable when multiphase thermovibrational flow is considered

Looking fist at the morphology of structures that form, Lappa [1] reports *tubular* structures when the vibrations are aligned with the x axis ($\phi = 0$) and *compact* structure when ($\phi = \pi/2$ and $\pi/4$). The tubular structures take on a tree like form as shown in Fig.2.15. As can be seen, a reflectional behaviour is visible about the y axis at x=0.5.

The *compact* structures posses reflectional symmetries and are ubiquitous pattern types observed in thermovibrational problems considered by Lappa [70]. These are classified in Fig.2.16.

Now moving to the specific effects that each parameter has on the formation time of the PAS, Lappa [1] showed that an increase in Ω leads to a decrease in the formation time meaning that for higher vibrational frequencies the structures take less time

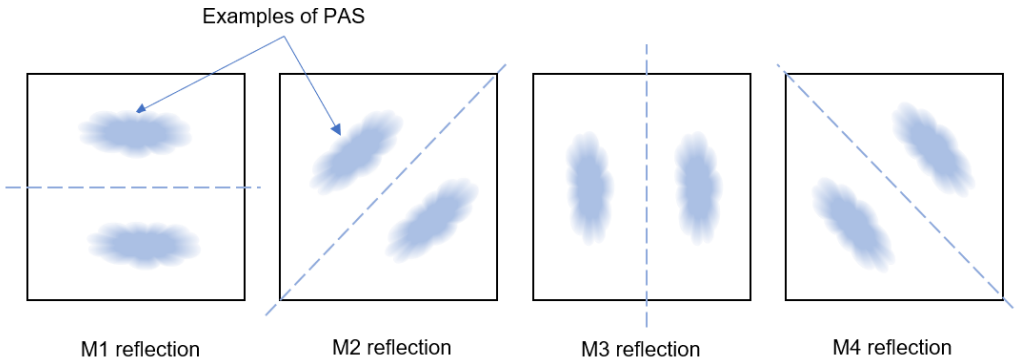

Figure 2.16: Reflection symmetries obtained in the square cavity when multiphase thermovibrational convection is considered

to form. This formation time can also be decreased when the Stokes number (St) is increased (i.e., the size of the particles in increased). The particle/fluid density ratio (ξ) is also a contributing factor where the formation time decreased when the value of ξ departs from $\xi = 1$ [71].

When looking at the morphology and more specifically, the size of the PAS, it has been shown that upon an increase in (St), the particle structures become more compact, for example, the vertical and horizontal extension of the lobes of the tree shown in Fig.2.15 decrease. Indeed, the size of the closed-circuit structures is the most manipulable characteristic when it comes to controlling the PAS. In addition to St influencing the size of the structures, the value of γ is also instrumental in determining the final extension of the closed loops. This was shown by Lappa and Burel [71], where an increase in γ leads to a decrease in the vertical and horizontal extensions of the PAS. This characteristic was also shown to depend on ξ where the extension of the PAS along the x, y and z axes, decreased when the value of ξ departed from $\xi = 1$.

The PAS formed in thermovibrational flow have also been found to also break the symmetry patterns shown in Fig.2.16 as was found by Lappa and Burel [71]. Indeed, when the effects of the time-averaged flow are more important than those of the instantaneous flow, as described in Sect.2.7.1, the PAS can display inherent asymmetry. This asymmetry occurs even if the streamlines of the mean flow are symmetrical, and

take on, for example the quadrupolar field or the inversional symmetry pattern shown in Fig.2.11.

This subsection can be summarised by stating that many factors influence the formation time, morphology and symmetry of the PAS. The physical laws discerning the formation of PAS are notoriously difficult to determine, however, increased investigation onto the filed of multiphase thermovibrational flow and further exploration of the map of non-dimensional parameters will contribute to the unavailing of this extraordinary phenomenon.

2.10 Chapter summary and ensuing research questions

This literature review has provided a comprehensive review of many fascinating topics and focuses mainly on introducing necessary prerequisite information and tools in order to prepare both the author and the reader to tackle novel problems concerning both single phase and multi-phase thermovibrational flow.

Indeed it has been identified that the behaviour of a thermovibrational system depends greatly on the direction of the temperature gradient in relation to that of the vibrations and that the case of RB type flows remains relatively unexplored therefore, the following question can be posed:

What thermovibrational effects can be achieved in a fluid when the direction of the vibrations is changed (from Hadley type flow to RB type flow)?

From this review it has been identified that a gap exists, whereby researchers have not yet considered the case where the strength on the convection is increased to the point where a turbulent flow is achieved, leading to the question:

What thermovibrational effects can be achieved in a fluid when turbulent thermovibrational convection is considered?

It has also been shown that the thermal boundary conditions can influence the response of a fluid system when natural convection is considered. However, the effects of varying the thermal boundary conditions at the side walls of a pure thermovibrational system are largely unknown, giving rise to the following question:

What thermovibrational effects can be achieved in a fluid when various sets of thermal boundary conditions are applied to the system?

Finally, it has been shown that when multiphase thermovibrational flow is considered, the numerous degrees of freedom associated with the system parameters makes it challenging to evaluate the individual effects of each parameter. Therefore in this work, an effort is made to answer the following question:

How do thermovibrational effects modify the behaviour of particle accumulation structures in multiphase systems?

Now that the gaps in knowledge and associated research questions have been identified, the next section is dedicated to the mathematical framework employed in this thesis.

Chapter 3

Mathematical framework

From Chap.2, the foundations of the problem have been laid down from a physical point of view and the gap in knowledge has been identified.

Before solving these problems numerically, one must first introduce the required mathematical framework. This chapter will therefore firstly introduce some commonly used non-dimensional numbers in the context of numerical simulation of thermovibrational convection. Secondly, governing equations and the related solution methods used in this work both for single phase and multiphase flows are presented.

3.1 Non-dimensional numbers

Although most non-dimensional numbers have already been introduced as this stage, in this section, a small recapitulation of these is provided.

The body force responsible for fluid flow in thermovibrational convection is produced by a sinusoidal displacement of the cavity with respect to time in addition to a temperature difference imposed either along or parallel to, the direction of shaking. The time periodic displacement (i.e., the vibrations) can be modelled mathematically as:

$$\underline{s}\,(t) = -bsin\,(\omega t)\,\underline{\hat{n}} \tag{3.1}$$

where b is the amplitude of the displacement (in m), $\omega = 2\pi f$ is the angular frequency of the displacement (in rad/s), and $\underline{n}$ is the unit vector along the direction of

vibrations. The ensuing time-varying acceleration can formally be obtained by taking the second derivative of Eq.3.1, which reads:

$$\underline{s}\,(t)' = -b\omega cos\,(\omega t)\,\underline{\hat{n}} \tag{3.2}$$

$$\underline{g}\,(t) = b\omega^2 sin(\omega t)\underline{\hat{n}} \tag{3.3}$$

and satisfies the condition:

$$\frac{\omega}{2\pi}\int_0^{2\pi/\omega} \underline{g}(t)dt = \frac{\omega}{2\pi}\underline{g}_\omega\underline{\hat{n}}\int_0^{2\pi/\omega} sin(\omega t)dt = -\frac{1}{2\pi}\underline{g}_\omega\underline{\hat{n}}[cos(\omega t)]_0^{2\pi\omega} = 0 \tag{3.4}$$

which shows that its time-averaged value over one period of oscillation $2\pi/\omega$ is zero.

Follows the well-known Prandtl number:

$$Pr = \frac{\nu}{\alpha} \tag{3.5}$$

where ν is the fluid kinematic viscosity and α is the fluid thermal diffusivity. The vibrational Rayleigh number (Ra_ω), analogue to the classical Rayleigh number used in standard gravitational convection problems (Ra), can be introduced by simply replacing the steady gravity vector with $\underline{g} = b\omega^2$.

$$Ra_\omega = \frac{b\omega^2\beta_T\Delta T^* L^3}{\nu\alpha} \tag{3.6}$$

where β_T is the coefficient of thermal expansion ΔT^* is the temperature difference across the system and L is the characteristic length of the cavity. Lastly, the non-dimensional angular frequency Ω of the vibrations can be expressed as:

$$\Omega = \frac{\omega L^2}{\alpha} \tag{3.7}$$

These non-dimensional numbers are employed when non-dimensionalising the governing equations, presented in the next section.

3.2 Governing equations

The balance equations for an incompressible flow, for mass, momentum and energy are given in their dimensional form as:

$$\underline{\nabla} \cdot \underline{V}^* = 0 \tag{3.8}$$

$$\rho \frac{\partial \underline{V}^*}{\partial t} + \rho \underline{\nabla} \cdot [\underline{V}^* \underline{V}^*] = -\underline{\nabla} p^* + \mu \nabla^2 \underline{V}^* + \rho \underline{g} \tag{3.9}$$

$$\frac{\partial T^*}{\partial t} + \underline{\nabla} \cdot [\underline{V}^* T^*] = \alpha \nabla^2 T^* \tag{3.10}$$

The non-dimensional form of the governing equations can be obtained by scaling the length by the referenced distance (L), the velocity by (α/L) the time by (L^2/α) and the pressure by ($\rho_0 \alpha^2/L^2$). By doing so the continuity equation becomes:

$$\underline{\nabla} \cdot \underline{V} = 0 \tag{3.11}$$

Where V is the non-dimensional velocity. For the momentum equation, the Boussinesq approximation can be applied. As the flow under consideration is buoyancy driven, the Boussinesq approximation can be used in order to take into account variations in density only in the terms multiplied by the buoyancy term whereby:

$$\rho = \rho_0 - \rho_0 \beta_T (T^* - T_0) \tag{3.12}$$

By applying the Boussinesq approximation and assuming that the individual term ρ_0 is absorbed into the modified pressure term $p^* = \rho_0 g h$, where $\rho_0 g h \approx 0$, the momentum equation becomes:

$$\frac{\partial \underline{V}^*}{\partial t^*} = -\underline{\nabla} \cdot [\underline{V}^* \underline{V}^*] + \frac{1}{\rho_0} \underline{\nabla} p^* - \mu \nabla^2 \underline{V}^* - \underline{g} \left[\beta_T \left(T^* - T_0\right)\right] \tag{3.13}$$

Replacing the buoyancy term by the time varying acceleration presented in Eq.3.3, the momentum equation becomes:

$$\frac{\partial \underline{V}^*}{\partial t^*} + \underline{\nabla} \cdot [\underline{V}^* \underline{V}^*] + \frac{1}{\rho_0} \underline{\nabla} p^* = \mu \nabla^2 \underline{V}^* - b\omega^2 sin(\omega t) \left[\beta_T \left(T^* - T_0\right)\right] \underline{\hat{n}} \tag{3.14}$$

The non-dimensional temperature is defined as $T = (T^* - T_0)/\Delta T$ giving $T\Delta T = (T^* - T_0)$. By applying this non-dimensionalisation, as well as the aforementioned scaling factors for distance, velocity, time and pressure the momentum equation becomes:

$$\begin{aligned} \frac{\partial \underline{V}^*}{\partial t^*} \left(\frac{\alpha^2}{L^3}\right) = -\frac{1}{\rho_0} \underline{\nabla} p^* \left(\frac{\rho_0 \alpha}{L^3}\right) - \nabla \cdot (\underline{V}^* \underline{V}^*) \left(\frac{\alpha^2}{L^3}\right) \\ + \mu \nabla^2 \underline{V}^* \left(\frac{\alpha}{L^3}\right) - b\omega^2 sin \left(\frac{\omega L^2}{\alpha}\right) (\beta_T T \Delta T) \underline{\hat{n}} \end{aligned} \tag{3.15}$$

which, when simplified becomes:

$$\frac{\partial \underline{V}}{\partial t} = -\nabla p - \nabla \cdot (\underline{V} \underline{V}) + Pr \nabla^2 \underline{V} - Pr Ra_\omega T sin\left(\Omega t\right) \underline{\hat{n}} \tag{3.16}$$

Finally, the same approach is applied to the energy equation giving:

$$\frac{\partial T^*}{\partial t^*} \left(\frac{\alpha}{L^2}\right) + \underline{V^*} \cdot \nabla T^* \left(\frac{\alpha}{L^2}\right) = \alpha \nabla^2 T^* \left(\frac{1}{L^2}\right) \tag{3.17}$$

giving:

$$\frac{\partial T}{\partial t} + \underline{V} \cdot \nabla T = \nabla^2 T \tag{3.18}$$

For simplicity, and unless stated otherwise, the temperature gradient is set on the y axis and the vibrations are imposed either on the x or y axis depending on the desired configuration (this differs however in Chap.5). The projection of the momentum equation on the coordinate axes is defined according to this configuration.

Both configurations for the simple 2D cases are represented in Fig.3.1. For the RB case, the projection of the momentum equation on the coordinate axes becomes:

$$\frac{\partial u}{dt} = \frac{\partial p}{dx} - (\underline{V} \cdot \underline{\nabla V})_u + Pr(\Delta \underline{V})_u \tag{3.19}$$

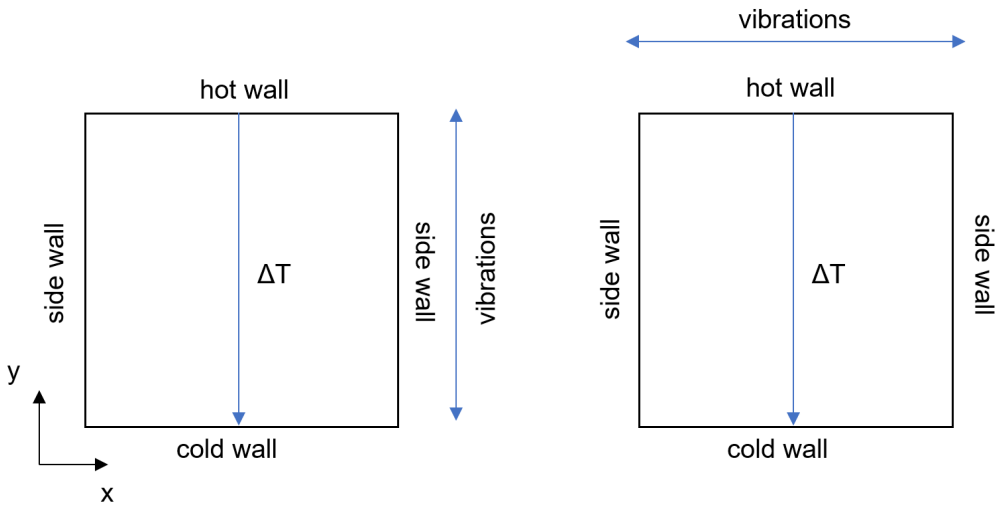

Figure 3.1: Direction of vibrations for Rayleigh-Benard type thermovibrational convection (left) and Hadley flow type (right)

$$\frac{\partial v}{dt} = \frac{\partial p}{dy} - (\underline{V} \cdot \underline{\nabla V})_v + Pr(\Delta \underline{V})_v + PrRa_\omega T sin(\Omega t) \tag{3.20}$$

For the Hadley flow case, this projection becomes:

$$\frac{\partial u}{dt} = \frac{\partial p}{dx} - (\underline{V} \cdot \underline{\nabla V})_u + Pr(\Delta \underline{V})_u + PrRa_\omega T sin(\Omega t) \tag{3.21}$$

$$\frac{\partial v}{dt} = \frac{\partial p}{dy} - (\underline{V} \cdot \underline{\nabla V})_v + Pr(\Delta \underline{V})_v \tag{3.22}$$

Where for both cases:

$$(\underline{V} \cdot \underline{\nabla V})_u = \left(u\frac{\partial u}{\partial x} + v\frac{\partial u}{\partial y} \right), (\underline{\nabla V})_u = \left(\frac{\partial^2 u}{\partial x^2} + \frac{\partial^2 u}{\partial y^2} \right) \tag{3.23}$$

$$(\underline{V} \cdot \underline{\nabla V})_v = \left(u\frac{\partial v}{\partial x} + v\frac{\partial v}{\partial y} \right), (\underline{\nabla V})_v = \left(\frac{\partial^2 v}{\partial x^2} + \frac{\partial^2 v}{\partial y^2} \right) \tag{3.24}$$

When considering a 3D square cavity (shown in Fig.3.2 , a 3^{rd} dimension must be considered, and an additional z component is modelled where the projection of the

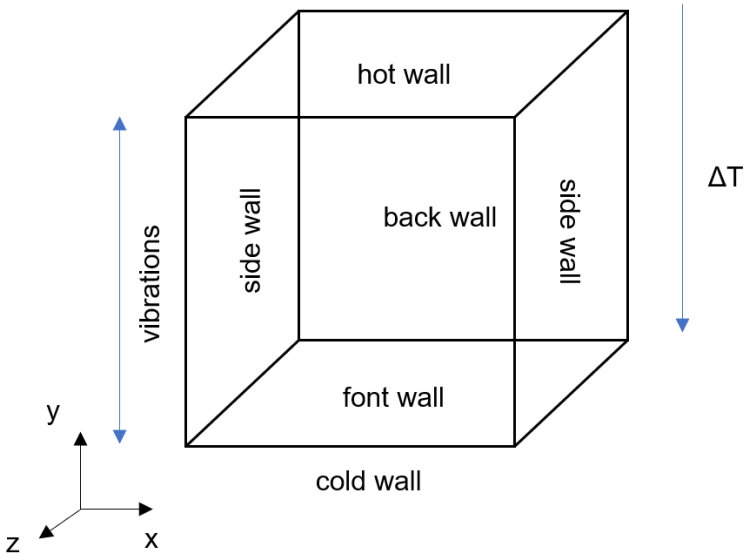

Figure 3.2: Three-dimensional model of Rayleigh-Benard type thermovibrational convection

momentum equation on the z axis reads:

$$\frac{\partial w}{dt} = \frac{\partial p}{dz} - (\underline{V} \cdot \underline{\nabla V})_w + Pr(\Delta \underline{V})_w \tag{3.25}$$

Given this additional dimension Eq.3.23 and Eq.3.24 become:

$$(\underline{V} \cdot \underline{\nabla V})_u = \left(u\frac{\partial u}{\partial x} + v\frac{\partial u}{\partial y} + w\frac{\partial u}{\partial z} \right), (\underline{\nabla V})_u = \left(\frac{\partial^2 u}{\partial x^2} + \frac{\partial^2 u}{\partial y^2} + \frac{\partial^2 u}{\partial z^2} \right) \tag{3.26}$$

$$(\underline{V} \cdot \underline{\nabla V})_v = \left(v\frac{\partial v}{\partial x} + u\frac{\partial v}{\partial y} + w\frac{\partial v}{\partial z} \right), (\underline{\nabla V})_v = \left(\frac{\partial^2 v}{\partial x^2} + \frac{\partial^2 v}{\partial y^2} + \frac{\partial^2 v}{\partial z^2} \right) \tag{3.27}$$

and gives rise to:

$$(\underline{V} \cdot \underline{\nabla V})_w = \left(u\frac{\partial w}{\partial x} + v\frac{\partial w}{\partial y} + w\frac{\partial w}{\partial z} \right), (\underline{\nabla V})_w = \left(\frac{\partial^2 w}{\partial x^2} + \frac{\partial^2 w}{\partial y^2} + \frac{\partial^2 w}{\partial z^2} \right) \tag{3.28}$$

Now that the governing equations have been presented and the general mathematical formulation of the thermovibrational problem has been introduced, the next section will treat the related numerical solution methods.

3.3 PISO algorithm

The integration of Eqs. 3.11, 3.16 and 3.18 in addition to the initial and boundary conditions allows for the unknown pressure (p), velocity (V), and temperature (T) fields to be found. The related procedure (time-marching algorithm) is described in the present section.

Along these lines, it is worth starting from the simple observation that, as implicitly made evident by the aforementioned set of equations, these three fundamental physical quantities ("primitive variables") display a varying degree of interrelation, depending on the specific couple considered. As an example, while V and p are intimately linked through the momentum equation, the temperature field (T) can be determined once the velocity field is known through the energy equation (Eq.3.18). In particular, the link between the first two unknowns is at the root of the so-called class of projection or fractional methods (Harlow and Welch [72]; Chorin [73]; Temam [74]; [75], Gresho [76]; Guermond and Quartapelle [77]; Guermond et al. [78]). These techniques rely on the so-called Hodge decomposition theorem, which states that any vector field can be decomposed into a divergence-free contribution and the gradient of a scalar potential (a curl-free part). Stripped to its essentials, the related computational scheme can synthetically be described as follows. Initially, the pressure is artificially neglected in the balance of momentum in order to obtain an equation (Eq.3.29) where only the velocity field requires solving for:

In this way, even though the pressure is initially unknown, a time-marching procedure can be started. However, the field $\underline{V}^{**}$ obtained through integration of this equation is called 'provisional' because, it does not account for the impact of pressure on fluid flow; moreover, it does not satisfy the incompressibility constraint (represented by the separate equation for the balance of mass). Nevertheless, using the aforemen-

tioned Hodge decomposition theorem, $\underline{V}^{**}$ can formally be split into two contributions as follows:

$$\underline{V}^{**} = \underline{V} + C\underline{\nabla} p \tag{3.29}$$

where V and ∇p play the role of divergence-free vector and the gradient of a scalar potential, respectively. This step is purely formal, as p is one of the unknowns. The next conceptual ingredient needed to obtain a complete time-marching procedure that consists of forcing $\underline{V} = \underline{V}^{**} - C\nabla p$ into Eq.3.11. In this way, a 'working' equation for the effective determination of the pressure is obtained:

$$\nabla^2 p = \frac{1}{\Delta t} \cdot \underline{V}^{**} \tag{3.30}$$

This equation represents the 'core' of all variants pertaining to the aforementioned class of projection (or fractional) methods. After Eq.**??** has been integrated, the pressure can be determined solving Eq.3.30; finally, the sought divergence-free velocity field can be computed from Eq.3.29 as $\underline{V} = \underline{V}^{**} - C\nabla p$ (assuming $C = \delta t$ where δt is the time integration step). The well-posedness of this approach is guaranteed by another important fundamental theorem—that is, the so-called theorem of the inverse calculus (see, e.g., Ladyzhenskaya [79]; it states that a vector field is uniquely determined when its divergence and curl are assigned; in the present case, these are $\underline{\nabla} \cdot \underline{V} = 0$ and $\nabla \wedge \underline{V} = \nabla \wedge \underline{V}^{**}$, where the latter equality follows from the well-known mathematical property of the curl operator to annihilate the gradient of a scalar function, i.e., $\nabla \wedge \nabla p$ ([76]; Lappa [80]; Lappa and Boaro [81]). In the present work, unless stated otherwise, the specific variant of this class of methods available in the OpenFOAM computational platform has been used. This includes the use of the so called PISO (Pressure Implicit Split Operator) approach (originally elaborated by Issa [82]). The OpenFOAM implementation of this method relies on a collocated grid approach, which means that the unknowns are defined in the centre of the computational cells. Moreover, in order to improve the coupling of velocity and pressure, a special interpolation of the velocity is applied on the cell faces (Rhie and Chow [83]), while the third unknown T is determined

in a segregated manner after the computation of V and p. As for what concerns the numerical schemes employed, the upwind and central differencing schemes in space for the convective and diffusion terms, have been employed respectively.

3.4 Particle modelling

3.4.1 Eulerian and Lagrangian tracking of the dispersed phase

As this work deals with multiphase flow, it is important to introduce the methods for computing and solving particle trajectories.

Two main categories of dispersed phase modelling are available: *Eulerian* formulation and *Lagrangian* particle tracking. In the case of the Eulerian formulation, the dispersed phase (similarly to the fluid) is assumed to be continuous. When the Eulerian formulation is used, the dispersed phase is treated as a modified scalar species and follows the following transport equation:

$$\frac{\partial \rho_f C}{\partial t} + \frac{\partial}{\partial x_i}\left(\rho_f \overline{u_i} C - \Gamma \frac{\partial C}{\partial x_i}\right) = S_c \tag{3.31}$$

Where C is the particle concentration, $i = (x, y, z)$, $\overline{u_i}$ is the average fluid velocity, Γ is the effective particle diffusivity and S_c is the particle source term, after Zhang [84].

In the Lagrangian tracking method, particles or parcels of particles, are tracked though the field and the local properties of the cloud are determined by the properties of the particle or parcel as they pass the point in the field [59]. As the continuous phase is always modelled using the Eulerian approach, the two methods outlined above can also be referred to as the Eulerian-Eulerian or the Eulerian-Lagrangian approach respectively. The type of particle tracking to be used depends predominantly on the type of multiphase flow under investigation. When solving for dilute systems, the cloud of particles cannot be treated as a continuous fluid due to the low volume fraction and therefore the low concentrations of particles in the fluid (although in some instances, Eulerian methods may account for the interparticle effects as these can be taken into account from a statistical stand point by assuming a certain viscosity of the particle

phase [85]). Therefore the optimum option in this case is to use the Lagrangian tracking method.

As for the particle wall interaction, the most common modelling approaches include:

- Rebound - where the elasticity (e) and restitution coefficients (μ) are specified.
- Stick - where particles are assigned zero velocity.
- Escape - where particles are removed from the domain.

  In this work the particle-wall interaction is set as *rebound*. The elasticity is set to $e = 1$ and the restitution coefficient is set to $\mu = 0$. This modelling approach leads to a perfectly elastic collision between the walls and the particles, where the total kinetic energy of the system is conserved (i.e., no energy is imparted on to the wall from the particles).

3.4.2 Equations for solving particle trajectories

The governing equation for the motion of spherical particles, bubbles or droplets in an incompressible fluid has enjoyed wide spread attention due the complexity of modelling such an intricate physical phenomenon. Today the most widely used form of this equation is the Maxey-Riley equation [86], due to its applicability to non-uniform, unsteady flows. The equation as presented by Babiano *et al.* [87] is written as:

$$\begin{aligned} \rho_p \frac{d\mathbf{v^*}}{dt^*} &= \rho_f \frac{D\mathbf{u^*}}{Dt^*} + (\rho_p - \rho_f)\mathbf{g} \\ &\quad - \frac{9\nu\rho_f}{2R_p^2}(\mathbf{v^*} - \mathbf{u^*} - \frac{R_p^2}{6}\nabla^2\mathbf{u^*}) \\ &\quad - \frac{\rho_f}{2}\Big(\frac{d\mathbf{v^*}}{dt^*} - \frac{D}{Dt^*}\Big[\mathbf{u^*} + \frac{R_p^2}{10}\nabla^2\mathbf{u^*}\Big]\Big) \\ - \frac{9\rho_f}{2a}\sqrt{\frac{\nu}{\pi}}\int_0^{t^*} &\frac{1}{\sqrt{t^* - \zeta}}\frac{d}{d\zeta}\Big(\mathbf{v^*} - \mathbf{u^*} - \frac{R_p^2}{6}\nabla^2\mathbf{u^*}\Big)d\zeta \end{aligned} \tag{3.32}$$

where $\mathbf{u^*}$ represents the dimensional fluid velocity and $\mathbf{v^*}$, the dimensional velocity of the particle.

The terms on the right hand side of Eq.3.32 represent the force exerted on the particle by the undisturbed flow, the buoyancy force, the Stokes drag, the added (or virtual) mass and the Basset-Boussinesq force respectively. Assuming that the forces associated with the drag force and the virtual mass are much larger than the Basset-Boussinesq force the equation can be simplified as follows:

$$\begin{aligned}\rho_p \frac{d\mathbf{v^*}}{dt} &= \rho_f \frac{D\mathbf{u^*}}{Dt} + (\rho_p - \rho_f)\mathbf{g} \\ &\quad - \frac{9\nu\rho_f}{2R_p^2}(\mathbf{v^*} - \mathbf{u} - \frac{R_p^2}{6}\nabla^2\mathbf{u^*}) \\ -\frac{\rho_f}{2}\Big(\frac{d\mathbf{v^*}}{dt^*} - \frac{D}{Dt^*}\Big[\mathbf{u^*} + \frac{R_p^2}{10}\nabla^2\mathbf{u^*}\Big]\Big)\end{aligned} \tag{3.33}$$

The terms associated with $R_p^2\nabla^2\mathbf{u^*}$ are known as the Faxen corrections [88]. These correction can also be neglected if the particles are much smaller that the characteristic length of the flow ($St \ll 1$). In this case the equation simplifies to:

$$\rho_p \frac{d\mathbf{v^*}}{dt^*} = \rho_f \frac{D\mathbf{u^*}}{Dt^*} + (\rho_p - \rho_f)\mathbf{g} - \frac{9\nu\rho_f}{2R_p^2}(\mathbf{v^*} - \mathbf{u^*}) - \frac{\rho_f}{2}\Big(\frac{d\mathbf{v^*}}{dt^*} - \frac{D\mathbf{u^*}}{Dt^*}\Big) \tag{3.34}$$

In the framework of this thesis, the gravity force is replaced by $g = b\omega^2 sin(\omega t)$, as vibrations are used in place of standard gravity. Eq.3.34 can also be divided through by the fluid density (ρ_p) resulting in:

$$\xi\frac{d\mathbf{v^*}}{dt^*} = \frac{D\mathbf{u^*}}{Dt^*} + (\xi - 1)\mathbf{g} - \frac{9\nu}{2R_p^2}(\mathbf{v} - \mathbf{u}) - \frac{1}{2}\Big(\frac{d\mathbf{v^*}}{dt^*} - \frac{D\mathbf{u^*}}{Dt^*}\Big) \tag{3.35}$$

The derivative $\frac{D\mathbf{u^*}}{Dt}$ is along the path of a fluid element and therefore can be written as:

$$\frac{D\mathbf{u^*}}{Dt^*} = \frac{d\mathbf{u^*}}{dt^*} + (\mathbf{u^*} \cdot \nabla)\mathbf{u^*} \tag{3.36}$$

Introducing the above substitution and nondimensionalising the length by the referenced distance (L), the velocity by (α/L) and the time by (L^2/α), Eq.3.35 becomes:

$$\frac{d\mathbf{v}}{dt} = \frac{1}{\xi + 1/2}\Big[- \frac{Pr}{St}(\mathbf{v} - \mathbf{u}) + \frac{3}{2}\frac{d\mathbf{u}}{dt} + \frac{3}{2}(\mathbf{u} \cdot \nabla \mathbf{u})\Big] + \frac{\xi - 1}{\xi + 1/2}\gamma sin(\omega t) \tag{3.37}$$

3.4.3 Choice of coupling particle coupling methods

As outlined in Chap.2, in this work, when particles are considered, a one way coupling approach is taken. In order to track the systems' evolution, a high number of particles are seeded in the cavity, that appears to violate the assumption of a dilute systems and the initial use of a one-way coupling approach. However, this number of particles is used for visualisation purposes only. Indeed, it must be stressed that the particle accumulation phenomena observed in this work does not depend on the number of particles introduced in the system as the particle structures are an intrinsic property of the flow. Practically, this means that the structures achieved in this work are a much denser that the real life structures that can be achieved in dilute fluid systems. This approach has been broadly accepted in the field of numerical modelling of multiphase thermal flows [1, 64, 127].

In this chapter the mathematical models, related governing equations and solution methods have been described. The next section aims so summarise the work presented in Part I.

3.5 Conclusions and transition to Part II

In Part I, the topics governing this thesis have been presented. From the concepts underpinning instabilities that occur in non-isothermal fluids to the equations governing the trajectories of spherical particles.

Part II will now present the findings of this thesis and provides answers to the research questions posed in Chap.1.

Part II

Results

Chapter 4

Rayleigh-Bénard type thermovibrational convection for moderate to high values of Ra_ω

This chapter is based on the following peer-reviewed publication:

Crewdson, G. and Lappa, M., 2021,"The zoo of modes of convection in liquids vibrated along the direction of the temperature gradient", *Fluids*, 6(1), p.30, https://doi.org/10.3390/fluids6010030.

The text in this chapter has been modified only when necessary in order to preserve the continuity and flow of this thesis.

4.1 Introduction

This chapter focuses on the problem of Rayleigh-Bénard type thermovibrational convection for moderate to high values of Ra_ω.

Indeed from the literature review it has been shown that, a number of authors have considered the case where vibrations are applied perpendicularly to the temperature gradient (Monti *et al.* [47, 89]; Alexander [90]; Alexander *et al.* [4]; Mialdun *et al.* [91,

92]; Melnikov *et al.* [93]; Lyubimova *et al.* [94]; Bouarab *et al.* [95]; Shevtsova *et al.* [96, 97]; Vorobev and Lyubimova [98]; Lappa [1, 99–102]; Lappa and Burel [71]).

Still, only Hirata *et al.* [36] considered the pure thermovibrational flow in a square cavity assuming zero gravity and no inclination between vibrations and the temperature gradient. In the present study, an attempt is made to extend that earlier investigation to larger values of the Rayleigh number in a attempt to elaborate a unified picture of the related hierarchy of instabilities and patterning behaviours.

4.2 Mathematical model and boundary conditions

In keeping with a large portion of the work outlined in the introduction for standard RB convection, a simple 2D square cavity is considered. Microgravity conditions are assumed (no steady gravity). The direction of the temperature gradient and vibrations as well as the wall boundary conditions can be seen in Fig.4.1

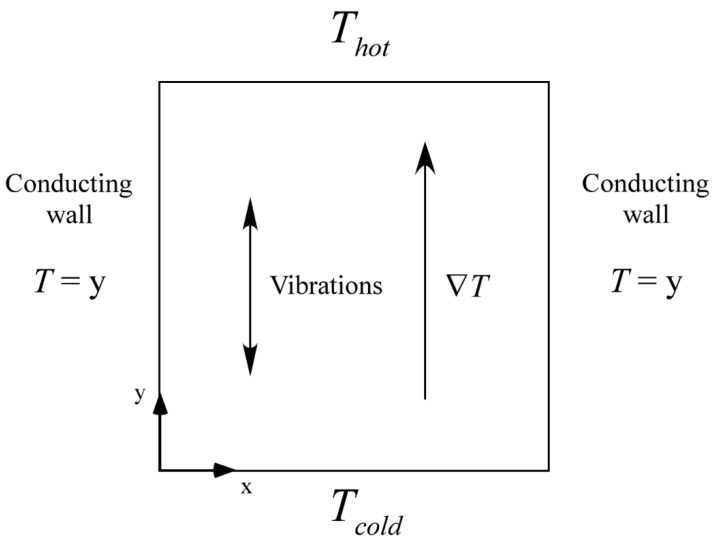

Figure 4.1: Square cavity with characteristic size L, delimited by solid walls (one at y= 0 cooled, the other at y = 1 heated, perfectly conducting conditions on the remaining sidewalls: T = y for x = 0 and x = 1.

4.3 Validation

Before numerical results can be interpreted, it is imperative that the related strategy for the solution of the governing equations is validated against available relevant benchmarks. Given our specific target, the earlier study by Hirata *et al.* [36] is specifically considered for such a purpose. The following case is considered $\Omega = 500, Ra_\omega = 1.00 \times 10^5$(the corresponding case is readily available to the reader in the original study, making the comparison with the current results straightforward). As the reader will realize by inspecting Fig.4.2, the present results are in excellent agreement with the original signals reported by Hirata *et al.* [36].

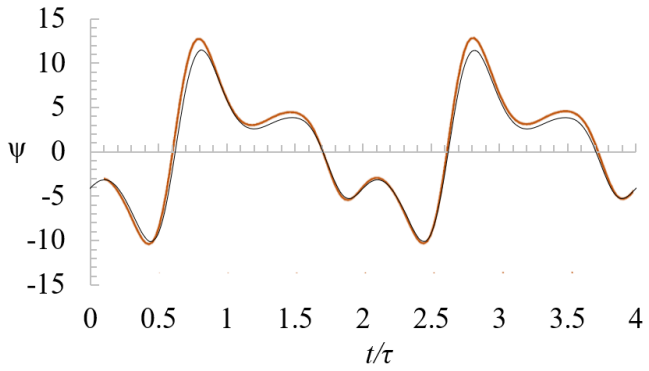

Figure 4.2: Time evolution of the streamfunction (Ψ), for the case $\Omega = 500, Ra_\omega = 1.00 \times 10^5$, probed at (0.25,0.25), where the orange line corresponds to the results obtained by Hirata *et al.*[36] and the black line corresponds to the results obtained in OpenFOAM.

4.4 Grid refinement

Due to the potential complexity of the flow considered in this study, close attention must also be given to the mesh adopted for the numerical simulations. Although mesh refinement criteria for thermovibrational flow are not available, meaningful indications in this regard can be obtained through 'analogies' with parent forms of convection. As an example, relevant similarities with standard gravitational convection in high-Pr fluids include the development of thermal boundary layers for relatively high values of

the Rayleigh number. For the case of standard buoyancy flow, as an example, Russo and Napolitano [103] showed that a working correlation for the thickness of the thermal boundary layer can be introduced as follows:

$$\delta_{th} \cong Ra^{-1/4} \tag{4.1}$$

The presence of such boundary layers cannot be ignored when designing an adequate mesh and can be translated into precise numerical requirements. As an example, relevant information along these lines can be found in the study on RB convection by Shishkina *et al.* [104] where the number of cells required in the thermal boundary layer (N_{BL}) has been specified directly as a function of Ra, i.e.

$$N_{BL} \cong Ra^{0.15} \tag{4.2}$$

Another important influential factor to be taken into account (especially when one targets high-Ra regimes) in the preliminary definition of a computational grid is the so-called Kolmogorov length scale, i.e. the need to keep the size of the computational cell sufficiently small to capture the 'eddies' that are produced when the flow assumes a turbulent behavior. It is known that for standard RB convection (De *et al.*) [105] this characteristic (non-dimensional) length scales as:

$$\zeta_{Ra} = 1.336(Ra)^{-0.32} \tag{4.3}$$

All these criteria should be regarded as a set of multiple requirements finally leading to a relevant mesh. Assuming the worst conditions considered in the present work, i.e. the highest possible value of (for $Ra_\omega = 10^6$, Pr=7 and $\Omega = 100$) all these constraints taken together would return a uniform mesh 102×102. To verify the consistency of this way of thinking with the standard approach generally used to define a suitable mesh (i.e. a 'classical grid refinement study'), the number of computational nodes have been increased progressively until convergence has been obtained. The outcomes of

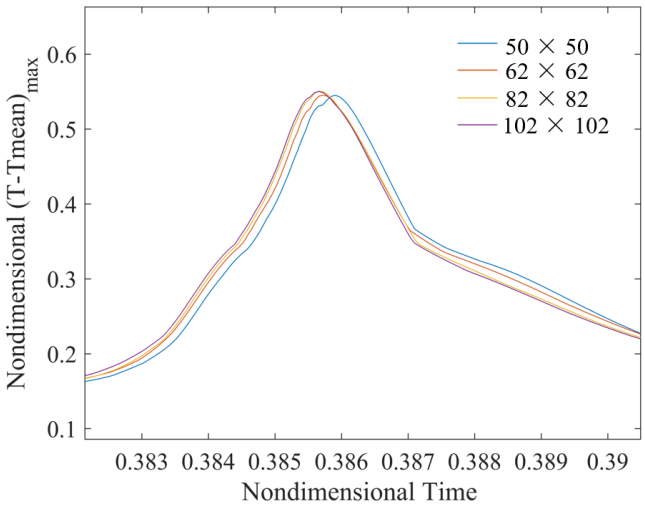

Figure 4.3: Convergence of the thermofluid-dynamic disturbances as a result of grid refinement for the case $Pr = 7, Ra_\omega = 10^6, \Omega = 100$.

such a study are presented in Fig.4.3, where the maximum of the difference between the instantaneous temperature and the corresponding time-averaged (over the period of vibrations) value (the so-called thermofluid-dynamic distortion) has been plotted. It can be seen that the results for a grid of size 82×82 are extremely close to that of the grid size 102×102, which implicitly indicates that (towards the end to save computational time) one may limit to considering the former coarser mesh. In order to meet all the possible criteria described before, however, the 102×102 mesh is selected for all the cases considered in the present work.

4.5 Simulation results

With the numerical approach robustly tested by (1) verifying its ability to capture available results in the literature and (2) checking its convergence under mesh refinement (forcing the used grids to also satisfy existing practical and theoretical criteria about mesh design), a vast range of cases have then been simulated by varying parametrically the vibrational Rayleigh number and the frequency of vibrations over three orders of magnitude. In particular, the same value of the Prandtl number originally considered by Lappa [106] has been examined ($Pr = 15$) with the two-fold purpose

of (1) extending that earlier study conducted for classical RB convection in a square cavity to the case of thermovibrational flow and (2) expanding the space of parameters originally examined by Hirata *et al.* [36]. In order to consider conditions for which the flow can still be considered laminar or weakly chaotic (the investigation of the fully turbulent regime being beyond the scope of the present work), the maximum value of the Rayleigh number has been limited to 10^6.

The work/study progresses with the aid and support of both global parameters and detailed velocity fields for a better representation of the emerging dynamics. While a coarse-grained macroscopic perspective is used at the beginning by providing results in terms of maps (Sect.4.5.1) and general trends in terms of 'distortions' and Nusselt number (Sect. 4.5.2), the problem is considered from a fine-grained micromechanical level (Sect. 4.5.3) (in terms of flow temporal behaviour and related symmetries). Finally in Sect.4.6 the resulting statistics are linked to the evolution of global parameters to provide useful information about the underlying cause-and-effect relationships.

4.5.1 Characterisation of thermovibrational fluid regimes at high Rayleigh numbers

As the present study has been expressly conceived as an extension of the numerical investigation originally conducted by Hirata *et al.* [36], the simplest way to place the present results in an adequate context is to start from an overview of that work. The diversity of flow regimes that exist for pure thermovibrational convection in a square cavity when the temperature gradient is imposed parallel to the vibration can be clearly seen in Fig.7 of Hirata *et al.* [36], where these regimes are split into four possible categories, namely, Synchronous (SY), Subharmonic (SU), Non-periodic (NP), and Stable (ST) solutions. Unfortunately, these authors limited themselves to considering values of the vibrational Rayleigh number in the range ($10^4 \leq Ra_\omega \leq 10^5$, the constraint on the upper value being essentially an outcome of the limited computational resources available at that time). This figure is instructive also for another reason. It shows the well-known stabilization of thermovibrational flow when the frequency of vibrations is increased (Zen'kovskaja and Simonenko [29]; Simonenko [39]; Gershuni and Zhukhovit-

skii [34, 35] Gershuni and Zhukhovitskii [30]); this fundamental concept is revisited at a later stage. A total of 66 new simulations have been conducted in the present work. In line with Hirata *et al.* [36], Ω has been varied from $\Omega = 1$ to $\Omega = 10^3$, with the addition of a very high value of $\Omega = 10^4$. As explained before, a fluid with Pr = 15 has been considered in place of Pr = 7. Another distinguishing mark of the present analysis is the extension to $Ra_\omega = 10^6$. Before starting to deal with the detailed discussion of these results, although the regimes (SY, SU, NP, and ST) were sufficient to compartmentalize the flow in the range of parameters considered by Hirata *et al.* [36], additional classes of flow have been identified for the cases simulated here in the interval ($10^5 < Ra_\omega < 10^6$). These new findings have implicitly led to the need to introduce a distinction within the synchronous regime whereby a flow may be synchronous and periodic or synchronous and non-periodic (SY-P or SY-NP). Relevant examples of such new solutions are shown in Figure 4.4 (a) and (b) respectively. In particular, Fig.4.4(a) relates to the circumstances where the velocity signal is identical over each period for all periods (therefore, the signal can be considered synchronous and periodic). By contrast, although the signal shown in Fig.4.4 (b) is still synchronous in time with the applied forcing (i.e., the vibrations), it also exhibits turbulent bursts every period (where the term *turbulent burst* is used to illustrate a short interval of time where the fluid response cannot be predicted based on the historical behaviour of the flow and where the amplitude of the flow varies substantially); moreover, the signal is not periodic, as the bursts display a more or less erratic evolution in time.

The main outcome of the present parametric investigation, i.e., the extended map, is presented in Fig.4.5. It is divided into regions where clusters of convective modes can be observed. Although stabilization is achieved at extremely high frequencies ($\Omega = 10^4$, where $u(x, y, z) = 0$), the predominant flow regime apparent for high vibrational Rayleigh numbers ($Ra_\omega > 5 \times 10^5$) is the aforementioned SY-NP case denoted by: (▲). The red sinusoidal signal included in the insets represents the forcing applied to the system; it is instrumental in making evident that the turbulent bursts for the SY-NP mode occur synchronously with the forcing but do not display the same behaviour for each period. These solutions are less ordered than those found for the lower vibrational

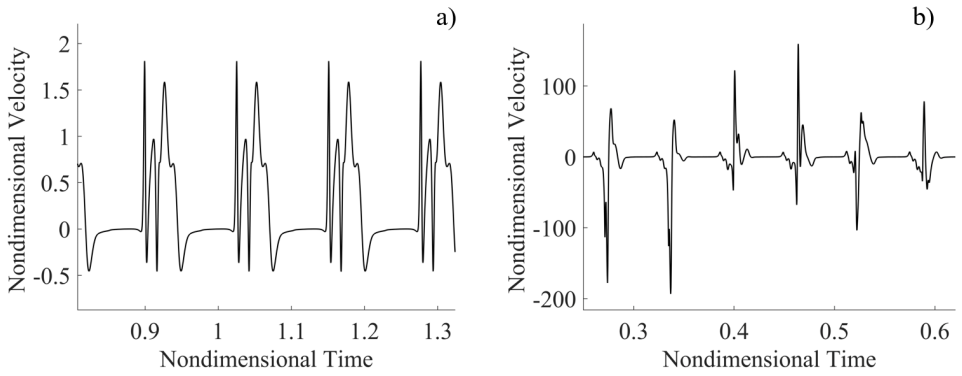

Figure 4.4: Cases $Ra_\omega = 2 \times 10^5$, $\Omega = 50$ and $Ra_\omega = 7 \times 10^5, \Omega = 100$ respectively (a) shows the case synchronous and periodic (SY-P) and (b) the case synchronous and non-periodic (SY-NP).

Rayleigh numbers whereby they appear in less organized clusters. The appearance of the SY-P regime is more sporadic. However, this mode of convection also exists at extremely high Rayleigh numbers ($Ra_\omega = 10^6$), which indicates that an increase in Ra_ω does not systematically lead to a more chaotic system (in some regions of parameters ($\Omega = 10^3$), the flow reverts from an NS-NP back to an SY-P state). In agreement with Hirata *et al.* [36], in the range of low frequencies $\Omega < 200$, the fluid displays a stationary behaviour over a certain sub-interval of the period $P(P = 2\pi/\Omega)$ of the applied vibrations. In addition to enlightening the reader on the complexity and unpredictability of the flow regime (with the exception of extremely high values of Ω for which the dynamics reduce to the emergence of a quiescent thermally diffusive state), this map provides a picturesque description of the velocity signals and the fluid behaviour. The thermal response of the system is described in the next section where some dedicated ('ad hoc') definitions and concepts are introduced.

4.5.2 Characterisation of the thermal response of the system

A further understanding of the observed dynamics can be gained through the so-called thermofluid-dynamic (TFD) distortions. These characteristic quantities have enjoyed a widespread use in past studies concerned with the effect of vibrations on non-isothermal fluid systems (see, e.g., Monti *et al.* [47]). They can be used to characterize in a syn-

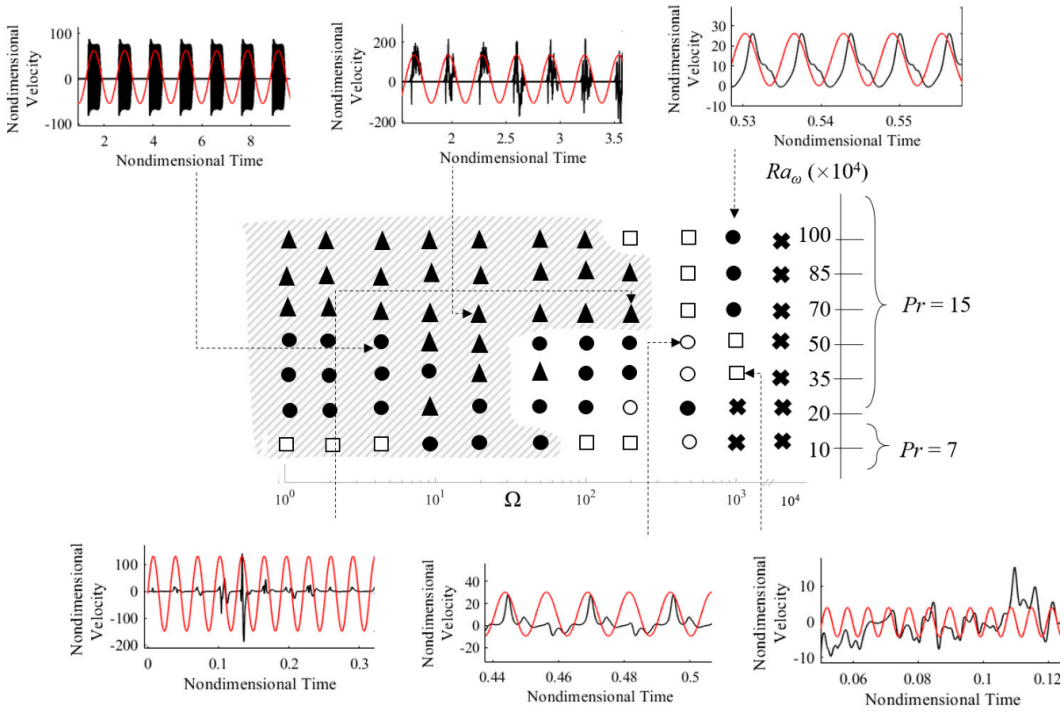

Figure 4.5: Response of the velocity field to the imposed periodic acceleration (Pr = 15): • Synchronous and periodic case (SY- P) ; ∘ 1/2 Subharmonic case (SU); ▲ Synchronous and non-periodic case (SY-NP) ; □ Non-periodic and non-synchronous case (NP-NS); × Stable case (ST).

thetic way the thermal response of the fluid to the application of a time-varying acceleration. However, a proper introduction of these characteristic quantities requires a short excursus on the peculiar properties of thermovibrational flows. In particular, it is worth recalling that a non-isothermal fluid subjected to vibrations can develop a stationary response in addition to the oscillatory velocity field directly induced by the time-periodic acceleration. The latter can easily be explained assuming a straightforward cause-and- effect relationship between the time-varying buoyancy force and the induced fluid motion. The former requires a more involved interpretation. This stationary response (detectable through analysis of the time-averaged flow field) is an outcome of the non-linear nature of the balance equations (Savino and Lappa [107]). It becomes significant when the frequency of vibrations is sufficiently high and their amplitude is relatively small, i.e., in the so-called Gershuni regime. Indeed, for the opposite circumstances for which the frequency is small and the amplitude large, the linear response

(direct proportionality between the oscillatory flow and the time-dependent acceleration) is dominant [107]. The time- averaged and fluctuating components of the velocity and temperature fields can formally be defined as:

$$\underline{\bar{V}} = \frac{\Omega}{2\pi}\int_0^{2\pi/\Omega} = \underline{V}dt \text{ and } \bar{T} = \frac{\Omega}{2\pi}\int_0^{2\pi/\Omega} = Tdt, \tag{4.4}$$

and

$$\underline{V'} = \underline{V} - \underline{\bar{V}} \text{ and } T' = T - \bar{T} \tag{4.5}$$

In the present work, these quantities have been determined "a posteriori" after evaluating V and T via direct numerical solution of the governing equations in their complete time-dependent and non-linear form, as illustrated in Sect 4.2. The above-mentioned distortions can be defined accordingly as follows:

$$\delta T(x,y,z) = T(x,y,z) - T_{diff}(x,y,z) \tag{4.6}$$

where T_{diff} represents the temperature field that would be established in the absence of convection (in other words, a purely diffusive temperature profile, which using the reference system indicated in Fig.4.1 would simply read $T_{diff} = y$). Taking into account that (as illustrated above) the local temperature can be split into a time-averaged steady component plus a fluctuating part , Eq.4.6 can be further expanded to:

$$\delta T = T'(x,y,z) + \bar{T}(x,y,z) - T_{diff}(x,y,z) = \delta\bar{T} + \delta T'(x,y,z) \tag{4.7}$$

where $\overline{\delta T}$ represents the companion averaged distortion, i.e.:

$$\overline{\delta T} = \bar{T}(x,y,z) - T_{diff}(x,y,z) \tag{4.8}$$

Global measures can be defined accordingly as:

$$TFD = max(\delta T) \text{ for } 0 \leq x \leq 1, 0 \leq y \leq 1, t_0 \leq t \leq t_0 + P \text{ where } P = 2\pi/\Omega \tag{4.9}$$

$$TFD_{averaged} = max(\delta\bar{T}) \text{ for } 0 \leq x \leq 1, 0 \leq y \leq 1 \tag{4.10}$$

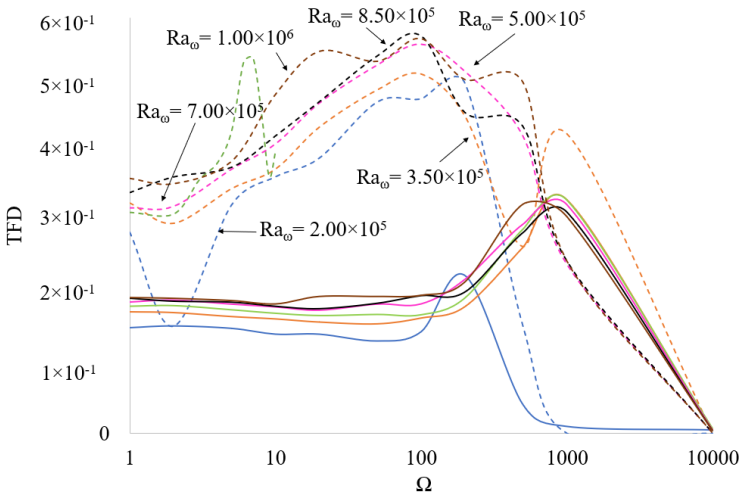

Figure 4.6: Influence of Ω on the global thermofluid-dynamic (TFD) disturbances (the dashed and solid lines indicating instantaneous and time-averaged variants, respectively).

As quantitatively substantiated by 4.6, the oscillatory thermofluid dynamic disturbance (TFD) is generally higher that the time-averaged one over the considered range of frequencies. In particular, the time-averaged disturbances are approximately constant if their dependence on either Ra_ω or Ω is considered until the critical value of $\Omega = 500$ is attained, where these disturbances are seen to increase (with the exception of the case $Ra_\omega = 2 \times 10^5$ for which the $TFD_{averaged}$ tends to 0). For what concerns the oscillatory disturbances, an increase in TFD occurs until the critical value of $\Omega = 100$, while for $\Omega > 100$, the opposite trend can be seen. Remarkably, all the TFD distortions tend to zero as the frequency grows. A simple way to think about this scenario is to consider that it reflects the existence of the almost quiescent states already reported in Fig.4.5. However, from a physical point of view, this trend can be interpreted directly, taking into account a well-known property of thermovibrational flow for high frequencies (for $\Omega \geq 10^4$, i.e., when the Gershuni regime is approached (Savino and Lappa [107]). As originally argued by Birikh at al. [108], indeed, in the limit as the frequency tends to infinity, if temperature distortions with respect to the purely diffusive case are present, the major role of the mean vibration force is that of forcing isotherms to turn and become perpendicular to the vibration direction. To elucidate further the significance

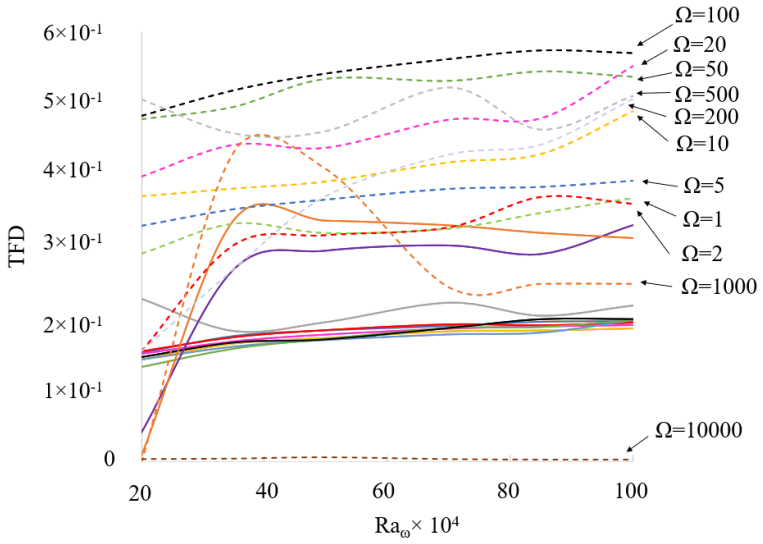

Figure 4.7: Influence of Ra_ω on the global thermofluid-dynamic (TFD) disturbances (the dashed and solid lines indicating instantaneous and time-averaged variants, respectively).

of this observation, one should keep in mind that in other words, this simply means that an intrinsic property of thermovibrational convection induced by vibrations parallel to the imposed temperature difference is to tend naturally to a quiescent thermally diffusive state as Ω is increased (which provides the sought physical justification for the ST states reported in the existence map). Apart from showing that the oscillatory disturbances prevail over the time averaged ones, Fig.4.6 and Fig.4.7 are also instrumental in revealing that the increase of the vibrational amplitude (Ra_ω) affects the two types of distortions differently: as already explained to a certain extent before, the time-averaged disturbances seem quasi-independent of the increase in Ra_ω (or value of Ω in fact), whereas the instantaneous (complete) TFD are appreciably affected by both Ra_ω and Ω.

In keeping with the previous section, further analysis of the thermal behaviour of the system may be carried out by looking at another global parameter, i.e., the classical Nusselt number, namely the ratio of heat transfer due to convection over the heat transfer due to conduction along a given boundary. In our case, this non-dimensional number can be defined as:

$$Nu = \int_0^1 \frac{\partial T}{\partial y} dx \tag{4.11}$$

and we introduce accordingly:

$$Nu_{max} = max(Nu) \text{ for } t_0 < t < t_{0+P} \tag{4.12}$$

In the case of high frequencies, it has been shown in the previous section that when parallel to the temperature gradient, the vibrations have a stabilizing effect on the flow. This trend can still be appreciated when cases with $Ra_\omega > 10^5$and the SY-NP and NS-NP regimes are considered. As witnessed by Fig. 4.8 a remarkable decrease in Nu_{max} occurs for $\Omega = 1000$ (Nu_{max} ideally tending to 1 in the limit as $\Omega \to \infty$). However, as still evident in this figure, a peak is located $\Omega = 100$. For all values ofRa_ω at low frequencies ($\Omega < 20$), Nu_{max} remains constant; then, it grows for intermediate frequencies ($50 < \Omega < 100$) and finally decreases for high values of Ω ($\Omega > 1000$).

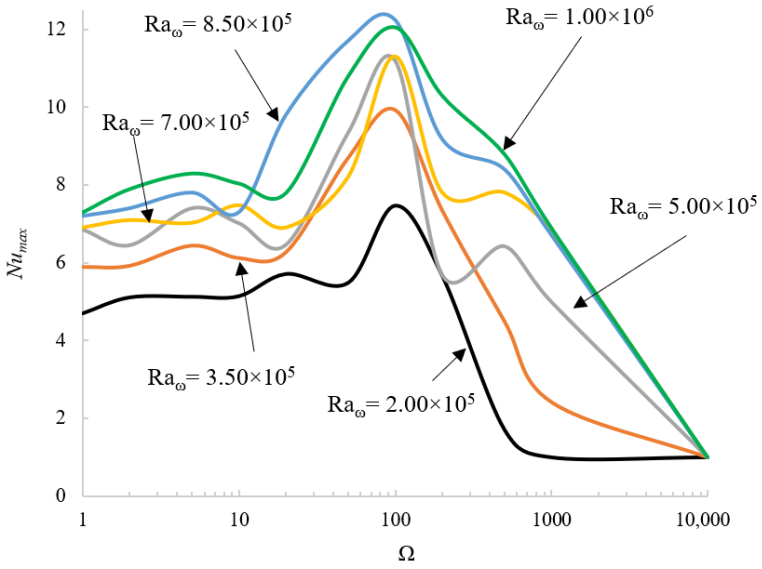

Figure 4.8: Influence of Ω on the maximum Nusselt number (Nu_{max}) across the heated wall of the cavity.

Notably, the peak located at $\Omega = 100$ is consistent with the maximum taken by the TFD (see again Fig.4.6 and 4.7), and the key to understanding this finding lies in considering that, given the dominance of instantaneous effects on time-averaged

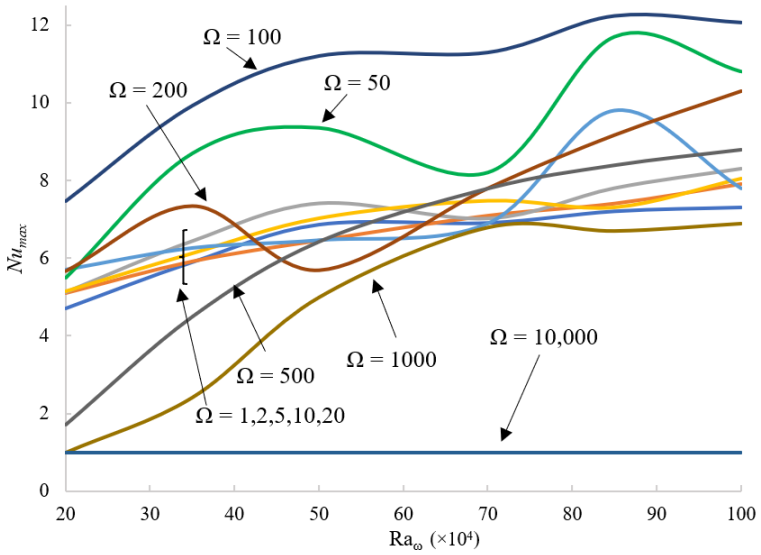

Figure 4.9: Influence of Ra_ω on the maximum Nusselt number (Nu_{max}) across the heated wall of the cavity.

ones, the effective configuration of the temperature field (in terms of topology of the isotherms and ensuing heat exchange at the boundaries) must essentially be ascribed to the fluctuating components of velocity and temperature. As already outlined above, the tendency of the Nusselt number toward the unit value as Ω is increased, is indirect evidence of the fact that fluid motion tends to be suppressed in those conditions.

4.5.3 Streamlines and patterning behaviours

In this section, focus in turned to the effective patterning behaviour of the flow for the different regimes reported in Fig.4.5. Emphasis is put on the interval $10^5 < Ra_\omega \leq 10^6$, as these circumstances were not covered in the earlier study by Hirata *et al.* [36]. Along these lines, the case $Ra_\omega = 10^6$, $\Omega = 10^4$, is considered i.e., a condition for which the flow is almost negligible ("stable state"). As shown by Fig.4.10, it manifests itself as an (ss) convective mode characterized by two rolls along each coordinate axis. This extremely weak flow starts as a four-roll configuration. From there, small rolls nucleate at the corners of the cavity and, as time passes, they tend to merge with their respective neighbours until the original quadrupolar arrangement is recovered. This nucleation occurs twice in the space of a period rapidly regaining the four-roll configuration. The

periodicity of this evolutionary scenario is consistent with the velocity signal (which is sinusoidal and synchronous with the forcing period).

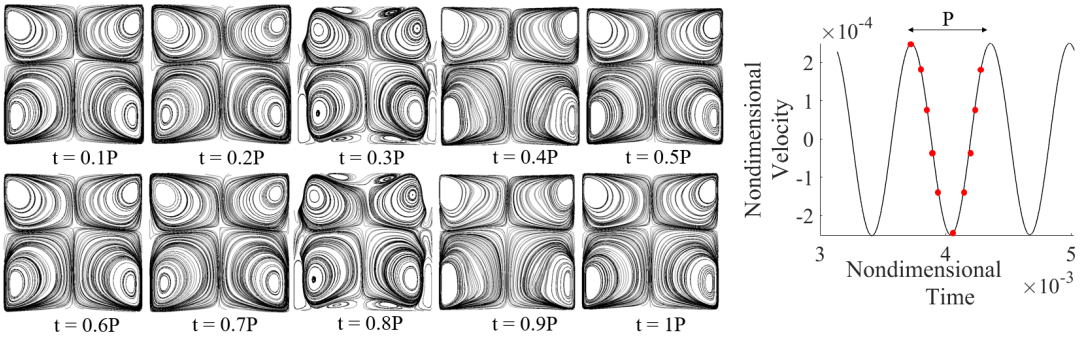

Figure 4.10: Instantaneous patterning behaviour for the case ST, where it is shown that the nucleation of the external rolls occurs at approximately 0.3P and 0.8P and that the four-roll configuration is re-established fully when the acceleration tends to zero.

Another characteristic type of solution present in the map (Fig.4.5) is the synchronous and periodic state (SY-P). This mode of convection can be found mainly at the centre and at the left side of the map for $Ra_\omega < 5 \times 10^5$. As illustrated in Fig.4.11 , this regime presents periodically identical instantaneous velocity fields and streamlines. In this case, the quadrupolar (four-roll) configuration is interrupted at each period by the genesis of two small rolls in the centre of the lower part of the cavity, which are eventually flattened, hence allowing the flow to return to the original pattern.

The next figure of the sequence (Fig.4.12) illustrates a Subharmonic case (SU). In this figure, the typical behaviour of a subharmonic mode of convection can be recognized in both the velocity field and streamlines snapshots. The period of the flow is double with respect to that of the forcing. However, the signature of the forcing period (P) can still be recognized if one considers the two spikes (one large and one small) visible in the signal (then, these spikes are repeated with a slightly lower amplitude in the second forcing period). This is also quantitatively substantiated by the panels (a) and (b), where the magnitude of the first velocity field is (slightly) higher than that of the second.

In terms of spatial symmetry, the (aa) type is dominant (one single roll). However, during one period of flow oscillation, modes with the (ss) symmetry are excited, which

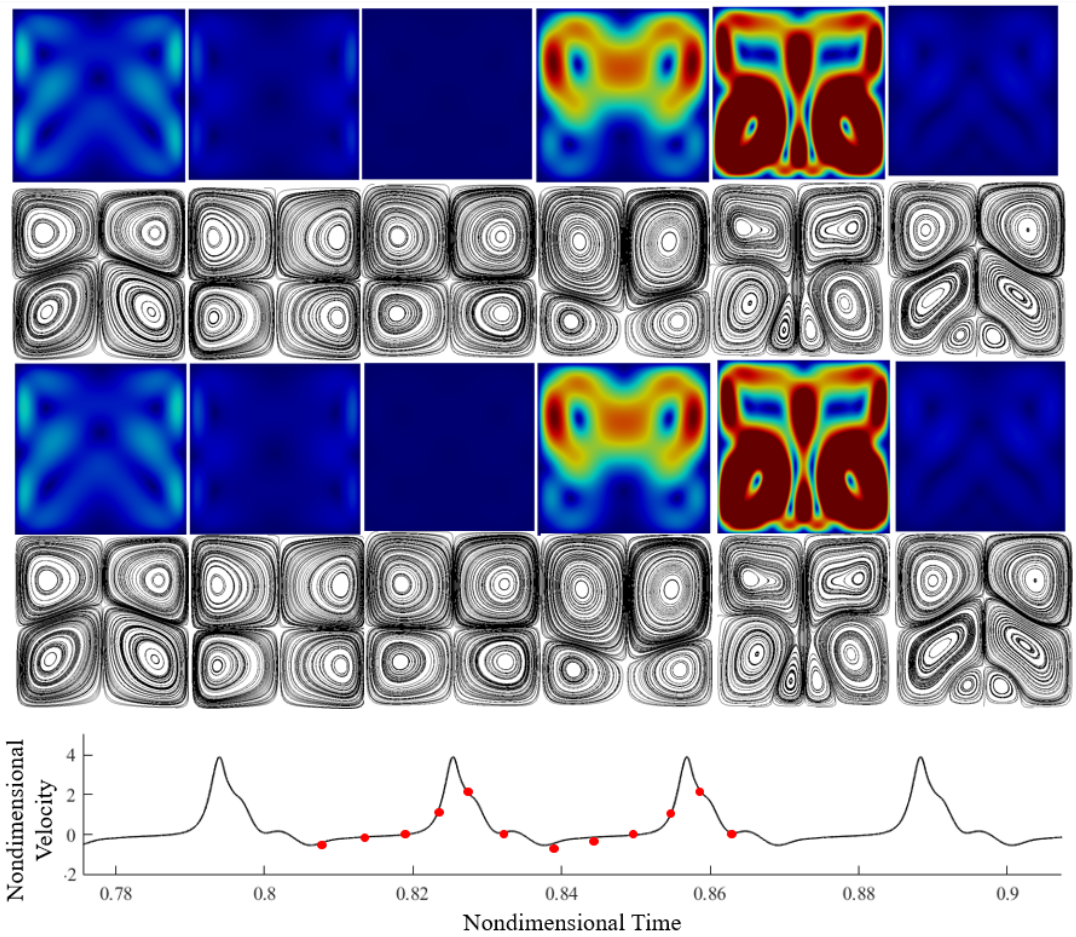

Figure 4.11: Instantaneous streamlines and velocity magnitude over two periods for the case $Ra_\omega = 3.5 \times 10^5$, $\Omega = 200$ (SY-P) accompanied by the velocity signal. The 12 red dots represent the time at which the snapshots are taken (six snapshots for each period)

combined with the main roll give rise to one diagonal clockwise-oriented vortex with two small counter-rotating eddies located in opposite corners of the cavity or a columnar arrangement of three superposed rolls slightly inclined to the left.

The next case serves to reveal the intrinsic features of the synchronous and non-periodic regime (SY-NP) found at higher vibrational Rayleigh numbers and at low and intermediate frequencies. As explained in Sect.4.5.1, a distinguishing mark of this type of solutions is the existence of bursts in the velocity signal, which display a more or less random nature. In particular, here, the case of $Ra_\omega = 8.5 \times 10^5$, $\Omega = 100$ is taken as a representative example (Fig.4.13). As a fleeting glimpse into this figure would

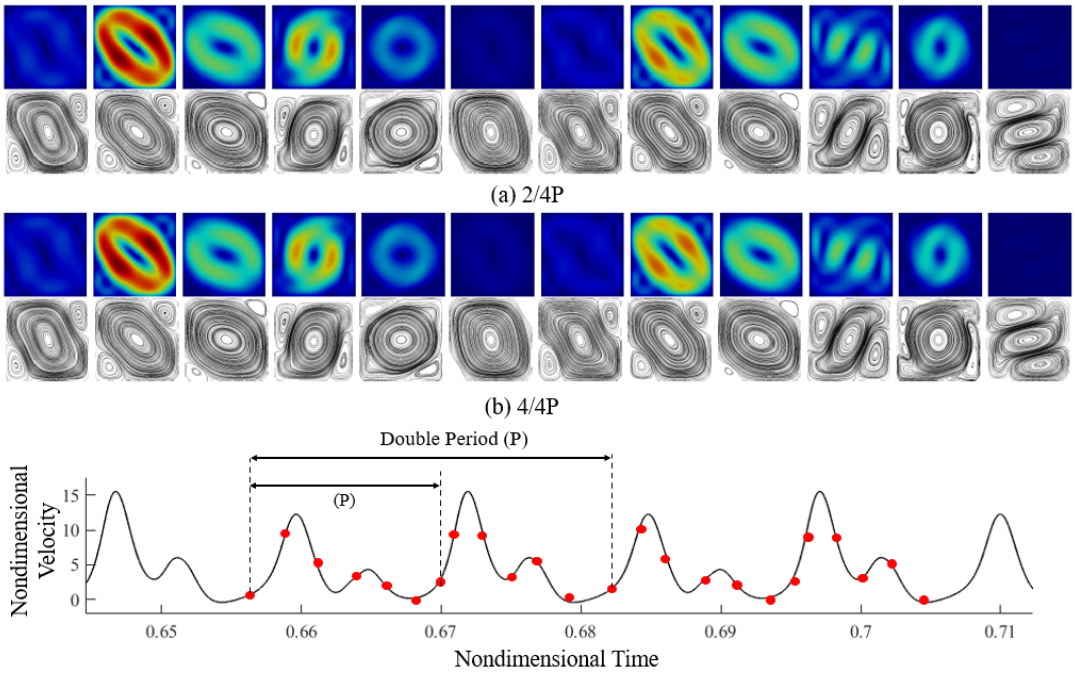

Figure 4.12: Instantaneous streamlines and velocity magnitude over two periods of forcing (panel (a): first period, panel (b): second period) for the case $Ra_\omega = 3.5 \times 10^5$, $\Omega = 500$ (SU), accompanied by the velocity signal. The 24 red dots represent the time at which the snapshots are taken (six snapshots for each period.)

immediately confirm, the fluid becomes almost quiescent over a fixed sub-interval of each period.

Although the velocity profile shows a large difference in behaviour over time, the instantaneous velocity field and streamlines witness that the actual pattern is different at each turbulent burst. This is evident in the third, fourth, and fifth snapshots of the sequence for each period. Although the burst occurs at the same point in time, the flow structure changes considerably. When the velocity magnitude is close to zero, the streamlines present again the four-roll configuration; when a burst occurs, as shown in snapshot 3, existing vortices merge, and new rolls appear randomly. In terms of spatial symmetry, although in certain sub-intervals of the period solutions with the (sa) symmetry also appear (two vertically extended rolls in a side-by-side configuration), the (ss) mode with four rolls is generally dominant. Fig.4.14 can be finally used to get insights into the non-synchronous and non-periodic regime (NS-NP) apparent in

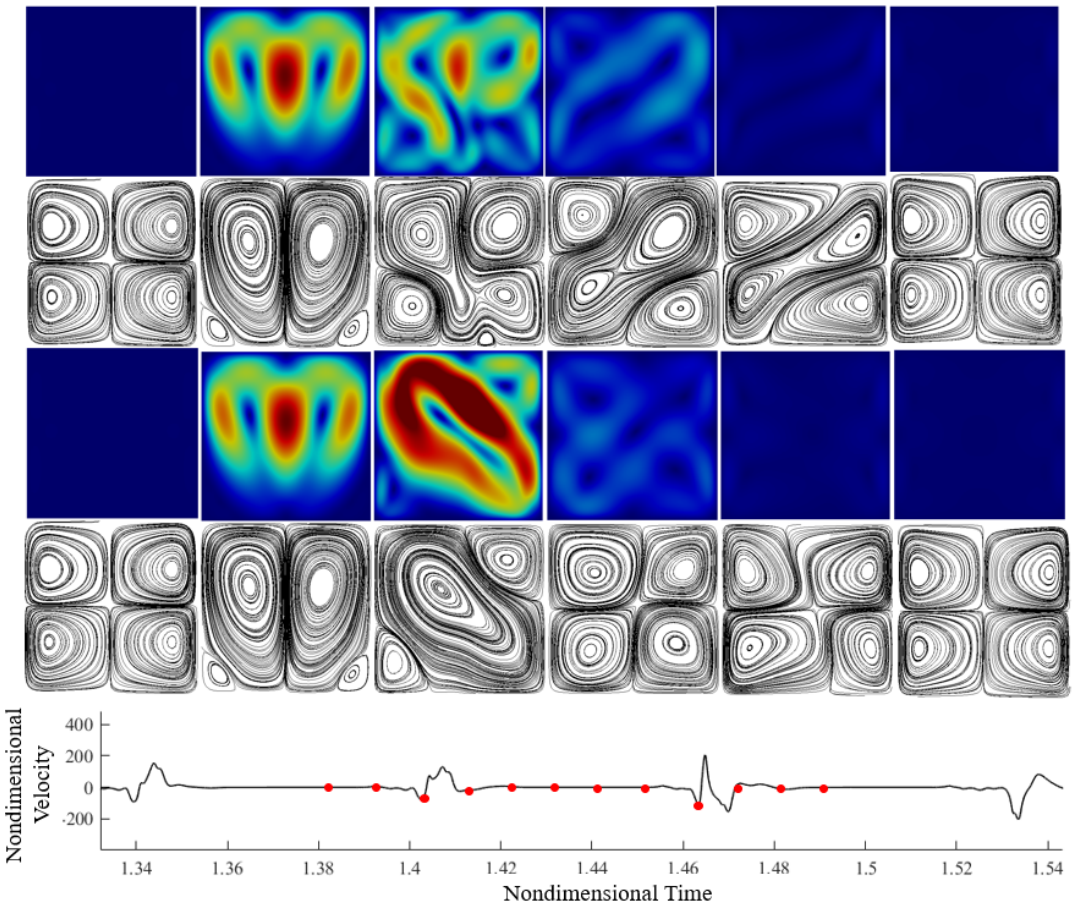

Figure 4.13: Instantaneous streamlines and velocity magnitude over two periods for the case $Ra_\omega = 8.5 \times 10^5$, $\Omega = 100$, accompanied by the velocity signal. The 12 red dots represent the time at which the snapshots are taken (six snapshots for each period.)

the region of high vibrational frequencies. Easily identifiable, these solutions exhibit no adherence to the imposed vibrational forcing.

As the reader will easily realize by inspecting Fig.4.14, the behaviour of the flow changes randomly and presents a number of interesting and unpredictable topological (in terms of streamlines) features, which essentially result from the excitation and superposition of convective modes with different symmetries.

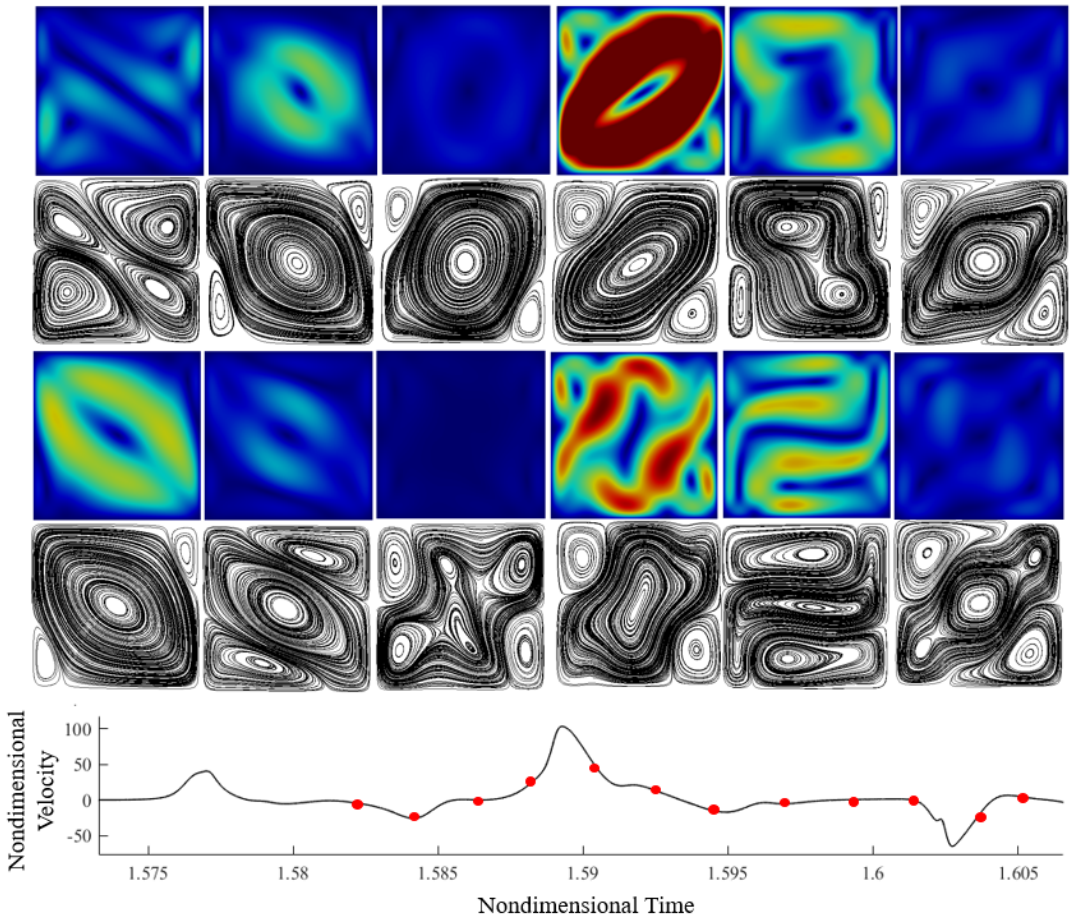

Figure 4.14: Instantaneous streamlines and velocity magnitude over two periods for the case $Ra_\omega = 10^6$, $\Omega = 500$ (NS-NP), which are accompanied by the velocity signal. The 12 red dots represent the time at which the snapshots are taken (six snapshots for each period)

4.6 Discussion

Originally conceived as an extension of other works in the literature, the present study has confirmed that a kaleidoscope of solutions can be obtained in an apparently innocuous configuration such as a square cavity subjected to vibrations parallel to the applied temperature difference. Considering relatively high values (heretofore unexplored) of the vibrational Rayleigh number and non-dimensional angular frequency, two new states have been identified in the space of parameters, namely, periodic and non-periodic synchronous modes of convection. The peculiarity of the latter resides in

its ability to produce turbulent bursts, which occur synchronously with the forcing but do not display the same behaviour in each period of oscillation. Although the appearance of the synchronous periodic solution is more sporadic, this mode of convection can manifest itself also for high Rayleigh numbers, which indicates that an increase in Ra_ω does not systematically lead to more chaotic phenomena. Comparison with equivalent studies conducted for the same value of the Prandtl number, same geometry, and same range of values of the Rayleigh number for classical Rayleigh–Bénard convection indicates that the set of potentially excitable modes with different symmetries is greatly expanded when the steady gravity is replaced by a time- periodic acceleration. From the limited series of snapshots included in the present work, the predominantly occurring symmetries are represented by the symmetric–symmetric mode (ss) (generally appearing as a quadrupolar pattern) and the diagonal mode characterized by a predominant central vortex ornated with two smaller outer corner rolls. However, occasional manifestations of other patterns are also possible, including (but not limited to) the vertical two-roll configuration (sa), the columnar arrangement of three horizontally stretched rolls, as well as other three-roll configurations. In line with earlier studies on the companion problem of standard RB convection, it can be argued that an explanation for this variety of multicellular states is rooted in the existence of multiple solutions, i.e., different possible modes of convection that coexist in the space of parameters and can be excited for comparable values of the driving force (Mizushima [19]; Hof *et al.* [109]; Leong [110]; Lappa [111]). These modes can be excited at different times or at the same time, resulting in new patterns due to their non-linear combination. A comparison of instantaneous and time-averaged effects also leads to meaningful conclusions. The former is generally dominant over the entire range of values of and Ω considered. The dependence on the problem parameters also displays notable differences. While time-averaged quantities are almost independent from the vibrational Rayleigh number, instantaneous ones grow (as expected) with this parameter. However, as the angular frequency of the imposed vibrations is increased, both fluctuating and time- averaged (stationary) effects (as properly quantified through the so-called TFD distortions) tend to be damped until a completely motionless state is attained (for a cut-off value of the frequency that grows

with the considered value of Ra_ω). This scenario is consistent with that revealed by the Nusselt number (which tends to 1 as this cut-off value is exceeded, thereby indicating that purely thermally diffusive conditions are established). It is also congruent with the so-called Birikh's law, i.e., the expected tendency of the time-averaged vibration force to create isotherms perpendicular to the direction of vibrations when the frequency becomes relatively high (thereby causing a strong increase in the value of the Rayleigh number needed to produce convection, which ideally tends to infinity in the limit as $\Omega \to \infty$, [35]). The peak visible in both the instantaneous TFD and Nu plot at $\Omega = 100$ for relatively high values of the vibrational Rayleigh number calls for a complementary explanation. This can be further elaborated in its simplest form on the basis of the argument that the fluctuating components of velocity and temperature are dominant and therefore play a crucial role in determining the intensity of the heat exchange at the solid boundaries. Moreover an explanation for the non-monotone behaviour must be sought in the spatial symmetries of the dominant flow. Indeed, the specific value of the angular frequency for which the maximum is attained ($\Omega \cong 100$) in the range of high values of the vibrational Rayleigh number corresponds to conditions where the (ss) symmetry (multicellular state) is dominant.

4.7 Conclusion

Given the lack of studies specifically conceived to investigate the properties of pure thermovibrational flow in conditions for which the temperature gradient is parallel to the direction of shaking, this work has been conducted under the optimistic idea that it may provide a common point of origin from which many studies in the community may depart (including meaningful extensions to three-dimensional configurations). These future works might be based on the same variegated approach proven instrumental in unravelling processes that are interwoven or overshadowed and successful at illuminating the dynamical mechanisms at play on these systems.

Chapter 5

Hadley flow type thermovibrational convection and turbulence for high values of Ra_ω

This chapter is based on the following peer-reviewed publication:

Crewdson, G and Lappa, M., 2021, "Thermally-driven flows and turbulence in vibrated liquids", *International Journal of Thermofluids*, 11, 100102, https://doi.org/10.1016/j.ijft.2021.100102.

The text in this chapter has been modified only when necessary in order to preserve the continuity and flow of this thesis.

5.1 Introduction

In this chapter cases where the direction of vibrations is perpendicular to the imposed temperature gradient are considered. The study is designed as a set of separate problems, where each problem aims to unravel the implications of the fundamental properties of thermovibrational convection. These include the symmetry of the emerging pattern as perceived by a real observer and as seen in a "time-averaged space", the synchronous or non-synchronous response of the velocity field to the applied forcing,

the magnitude of the so- called Thermofluid-dynamic (TFD) distortions and the peculiar route of evolution towards chaos. A kaleidoscope of previously unknown solutions is reported giving emphasis to some still poorly known aspects such as the complex nature of the textural transitions that take place in the flow as the Gershuni number is increased (from 3.30×10^2 to 5.00×10^7 for Pr = 15). It is shown that the low-frequency regime is relatively stable over this range. In addition to the standard quadrupolar pattern, in such a case, peculiar convective structures emerge where the time-averaged rolls display a very regular columnar arrangement, which has been rarely observed in earlier studies. Chaotic states are enabled when larger frequencies of vibration are considered. While for intermediate frequencies concurrent aspects of the Feigenbaum and Manneville and Pomeau mechanisms can be recognized, the hallmark of the high frequency regime is its adherence to the standard Ruelle-Takens scenario.

5.2 Mathematical model and validation

In this study, the vibrations are applied along the horizontal axis and the temperature gradients sits along the vertical axis as shown in 5.1.

To demonstrate the reliability of the numerical method presented in the next section (and the related implementation available in OpenFOAM), preliminary simulations have been compared with well established benchmarks available in the literature. In particular, the patterns reported by Lappa and Monti and Savino [14, 107] have been selected given the similarity between their configuration and that examined in the present work. Indeed, in these works, the steady gravity field was replaced by a time periodic body force and set perpendicular to the temperature gradient. The outcomes of such simulations are presented Fig.5.2 for Pr=15 and $Gs = 3.30\times10^2$ and 3.30×10^4, where the pattern of the time-averaged velocity field is shown. The classical transition from the so-called quadrupolar flow field to the inversional symmetry pattern, as the Gershuni number is increased, is observed here. For the sake of additional validation, and given the scarcity of relevant results in the literature, the solution method has been verified further through 'ad hoc' comparisons between the results provided by OpenFOAM

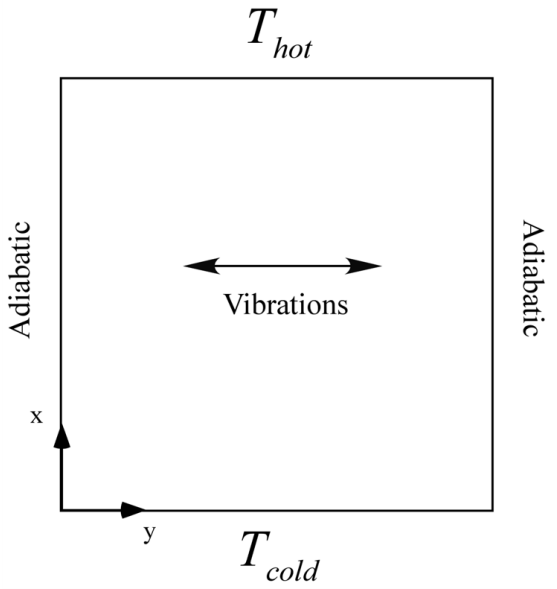

Figure 5.1: Square cavity with characteristic size L, delimited by solid walls (one at y=0 cooled, the other at y=1 heated, adiabatic conditions on the remaining sidewalls). The vibrations are directed along the y axis, i.e. they are perpendicular to the imposed temperature difference.

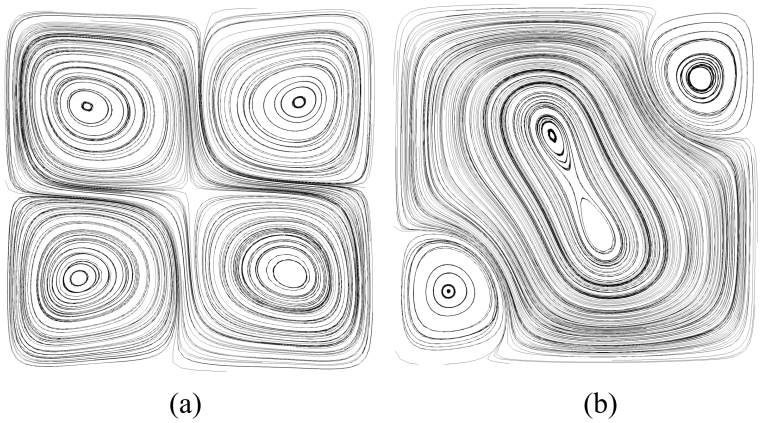

Figure 5.2: Benchmark simulations corresponding to Pr=15: a) $Gs = 3.30 \times 10^2$ and b) 3.30×10^4 (the classical transition from the so-called quadrupolar flow field to the inversional symmetry pattern can be seen, as the Gershuni number is increased).

and those yielded by an alternate computational platform (namely, the same software implemented by Lappa [1] and Lappa and Burel [71], used also in the validation study shown in Sect.4.3). Although, the same class of pressure-velocity methods discussed before is at the root of both implementations, they differ in regard to temporal schemes

(which are implicit and explicit for OpenFOAM and Lappa's algorithm, respectively). Another distinguishing mark is represented by the level of coupling for velocity and pressure (this being based on a staggered arrangement of primitive variables in the latter software). The outcomes of the focused comparisons conducted for a series of values

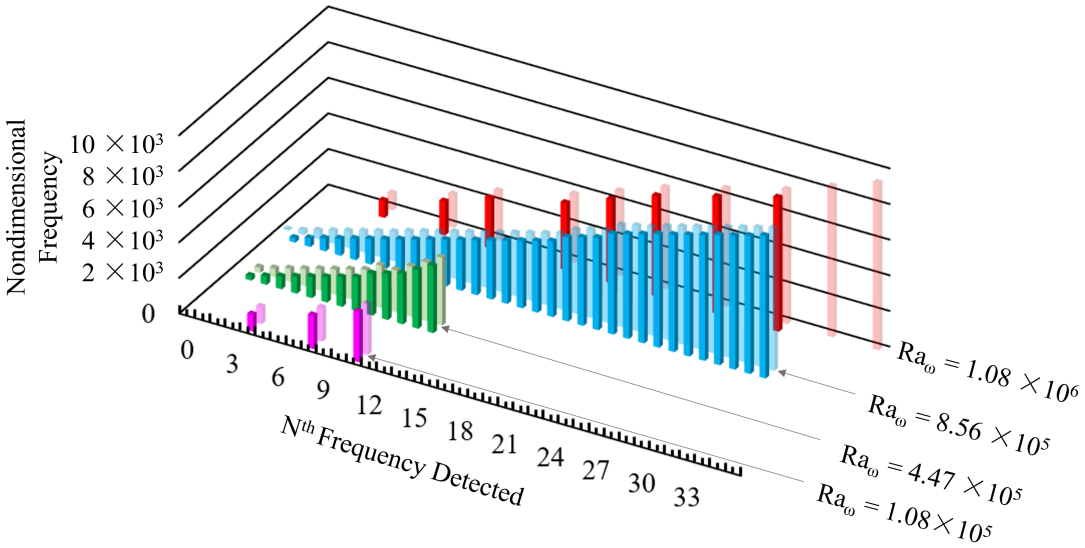

Figure 5.3: Detected frequencies for 4 cases (Pr=15 ,$\Omega = 9.38^2$, $Ra_\omega = 1.08 \times 10^5$, $Ra_\omega = 4.47 \times 10^5$, $Ra_\omega = 8.56 \times 10^5$, and $Ra_\omega = 1.08 \times 10^6$). In full colour are presented the results from OpenFOAM and in semi-transparent are presented the results from the in-house code.

of the vibrational Rayleigh number (namely, $Ra_\omega = 1.08 \times 10^5$, $Ra_\omega = 4.47 \times 10^5$, $Ra_\omega = 8.56 \times 10^5$, and $Ra_\omega = 1.08 \times 10^6$, for Pr=15 and $\Omega = 9.38 \times 10^2$) are quantitatively substantiated in Fig.5.3. The reported frequencies are provided by a Fast Fourier Transform (the x, y and z axes representing the number of frequencies detected in the spectrum, the frequency value and the corresponding vibrational Rayleigh number, respectively). As evident in this figure, the two codes provide an almost perfect agreement in terms of frequency spectrum (the only minor difference relates to the slightly higher number of frequencies obtained with the in-house code in one of the cases, for which, however, the related amplitude has been found to be almost negligible).

5.3 Grid refinement

Given that the specific nature of the considered problem may potentially lead to the development of instabilities and even transition to turbulence in some conditions, special attention has been paid to build relevant grids, i.e. meshes able to capture properly all the spatial scales involved in the emerging phenomena. In the absence of relevant (observational) information to properly address this point (due to the limited number of earlier investigations on the subject), this study is based on general criteria available in the literature for problems that share common aspects with the present one. Simirlarly to Sect.4.3, as a first requirement to be met, the need to have a sufficient resolution inside the thermal boundary layers is considered. Though a dichotomy is often drawn between buoyancy convection induced by steady gravity or a time-periodic acceleration, indeed, these phenomena display some affinities. For relatively high values of the Prandtl number, both are prone to develop regions of limited thickness located in proximity to the solid boundaries, where temperature displays strong gradients or steep profiles. Russo and Napolitano's The Order of Magnitude Analysis for the boundary layer thickness [103] and Shishkina's boundary layer resolution requirements [104] touched upon in Sect.4.3, (Equations 4.4 and 4.4) are also evaluated here. Superimposed on these constraints is the need to capture the smallest flow feature eventually present in the fluid flow when it enters the turbulent regime. For the case of perpendicular vibrations, the flow problem can be considered as the vibrational analogue to the classic Hadley flow estimated using the correlation originally elaborated by Paolucci [112] and Farhangnia *et al.* [113].

$$\zeta_{Ra_\perp} = \pi \left(\frac{16Pr}{Ra} \right)^{3/8} \tag{5.1}$$

A summary of the theoretical grids defined using the above criteria under the assumption of uniform mesh are presented in Table 5.1 together with the corresponding thickness of the thermal boundary layers (as provided by effective numerical simulations based on such grids). It can be noted that, in the frame of this initial assessment

of the required spatial resolution, the number of cells required in the boundary layer following Shishkina's formulation (Eq.4.4) has been found to be the most restrictive mesh-resolution controlling factor over the considered range of values of the vibrational Rayleigh number. In order to circumvent difficulties deriving from the prohibitively ex-

Table 5.1: Theoretical and measured boundary layer properties

Ra_ω	Theoretical $\delta_{th.BL}$	Actual $\delta_{th.BL}$	Theoretical $N_{th.BL}$	Actual $N_{th.BL}$	Grid resolution
$6.22 \times 10^4 < Ra_\omega < 1.08 \times 10^6$	n/a	n/a	n/a	n/a	80 by 80
2.42×10^6	2.53×10^{-2}	2.49×10^{-2}	3.17	7	100 by 100
3.42×10^6	2.32×10^{-2}	2.08×10^{-2}	3.34	6	100 by 100
7.66×10^6	1.90×10^{-2}	1.90×10^{-2}	3.77	7	125 by 125
1.08×10^7	1.74×10^{-2}	1.60×10^{-2}	3.97	6	125 by 125
2.42×10^7	1.43×10^{-2}	1.03×10^{-2}	4.48	4	125 by 125

pensive computing cost resulting from the enhanced computational overhead required by uniform grids satisfying all these requirements, a non-uniform distribution of computational cells is used. Along these lines, Fig.5.4 illustrates the different mesh types

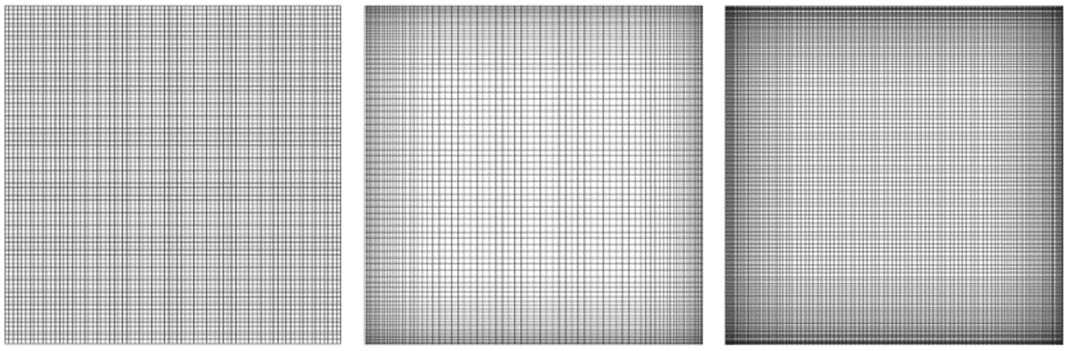

(a) 80 by 80 (no bias) (b) 100 by 100 (including bias at wall) (c) 125 by 125 (including bias at wall)

Figure 5.4: Different mesh sizes used depending on Ra_ω

adopted for the ensuing additional mesh refinement study. It can be noted that a bias is included towards the walls of the cavity. By doing so, the number of nodes in the boundary layer is increased instead of increasing the number of nodes across the whole domain, thereby reducing the required computational power. Though the above discussion might be regarded as an exhaustive treatment of the problem in terms of space resolution requirements, it does not consider another important restrictive condition that plays a crucial role when flows induced by non-constant driving forces are considered, i.e., the needed temporal resolution. This specific aspect requires the con-

sideration of two additional concurrent factors. For thermovibrational flow, both the instantaneous and time average velocities can be analysed by means of Fast Fourier Transforms (FFT), whereby the velocities are presented as a function of frequency rather than a function of time. The appropriate sampling rate must be chosen in order to ensure all frequencies are taken into account. Traditionally, the minimum sampling rate of a continuous signal must obey the Nyquist-Shannon Sampling Theorem. The theorem states that the signal must be sampled at a frequency superior to twice the frequency of the signal f_s (the Nyquist Frequency), giving $fs/2 < f$. The time step of the simulation is defined as: $\Delta t = 2\pi/\omega N_p$, where, N_p is the number of samples per period and must satisfy the Nyquist Sampling Theorem whereby $N_p > 2f$. The second constraint to be aware of is the well-known effect of the Courant number (C), which must be smaller than one to ensure numerical algorithm stability. For all the simulations presented in this study, the time integration step (satisfying both abovementioned requirements) has been selected in such a way to have a minimum of 400 steps for each cycle of vibrational modulation. In order to confirm the viability of all these theoretical requirements, an additional mesh refinement study has been carried out on two cases, shown in Fig.5.5, where the frequency spectrum has been chosen as the comparative output parameter. In case (a) ($\Omega = 9.38 \times 10^3$, $Ra_\omega = 1.08 \times 10^6$, $Gs = 1.00 \times 10^5$), a grid resolution of 80 by 80 cells satisfies the theoretical requirements. Accordingly, two peripheral simulations have been carried out, one with a coarser grid (60 by 60 cells) and one with a finer grid (100 by 100 cells). The results from the higher resolution grid are quasi-identical to those obtained with the predicted 80 by 80 grid, therefore this grid resolution has been used in the present study for all cases with $Ra_\omega < 1.08 \times 10^6$. As for case (b) ($\Omega = 9.38 \times 10^3$, $Ra_\omega = 7.66 \times 10^6$, $Gs = 1.00 \times 10^6$), a grid resolution of 125 by 125 cells satisfies the theoretical requirements. For this case, the two additional simulations have been carried out on a 100 by 100 cell grid for the coarser case, and a 140 by 140 cell grid for the finer case. It can be noted that for any mesh exceeding 100 by 100 cells a bias is applied at the walls as indicated in Fig.5.4. As this case is considered weakly turbulent (this is expanded on in following sections), the exact frequencies and amplitudes can vary from simulation to simulation, however, it is evident here that

the response of the system is very similar for all three grid resolutions. Therefore, a grid size of 125 by 125 is acceptable in this case. These two representative cases have shown that the theoretical requirements based on the complex set of criteria illustrated before can be used as a relevant basis to determine 'a priori' the needed resolution.

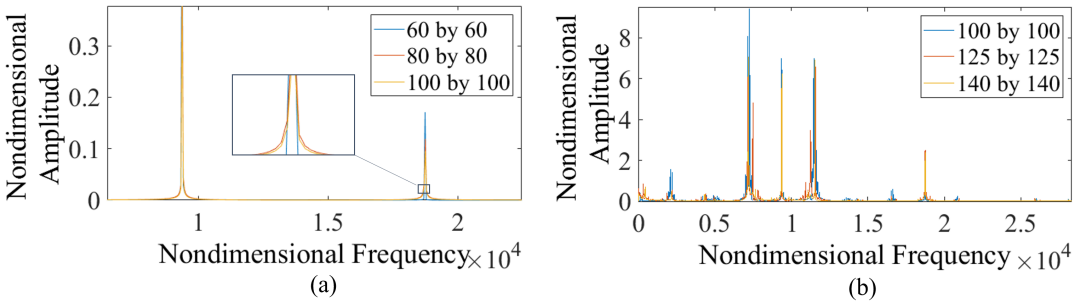

Figure 5.5: Grid refinement study for the case $\Omega = 9.38 \times 10^3$ (a) $Ra_\omega = 1.08 \times 10^6$, ($Gs = 1.00 \times 10^5$), and (b) $Ra_\omega 7.66 \times 10^6$, ($Gs = 5.00 \times 10^6$).

5.4 Simulation results

5.4.1 The high frequency case: The Ruelle-Takens scenario

In the present sub-section, the Gershuni number is varied parametrically from the first reference case $Gs = 3.30 \times 10^2$, (corresponding to $Ra_\omega = 6.22 \times 10^4$) to $Gs = 5.00 \times 10^7$, ($Ra_\omega = 2.42 \times 10^7$), thereby spanning 5 orders of magnitude. Although a total of 12 cases are simulated for a given frequency $\Omega = 9.38 \times 10^3$, in the following, only 6 of these cases are discussed to illustrate the different possible 'solutions' (the reader being referred to Table 5.2 for a complete description of all simulations and the respective regimes). For $3.30 \times 10^2 < Gs < 5.00 \times 10^3$ (or $6.22 \times 10^4 < Ra_\omega < 2.40 \times 10^5$) the streamlines of the time-averaged velocity field show the quadrupolar flow field already discussed in relation to the first validation case (the first fundamental mode displaying central symmetry, see Fig.5.6, left panel). Starting from a single roll, the instantaneous flow field (Fig.5.6, right panels) changes periodically in time, whereby four small rolls emerge at the outer corners of the cavity and then disappear leaving behind them again one single roll (this behaviour occurring twice per period). Following up on this point, it is worth recalling that the single vortex pervasive throughout the entire square cavity, regularly

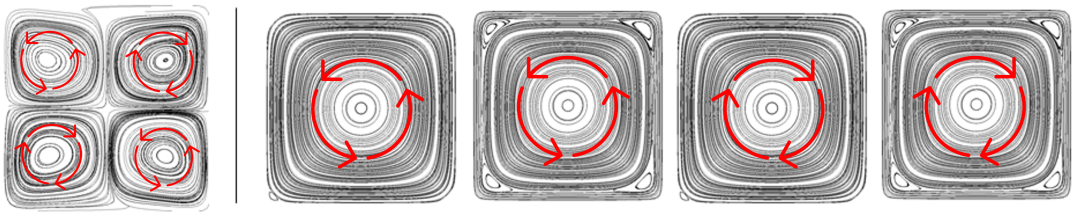

Figure 5.6: $Gs = 3.30 \times 10^2$, $Ra_\omega = 6.22 \times 10^4$, $\Omega = 9.38 \times 10^3$: time-averaged flow (left) and instantaneous flow (right), where the instantaneous snapshots are taken at t=0, 0.1P, 0.5P and 0.6P (where $P = 2\pi/\Omega$). The arrow indicates the counter clockwise or clockwise motion of the fluid.

changes its sense of circulation (from the counter clockwise to the clockwise orientation) according to the sign of the acceleration. As the order of magnitude of the Gershuni

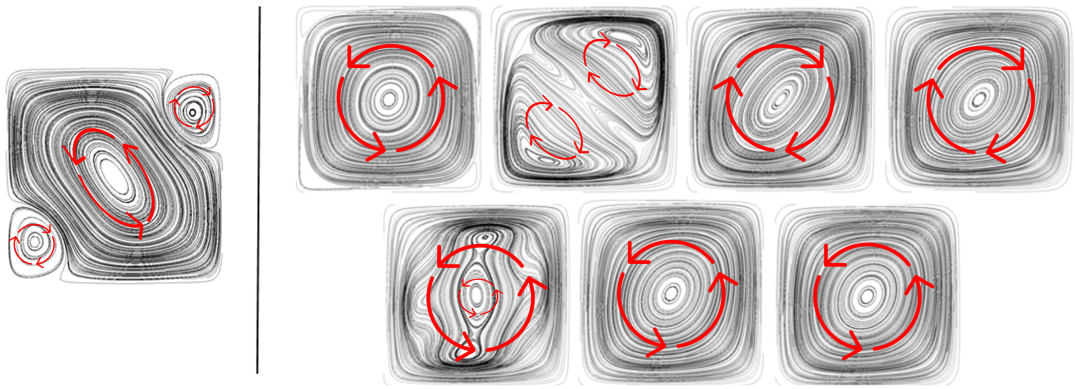

Figure 5.7: $Gs = 1.00 \times 10^4$, $Ra_\omega = 9.38 \times 10^3$: time-averaged flow (left) and instantaneous flow (right) where the instantaneous snapshots are taken at t=0, 0.1P, 0.2P, 0.4P, 0.6P, 0.8P, 0.9P and 1P.

number shifts from $O(10^3)$ to $O(10^4)$, the time-averaged flow field transitions from the quadrupolar field to a diagonal state (the second fundamental mode, Fig.5.8, left panel), in agreement with the validation case. The instantaneous flow field also undergoes some modifications; indeed, it displays a more involved sequence of snapshots, where occasional manifestations can be seen of a diagonal convective structure ($t = t_0 + 0.1P$) due to the superposition of (ss) and (aa) modes and a columnar arrangement of rolls ($m_y = 1$, $m_x = 3$) embedded in a larger scale circulation for $t = t_0 + 0.8P$. On increasing the Gershuni number to $Gs = 10^5$ ($Ra_\omega = 1.08 \times 10^6$), substantial changes can be spotted in both the time-averaged and instantaneous fields (Fig.5.8). In what concerns

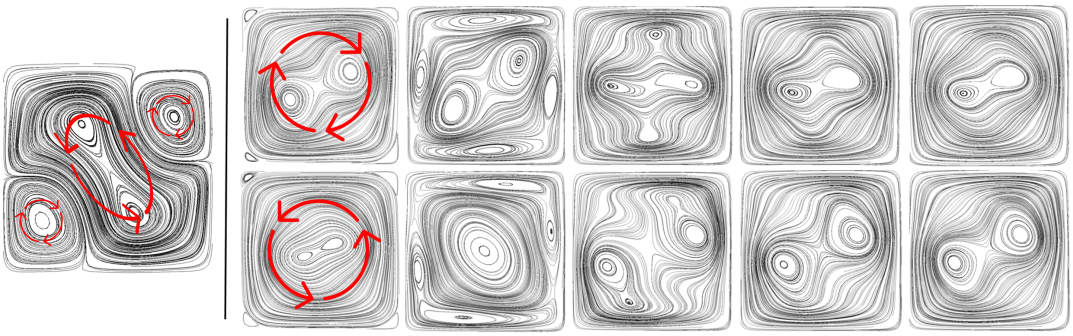

Figure 5.8: $Gs = 10^5$, $Ra_\omega = 1.08 \times 10^6$, $\Omega = 9.38 \times 10^3$: time-averaged flow (left) and instantaneous flow (right), where the instantaneous snapshots are taken at 0.1P intervals from t=0 to t=P.

the time-averaged velocity, the dominant diagonal orientation of the main circulation is conserved, however the two inner roll seems to be 'squashed' by the growing of two smaller rolls in the outer corners of the cavity. As for the instantaneous field, a time periodic scenario is still observed. However, an increase in complexity in the patterning behavior of the fluid is evident. The single roll pervasive throughout the cavity ((aa) mode with $m_y = m_x = 1$), seen for lower values of Ra_ω and Gs, does no longer represent the preferred transitional stage of evolution; it is replaced by transitional states with 2 dominant central rolls (essentially aligned along the direction of vibrations), ornated by external eddies which nucleate along the side walls and/or the cavity corners. Moving on to the case $Gs = 10^6$ ($Ra_\omega = 3.42 \times 10^6$), although the topological configuration of the time-averaged flow field remains unchanged, some morphological alterations can be seen (Fig.5.9, left panel). The two inner rolls embedded into the main circulation, which previously were perfectly aligned with the NW-SE diagonal direction, are now displaced towards the lateral (external walls) and, at the same time, towards the cavity midplane x=1/2 (thereby creating the illusion of an inclined Z-shaped vortex). This is accompanied again by an increase in complexity in the instantaneous field. As in this case the velocity signal is no longer strictly synchronous with the forcing frequency (this will be expanded on in the next section), a selection of snapshots illustrating the various possible multi-cellular states is presented in, Fig.5.9 right panel. The next interesting transition occurs when Gs is increased to 5.00×10^6 (and Ra_ω to 7.66×10^6).

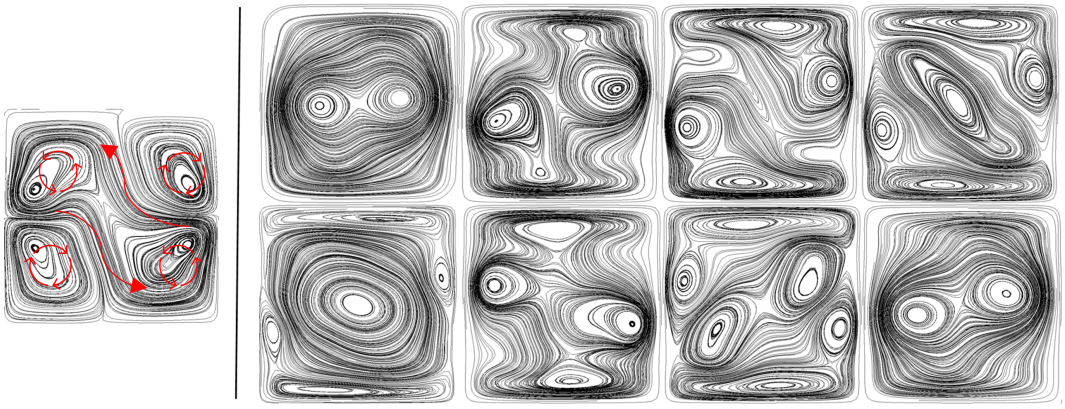

Figure 5.9: $Gs = 1.00 \times 10^6$, $Ra_\omega = 3.42 \times 10^6$, $\Omega = 9.38 \times 10^3$: time-averaged flow (left) and instantaneous flow (right). As the synchronicity is broken, the instantaneous snapshots are taken at arbitrary times in order to illustrate the myriad of possible 2, 4, 5 and 6-roll patterns.

In such conditions, notably, the time-averaged field presents a slight fluctuation in time (it becomes time dependent, Fig.5.10 (a)). Surprisingly, the 4-roll configuration is recovered. Qualitative comparison with Fig.5.6, however, reveals that the distribution of streamlines is seemingly distorted. For what concerns the instantaneous field (as the reader will easily realize by inspecting the related sequence of snapshots in Fig.5.10 (b)), the temporal evolution of the flow can be seen as a continuous swap between a two-roll diagonal mode (oriented along the NW-SE or the NE-SW directions depending on the considered instant) and a zig-zag configuration of four rolls all embedded in a larger circulation. The next figure of the sequence simply illustrates that as Gs is increased to $Gs = 5.00 \times 10^7$ ($Ra_\omega = 2.42 \times 10^7$), both the time-averaged field and the instantaneous field become relatively chaotic (Fig.5.11 (a) and (b), respectively). Symmetry along the diagonal axis is (mostly) lost in both the instantaneous and time averaged field. This is accompanied by an increase in the number of eddies that appear in the flow, emerging from multiple locations in the cavity. In the following, the earlier arguments developed for the topology of the streamlines of the time-averaged and instantaneous flow field and the related temporal and morphological evolution are complemented by a frequency spectrum analysis based on the velocity signal measured by a numerical probe located in the geometrical centre of the cavity. To extract these frequency spectra from the velocity

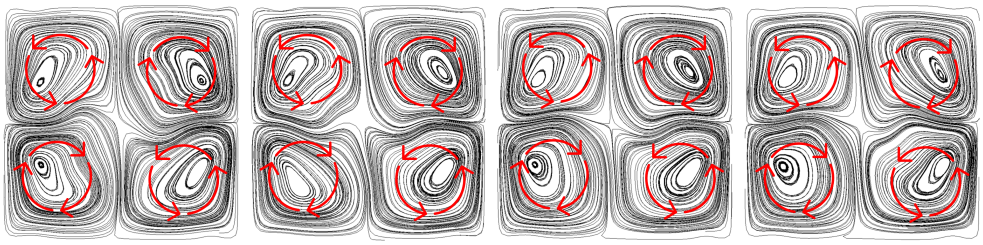

(a)

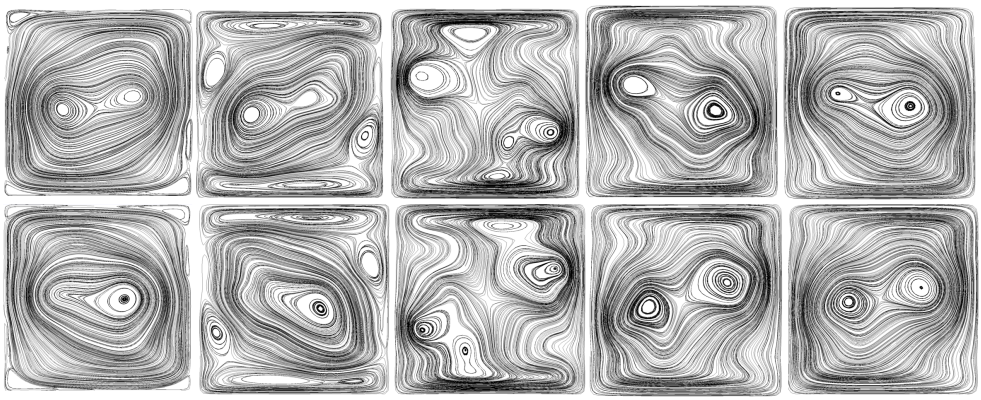

(b)

Figure 5.10: $Gs = 5.00 \times 10^6$, $Ra_\omega = 7.66 \times 10^6$, $\Omega = 9.38 \times 10^3$: a) time-averaged flow; b) instantaneous flow Time-averaged snapshots taken at non-dimensional time t=1.206, 1.219, 1.233 and 1.246, instantaneous snapshots taken at intervals of 0.1P starting at t=1.219 and ending at t=1.219+P.

signal, for each simulation a Discrete Fourier Transform has been implemented using a Fast Fourier Transform algorithm (FFT), whereby the time domain is transformed to the frequency domain. In this regard, Fig.5.12 is instrumental in revealing that (as expected) an increase in Gs for a fixed Ω(equivalent to an increase in Ra_ω makes the number of detected signal frequencies higher. In the following, for simplicity, the following symbols are used to indicate integer multiples of the forcing frequency present in the spectrum: $\Omega_2 = 2\Omega$, and$\Omega_3 = 3\Omega$. As the reader will realize through inspection of Fig.5.12, over the extended range $3.30 \times 10^2 < Gs < 5.00 \times 10^5$, ($6.22 \times 10^4 < Ra_\omega = 2.42 \times 10^6$) the emerging flow can be considered synchronous with the imposed forcing (as all detected frequencies are harmonics of the original non-dimensional frequency of vibrations Ω). However, from $Gs = 10^6$, $Ra_\omega = 3.42 \times 10^6$ and $Gs = 5 \times 10^6$, $Ra_\omega = 7.66 \times 10^6$ the FFTs show a wide range of frequencies. Additional frequencies are seen to

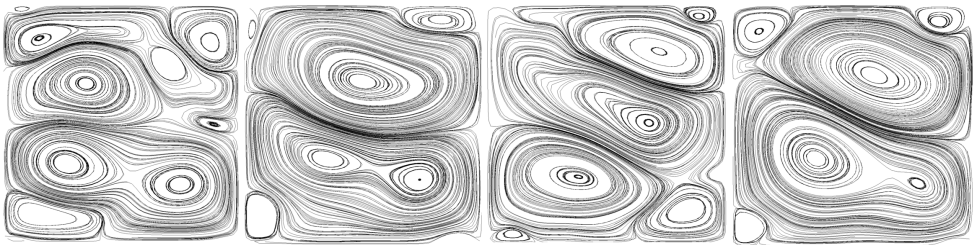

(a)

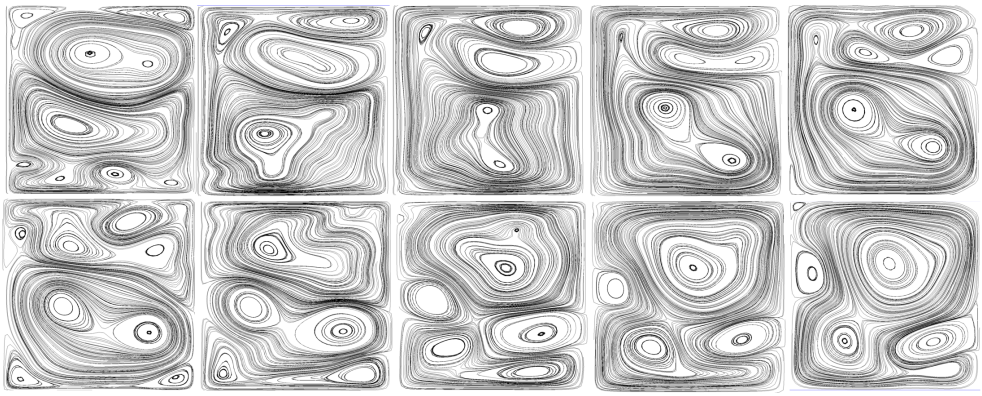

(b)

Figure 5.11: $Gs = 5.00 \times 10^7$, $Ra_\omega = 2.42 \times 10^7$, $\Omega = 9.38 \times 10^3$: a) time-averaged flow; b) instantaneous flow The time averaged snapshots are taken at t=2.023, 2.030, 2.036, 2.043 the instantaneous snapshots are taken at 0.1P intervals starting at t=2.339 and ending at t=2.339+P.

appear at the right and left-hand side of Ω and its harmonics (Fig.5.13). Although these frequencies are non-synchronous with the main frequencies Ω, Ω_2 and Ω_3, they follow an interesting pattern whereby: $\Omega_{2R} = 2\Omega_R$ and similarly, $2\Omega_L = 2\Omega_{1L}$, where Ω_R and Ω_L represent incommensurate frequencies that appear to the right and left of Ω respectively. As a final look at the lower panels in Fig.5.13 would indicate, when the Gershuni number is increased beyond $Gs = 5 \times 10^6$ (and the Rayleigh number beyond $Ra_\omega = 7.66 \times 10^6$) the behaviour becomes more turbulent (as witnessed by the continuous distribution of frequencies in the spectrum, which quantitatively substantiate the complex patterning behaviour reported in Fig.5.11). From the streamlines of the instantaneous and time-averaged velocity fields, combined with the frequency spectrum analysis, the overall behaviour of the considered system can therefore be categorised as illustrated in Table 5.2. As the appearance of turbulence (a continuous frequency spectrum is preceded by

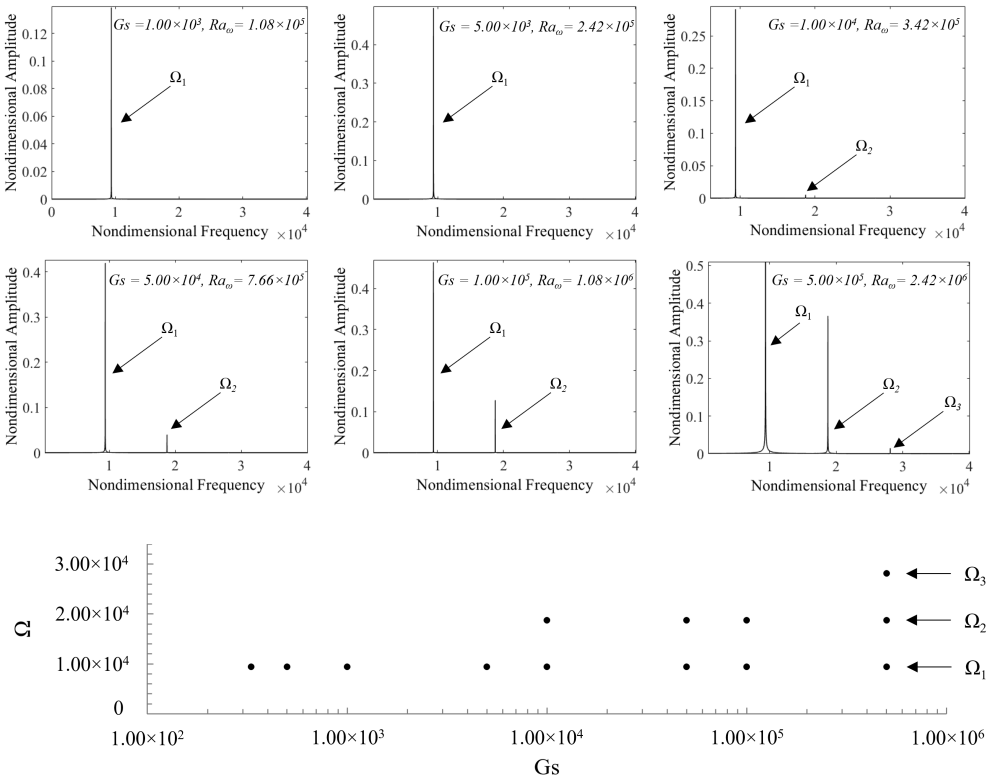

Figure 5.12: Harmonic frequencies detected at increasing values of Gs ($\Omega = 9.38 \times 10^3$)

the existence of three incommensurate frequencies and related higher-order harmonics), it can also be argued that in the range of high frequencies ($\Omega \approx 10^4$), the transition to chaos essentially adheres to the Ruelle-Takens-Newhouse scenario [53].

Table 5.2: Summary of system responses for increasing values of Gs and Ra_ω at $\Omega = 9.38 \times 10^3$

Gs	Ra_ω	Time-averaged velocity field pattern Regime	
3.30×10^2	6.22×10^4	Quadrupolar	Synchronous
5.00×10^2	7.66×10^4	Quadrupolar	Synchronous
1.00×10^3	1.08×10^5	Quadrupolar	Synchronous
5.00×10^3	2.42×10^5	Quadrupolar	Synchronous
1.00×10^4	3.42×10^5	Predominant diagonal roll	Synchronous
5.00×10^4	7.66×10^5	Predominant diagonal roll	Synchronous
1.00×10^5	1.08×10^6	Predominant diagonal roll	Synchronous
5.00×10^5	2.42×10^6	Z Shape containing two small inner rolls	Synchronous
1.00×10^6	3.42×10^6	Z Shape containing two small inner rolls	Weakly Turbulent
5.00×10^6	7.66×10^6	Oscillating quadrupolar	Weakly Turbulent
1.00×10^7	1.08×10^7	Oscillating quadrupolar	Turbulent
5.00×10^7	2.42×10^7	No distinct pattern	Turbulent

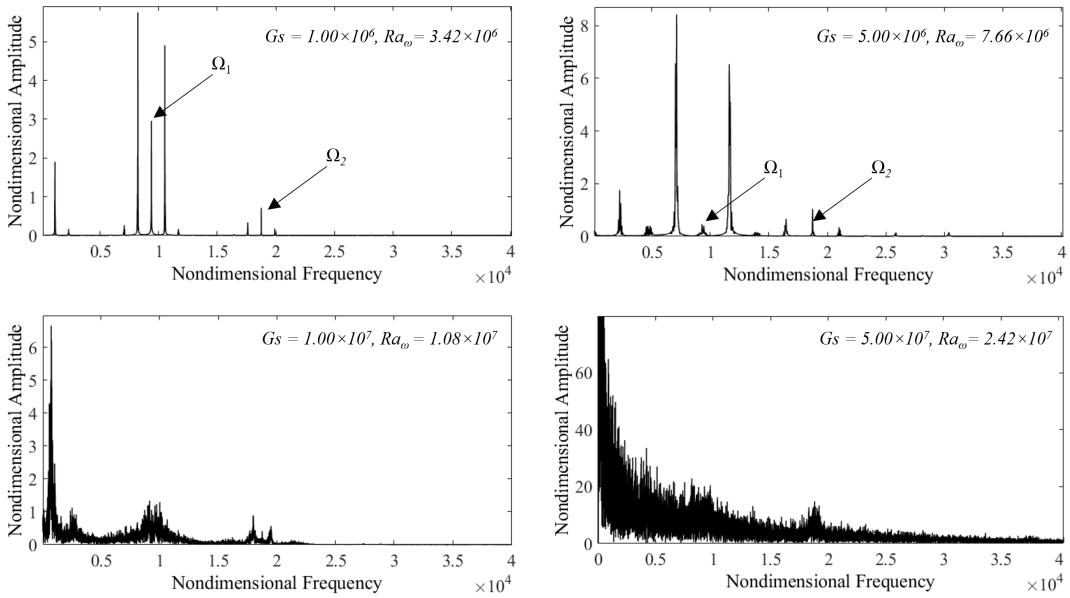

Figure 5.13: Fourier Transforms for the non-synchronous and turbulent cases $10^6 < Gs < 5 \times 10^7$and $3.42 \times 10^6 < Ra_\omega = 2.42 \times 10^7$.

5.4.2 Intermediate frequencies and the Feigenbaum sequence

Having completed a sketch of the dynamics in the high-frequency regime, in the present section the circumstances for which the frequency of the imposed vibrations is smaller (decreased by one order of magnitude, i.e. $\Omega = 9.38 \times 10^2$) is considered. Following the same approach already undertaken for the higher frequency case, first, a description of the velocity field in terms of its various manifestations as a function of Gs at fixed Ω is provided. As evident in Fig.5.14, for $Gs = 10^5$, $Ra_\omega 1.08 \times 10^5$, the time averaged field is steady in time and takes the form of a large inner roll accompanied by two very small rolls at two of the outer corners. The instantaneous field shows an evolving patterning behaviour displaying various realizations and superposition of convective modes with (aa) and (as) symmetry (columnar arrangements of two or three rolls embedded into a larger scale circulation). On increasing the Gershuni number to $Gs = 5.83 \times 10^6$ ($Ra_\omega = 8.27 \times 10^5$), the dynamics become weakly chaotic as witnessed by the unsteady time averaged flow undergoing random switches between distorted three-roll and four-roll patterns. As shown in Fig.5.15, the increased complexity of the flow is also very

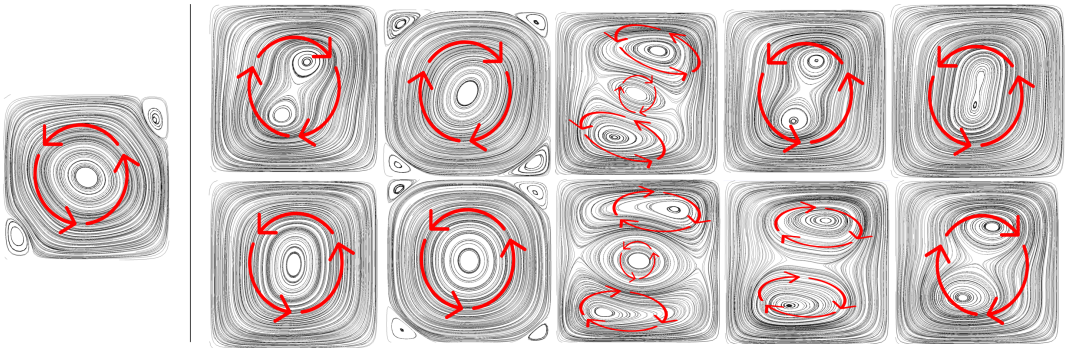

Figure 5.14: $Gs = 1.00 \times 10^5$, $Ra_\omega = 1.08 \times 10^5$, $\Omega = 9.38 \times 10^2$: Time-averaged flow (left), instantaneous flow (right) where the instantaneous snapshots are taken at 0.1P intervals from $t_0 = 0$P to $t = t_0$+P.

evident in the instantaneous velocity field, where, though the dominance of columnar modes can still be identified, a variety of textural transitions take place. An interesting change occurs for $7.08 \times 10^6 < Gs < 1.00 \times 10^7$, ($9.12 \times 10^5 < Ra_\omega < 1.08 \times 10^6$, see, e.g., Fig.5.16), where, most surprisingly, a back transition to a steady state is observed in terms of time-averaged field. Such a simplification can also be spotted in the instantaneous velocity, where only a limited number of textural transitions can be detected. Setting Gs to 5.00×10^7, $Ra_\omega = 2.42 \times 10^6$, however, makes the flow relatively turbulent (see Fig.5.17). While the time-averaged field fluctuates between a three-roll structure similar to that seen in previous cases and more complex three, four and five-roll patterns in a seemingly random manner, the instantaneous velocity gives rise to a rich set of patterns, which include many eddies as already seen previously for chaotic flow in the high-frequency regime. Given the counter-intuitive evolution displayed by the system as a function of the Gershuni number (or vibrational Rayleigh number), unlike Sect.5.4.1 (where the analysis was limited to determining the frequency spectrum and showing its increasing complexity with Gs), here a more sophisticated strategy is employed. This (multi-faceted) approach involves additional tools generally used for the assessment or 'quantification' of the level of chaos embedded in a non-linear system. To do so, inspiration is taken from the work by Ueno *et al.* [114] . Although this referenced study was focused on a different type of convection (Marangoni flow in liquid bridges), the authors demonstrated that an alternate approach (with respect to standard two-dimensional

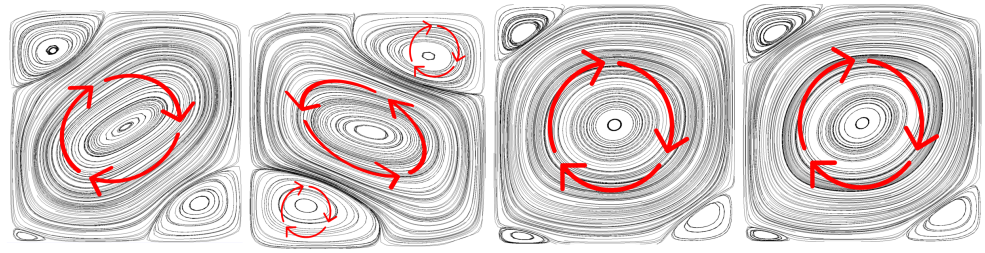

(a)

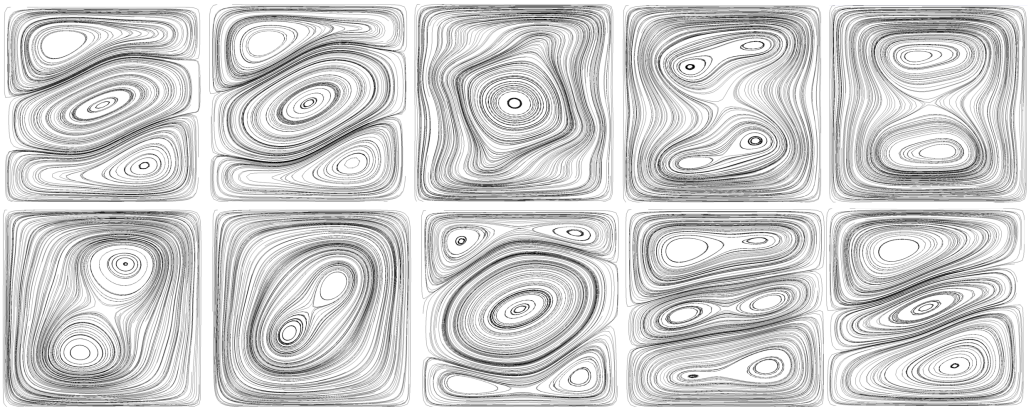

(b)

Figure 5.15: $Gs = 5.83 \times 10^6$, $Ra_\omega = 8.27 \times 10^5$, $\Omega = 9.38 \times 10^2$: a) Time-averaged flow, b) instantaneous flow. Time averaged flow snapshots are taken at t=7.904, 7.938, 7.971 and 8.005 and instantaneous snapshots are taken at 0.1P intervals from t= 8.146 to t=8.146+P.

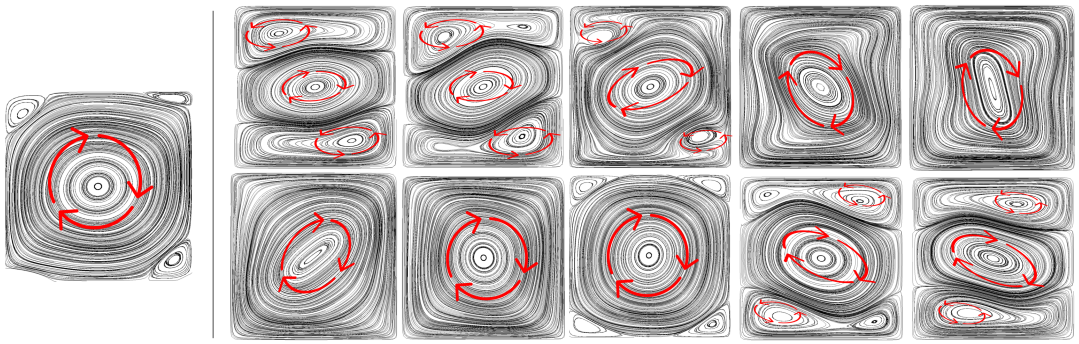

Figure 5.16: $Gs = 1.00 \times 10^7$,$Ra_\omega = 1.08 \times 10^6$, $\Omega = 9.38 \times 10^2$: time-averaged flow (left) and instantaneous flow (right), where the instantaneous snapshots are taken at 0.1P intervals from $t_0 = 0$P to $t = t_0$+P.

Poincarré maps) based on the reconstruction of the pseudo-phase space from the time series of the surface temperature can be used to acquire useful insights into the chaotic

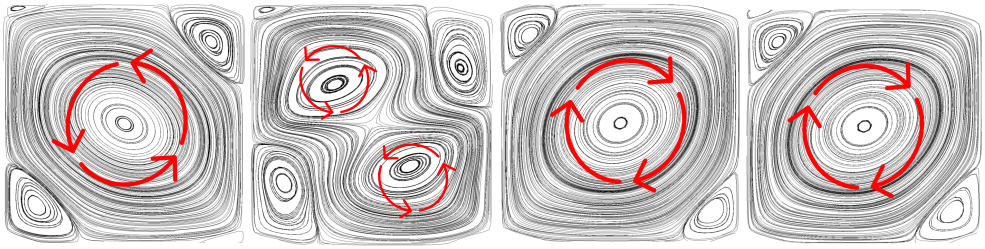

(a)

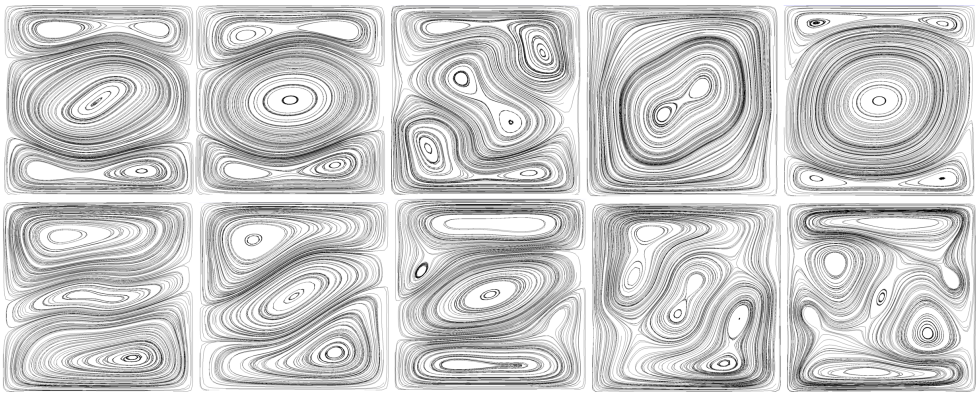

(b)

Figure 5.17: $Gs = 5.00 \times 10^7$, $Ra_\omega = 2.42 \times 10^6$, $\Omega = 9.38 \times 10^2$: a) Time-averaged flow, b) instantaneous flow. Instantaneous snapshots taken at 0.1P intervals starting t=7.343 and ending at t=7.343+P. Time averaged snapshots are taken at t=7.322, 7.329, 7.335 and 7.342,

behavior of a flow. Although in the present work, the velocity time series is used in place of the surface temperature time series, the underlying principles are essentially the same. The sequence of plots in Fig.5.18 represents the outcome of such an analysis. This figure illustrates in an ordered fashion the instantaneous velocity field, the related Fourier transform and finally the reconstructed phase space for increasing values of Gs (Ra_ω). It can be recalled that this fruitful three-fold representation method has also been employed by other authors such as Paolucci and Chenworth [50] and Guzman and Amon [56]. In the present study, the phase space reconstruction has been achieved by using the time delay embedding procedure, stemming from the mathematical framework proposed by Takens [53]. Where the observed time series (in terms of v, where v is the velocity component along y) lies on an 'unobservable' attractor, the time series is used to reconstruct this attractor by plotting the lagged coordinated vectors:

$v(t), v(t+\tau), v(t+2\tau)...v(t+(m-1\tau)$, where m is the embedding dimension and τ is the time delay (or lag). This method is highly informative of the specific behaviour of the dynamic system as an increase in complexity in the velocity signal leads to an increase in complexity of both the frequency spectrum and the reconstructed phase space. As a first example, looking at the panel Fig.5.18a, it can be seen that the velocity signal is initially monochromatic and strictly synchronous with the forcing frequency; the associated reconstructed phase space is composed of a single loop.

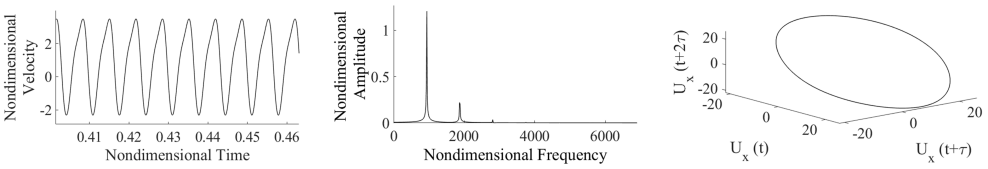

(a) $Gs = 10^5, Ra_\omega = 1.08 \times 10^5$

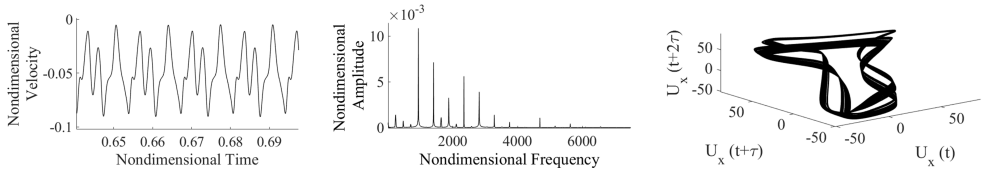

(b) $Gs = 1.70 \times 10^6, Ra_\omega = 4.47 \times 10^5$

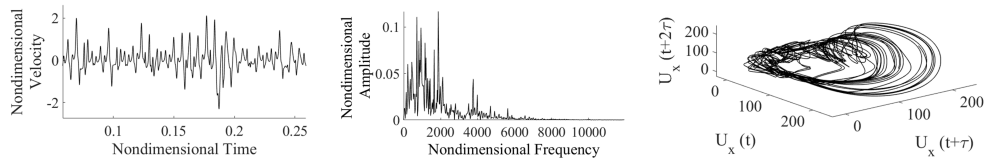

(c) $Gs = 5.83 \times 10^6, Ra_\omega = 8.27 \times 10^5$

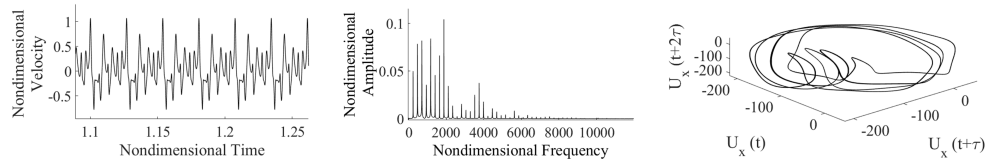

(d) $G = 6.25 \times 10^6, Ra_\omega = 8.56 \times 10^5$

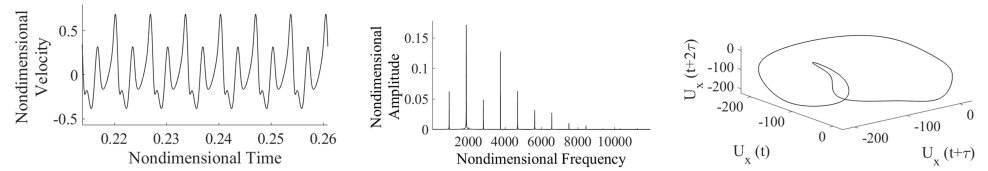

(e) $Gs = 10^7, Ra_\omega = 1.08 \times 10^6$

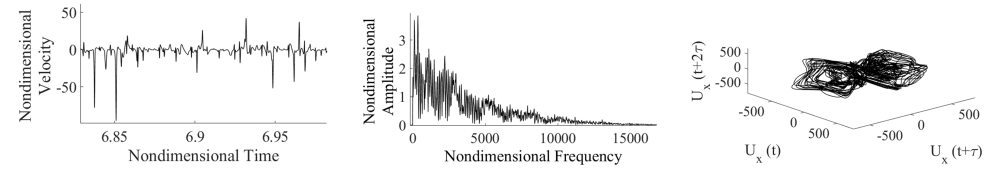

(f) $Gs = 5 \times 10^7, Ra_\omega = 2.42 \times 10^6$

Figure 5.18: Velocity signals, Fourier transforms and phase space reconstructions for 6 values of Gs and Ra_ω(a-f), illustrating the transition to chaos followed by a back transition to a synchronous, single frequency state and again, back to a turbulent state ($\Omega = 9.38 \times 10^2$).

When looking at panel Fig.5.18b however, although the signal is still regular, the presence of a second frequency equal to $\Omega/2$ can be recognized; accordingly, a second loop appears in the phase space. This in an indication that for $Gs = 1.70 \times 10^6, Ra_\omega = 4.47 \times 10^5$, a period- doubling bifurcation has taken place. Careful analysis of Fig.5.18 (the reader being also referred to the information summarized in Table 5.3) also reveals that while for $Gs = 5.83 \times 10^6, Ra_\omega = 8.27 \times 10^5$ (Fig.5.18, panel (c)) the flow can be considered turbulent, for $Gs = 6.25 \times 10^6, Ra_\omega = 8.56 \times 10^5$ (Fig.5.18, panel (d)), a two- frequency state (consisting of $\Omega, \Omega/2$ and related harmonics) is recovered, which is in line with the counter-intuitive trend detected through analysis of the patterning behaviour. Most surprisingly a further increase in the Gershuni number ($Gs = 1.00 \times 10^7, Ra_\omega = 1.08 \times 10^6$, Fig.5.18 panel (e)) causes a further simplification in the spectrum, i.e. the flow returns a single frequency response. This peculiar evolution might be seen as reminiscent of a mechanism of the Feigenbaum type [115] occasionally mediated by intermittent events (these important concepts will be revisited in the discussion). Nevertheless, period doubling bifurcation for the final transition from the last harmonic state to the next turbulent case was not identified (Fig.5.18 panel (f)); additional simulations at intermediate values of Gs and Ra_ω e.g., $Gs = 3.00 \times 10^7, Ra_\omega = 1.88 \times 10^6$ have simply revealed a single-frequency state akin to its predecessor for $Gs = 10^7, Ra_\omega = 1.08 \times 10^6$.

Table 5.3: Summary of system responses for increasing values of Gs and $Ra\omega$ at $\Omega = 9.38 \times 10^2$

Gs	Ra_ω	Flow Regime
1.00×10^5	1.08×10^5	Synchronous
1.70×10^6	4.47×10^5	Periodic doubling
5.83×10^6	8.27×10^5	Turbulent
6.25×10^6	8.56×10^5	Periodic doubling
1.00×10^7	1.08×10^6	Synchronous
5.00×10^7	2.42×10^6	Turbulent

5.4.3 Low frequencies

While a fairly comprehensive picture has been elaborated in the previous two sections about a high frequency ($\Omega = O(10^4)$) and an 'intermediate' frequency ($\Omega = O(10^3)$), for

the sake of completeness, this section continues this investigation by probing the role of a low frequency ($\Omega = 93.8$). It can be anticipated that these cases will require a more contained discussion given their relative simplicity with respect to the more complex dynamics examined for larger values of Ω. In fact, for half of the cases simulated here (yet for Gs up to 5.00×10^7) the instantaneous field has been found to display a single possible state (in the range $10^5 < Gs < 10^6$). This class of solutions takes the form of the (aa) mode with a single cell, undergoing a periodic swap in the sense of orientation (from the clockwise orientation to the counterclockwise one, as illustrated in Fig.5.19). Only a minor change in behavior can be seen in Fig.5.19, panel (c), where a slight lengthening of the central roll in the vertical direction is observed in the 4^{th} and 9^{th} snapshot of the sequence. Although for $\Omega = 93.8$, two- and three-roll configurations are observed at high values of Gs (5.00×10^7) these textural transitions affecting the instantaneous velocity field are relatively simple compared to the same values of Gs and Ra_ω at higher values of Ω. Nevertheless, for all cases simulated in this sub-section, four and eight roll configurations have been found for what concerns the time-averaged field ((ss) modes). These are illustrated in Figs.5.19 and 5.20 for $Gs = 1.00\times10^5, 5.00\times10^5, 1.00\times 10^6, 5.00 \times 10^6, 1.00 \times 10^7$ and 5.00×10^7 (the corresponding Rayleigh numbers being $Ra_\omega = 1.08 \times 10^4, 2.42 \times 10^4, 3.42 \times 10^4, 7.66 \times 10^4, 1.08 \times 10^5, 2.42 \times 10^5$, respectively). As a concluding remark for this section, it can be highlighted that recently Boaro and Lappa [116] have expanded this specific line of research (thermovibrational flow in the low-frequency regime) by addressing the companion problem in which the fluid has a viscoelastic behaviour. For $Pr = 10, \Omega = 100$, comparable values of Gs, and limiting conditions for which the elasticity of the fluid is negligible (Newtonian case), they have found columnar modes of convection for $Gs = 5.00 \times 10^6, 1.00 \times 10^7$ and 5.00×10^7 somehow similar to those reported here, which indicated that these are the preferred modes of convection in this range of frequencies and $Pr = O(10)$.

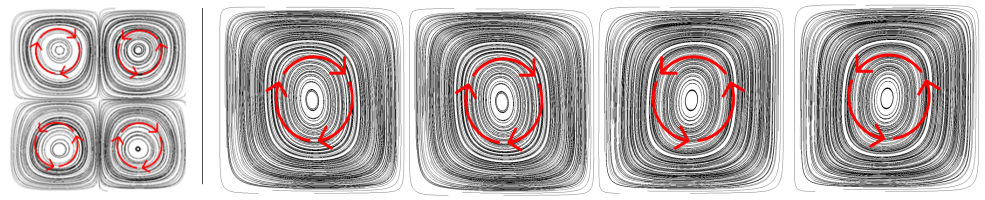

(a)$Gs = 10^5, Ra_\omega = 1.08 \times 10^4$

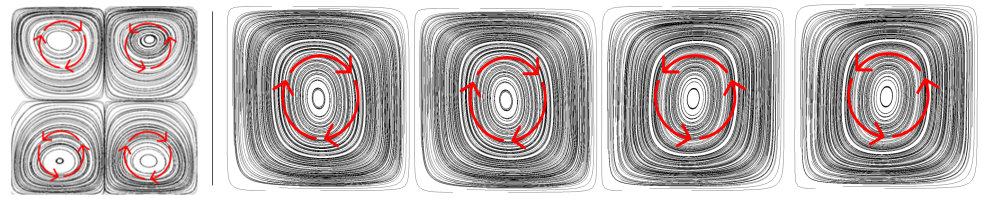

(b)$Gs = 5.00 \times 10^5, Ra_\omega = 2.24 \times 10^4$

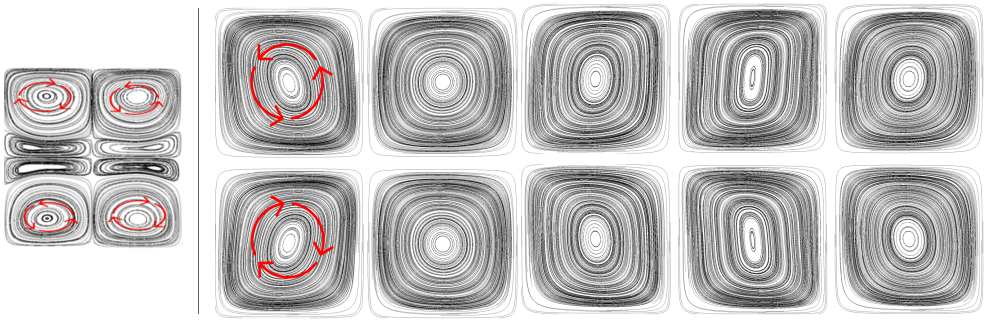

(c)$Gs = 10^6, Ra_\omega = 3.42 \times 10^4$

Figure 5.19: Time-averaged flow (left) and instantaneous flow (right), for $\Omega = 93.8$ and the three (lower) considered values of Gs and Ra_ω. For (a) and (b) the instantaneous snapshots are taken at 0.1P, 0.2P, 0.5P and 0.6P. For (c) they are taken at 0.1P intervals from $t_0 = 0$P to $t = t_0$+P.. The arrow indicates the clockwise or counterclockwise motion of the fluid that changes according to the sign of the acceleration.

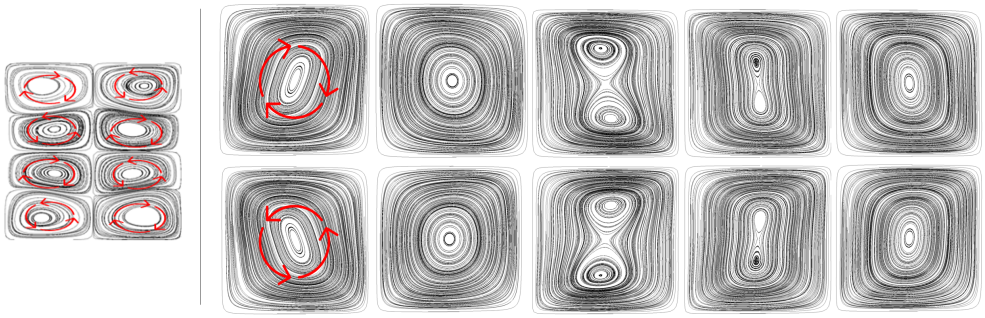

(a)$Gs = 5.00 \times 10^6, Ra_\omega = 7.66 \times 10^4$

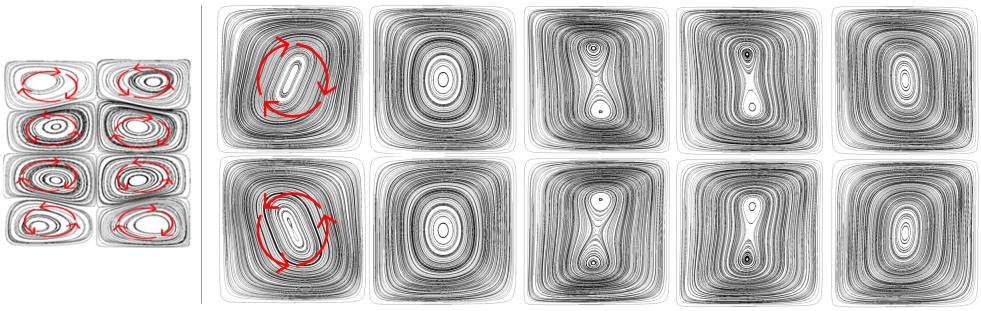

(b)$Gs = 10^7, Ra_\omega = 1.08 \times 10^5$

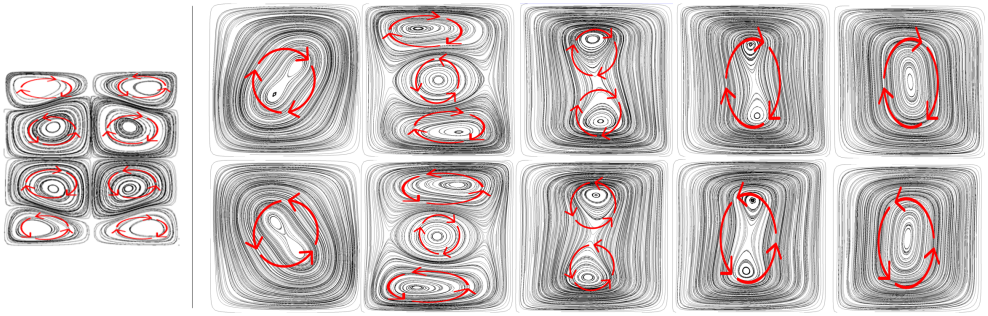

(c)$Gs = 5.00 \times 10^7, Ra_\omega = 2.42 \times 10^5$

Figure 5.20: Time-averaged flow (left) and instantaneous flow (right), for $\Omega = 93.8$ and the three (higher) considered values of Gs and Ra_ω. For all cases the instantaneous snapshots are taken at 0.1P intervals from $t_0 = 0$P to $t = t_0$+P. The arrow indicates the clockwise or counter-clockwise motion of the fluid that changes according to the sign of the acceleration and as a result of complex textural transitions.

5.4.4 Thermal characterization: TFD distortions

After analysing thermovibrational convection from a fine-grained mechanical level (the physicist's point of view, leading to treat the problem on the same footing as a classical study of instability or transition to chaos), this section is used to provide the reader

with a more 'engineering' point of view, i.e. a coarse-grained macroscopic perspective connected to the evaluation of factors by which the thermal behavior of the system can be characterized 'globally'. In particular, in line with the existing literature on this specific form of convection, we use the so-called thermofluid-dynamic (TFD) distortions (these are introduced previously in Chap.4). From the literature, it is known that for thermovibrational systems, amplitudes of the fluctuating temperatures disturbances tend to decrease with frequency, and the average quantities are less dependent on the frequency so that the time-averaged distortions prevail over the fluctuating distortions at high frequencies and the fluctuating distortions prevail over the time averaged ones at low frequencies [46, 117]. With this information in hand, it is of interest not only to explore the behavior of a fluid cell under vibrations, when the Gershuni and Rayleigh numbers are increased, but it is also of interest to study the effect of a change in the vibrational frequency. In Fig.5.21, the dashed data lines represent $\delta T'$, and the solid lines represent $\overline{\delta T}$. It is clear here that as the forcing frequency grows, the more the contributions of the time averaged part become predominant and vice versa, which is in agreement with the literature cited above. Interestingly, while $\delta T'$ has a maximum for $\Omega = 10^2$, $\delta T'$ is characterized by the presence of some peaks for $\Omega = 10^3$ (not for all values of Gs). The non monotonic behaviour of the latter quantity in some circumstances can be ascribed to the complex (intermittent) dynamics, which take place for $\Omega = 10^3$, as discussed in Sect.5.4.2. To compliment this quantitative analysis, Fig.5.22 shows the time-averaged temperature fields for the three values of Ω considered in the present work and a representative fixed value of the Gershuni number, $Gs = 10^6$. Although the temperature field is relatively undisturbed for the lowest frequency, as expected and in line with the trends reported in Fig.5.22 for cases (b) and (c), the increase in Ω leads to an increased distortion.

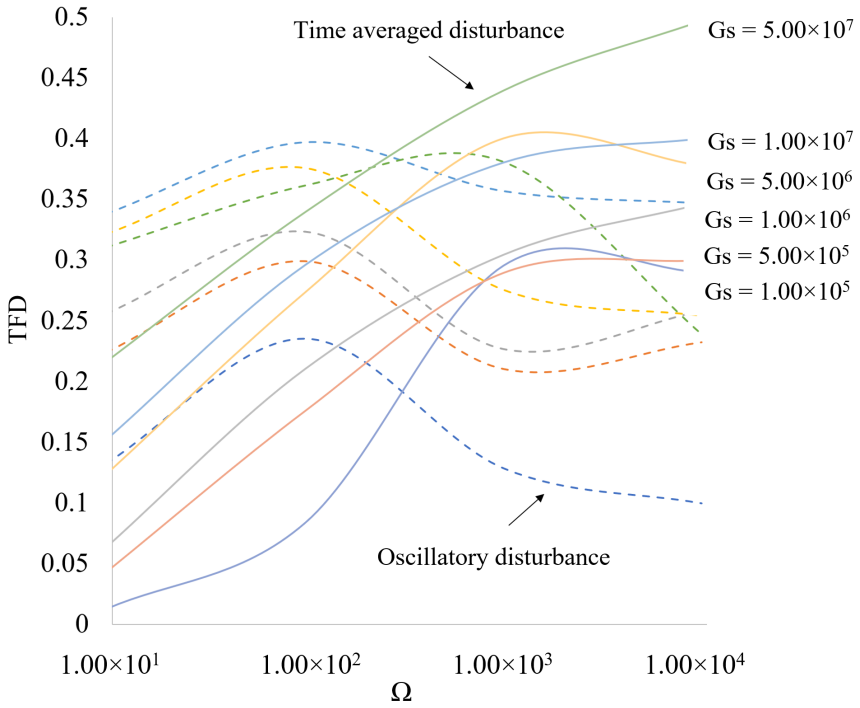

Figure 5.21: TFD Distortions as a function of the frequencies of the imposed vibrations for different values of the Gershuni number.

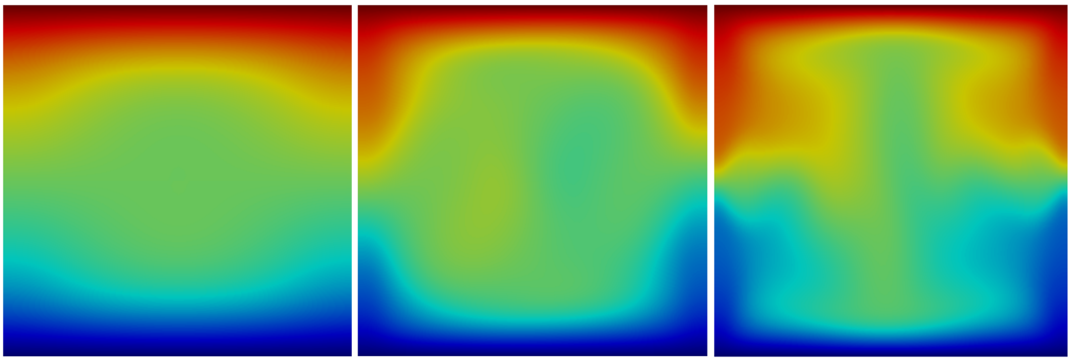

Figure 5.22: Time averaged temperature field for the case $Gs = 10^6$, and frequencies (a) $\Omega = 9.38 \times 10$, (b) $\Omega = 9.38 \times 10^2$ and (c) $\Omega = 9.38 \times 10^3$.

5.5 Discussion and conclusion

The mechanisms through which a closed system undergoes transition to chaos can be categorized into three main types. Firstly the Ruelle-Taken-Newhouse scenario [52, 54]

where a flow can be assumed to be chaotic after three incommensurate frequencies have been produced (the ensuing evolution of the system generally consisting of a corrugation of the related T3 torus). The second known route to chaos is the so-called Feigenbaum sequence [115] where, following an increase of the control parameter, a series of period doubling bifurcations takes place. Finally, the Manneville and Pomeau [118] mechanism, where intermittent bursts occur in the time series of characteristic quantities (temperature or velocity); these bursts become more and more frequent with an increase in control parameter, resulting ultimately in a signal composed of only turbulent bursts (giving rise to a fully turbulent frequency spectrum). It is known that these possible routes are not mutually exclusive, nor are they truly progressive, that is, they can mutually 'contaminate' one another. In an attempt to fill a gap still affecting the existing literature, in the present work, the focus was on the evolution of pure thermovibrational flow. Given the known dependence of this form of thermal convection on the frequency of the applied forcing (leading to partition the space of parameters into two main regions, namely, the ranges of small and high frequencies), such frequencies are allowed to span a relatively wide interval of orders of magnitude. Starting from the case for which the frequency is high (a common point of origin from which many past studies have departed owing to the inherent simplifications allowed in terms of governing equations) [107], and assuming a fixed range of values of the Gershuni number (known to be the main parameter controlling the evolution of the system in the time-averaged space), the frequency has been gradually decreased with a three-fold purpose; firstly, to discern the influence of Ω on the magnitude and patterning behavior of the time-averaged velocity (especially for high values of the Gershuni number for which no results exist in the literature); secondly, to reveal the underlying textural transitions affecting the instantaneous flow field, and thirdly, to decode the typical route of evolution towards chaos. Remarkably, it has been found that the two aforementioned regimes (generally distinguished according to the relative importance of time- averaged and fluctuating effects) also differ in regard to the preferred sequence of events (the hierarchy of instabilities), which take place as the control parameter is increased. For high frequencies ($\Omega = 10^4$), the present numerical results have shown that thermovibrational convection

considered in the time- averaged space (i.e. in terms of V) is initially steady and it becomes time-periodic if the Gershuni number is increased. In this case, the typical mechanism of transition to chaos is represented by the classical Ruelle-Takens path of evolution (requiring the presence of three independent frequencies in the instantaneous velocity signal [52].) For intermediate frequencies ($\Omega = 10^3$), however, the scenario is more complex. The ranges of existence of the time-averaged modes of convection corresponding to the quadrupolar field and the inversional symmetry pattern dramatically change. A significant modification can also be spotted in the chain of transitions leading to the development of chaos. While the hallmark of the high frequency regime is its adherence to the standard Ruelle-Takens route (which has emerged as a leading candidate to interpret most of turbulent phenomena in nature), for $\Omega = 10^3$, concurrent aspects of the Feigenbaum and Manneville and Pomeau mechanisms can be recognized. We wish to remark that, in order to eliminate the possibility that these results ensue from numerical error or solver inaccuracy, these cases were also ran using the in-house code developed by Lappa and Burel [71], and the exact same solutions obtained with OpenFOAM were found. According to both computational platforms, the uprising towards chaos as a result of the increase of the control parameter Gs (or Ra_ω) is via the Feigenbaum mechanism and the related period-doubling bifurcations; nevertheless, occasional back transitions from a chaotic condition to a sub-harmonic state can also be observed. As a concluding remark, we wish to highlight that similar behaviors have been reported for a set of companion problems not necessarily involving the presence of an external forcing. For instance, when simulating a converging diverging channel flow, taking the Reynolds number as the control parameter, Guzman and Amon [56] observed frequency-locked periodic solutions, where the periodic behavior of the flow is restored for a particular intermediate value of Re. This was interpreted as the result of a synchronization of two oscillators spontaneously produced by the system. Similar events were also reported by Berge *et al.* [119]. Even more relevant examples can be found in the literature about problems where a horizontal temperature gradient interacts with a constant-gravity field modulated by small harmonic oscillations. As an example, for the square cavity case, Farooq and Homsy [120, 121] demonstrated that,

under certain parametric conditions of finite frequency, resonant states can be induced by the interplay of convective motion of vibrational origin with the fundamental instabilities of the base flow induced by the constant gravity (similar findings are also due to Chen and Chen, and Kim *et al.*) [122–124]. In such a context, it is also worth citing Lizée and Alexander [58] who examined the case with gravity perpendicular to the applied temperature gradient and vibrations in the horizontal direction and reported on the existence of period-doubling transitions, periodic windows, strange attractors, and intermittencies as a function of the classical gravitational Rayleigh number. Keeping in mind also the arguments about the relevance of the concept of anti-resonance elaborated by Boaro and Lappa [116] in regard to the stabilization of flows which admit multiple oscillators there is no doubt that in addition to its relevance to space research and microgravity science, there are other benefits tied to a better understanding of these attractive 'vibrational' fluid systems. Looking forward, one may see turbulent thermovibrational fluid motion as a tool for finding exotic states of convection that, for now, have not been encapsulated yet in the major theories for transition to chaos.

Chapter 6

Spatial and temporal evolution of three-dimensional Rayleigh-Bénard type thermovibrational convection in a cubic cavity with various thermal boundary conditions

This chapter is based on the following peer-reviewed publication:

Crewdson, G. and Lappa, M., 2022 "Spatial and temporal evolution of three-dimensional thermovibrational convection in a cubic cavity with various thermal boundary conditions", *Physics of Fluids*, 34, 014108. https://doi.org/10.1063/5.0078270.

The text in this chapter has been modified only when necessary in order to preserve the continuity and flow of this thesis.

6.1 Introduction

As seen in Chap.4, attention has been paid to the study of thermovibrational flow, where the vibrations are parallel to the temperature gradient. Unfortunately, however, these studies have been limited to two-dimensional (2D) configurations, thereby filtering out the inherent complexities typical of effective three-dimensional (3D) flows. In order to fill this gap, in the present chapter, the set of predictive links between flow properties and related influential factors is expanded through consideration of a real (3D) cavity. Given the lack of equivalent results in the literature, in particular, a cubic enclosure is considered. This specific choice is motivated by the availability of a significant amount of existing data for the companion case of standard Rayleigh-Bénard convection (i.e. cubic enclosures uniformly heated from below and cooled from above with parallel steady gravity), which can be considered for comparison and/or as a guide to interpret the still completely unknown behaviour of thermovibrational flow in similar conditions. Along these lines, the earlier investigation by Pallarès *et al.* may be recalled, who addressed the RB problem both numerically [22] and experimentally [23]. In their studies, seven fundamental modes of convection were identified for fluid motion driven by gravity in parallelepipedal cavities heated from below (these including single roll, two roll and other toroidal roll-type states; we will provide a more detailed description of these structures at a later stage in the chapter). The stability of these solutions was found to be dependent on the Rayleigh number (Ra), Prandtl number (Pr) of the fluid and the aspect ratio of the cavity. Puigjaner *et al.* [24, 25], conducted a stability analysis of this problem and found that by increasing the strength of convection (i.e. Ra), a series of possible steady, stable and unstable patterns emerge resulting in a complex bifurcation diagram. Despite some differences, the greatest merit of these valuable efforts resides in the related evidence that the study of classical thermal convection in a 3D cubic cavity can offer a rich playground for researchers due to the richness of possible dynamics and the extent of related parametric variations. Lappa [26] argued that the discrepancies affecting Pallarès *et al.*[23], and Puigjaner *et al.*[24], might be justified when considering that the transition from one solution to another, upon an

increase in the Rayleigh number, is dependent on the presence of thermal and/or momentum boundary layers, which in turn depend on the value of Pr, and the specific thermal behaviour of the sidewalls. The effect of such conditions on flow structures has been investigated experimentally by Pallarès *et al.*[23], for Pr=130 over a range of moderate Rayleigh numbers ($Ra < 8 \times 10^4$). Both adiabatic and conducting wall conditions were found to yield similar results in terms of flow patterns and transitions up to $Ra \approx 5 \times 10^3$. After that, the flow structures formed differ for both conditions and occur at different values of the Rayleigh number. Motivated by this observational tide, we therefore concentrate on the case of thermovibrational convection in a cubic cavity driven by vibrations parallel to the imposed temperature gradient and assume different types of thermal boundary conditions for the sidewalls. Specifically, in addition to the canonical configurations where these are either completely adiabatic or conducting, a hybrid situation is also investigated where, while two opposing walls are adiabatic, the other couple maintains a linear temperature profile. The ensuing numerical results are presented in terms of flow structures, patterning behaviour and the (often not obvious) relationship that is established between the forcing (the vibrations) and the temporal response of the flow.

6.2 Mathematical model and boundary conditions

A simple 3D cubic cavity is used in this study and microgravity conditions are considered. The bottom wall is cold and the top wall is hot. As anticipated in the introduction, the vibrations are applied parallel to the temperature gradient and three thermal wall conditions are investigated as shown in Fig.6.1.

At t=0 the velocity field across the cavity for all cases is 0 and a linear temperature profile is assumed along y:

$$Ux = Uy = Uz = 0 \text{ and } T = y \text{ for } 0 \leq x \leq 1, 0 \leq y \leq 1, 0 \leq z \leq 1 \qquad (6.1)$$

No-slip conditions are applied for all the solid walls everywhere for $t > 0$. The balance equations have to be complemented with different thermal boundary conditions

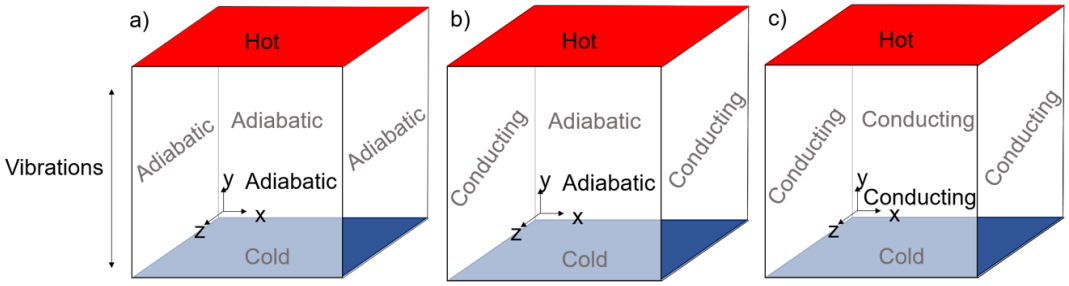

Figure 6.1: Sketch of the considered geometry and related thermal boundary conditions (a) all lateral walls are perfectly adiabatic, (b) two lateral walls are perfectly conducting, and the front and back walls are adiabatic, (c) all side walls are perfectly conducting.

depending on the chosen set-up (as shown in Fig.6.1). For the case illustrated in Fig.6.1 (a) the side walls are considered adiabatic.

$$\frac{\delta T}{\delta x} = 0 \text{ for } z = 0, z = 1, 0 \leq y \leq 1, \text{ and } t > 0 \tag{6.2}$$

$$\frac{\delta T}{\delta z} = 0 \text{ for } x = 0, x = 1, 0 \leq y \leq 1, \text{ and } t > 0 \tag{6.3}$$

For the case illustrated in Fig.6.1 (b) the side walls in the z-plane are considered perfectly conducting and the walls in the x-plane are considered adiabatic following the condition:

$$\frac{\delta T}{\delta x} = 0 \text{ for } z = 0, z = 1, 0 \leq y \leq 1, \text{ and } t > 0 \tag{6.4}$$

$$T = y \text{ for } x = 0, x = 1, 0 \leq y \leq 1, 0 \leq z \leq 1, \text{ and } t > 0 \tag{6.5}$$

For the case illustrated in Fig.6.1 (c) all the side walls in are considered perfectly conducting following the condition:

$$T = y \text{ for } 0 \leq x \leq 1, 0 \leq y \leq 1, \text{ and } t > 0 \tag{6.6}$$

Finally, different constant temperatures are set for all three cases for y=0 and y=1:

$$T = 0 \text{ for } y = 0, 0 \leq x \leq 1, 0 \leq z \leq 1, \text{ and } T = 1 \text{ for } y = 1, 0 \leq x \leq 1, 0 \leq z \leq 1 \tag{6.7}$$

6.3 Validation and grid refinement

Similarly to the Chapters 4 and 5, a cross-validation approach has been adopted here as limited to no literature or benchmark solutions exist for thermovibrational convection (especially for the case where vibrations are parallel to the temperature gradient; an exception being the study shown in Chapter 4, which however was validated for a different value of Pr). For simplicity and to save computational time, this assessment has been carried out for a 2D square cavity with adiabatic side walls. The average Nusselt number across the hot wall and both the vertical and horizontal velocity components at the centre of the cavity have been compared. As quantitatively substantiated by Table 6.1 and the velocity signals reported in Fig.6.2 and Fig.6.3, a satisfactory agreement has been found. Thereafter, a grid refinement study has been carried out on the 3D cavity with adiabatic sidewalls for $Ra_\omega = 8.34 \times 10^5$. In order to make the overall process more efficient, some theoretical criteria have been applied in the attempt to estimate 'a priori' the required number of grid points. Firstly, given the tendency of thermal convection to display turbulent behaviour when the Rayleigh number attains high values, the Kolmogorov length scale has been evaluated using Eq.4.4 introduced in Chapter 4. This length scale provides a restrictive condition where the nondimensional size of the mesh (Δx_c) should satisfy the condition $\Delta x_c < \zeta_{Ra}$. This can in turn be translated into the number of divisions required across the domain and defined as: $N_{div1} = 1/\zeta_{Ra}$. Assuming the worst condition, i.e. the maximum value of the vibrational Rayleigh number being considered in the present work, $Ra_\omega = 8.34 \times 10^5$. From this, it is deemed deemed it necessary to perform a mesh refinement study allowing the number of divisions to range in a certain neighbourhood of this value.

Table 6.1: Comparison of current results with those obtained with the in-house code for the fully conducting 2D case $Ra_\omega = 4.00 \times 10^4$, $\Omega = 5$, $Pr = 7$, grid side 100 by 100.

Solver	Nu_{max}	Nu_{mean}
OpenFOAM	3.350	1.575
In-house code	3.310	1.650
Results difference in %	1.19	4.78

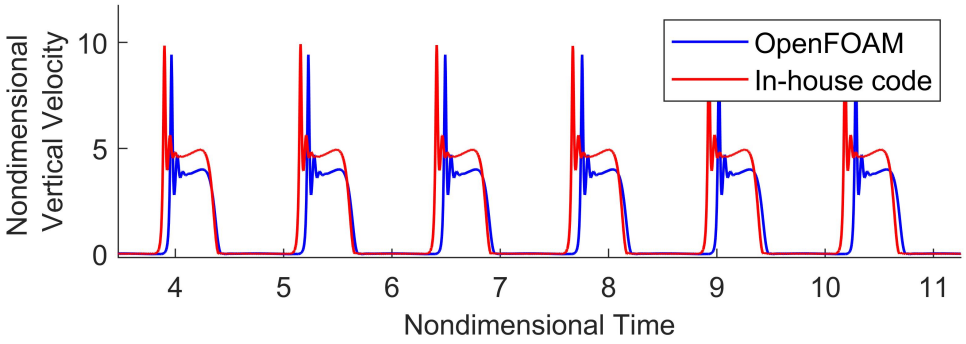

Figure 6.2: Vertical velocity signals (Uy) for the case $Ra_\omega = 4 \times 10^4$, $\Omega = 5$ and Pr=7 for OpenFOAM and the in-house code. A grid size of 100 by 100 is used.

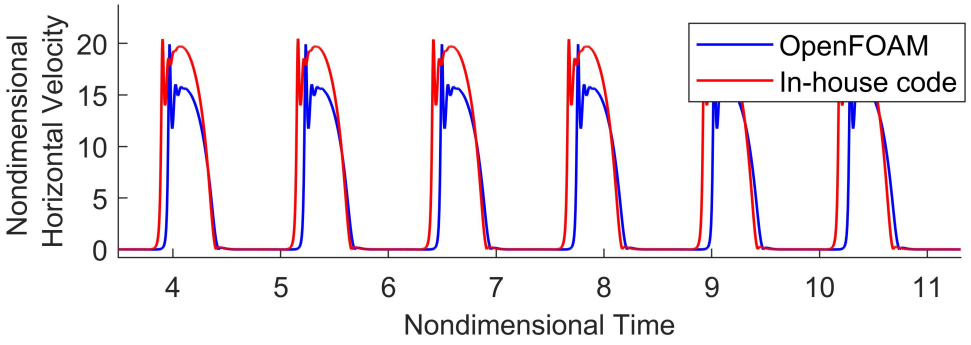

Figure 6.3: Horizontal velocity signals (Uy) for the case $Ra_\omega = 4 \times 10^4$, $\Omega = 5$ and Pr=7 for OpenFOAM and the in-house code. A grid size of 100 by 100 is used.

Moreover, since it is known that for these high values of Ra and a relatively high value of Pr, thermal boundary layers are prone to develop across the top and bottom wall of the cavity, the number of cells required in this boundary layer has also been taken into account following the criteria provided by Shishkina *et al.* [104], previously used, and defined in Eq.4.4.

Russo and Napolitanos correlation is also used here (see Eq.4.4).From these two requirements the following values have been obtained: $N_{BL} = 2.70$ and $\delta_{th.BL} = 3.31 \times 10^{-2}$. Using these two values, for a uniform grid, the number of divisions can be determined as:

$$N_{div2} = \frac{N_{BL}}{\delta_{th.BL}} \tag{6.8}$$

which gives $N_{div2} = 81.75$.

With these theoretical requirements in hand, a mesh refinement study has been carried out. Including firstly a mesh containing 60^3 elements and followed by 80^3, 100^3 and finally 120^3. The ensuing results shown in Fig.6.4 are taken when the flow is the most disturbed. It can be noted that the data for the 60^3 and 80^3 are similar, however as the theoretical requirement outlined by $N_{div2} = 81.75$ is only just satisfied a further jump of 20 divisions has been considered. From 80^3 to 100^3 a significant variation in value is observed therefore a further jump to 120^3 has been implemented. The result obtained from the 100^3 and 120^3 meshes are indecipherable and therefore the 100^3 mesh has finally been chosen as the required mesh for $Ra_\omega = 8.34 \times 10^5$.

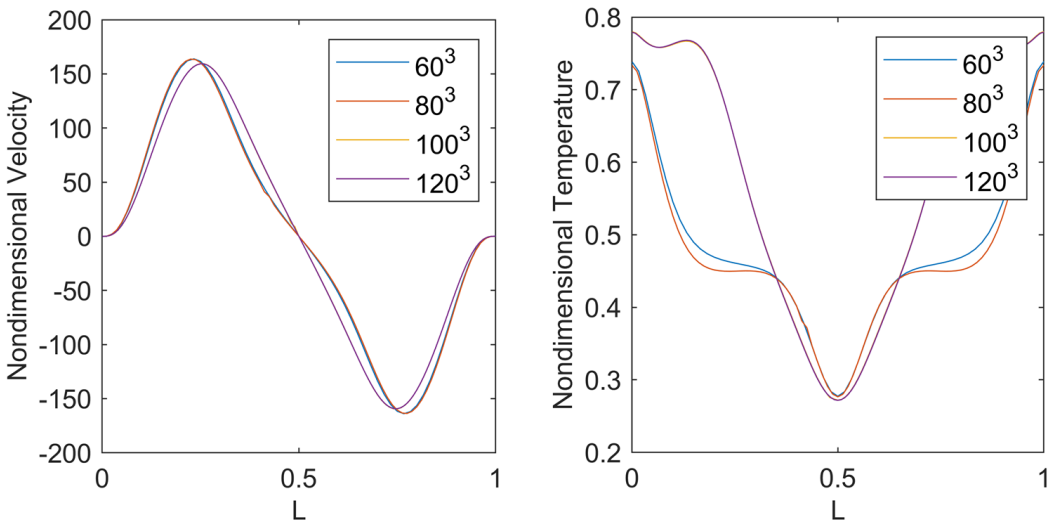

Figure 6.4: Mesh refinement study. Comparison of the nondimensional vertical velocity and nondimensional temperature across a line starting at point (0,0.5,0.5) ending at (1,0.5,0.5), for t=0.1P.

6.4 Simulation Results

In this section, results from six individual simulations are presented. These cases encompass the three types of boundary conditions defined in Sect.6.2 for two different values of Ra_ω ($Ra_\omega = 8.34 \times 10^4$ and $Ra_\omega = 8.34 \times 10^5$). From Hirata *et al.* [36] and Crewdson and Lappa [125], it is known that, even under the constraint of two-dimensionality, a rich map of solutions is possible in systems where the vibrations are set parallel to

the temperature gradient when both the vibrational Rayleigh number and frequency of vibration are varied. By allowing these systems to develop in a realistic 3D space, an even larger set of states must be expected. In turn, these can differ in regard to the instantaneous spatial organization (the flow structure and associated symmetries) and the related evolution in time (the system 'temporal' response). Given the inherent complexity of the problem, in the following we implement a peculiar approach where an attempt is made to treat these (spatial and temporal) aspects in a separated manner (however, still creating the relevant links as necessary). Given the otherwise intractable scale of the problem, without loss of generality, the angular frequency of the vibrations is fixed to $\Omega = 50$, a value for which (as illustrated in the next sub-section) the flow is expected to develop a remarkable degree of unsteadiness.

6.4.1 Fluid response and velocity signals

Before entering into a discussion regarding the three-dimensional textural transitions affecting the patterning behavior, the velocity signals obtained from probes (similar to those exploited for the validation study) can be used to identify the regime embodied by the flow. Along these lines, it is worth recalling that four possible solutions or regimes have previously been recognized in the 2D study by Hirata *et al.* [36]: synchronous (SY), subharmonic (SU), non-periodic (NP), and stable (ST). Two additional solutions were identified in the later analysis by Crewdson and Lappa [125] as described in Chapter 4, namely, the synchronous and periodic or synchronous and non-periodic (SY-P or SY-NP) solutions. Two of these possible behaviours can yet be recognized in the results obtained for the 3D configuration examined in the present work. These include the SY-P and SU regimes. For the former (SY-P), the flow repeats itself periodically. For the latter (the SU case), the frequency of repetition of the fluid behaviour is halved with respect to the forcing frequency, resulting in a period twice as long as the forcing period. In particular, Fig.6.5 shows the velocity signals for the lower value of Ra_ω considered here ($Ra_\omega = 8.34 \times 10^4$), where the SY-P regime is evident for all the three variants of thermal boundary conditions defined in Sect.6.2. Additional insights can be gathered from Fig.6.6, where, it can be seen that the signals appear to be of the type

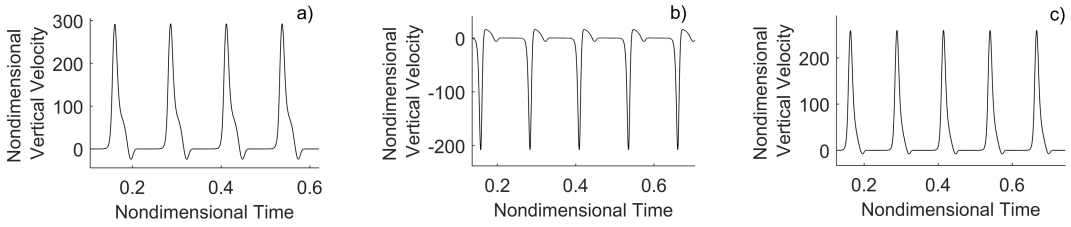

Figure 6.5: Vertical velocity components (Uy) recorded at the centre of the cavity (0.005, 0.005, 0.005) for a) the fully adiabatic case, b) the case where the front and back of the cavity are adiabatic and the two side walls are conducting and c) the case where all side walls are conducting for $Ra_\omega = 8.34 \times 10^4$.

SY-NP (displaying turbulent bursts) as the Rayleigh number is increased by one order of magnitude. A closer inspection of these signals, further reveals that a SU behaviour is enabled for case (b) (indeed, the periodicity in shape of the signal is repeated every two periods in this case). On the basis of this initial assessment (relying solely on arguments

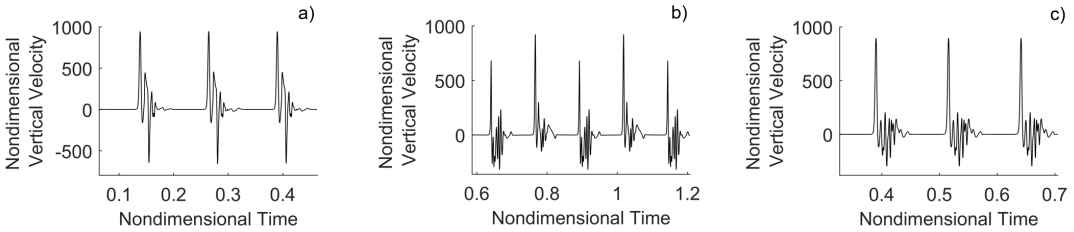

Figure 6.6: Vertical velocity components recorded at the centre of the cavity (0.005, 0.005, 0.005) for a) the fully adiabatic case, b) the case where two side walls are adiabatic and two are conducting and c) the case where all side walls are conducting and $Ra_\omega = 8.34 \times 10^5$.

based on the time response of the flow), it may therefore be concluded that when 3D configurations are considered, even an apparently innocuous change in the thermal boundary conditions can cause a remarkable variation in the temporal behaviour of the flow. As illustrated in detail in the next two sections, such responses are intimately coupled with a variety of textural transitions in the flow structure, which deserve their own treatment.

6.4.2 Flow structure characterization for small Rayleigh numbers

In order to support the reader's understanding of such dynamics, (before diving into a purely spatial characterization of them), it is worth recalling some key aspects of thermal convection which will prove very useful later for their interpretation. In particular, it is instructive to recall that this kind of fluid motion is governed by the same equations everywhere in space, yet it takes a form that has periodic spatial variations, with 'nodes' (velocity or temperature extremes) positioned at given points. Physicists say that it "spontaneously breaks space-translation symmetry". As already explained to a certain extent in the introduction, this useful concept can be used as a tool to characterize or categorize the flows in certain universality classes, which transcend the specific nature of the considered flow (be it driven by steady gravity or vibrations). The present section is therefore dedicated to the provision of some necessary propaedeutical arguments along these lines.

Textural transitions and patterning behaviours

Having completed a sketch of the observed temporal behaviours of the considered flow in Sect.6.4.1, the focus is now shifted to the specific spatial behaviour of the fluid over one vibrational period. Along these lines, starting with the case where $Ra_\omega = 8.34 \times 10^4$ and $\Omega = 50$, and all four side walls are set as adiabatic, Fig.6.7 shows the related evolution of the fluid streamlines. Most conveniently, the sequence of snapshots of the flow structure has been reported in conjunction with the signal already shown in Fig.6.5. This is instrumental in showing that the degree of complexity displayed by the flow strongly depends on the considered specific sub-region of the period. In particular, a relatively wide sub-interval exists where convection can be considered relatively weak (almost quiescent condition, hereafter referred to as 'quasi-stationary state'), whereas its amplitude greatly grows as conditions are examined that correspond (or are located in proximity to) to the signal peak. Accordingly, we split the analysis into two parts, the first part, being the time over which the fluid is quasi-stationary (where the flow adopts a resting configuration and the velocity of the fluid is minimal) and secondly, the time

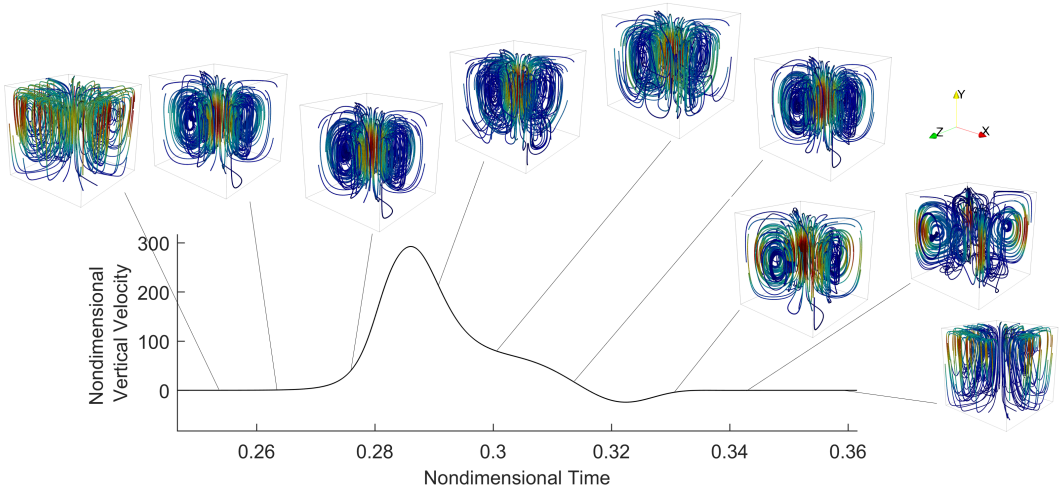

Figure 6.7: Streamlines across one period of vibration for $Ra_\omega = 8.34 \times 10^4$ and the case where all side walls are adiabatic (the blue colour represents a lower velocity and the red colour represents a higher velocity at a given point in time, colour bars are omitted for brevity).

region where the aforementioned convective pulse occurs. Looking at Fig.6.7, the first and last frames show that the resting configuration of the flow is essentially a singular toroidal roll. During the convective phase, the toroidal roll symmetry is maintained; however the roll becomes more compact at first and then undergoes a series of minor textural transitions before regaining its resting configuration. In particular, a more detailed view of the streamline behaviour at t=0.3P as well as the distribution of the related velocity components Ux, Uz and Uy in the xz plane (at y=0.5) can be gathered from Fig.6.8.

In order to identify universality classes in these behaviours, reference could be made to meaningful classifications introduced in the past for classical RB convection. Relevant examples of this modus operandi can be found, e.g., in the work by Mizushima [19] and Mizushima and Adachi [20] for the case of 2D RB flow.

When moving to the 3D case (i.e., the cubic cavity shown in Fig.6.1), however, the simple criteria for characterization of 2D flow illustrated above become rather inadequate (only partially able to account for certain properties of the flow). A more exhaustive characterization approach may therefore be based on the (seven) fundamental modes that Pallarès *et al.* [22], originally identified for standard RB convection

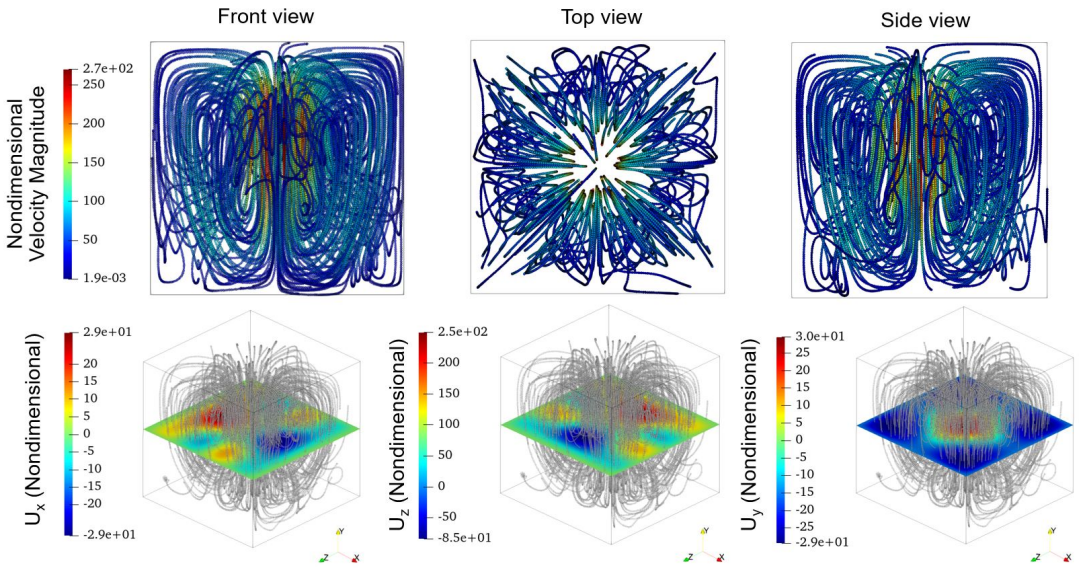

Figure 6.8: Snapshots of flow streamlines (top) and velocity components across the mid-plane of the cavity (bottom) for the case where all sidewalls are adiabatic and $Ra_\omega = 8.34 \times 10^4$ at t=0.3P

in a cubic enclosure, in the range $3.5 \times 10^3 < Ra < 6 \times 10^4$ for Pr=0.71,10 and 130. These solutions are denoted in the following with Sn with n= (1, 2..7), see Table 6.2 and Fig.6.9. Additional structures have been identified by Puigjaner *et al.*[24], however, a description of their geometric qualities is not provided, these included S9, S11-S15.

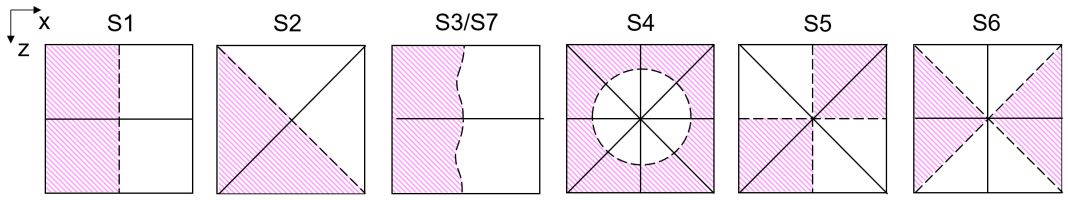

Figure 6.9: Flow structure characteristics in the xz plane (i.e. a plane perpendicular to gravity) for 3D RB convection, the dashed lines represent the roll axis and the solid lines represent the axes of symmetry, the hatched area indicates the region of positive vertical velocity and the blank area represent a negative vertical velocity.

As the reader will realize by inspecting Table 6.2 and Fig.6.9, these solutions essentially reflect the symmetries of the group $D_{4h} = Z_2 \times D_4$. The sub-group D_4 includes the symmetries of a regular polygon with 4 vertices. In turn, these consist of the mirror reflections with respect to the middle (x=1/2 and z=1/2) and diagonal (x=z and z=1-

Table 6.2: Description of flow structures identify by Pallarès *et al.* [22, 23] and Puigjaner *et al.* [25]

Structure names	Pallares *et al.* [22, 23]	Puigianer *et al.*[25]
S1	Single roll	
S2	Single roll oriented diagonally	
S3	Single roll elongated towards two opposite horizontal edges	Not identified
S4	Nearly toroidal roll	
S5	Four roll structures, each one with its axis perpendicular to one side wall	
S6	Two parallel rolls	
S7	Structure S3 with merged ascending currents	
S8	Not identified	two asymmetric counter-rotating rolls aligned along one of the x=z diagonals (similar to S2)
S10	Not identified	two asymmetric counter-rotating rolls aligned along one of the x=z diagonals, similar to S8 possessing no symmetry element

x) vertical planes and related combinations. In the framework of this sub-group, the solution corresponding to the toroidal roll (dominant in the quasi-stationary regime) might be therefore considered as a fundamental mode S4 (Pallarès *et al.* [22], see Table 6.2). The symmetry with respect to the horizontal midplane (y=0.5), however, must be also considered. Unlike the other symmetries pertaining to the above-mentioned dihedral sub-group $_{4h}$, which are also applicable to the temperature field, this symmetry obviously applies only to the velocity field (it is equivalent to rotations of the velocity field of an angle π around one of the x or z horizontal directions in the y=1/2 plane; the reader may consider Puigjaner *et al.* [23] for an exhaustive mathematical description of all these groups of symmetry, which is not reported here for the sake of brevity).

Looking forward to the next cases, we omit the representation of the velocity signal as, from Fig.6.5 we know that the three cases display a high degree of similarity from a temporal point of view. Fig.6.10 illustrates the corresponding evolution of convective modes for the other two boundary condition configurations (still for $Ra_\omega = 8.34 \times 10^4$).

In particular, in Fig.6.10 (a), a planar configuration along the z axis of four separate rolls can be recognized. This quadrupolar roll configuration is a well-known solution

in 2D thermovibrational studies, reported early on by Gershuni *et al.* [35]. A similar steady state has been found by Pallarès *et al.* [22, 23] (S5), described as four roll structure, where each roll axis is perpendicular to one sidewall. In the present case however (Fig.6.10 (a)), the axes of rotation of the rolls are perpendicular only to the two conducting side walls, thus resulting in a planar structure rather than the S5 mode where symmetry was found about the diagonal x=z. A graphical representation of the resting configuration shown in Fig.6.10 (a), akin to the classification style of Pallarès *et al.* [22, 23] is provided in Fig.6.11. The symmetry with respect to the y=1/2 midplane is embodied here where an even number of rolls is found along the x and y axis, with no rolls found along the z axis due to the planar (almost 2D) nature of the flow. The advent of the convective phase, for the case shown in Fig.6.10 (a), brings about a transition from the four-roll to a two-roll planar structure followed by the planar structure disappearing past t=0.3P. This next convective mode (shown in more detail in Fig.6.12) is the result of the fluid motion attempting to overcome the constraining boundary conditions and form a toroidal structure, similar to that seen for the fully adiabatic situation (however, bound by the side walls a fully toroidal structure is not achieved). Finally, the resting configuration is re-established. The next figure of the sequence (Fig.6.13) refers to the case where all four side walls are conducting. It can be seen that during the resting phase, the flow adopts a hybrid configuration of the fully adiabatic case and the half adiabatic, half conducting case. The toroidal S4 structure seen in Fig.6.9 is still visible, however, the cavity hosts two torii instead of one. In this case, an (ss) mode can be therefore recognized if the flow is observed from the front and side view of the cavity. For what concerns the transitional behaviour during the convective phase, the stages of evolution are similar to those found for the fully adiabatic case, however past t=0.3P, the dominant convective mode is compressed at the lower half of the cavity preceding the advent of small rolls eventually responsible for the two separate torii visible in the resting configuration. On the basis of this initial set of results, the following conclusions can therefore be drawn. When comparing the effects of the three types of boundary conditions on the flow, it becomes evident that the fully adiabatic and fully conducting cases bare much similarity as symmetry about

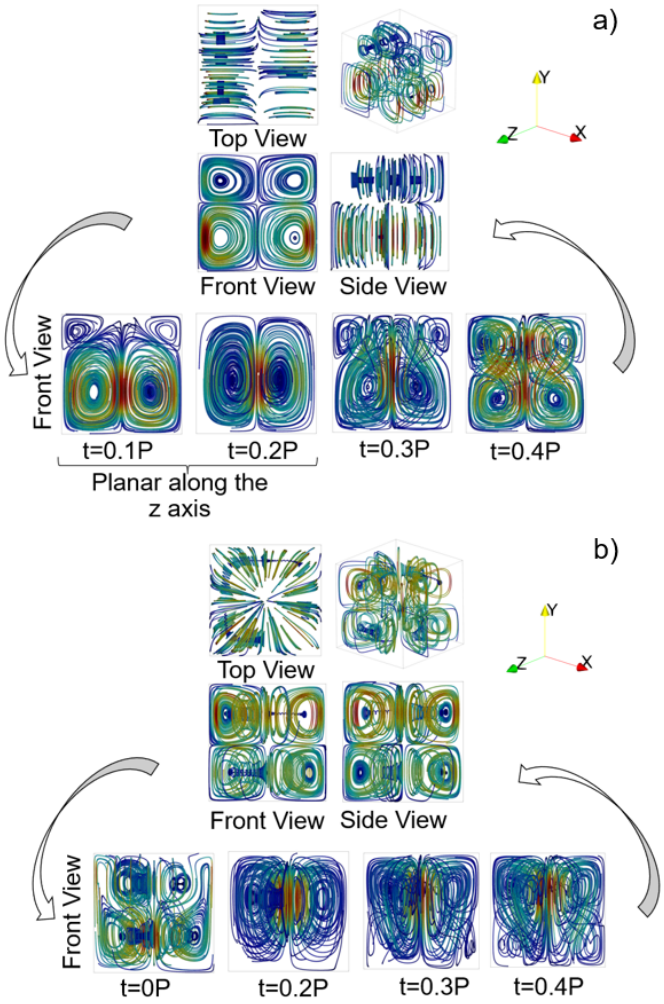

Figure 6.10: Velocity streamlines for $Ra_\omega = 8.34 \times 10^4$ where (a) the front and back walls of the cavity are set to adiabatic while the two sidewalls are set to be perfectly conducting, and (b) all sidewalls are perfectly conducting, where the blue colour represents a lower velocity and the red colour represents a higher velocity at a given point in time. The top part of the panels (a) and (b) correspond to the resting configuration of the flow before and after the convective burst, where the velocity of the fluid is close to zero (i.e. a quasi-stationary state is attained, as explained in the text).

the x and z axis at the zx mid-plane is maintained through both the resting and the convective phases. However due to the different resting configurations, an additional transitional structure is observed for the fully conducting side-wall case. By contrast, the case with two adiabatic and two conducting side walls is different as the flow structure is essentially planar in the quasi-stationary regime. Another striking analogy

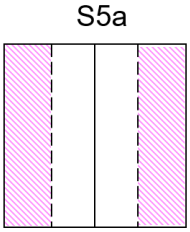

Figure 6.11: Graphical depiction of the convective state for the case where the two side walls are conducting and the front and back wall are adiabatic, in keeping with the description method of Pallarès *et al.* [22, 23]

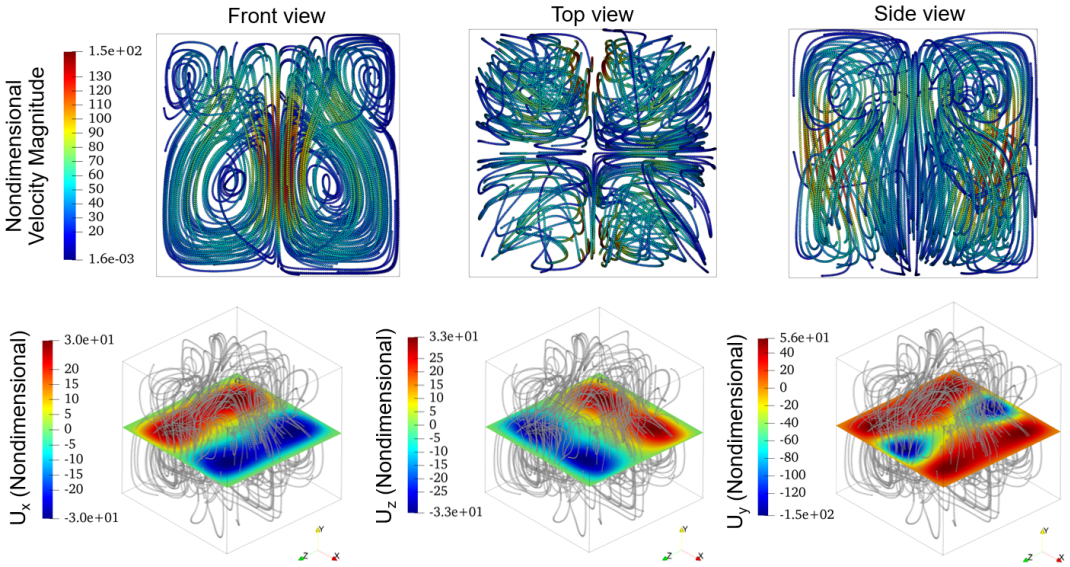

Figure 6.12: Snapshots of flow streamlines (top) and velocity components across the mid plane of the cavity (bottom) for the case where the side walls are conducting and the front and back of the cavity are adiabatic for $Ra_\omega = 8.34 \times 10^4$ at t=0.3P.

applies to the configuration with the conducting walls. For both the hybrid case and the fully conducting sidewall case, an antisymmetry emerges along the y axis. This leads to the classic quadrupolar field in the case with hybrid thermal boundary conditions (displaying a planar 4 roll structure) and produces a dual-toroidal structure in the fully conducting situation. As the reader will easily realize by taking a closer look at Figs. 6.7, 6.10,6.12 and 6.13, due to the complexity of the structures observed during the convective phase (when the fluid is not at rest), the application of earlier classifications such as those developed by Pallarès *et al.* [22, 23] are not always possible.

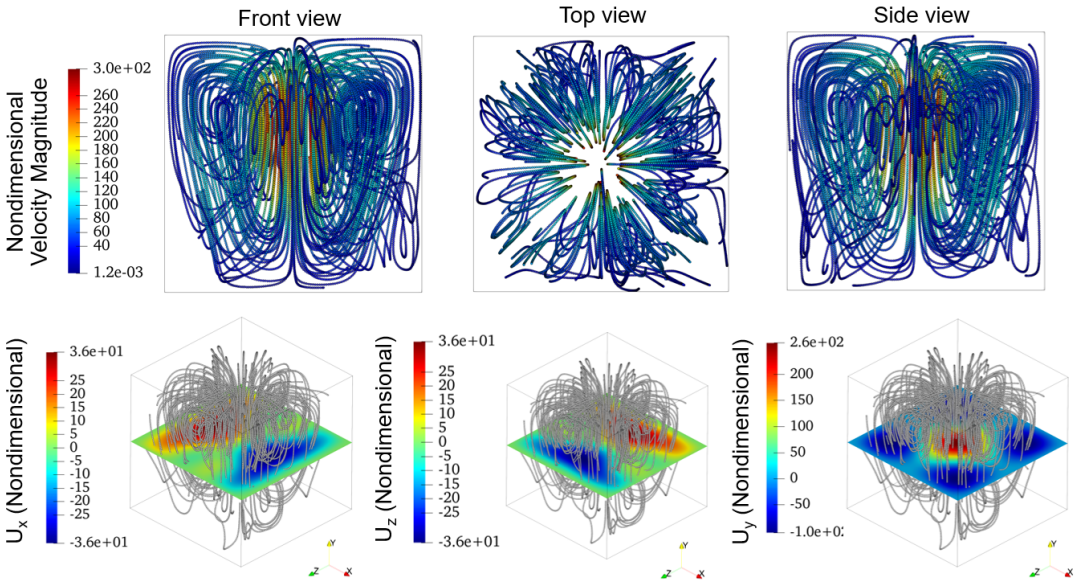

Figure 6.13: Snapshots of flow streamlines (top) and velocity components across the mid plane of the cavity (bottom) for the case where all side walls are conducting for $Ra_\omega = 8.34 \times 10^4$ at t=0.3P.

In the following sections, a further level of analysis is implemented through the consideration of specific aspects emerging from observation of the profiles of the different velocity components and/or the related distributions (maps) in certain planes as a function of time. In particular, Fig.6.14 shows the lines over which the velocity profiles are taken. The x, y and z velocities (U_x, U_y and U_z) are taken over both (dashed) centrelines for all three cases.

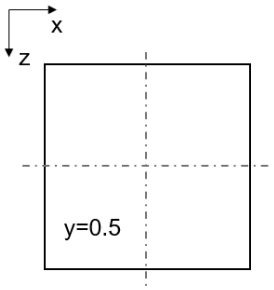

Figure 6.14: Top view of the cavity showing the two centerlines of the zx plane (dashed) over which the velocity profiles are taken.

6.4.3 Velocity profiles and emerging symmetries

Starting with the fully adiabatic case, Fig.6.15, depicts the velocity profiles taken at intervals of 0.1P over one vibrational period. The highest velocity magnitude occurs at t=0.3P for both the vertical and horizontal components. Fig.6.15 (a) shows a positive Ux over the first half of the x axis and a negative U_x of the second half of the x axis, indicating that the centre of the cavity acts as an attractor for the duration of the entire period. The profile displayed in Fig.6.15 (b) exhibits a positive vertical velocity U_y at the centre of the cavity indicating an upward motion of the fluid. This is in agreement with the arguments provided earlier about the flow observed to be circulating up and outwards from the centre of the cavity. The U_z velocity profiles are not provided, and neither is the U_x velocity along the z axis, owing to the fact the flow adopts the toroidal structure, and therefore such information would be redundant (U_x along the x axis = U_z along the z axis, and U_x=0 along the z axis = 0 and U_z along the x axis = 0 and finally U_y along the x axis = U_y along the z axis; Fig.6.16 shows the velocity fields confirming that these equalities hold for y=0.5). For the situation where two side

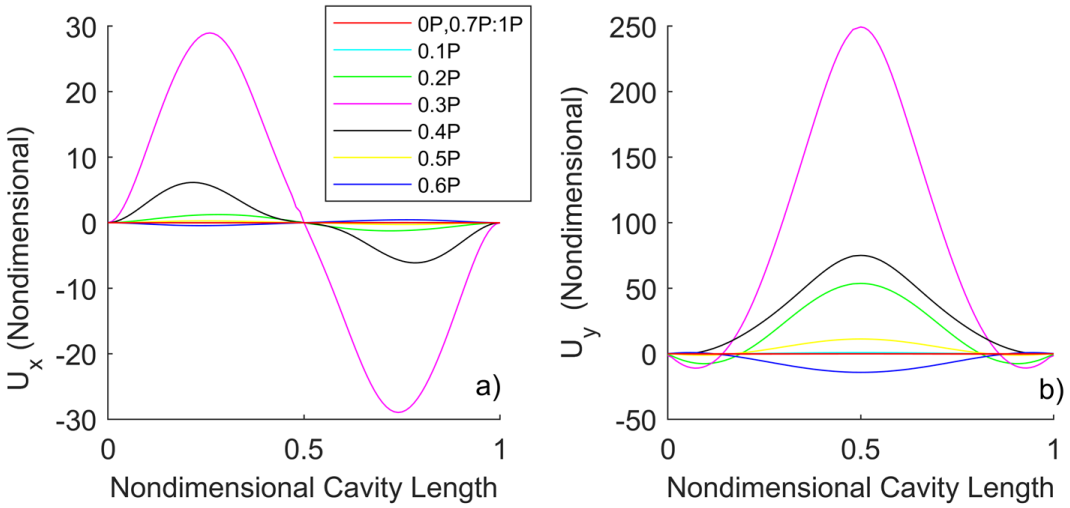

Figure 6.15: Velocity profiles of (a) U_x and (b) U_y along the x axis for $Ra_\omega = 8.34 \times 10^4$ and the case where all side walls are adiabatic.

walls are conducting and the front and back walls are adiabatic, we look first at the horizontal velocity components (U_x) and (U_z). Unlike the fully adiabatic case, this case

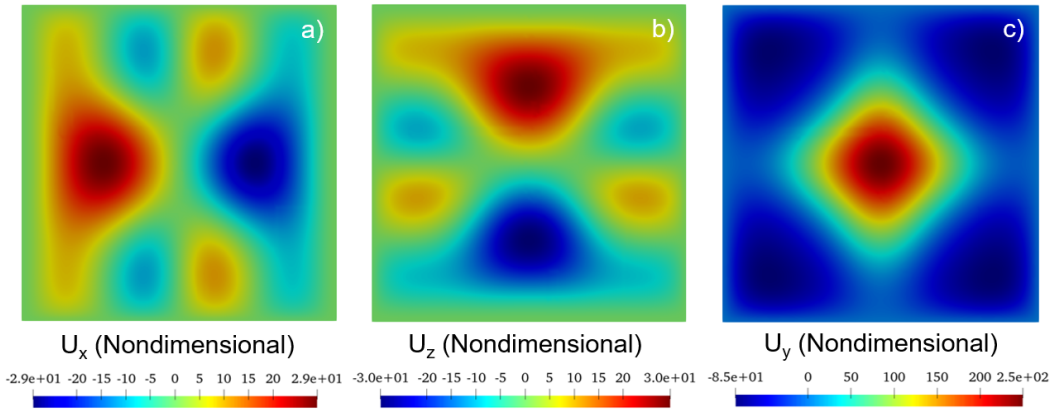

Figure 6.16: Top view of (a) horizontal velocity component (U_x), (b) horizontal velocity component (Uz) and (c) vertical velocity component (U_y) at y=0.5, for the case $Ra_\omega = 8.34 \times 10^4$ where all side walls are adiabatic at t=0.3P.

does not display perfect agreement between the U_x and U_z velocity profiles. This is seen in Fig.6.17 and confirmed in Fig.6.19 (a) and (b). The vertical velocity profile, however, can be seen to vary significantly depending on the sampling axis. Having found many

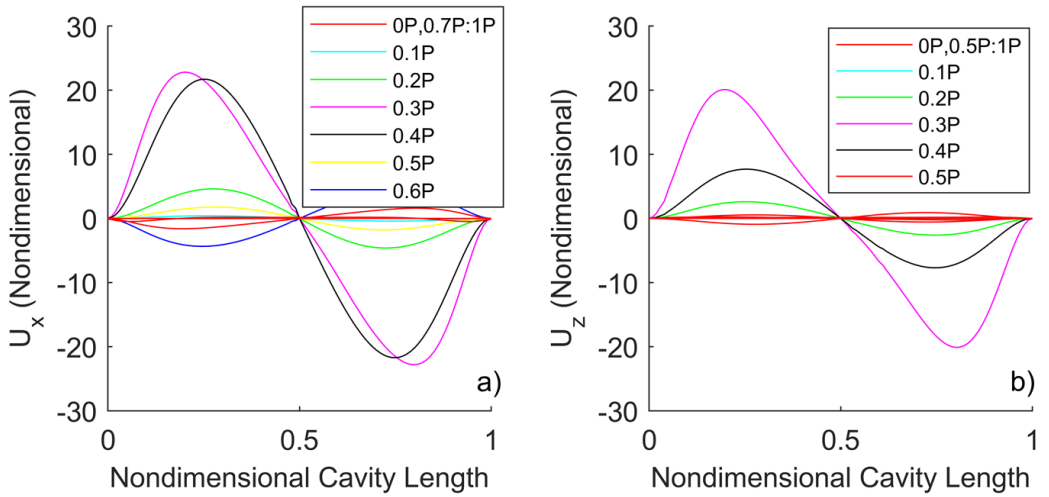

Figure 6.17: Velocity profiles of U_x along the x axis and (b) U_z along the z axis for $Ra_\omega = 8.34 \times 10^4$ and the case where the side walls are conducting, and the front and back walls are adiabatic.

similarities between the fully adiabatic and fully conducting case during the convective pulse stage, related results are not described in this section for brevity.

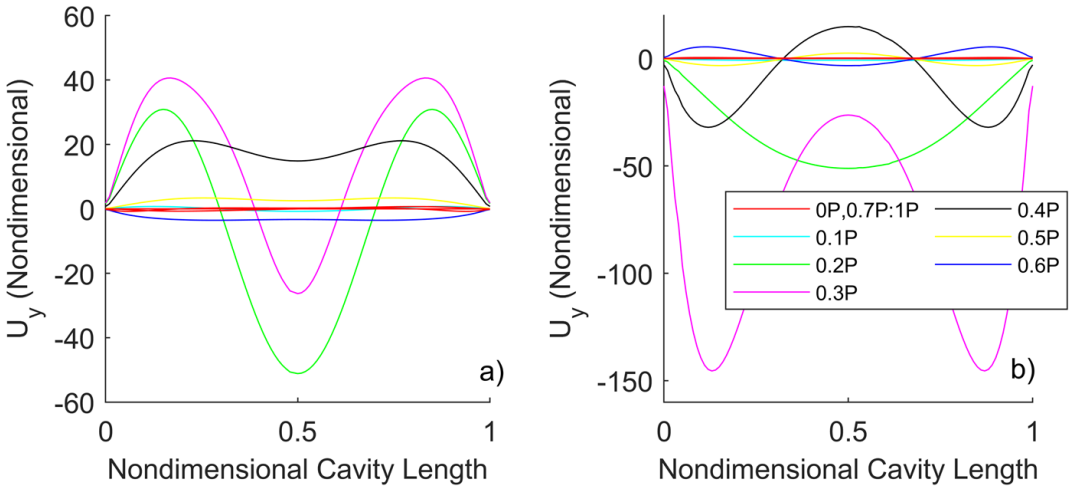

Figure 6.18: Velocity profiles of U_y along (a) the x axis and (b) the z axis for $Ra_\omega = 8.34 \times 10^4$ and the case where the side walls are conducting, and the front and back walls are adiabatic.

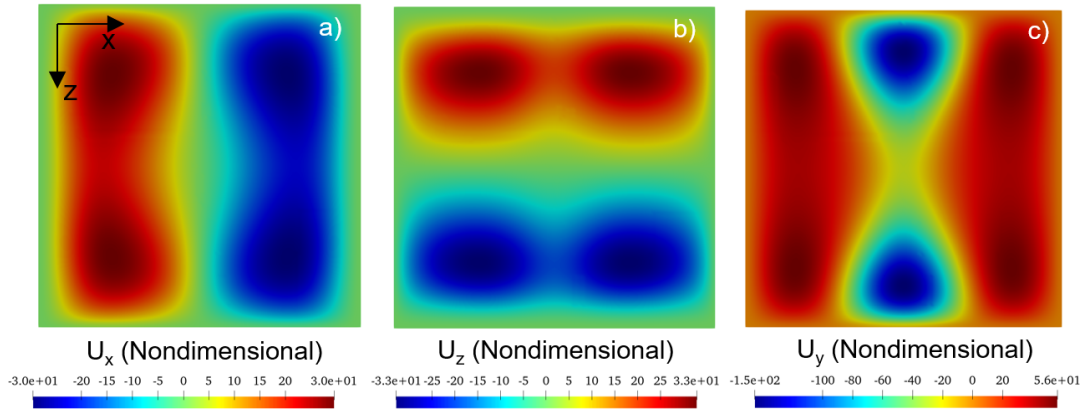

Figure 6.19: Top view of (a) horizontal velocity component (U_x), (b) horizontal velocity component (Uz) and (c) vertical velocity component (U_y), for $Ra_\omega = 8.34 \times 10^4$ and the case where the side walls are conducting, and the front and back walls are adiabatic at t=0.3P.

6.4.4 High Rayleigh numbers

Looking now at the second value of the vibrational Rayleigh number considered in the present study ($Ra_\omega = 8.34 \times 10^5$), it is worth starting from the simple remark that similarly to the previous case, the flow embodies either a quasi-stationary state or a convective burst (this being illustrated in Fig.6.20). The convective burst, however,

displays a much more complex behaviour as the fluid is more disturbed during this part of the period in comparison to the equivalent behaviour seen for the lower value of Ra_ω. If the Rayleigh number is increased by one order of magnitude, a myriad of solutions emerge and disappear. Here we look first at the resting configurations for all three boundary conditions. In particular, as qualitatively substantiated by Fig.6.21, the resting configurations for the case $Ra_\omega = 8.34 \times 10^5$ are identical to the equivalent configurations identified in Sect.6.4.2 for $Ra_\omega = 8.34 \times 10^4$. Fig.6.22 complements Fig.6.20

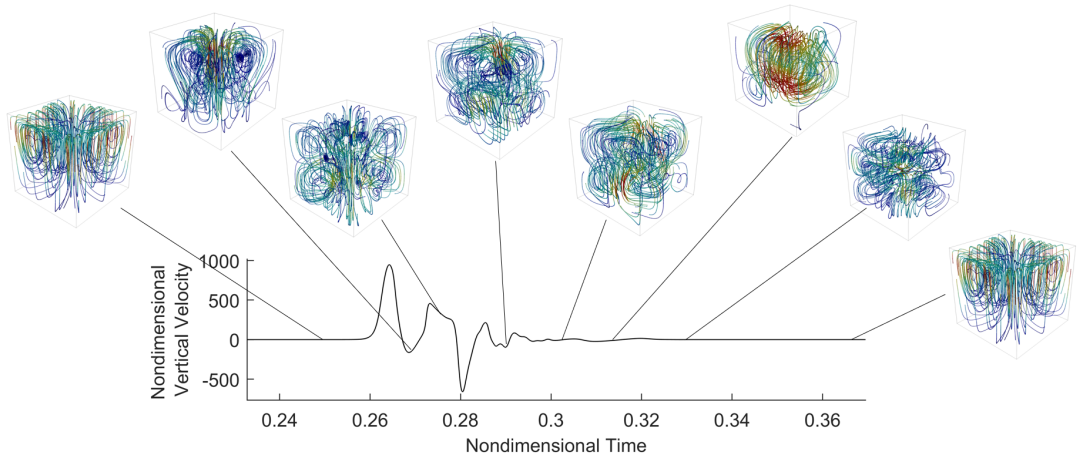

Figure 6.20: Streamlines coloured by velocity magnitude, across one period of vibration for $Ra_\omega = 8.34 \times 10^5$ and the case where all walls are adiabatic.

by revealing the evolution of the system over one vibrational period and the related multiplicity of solutions excited during the convective stage (burst). Looking first at the panel t=0, the toroidal structure is accompanied by a quasi-stationary fluid and a linear temperature distribution along the y axis. As evident in the close-up in Fig.6.23, although the fluid pattern displays symmetry about the x and z axis at the zx mid-planes, at t=0.1P the convective burst is enabled and the application of the concepts developed by Pallarès *et al.*, [22, 23] becomes rather challenging. Moving through the period, the symmetry of the system and the number of rolls and their orientation seem to vary in a relatively random way. The behaviour of the flow is reported in Fig.6.24, where the velocity profiles of all three cases are shown. The velocities are taken over a line cutting through the centre of the cavity as per Fig.6.14.

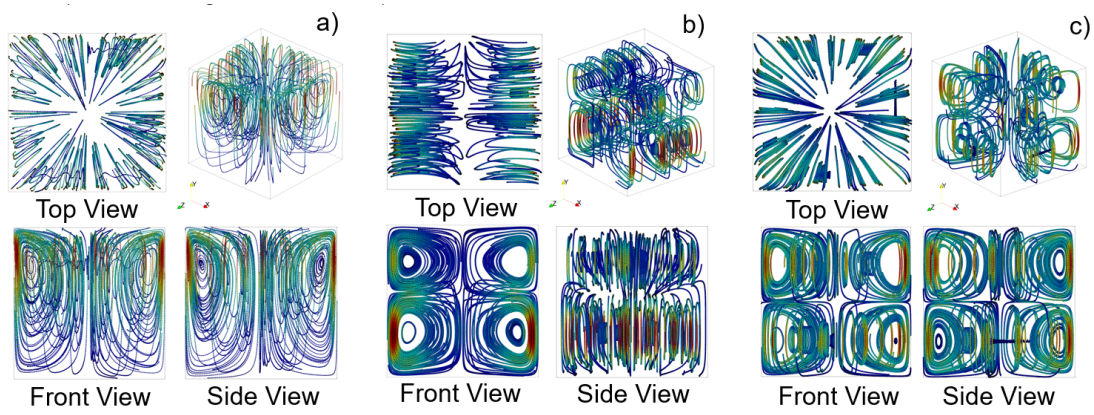

Figure 6.21: Streamlines coloured by velocity magnitude, taken during the sub-period when the flow embodies a quasi-stationary state for $Ra_\omega = 8.34 \times 10^5$, and a) the case where all walls are adiabatic, b) the case where two side walls are conducting and two are adiabatic and c) the case where all side walls are conducting (the blue colour represents a lower velocity and the red colour represents a higher velocity).

Looking first at the vertical velocity component (U_y) taken parallel to the x axis, symmetry is visible with respect to the centre of the cavity (x=0.5), where a peak in velocity is seen for all three cases, excepting at t=0.3P for the fully adiabatic wall case. This is also observed when looking at vertical velocity component taken parallel to the z axis, reported in Fig.6.25 (a). With exception of this momentary break in symmetry, the vertical velocity profiles are inherently symmetrical and remain so at least until t=0.4P. After this point, the velocity of the fluid is low compared to the first instances of the convective burst (t=0.P to 0.4P). Even though the velocity is low, many textural transitions are observed (as evident in Fig.6.22 and 6.22) while the fluid settles from the convective state to the quasi-stationary state. As for the horizontal velocity components, the temporary asymmetry observed in the vertical velocity component in the fully adiabatic case, is widespread through the whole period indicating that for the case where all walls are adiabatic, the fluid is less stable that for the situation when conducting sidewalls are considered. Indeed, looking at Fig.6.26 (b) and (c) and Fig.6.27 (b) and (c), symmetry is apparent about the centre of the sampling line. For the sake of completeness, the spatio-temporal maps, providing a visualization of the symmetry (or asymmetry) embodied by the flow over time are also provided (Figs.6.28-6.30). The asymmetry embodied by the fully adiabatic case can be recognized in Fig.6.28 (a)

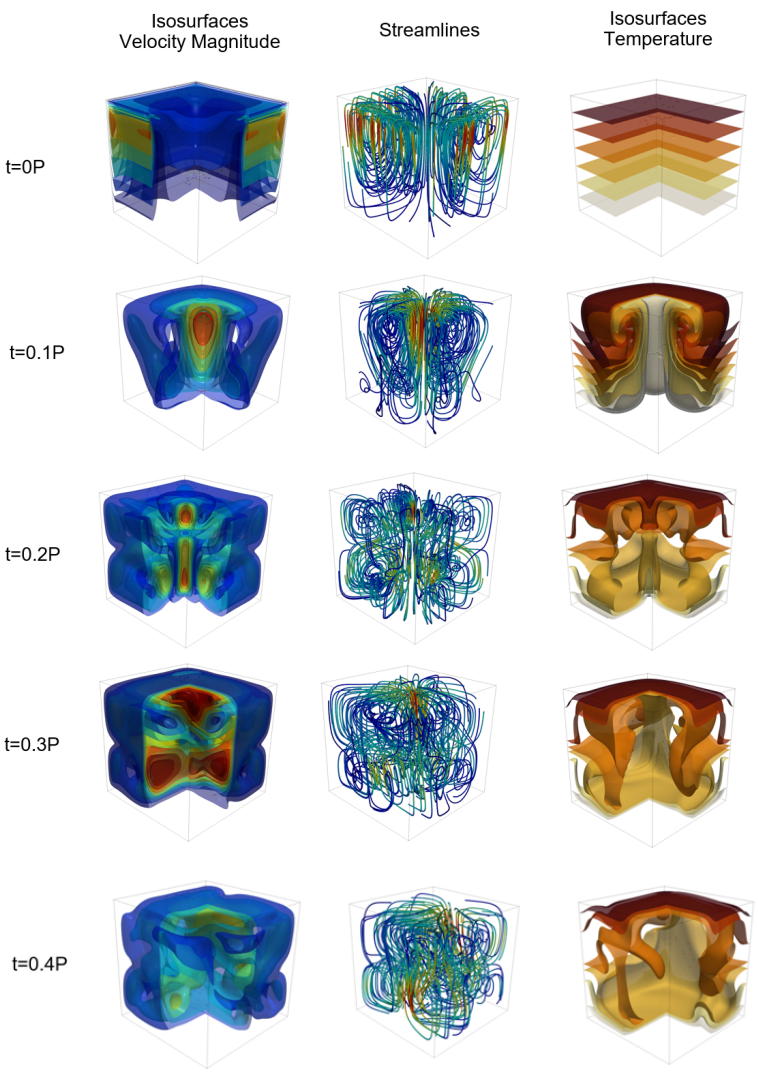

Figure 6.22: Velocity magnitude, streamlines and temperature contours for $Ra_\omega = 8.34 \times 10^5$, all walls are adiabatic. From t=0 to t=0.4P

and (d), Fig.6.29 (a) and (d) and Fig.6.30 (d). However, a near symmetrical pattern is maintained for the vertical velocity component along the x axis for the fully adiabatic case (Fig.6.30 (a)). Moving on to the next two cases, the half conducting half adiabatic and the fully conducting configuration, it is worth noting that both situations present a high level of symmetry for the horizontal velocity components, especially at the point where the fluid is most disturbed (as in the reader will realize by inspecting Figs.6.28 (b) and (c) and Figs.6.29 (e) and (f)). It is noticeable however, that the horizontal

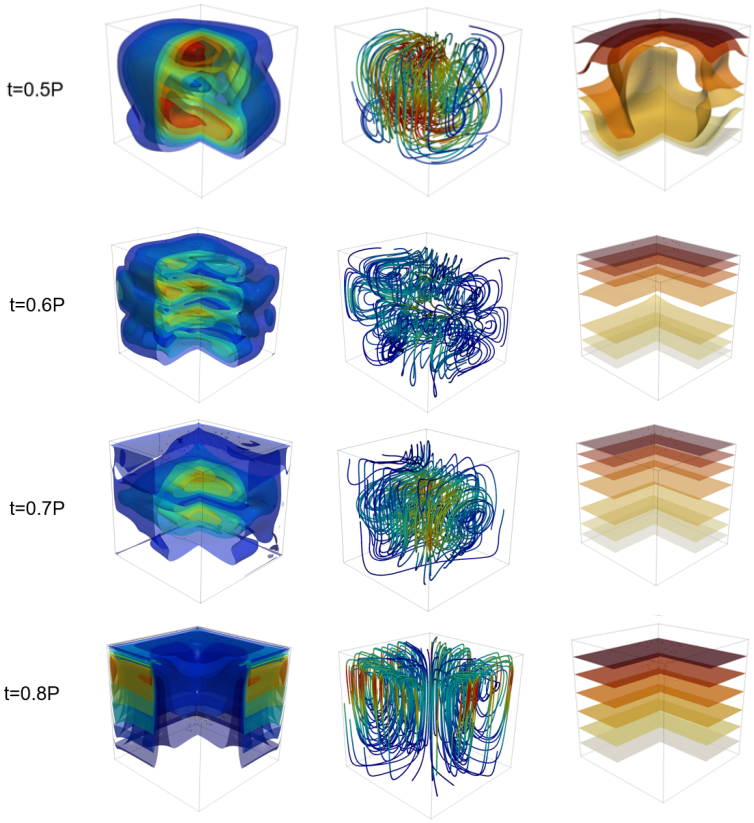

Figure 6.22: Velocity magnitude, streamlines and temperature contours for $Ra_\omega = 8.34 \times 10^5$, all walls are adiabatic. From t=0.5 to t=0.8P

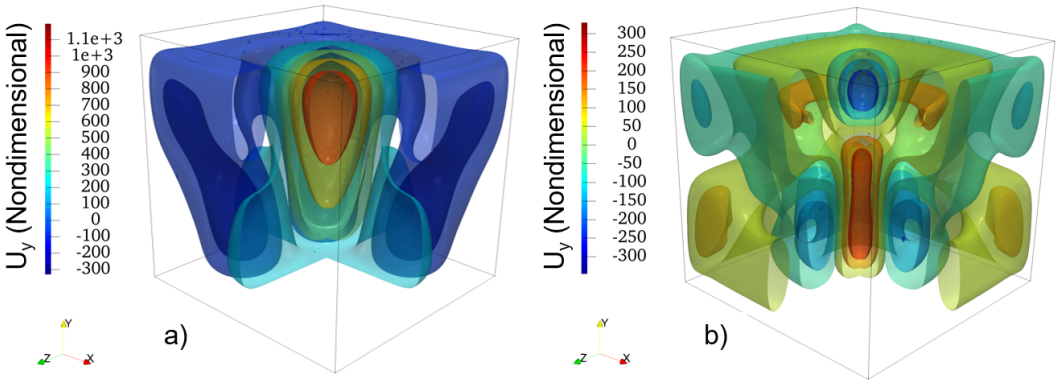

Figure 6.23: Contour of velocity magnitude at (a) t=0.1P and (b) t=0.2P for $Ra_\omega = 8.34 \times 10^5$, where all walls are adiabatic.

velocity U_x sampled over the z axis (Figs.6.28 (e) and (f)) and the horizontal velocity U_z sampled over the x axis (Figs.6.29 (b) and (c)), show a velocity which is close to 0,

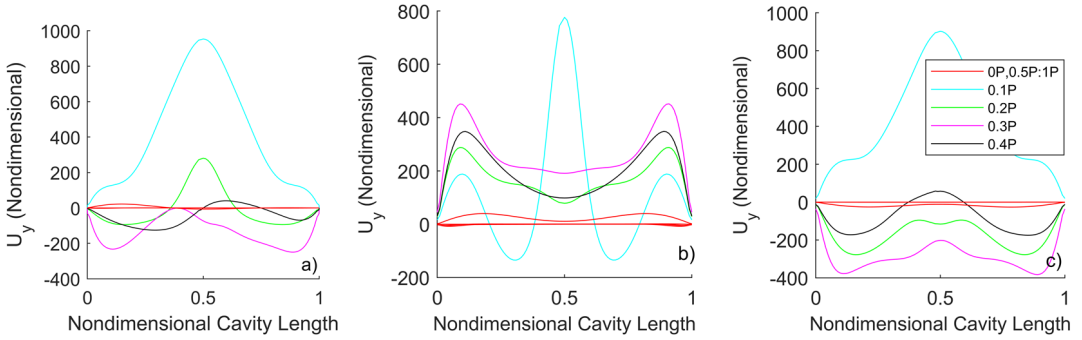

Figure 6.24: Non-dimensional vertical velocity (Uy) across the length of the cavity along the centerline of the zx plane parallel to the x axis at y=0.5. For For $Ra_\omega = 8.34 \times 10^5$, where (a) the side walls are adiabatic (b) the front and back walls are adiabatic, and the side walls are conducting and (c) all side walls are conducting.

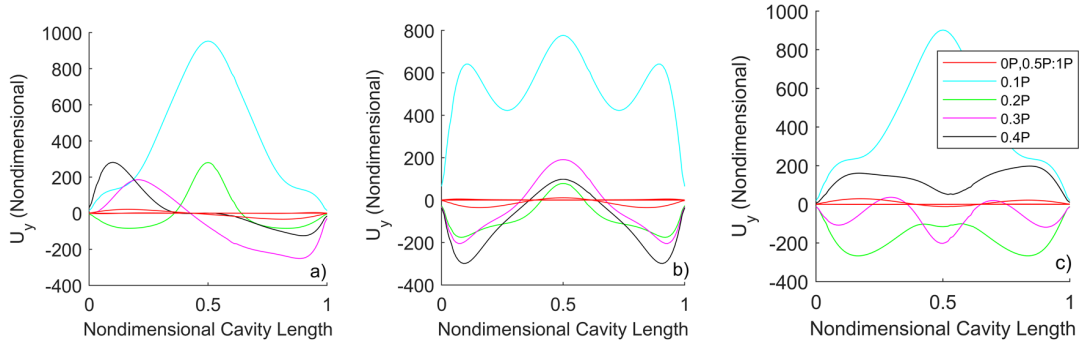

Figure 6.25: Non-dimensional vertical velocity (U_y) across the length of the cavity along the centerline of the zx plane parallel to the z axis at y=0.5. For $Ra_\omega = 8.34 \times 10^5$ where (a) the side walls are adiabatic (b) the front and back walls are adiabatic, and the side walls are conducting and (c) all side walls are conducting.

indicating a possible symmetry axis as show in Fig.6.16 (a) and (b) and Fig.6.19 (a) and (b), maintained over the whole period. Finally, an additional relevant remark can be made regarding the periodicity of the hybrid case. For all maps pertaining to this case the period over which the fluid repeats itself is twice that of the forcing period. This is in agreement with the velocity signals provided in Sect.6.4.1.

6.4.5 Thermal response

This section is finally devoted to an analysis of the thermal response of the system. Along these lines, Fig.6.31 shows the ratio of heat transfer due to convection over that

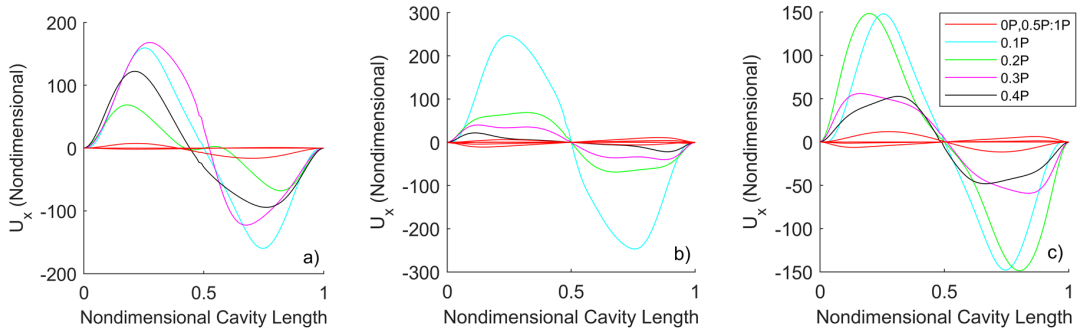

Figure 6.26: Non-dimensional horizontal velocity (U_x) across the length of the cavity along the centerline of the zx plane at y=0.5. plane parallel to the x axis at y=0.5. For $Ra_\omega = 8.34 \times 10^5$, where (a) the side walls are adiabatic (b) the front and back walls are adiabatic, and the side walls are conducting and (c) all side walls are conducting.

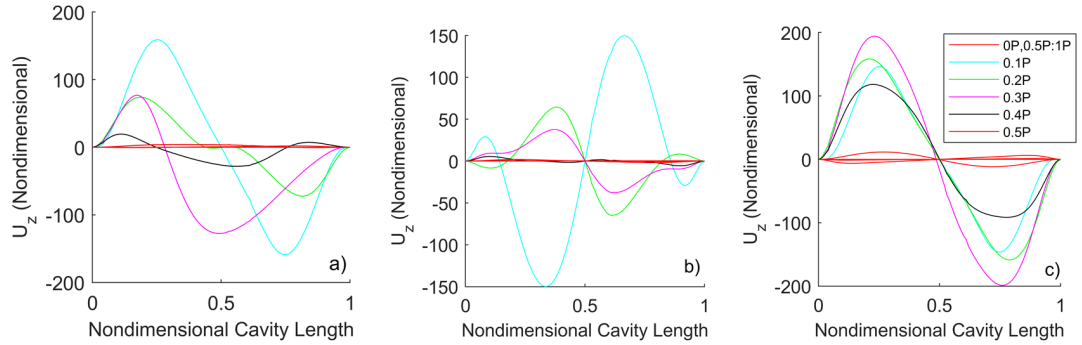

Figure 6.27: Non-dimensional horizontal velocity (U_z) across the length of the cavity along the centerline of the zx plane at y=0.5. plane parallel to the z axis at y=0.5. For For $Ra_\omega = 8.34 \times 10^5$, where (a) the side walls are adiabatic (b) the front and back walls are adiabatic, and the side walls are conducting and (c) all side walls are conducting.

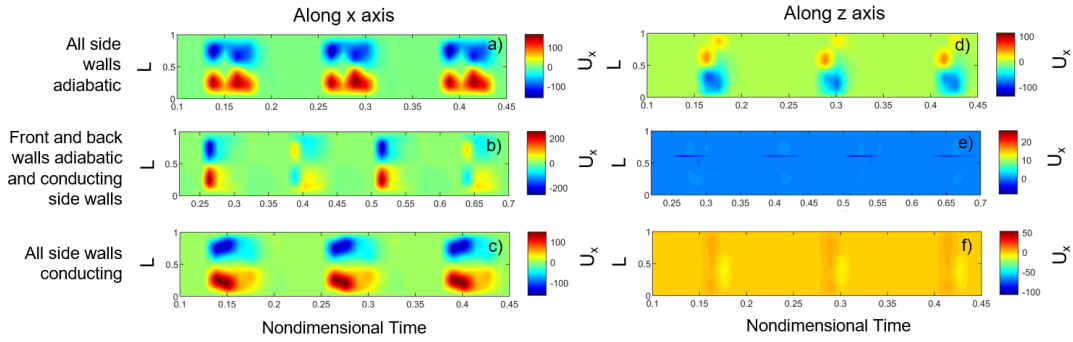

Figure 6.28: Horizontal velocity component Ux along the x-axis (a-c) and the z-axis (d-f) for all three boundary conditions and $Ra_\omega = 8.34 \times 10^5$.

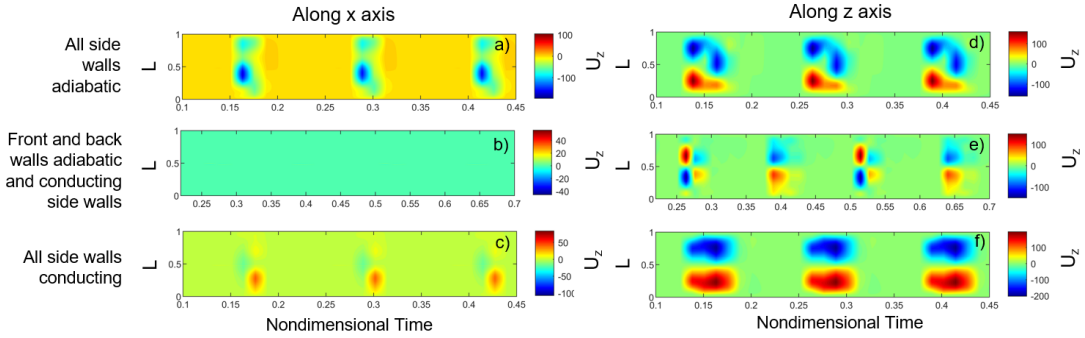

Figure 6.29: Horizontal velocity component Uz along the x-axis (a-c) and the z-axis (d-f) for all three boundary conditions and $Ra_\omega = 8.34 \times 10^5$.

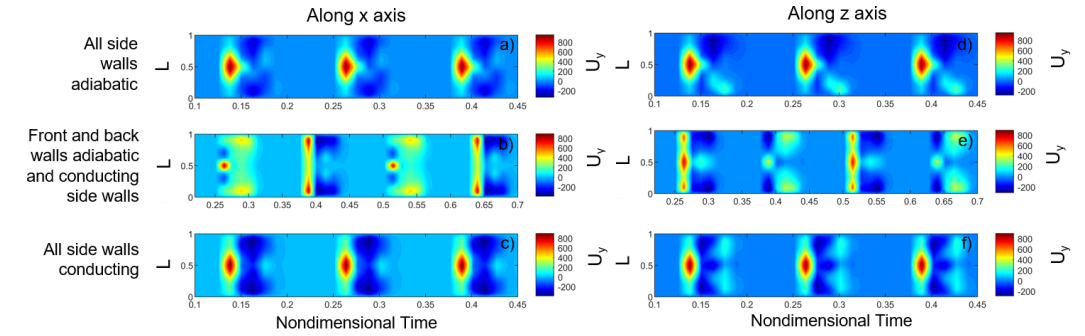

Figure 6.30: Vertical velocity component Uy along the x-axis (a-c) and the z-axis (d-f) as per Fig.6.14., for all three boundary conditions and $Ra_\omega = 8.34 \times 10^5$.

of conduction along a given boundary, i.e. the Nusselt number ($Nu_{overall}$) across the hot wall, where: Similarly to the velocity signals, the Nu signal associated with the lower value of Ra_ω is of the type SY-P, whereas the responses associated with the higher value of Ra_ω, although still technically classifiable as SY-P, border on the verge of the SY-NP regime where a turbulent burst appears after the convective peak. It must be noted that the behavior related to the heat transfer of the system is quasi-identical when comparing the different sidewall conditions, especially when the value of Ra_ω is increased.

Temperature maps are also included here for all considered cases. Focusing first on Fig.6.32 ($Ra_\omega = 8.34 \times 10^4$), perfect agreement is observed between the thermal behaviour of the flow along the x and z axis, for the situation where all four walls are

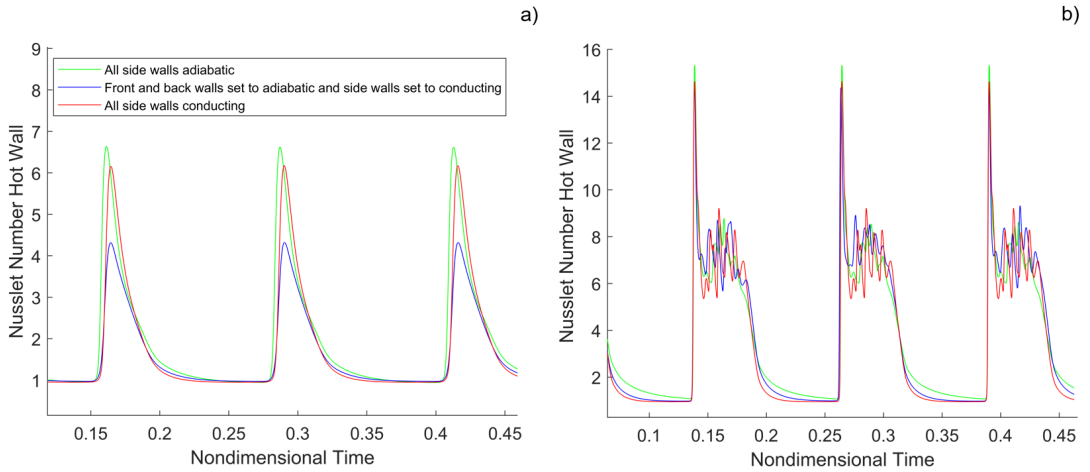

Figure 6.31: Nusselt number across the hot wall for (a) $Ra_\omega = 8.34 \times 10^4$ and (b) $Ra_\omega = 8.34 \times 10^5$,

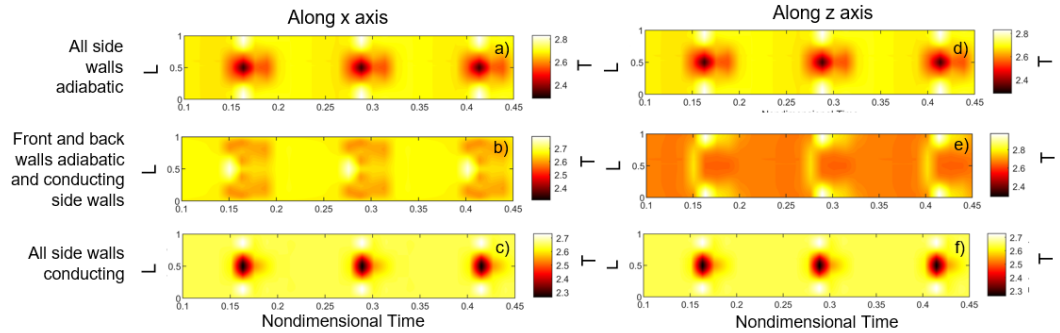

Figure 6.32: Nondimensional temperature (T) along the x-axis (a-c) and the z-axis (d-f) for all three boundary conditions and $Ra_\omega = 8.34 \times 10^4$.

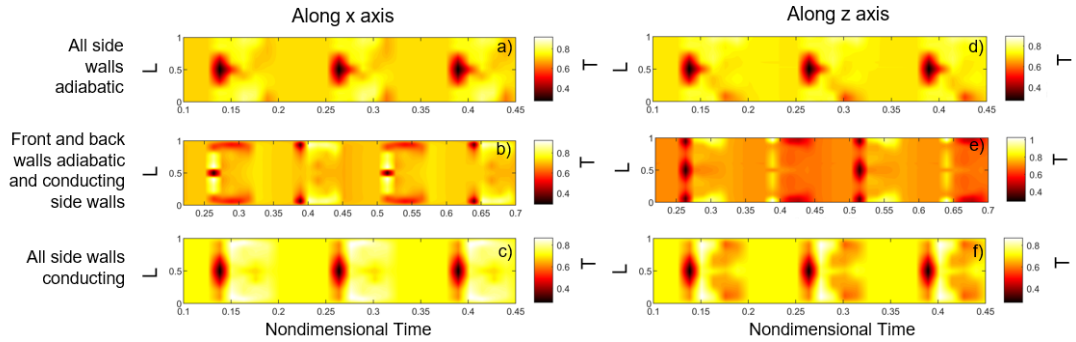

Figure 6.33: Nondimensional temperature (T) along the x-axis (a-c) and the z-axis (d-f) for all three boundary conditions and $Ra_\omega = 8.34 \times 10^5$.

either adiabatic or conducting, this is however not the case when a higher value of Ra_ω is examined (Fig.6.33).

Indeed, a slight deviance is observed in the temperature profile across the z axis in this case, also detectable in the velocity maps provided in Figs.6.28,6.29 and 6.30.

6.5 Conclusion

Although numerous investigations have been carried out in the general area of thermal convection, an insightful and complete understanding of the properties of the specific variant driven by time-varying accelerations has hitherto been unclear. This study is a contribution to improve the present unsatisfactory situation, especially for what concerns the poorly considered situation in which vibrations are parallel to the imposed temperature gradient. The strategy undertaken in earlier author's work based on the numerical solution of the two-dimensional Navier-Stokes and energy equations has been further pursued by allowing the flow to develop in a realistic 3D physical domain for which the problem of pattern selection has long been a theoretical puzzle even for the canonical case of standard steady RB convection. The simulations have shown that an increase in the (spatial) dimensionality of the problem has a dramatic influence on the richness of the fundamental modes of convection that can be excited. These can be partially grouped in different categories according to some possible classifications based on various symmetries which are broken or retained and the number of convective structures present at the same time in the physical domain. Given the intrinsically time-varying nature of thermovibrational convection in systems where the vibrations and the temperature gradient are concurrent, many of these fundamental modes can be produced for a fixed value of the vibrational Rayleigh number and given thermal boundary conditions. Although two well-defined convective stages can always be identified in the period of vibrations (one corresponding to an almost quiescent quasi-stationary state, and another where a convective pulse occurs), however, the enabled modes are not mutually exclusive, nor are they truly progressive. Moreover, their multiplicity tends to be enhanced as the vibrational Rayleigh number is increased and the convective pulse is turned into a turbulent burst. The numerical simulations have

also revealed that, despite this multiplicity, some control on the morphology of the emerging convective structures can be exerted by forcing the system to break or adhere to some spatial symmetries 'a priori' by imposing non uniform thermal boundary conditions along the sidewalls. An ordered combination of adiabatic and conducting walls can indeed limit the ability of the flow to produce toroidal states in favour of more two-dimensional solutions. The intentional use of hybrid thermal boundary conditions can also be instrumental in inducing changes in the temporal response of these systems, causing a shift from synchronous (flow oscillating at the same frequency of the forcing) to sub-harmonic (period doubling bifurcation) behaviours or vice versa. Moreover, we have shown that cases containing a pair or two pairs of conducting side walls are more stable than the configuration with adiabatic sidewalls.

An exciting prospect for the future (as explored in the following chapter) is to enrich this problem with the addition of solid particles, thereby, giving rise to a new line of inquiry running in parallel with that where the interplay of thermovibrational effects and particle inertial effects in cubic cavities with vibrations perpendicular to the temperature gradient has been found to support fascinating particle self-organization phenomena (formation of highly ordered, high resolution structures with the morphology of quadric surfaces).

Chapter 7

Particle Accumulation Under Parallel Vibrations

This chapter is based on the following article currently under review for Physics of Fluids:

Crewdson, G. and Lappa, M., "3D Solid Particle Self-assembly in Thermovibrational Flow: The case with Unidirectional Temperature gradient and Concurrent Vibrations".

The text in this chapter has been modified only when necessary in order to preserve the continuity and flow of this thesis.

7.1 Introduction

Following the work carried out in Chap.6, where the main focus was on the modes of convection emerging in a three-dimensional cubic enclosure undergoing vibrations in a direction 'parallel' to the imposed temperature gradient, the present study considers the phenomena of particle accumulation, which occur when solid mass is added to the fluid in the form of small rigid spheres. The main objective is an understanding of the relationship between 'particle attractee' in the physical space and the conditions in the space of parameters for which they are enabled. The governing equations for the fluid and solid phases are numerically solved in their complete, time-dependent and

non-linear form and it is shown that the hallmark of the phenomena occurring in this case is an endless squeezing and expansion of particle formations along the direction of the temperature gradient. The related explosion of textural transitions is discussed in detail together with a critical analysis of the mechanisms that drive their remarkable diversity with respect to the stationary morphologies typical of the companion case with 'perpendicular' vibrations.

7.2 Numerical model and boundary conditions

The mathematical model used in this chapter is identical to that used in Chap.6. The software OpenFOAM has been employed to solve the numerical simulations in Chap.6, provide a detailed explanation of the specific schemes used in the treatments of the fluid part.

In this case however, an additional solid phase is introduced, taking the form of small, finite and spherical particles. The equations for solving particle trajectories have been outlined and expanded upon in Chap.3, Sect.2.9, the governing equation used to compute particle trajectories is know as the Maxey-Riley equation defined in Eq.3.37. Here, the particles are tracked using a Lagrangian framework, where a one-way coupling approach is used. The system is considered dilute, where the volume fraction of the dispersed phase remains below the threshold where one-way coupling is allowed. (i.e., $\alpha_p \leq 10^{-6}$, where $\alpha_p = V_p/V$).

The same system originally considered in Chap.6 is shown in Fig.7.1. The bottom wall of the three-dimensional (3D) cubic cavity is set to $T = T_{cold}$ wall and the top wall to $T = T_{hot}$. The sides of the cavity are all adiabatic, all conducting, or a hybrid configuration is assumed, and the vibrations are applied parallel to the temperature gradient (along the y axis).

7.3 Validation

The fluid-dynamic kernel of OpenFOAM used to solve the thermovibrational flow was already validated by Crewdson and Lappa [126] (Chap.6). A verification of the particle-

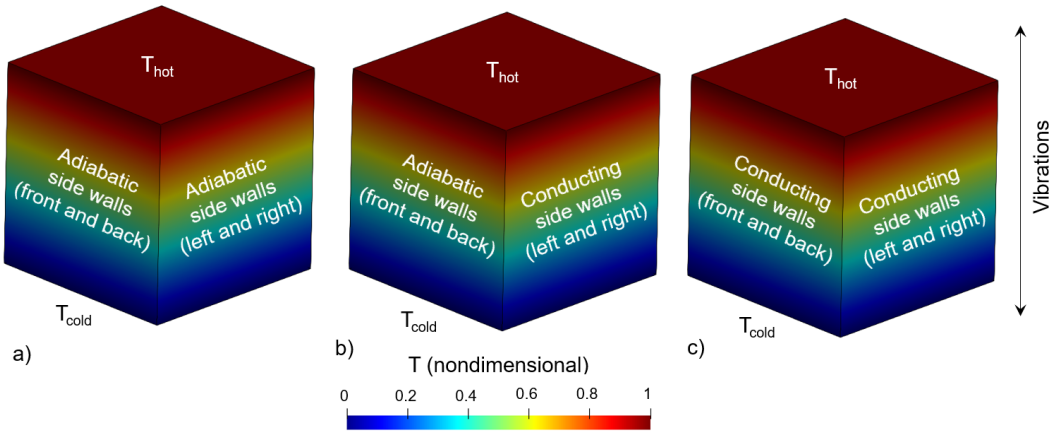

Figure 7.1: Considered fluid domain and related thermal boundary conditions

tracking kernel can be found in Capobianchi and Lappa [127], where its ability to predict correctly particle dynamics and related accumulation effects was tested against another category of phenomena, that is, the occurrence of particle accumulation structures (particles distribution) in time-dependent thermocapillary flows (see, e.g., Melnikov and Shevtsova [128]; Gotoda *et al.* [129]; Sakata *et al.* [130]). As a third-level stage in such a validation hierarchy, in the present study, a direct comparison is implemented between the results provided by OpenFOAM for the specific problem under investigation and those obtained using an in-house code (the same used to produce the results published in Lappas works [100, 101, 131–133]. In particular, such a comparison is made firstly between the vertical velocity signals at the centre of the cavity and the Nusselt number across the hot wall of the cavity. The non-dimensional values associated with the validation case are $Ra_\omega = 4 \times 10^4$, $\Omega = 50$,$\gamma = 1.25 \times 10^7$, $\xi = 1.85$ and $St = 10^{-5}$.

Figure 7.2, clearly confirms that, in using two different computational platforms, perfect agreement in the fluid behaviour is obtained. The validation has then been extended to the dispersed phase. Along these lines, the evolution of the following non-dimensional quantities has been considered:

$$Q^- = \frac{\sum_{u_{part}<0} m_{part} u_{part}}{M_{tot}} \tag{7.1}$$

and

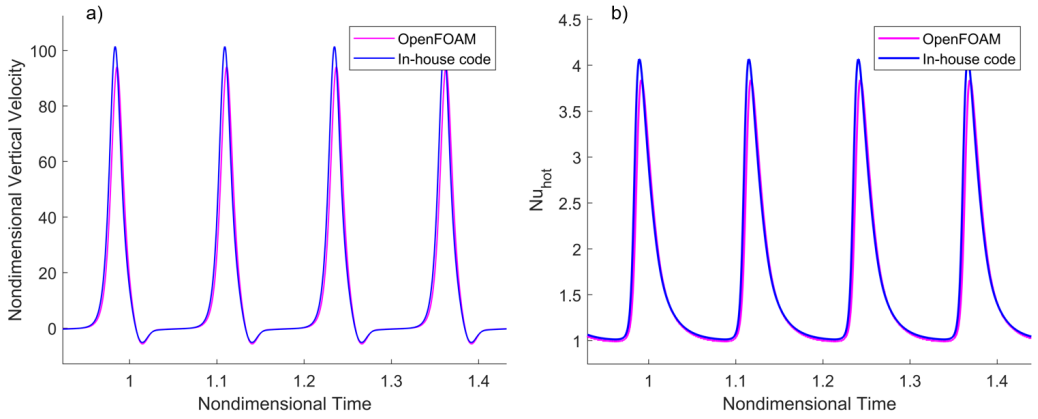

Figure 7.2: Validation of OpenFOAM against in-house code for the 2D case $Ra_\omega = 4 \times 10^4$, $\Omega = 50$,$\gamma = 1.25 \times 10^7$, $\xi = 1.85$ and $St = 10^{-5}$ for a) the non-dimensional vertical velocity of the fluid (U_y) at the centre of the cavity and b) the Nusselt number across the hot wall (Nu_{hot}).

$$Q^+ = \frac{\sum_{u_{part}>0} m_{part} u_{part}}{M_{tot}} \tag{7.2}$$

where m_{part} is the mass of the generic particle and the M_{tot} accounts for the mass of all particles dispersed in the fluid (according to this definition Q may be regarded as the mass averaged velocity possessed by all particles moving in the same direction [134]).

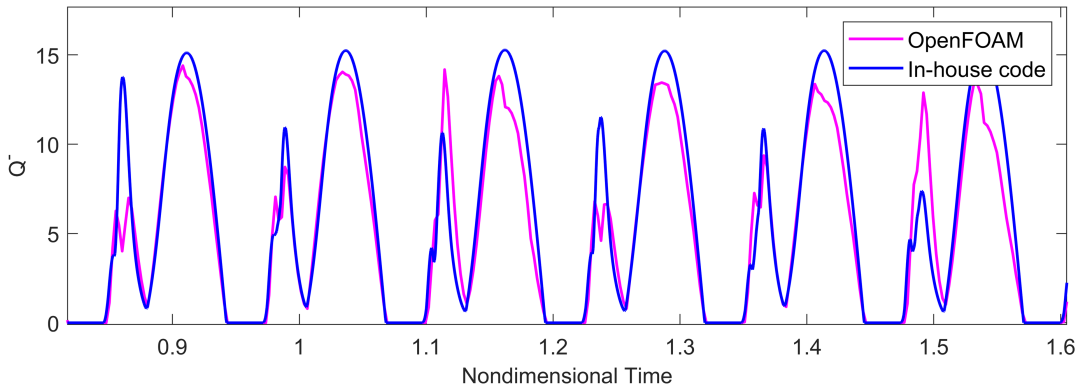

Figure 7.3: Evolution Q^- over time for the case $Ra_\omega = 4 \times 10^4$, $\Omega = 50$,$\gamma = 1.25 \times 10^7$, $\xi = 1.85$ and $St = 10^{-5}$for OpenFOAM and the in-house code.

	OpenFOAM	**In-house code**	**% difference**
Q^-_{mean}	5.31	6.00	10.50%
Q^-_{max}	15.07	15.39	2.08

Table 7.1: Differences in results when Q^-_{mean} is concidered when OpenFOAM and an In-house code is used.

Also in this case good agreement is found between the two platforms. Indeed, the evolution in time of the global quantity Q^- is essentially the same both in terms of amplitude and frequency spectrum content. In particular, two temporal characteristics stand out from Fig.7.3: a small peak is visible before the convective burst, followed by a higher peak in Q^-during the convective burst. Table 7.1 indicates that the maximum discrepancy between the two signals occurs for the value of Q^- max where a difference of approx. 10 % can be noticed in some cases, to which can be ascribed the slightly different interpolation schemes used by the two considered solvers. OpenFOAM makes use of a linear weighted interpolation based on cell values while the in house code relies on simple linear interpolations starting from velocity component values located on the boundary of each computational cell. Figure 7.4, finally shows a snapshot of the particle behaviour obtained using both codes at the same point in (non-dimensional) time (t=1.88). In both cases particles form a symmetrical pattern along the y axis at x=0.5. All these observations lead to the conclusion that OpenFOAM and the in-house code provide essentially the same results both in terms of fluid flow and particle behaviour, as qualitatively and quantitatively substantiated by these figures.

7.4 Grid refinement

The range of non-dimensional parameters explored in this study has its origin in the previous numerical investigation by Crewdson and Lappa [126] (Chap,6). It was shown there that for a vibrational Rayleigh number spanning the range 8.34×10^4 to 8.34^5 and a fixed angular frequency of the vibrations (Ω=50), a mesh size of 100^3 elements could produce grid independent results in all cases. As this work is limited to considering the lower end of this interval, i.e. $Ra_\omega = 8.34 \times 10^4$, one may expect the requirement in terms of needed grid points to be smaller. Indeed, as the reader will realize by inspecting

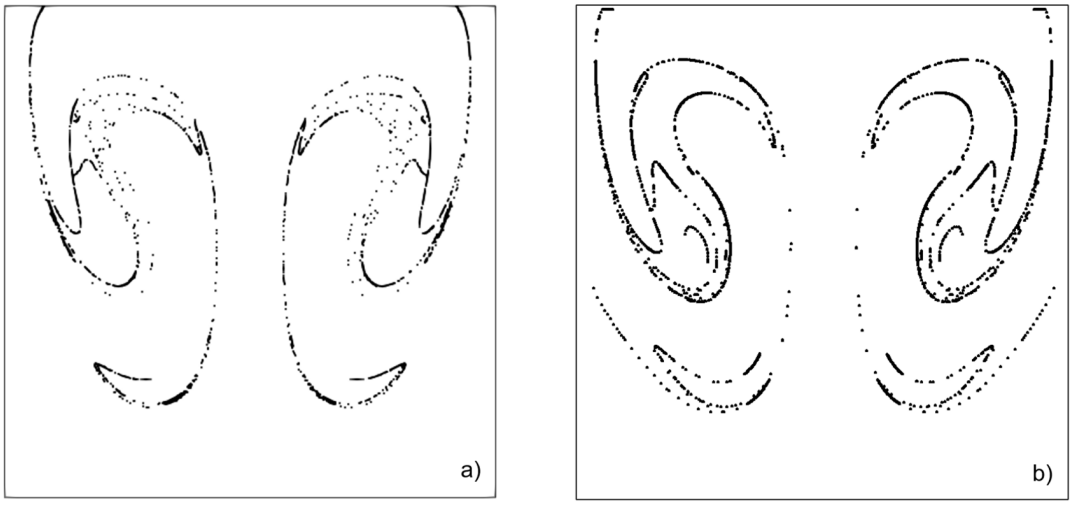

Figure 7.4: Snapshots of the particle behaviour for the 2D case $Ra_\omega = 4 \times 10^4$, $\Omega = 50$, $\gamma = 1.25 \times 10^7$, $\xi = 1.85$ and $St = 10^{-5}$ for a) OpenFOAM and b) in-house code at t=1.88 (nondimensional time).

Fig.7.5, grid independence is achieved for both the Nusselt number across the hot wall and the nondimensional vertical velocity over time if a 80^3 mesh is used.

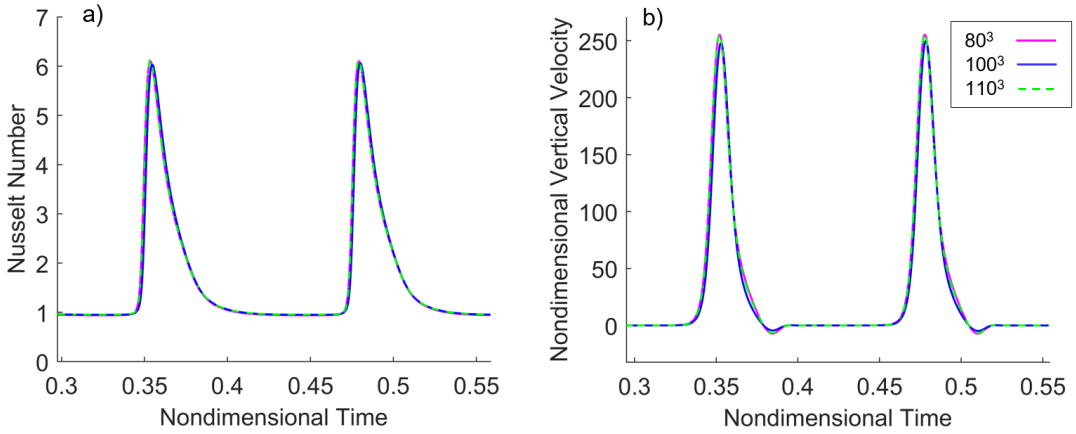

Figure 7.5: Evolution of a) the Nusselt number across the hot wall and b) the nondimensional vertical velocity (Uy) over time for the case $Ra_\omega = 8.34 \times 10^4$, $\Omega = 50$, $\gamma = 1.68 \times 10^7$, $\xi = 1.85$ and $St = 1.25^{-5}$ for meshes comprised of 80^3, 100^3 and 110^3 elements.

The next step of this process obviously consists of assessing whether such a numerical resolution is sufficient to obtain grid-independence in the computation of the dispersed solid phase, or not. In this regard, reference can be made once again to the

global parameter defined before, i.e., the mass-averaged velocity of particles along the positive or negative sense of the y axis, and the outcomes of such an assessment are reported in Fig.7.6. It can be seen there that although a 80^3 resolution is sufficient to guarantee mesh independence of purely fluid-dynamic quantities, the density of grid points must be increased to 100^3 in order to extend this property to the transported solid phase (when looking at the signal produced for both Q^- and Q^+ for the 100^3 and the 110^3 grid, almost perfect agreement is achieved). From this it can be concluded that, although the Rayleigh number is set to a relatively small value, a grid size of 100^3 (1 million) elements is required to effectively capture at the same time the fluid dynamic and the particle dynamics aspects of the problem.

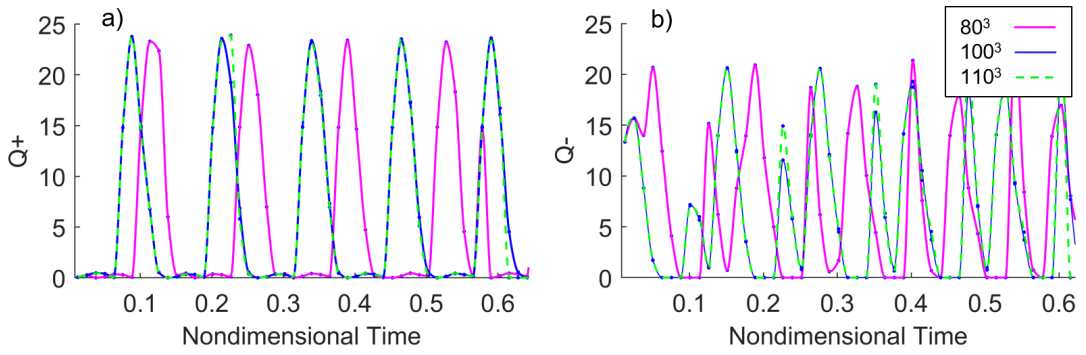

Figure 7.6: Evolution of Q^+ and Q^- for the case $Ra_\omega = 8.34 \times 10^4$, $\Omega = 50$, $\gamma = 1.68 \times 10^7$, $\xi = 1.85$ and $St = 1.25^{-5}$ for meshes comprised of 80^3, 100^3 and 110^3 elements.

7.5 Results

Results about the particle dynamic evolution are provided in this section for all the thermal configurations shown in Fig.7.1, namely the cases where all the sidewalls are adiabatic, conducting, or a hybrid configuration is considered with two adiabatic and two conducting walls. Moreover, both cases with particles denser ($\xi = 1.85$) and less dense that the carrier liquid ($\xi = 0.3$) are examined (hereafter simply referred to a 'heavy' and 'light' particles, respectively). The vibrational Rayleigh number and the related non-dimensional angular frequency are fixed to $Ra_\omega = 8.34 \times 10^4$ and $\Omega = 50$,

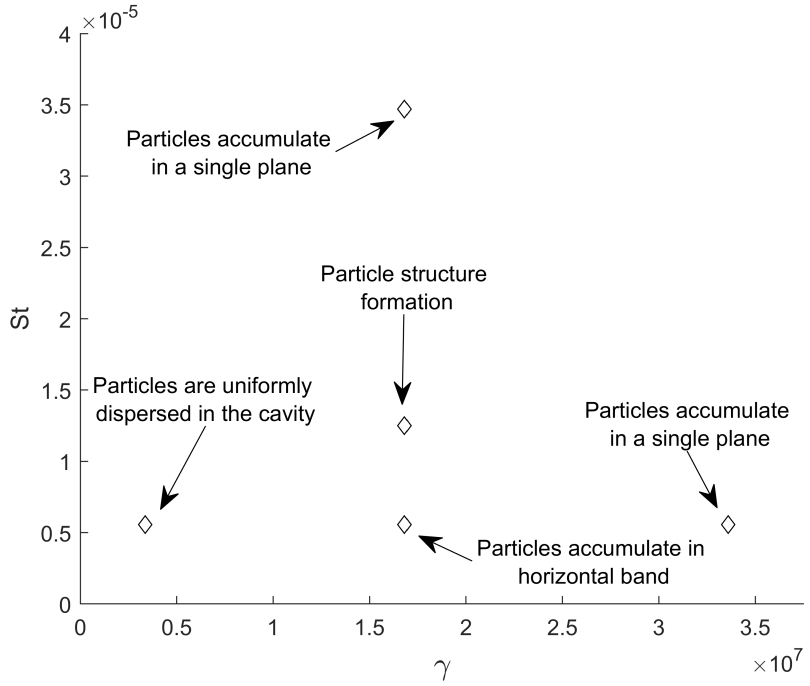

Figure 7.7: Map of emerging states in the (γ, St) space of parameters.

respectively as in the earlier (propaedeutical) study by Crewdson and Lappa [126] (Chap.6). Similarly, the Prandtl number is fixed to Pr=7. The typical outcomes of the simulations for the vibration acceleration and particle Stokes number spanning relatively wide intervals are synthetically reported in Fig.7.7.

The significance of this figure resides in its ability to make evident that while trivial behaviors occur over large intervals of γ and St (states where particles simply accumulate all in a single planar surface or they remain more or less uniformly distributed in the physical domain), interesting phenomena are localized in a certain sub-region. This explains why in the following we concentrate on two typical values of the vibration acceleration and particle Stokes number, namely, $\gamma = 1.68 \times 10^7$ and $St = 1.25 \times 10^{-5}$, whereas the dynamics obtained in the other cases are no longer discussed.

7.5.1 Evolution of Q^- and Q^+

Before starting to deal with the particle patterning behaviour, in order to get a clear idea of the system dynamics from a global (ensemble) point of view, it is convenient to

initially assess the response of the system using the global quantities already defined in the previous section. Along these lines, Figs.7.8 to 7.11, show the temporal evolution of Q^+ and Q^- for both the light and heavy particles, for all the three variants of thermal boundary conditions assumed in this study.

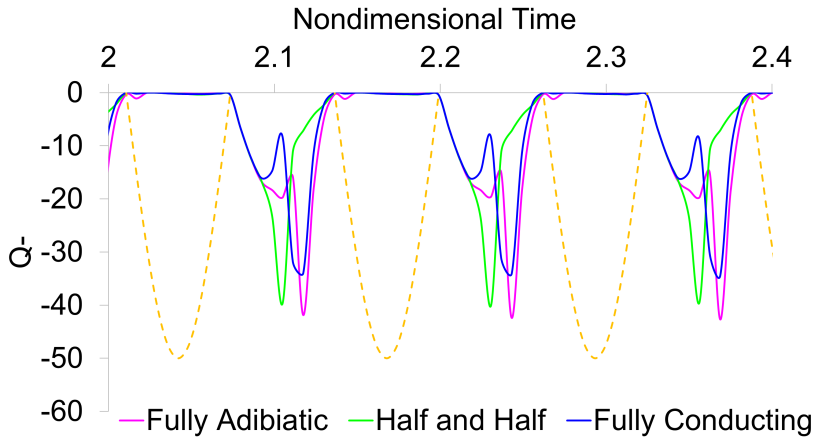

Figure 7.8: Evolution of Q^- over time for the case Pr=7, $Ra_\omega = 8.34 \times 10^4$, $\Omega = 50$, $\gamma = 1.68 \times 10^7$, $St = 1.25 \times 10^{-5}$ for all three boundary conditions for the case $\xi = 0.3$. The yellow dashed line represents the acceleration applied to the cavity for the given non-dimensional frequency $\Omega = 50$.

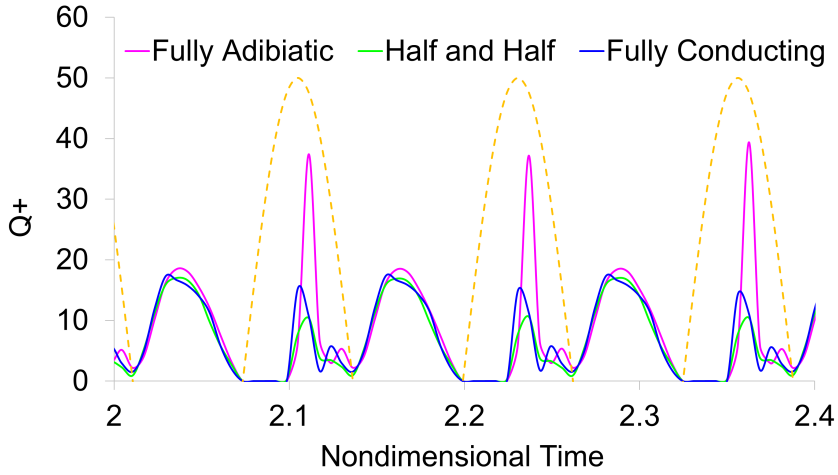

Figure 7.9: Evolution of Q^+ over time for the case Pr=7, $Ra_\omega = 8.34 \times 10^4$, $\Omega = 50$, $\gamma = 1.68 \times 10^7$, $St = 1.25 \times 10^{-5}$ for all three boundary conditions for the case $\xi = 0.3$. The yellow dashed line represents the acceleration applied to the cavity for the given non-dimensional frequency $\Omega = 50$.

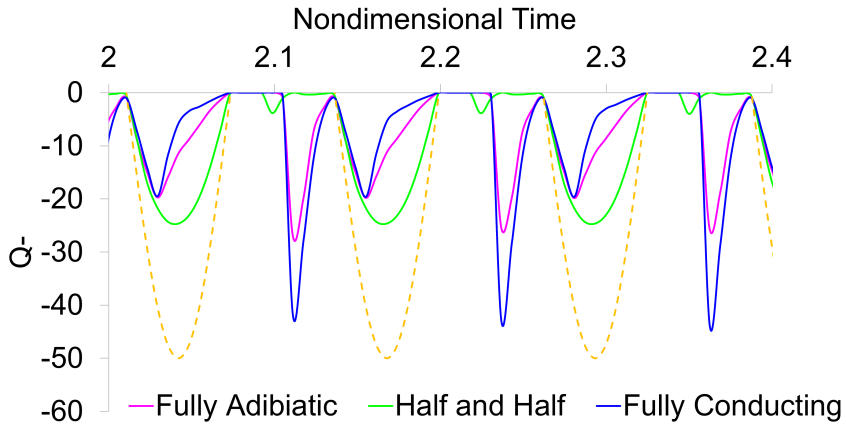

Figure 7.10: Evolution of Q^- over time for the case Pr=7, $Ra_\omega = 8.34 \times 10^4$, $\Omega = 50$, $\gamma = 1.68 \times 10^7$, $St = 1.25 \times 10^{-5}$ for all three boundary conditions for the case $\xi = 1.85$. The yellow dashed line represents the acceleration applied to the cavity for the given non-dimensional frequency $\Omega = 50$.

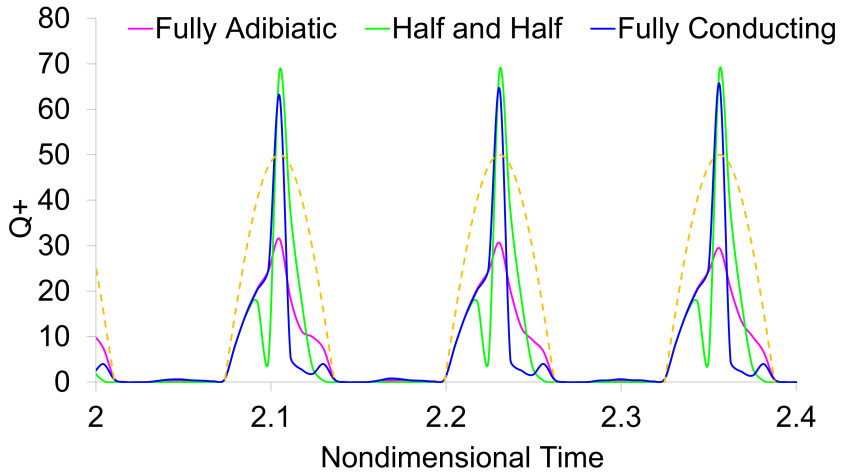

Figure 7.11: Evolution of Q^+ over time for the case Pr=7, $Ra_\omega = 8.34 \times 10^4$, $\Omega = 50$, $\gamma = 1.68 \times 10^7$, $St = 1.25 \times 10^{-5}$ for all three boundary conditions for the case $\xi = 1.85$. The yellow dashed line represents the acceleration applied to the cavity for the given non-dimensional frequency $\Omega = 50$.

At first glance, the behaviour of Q (both Q^- and Q^+) is periodic for all four scenarios. Indeed, apparently the particles closely follow the convective burst that occurs for this specific type of thermovibrational convection within the range of considered parameters. Purely fluid-dynamic aspects and related patterning behaviours have already

been described by Crewdson and Lappa [126] and such a treatment is not duplicated here for the sake of brevity. In order to interpret properly the corresponding dynamics in terms of solid mass displacement it can be recalled that the fluid response is of type SY-P [36, 125], i.e., the fluid flow is both synchronous and periodic with respect to the external forcing (the vibrations). More specifically, the fluid remains in almost quiescent conditions over a certain portion of the vibration period (the so-called "resting" or "frozen" state) and it is then disturbed by a convective burst, characterized by a 'peak' in terms of vertical (along y) fluid velocity. An example of these events is presented in Fig.7.12 where the yellow dashed line represents the acceleration applied to the cavity.

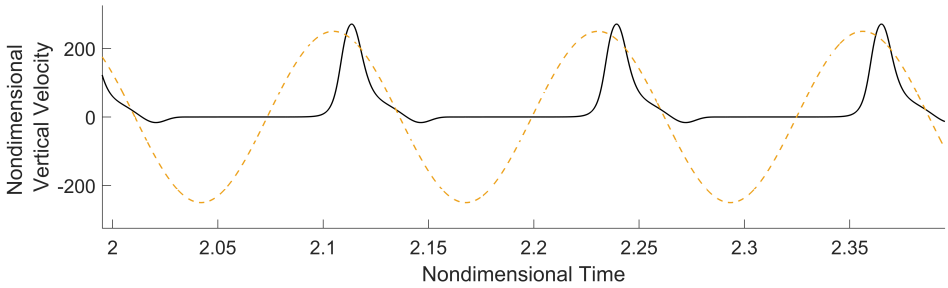

Figure 7.12: Non dimensional vertical velocity (Uy) for the case where all side walls are adiabatic for the case Pr=7, $Ra_\omega = 8.34\times10^4$, $\Omega = 50$, $\gamma = 1.68\times10^7$, $St = 1.25\times10^{-5}$ for all three boundary conditions for the case $\xi = 1.85$. The yellow dashed line represents the acceleration applied to the cavity for the given non-dimensional frequency $\Omega = 50$.

A first glimpse into the ensemble particle dynamics can be obtained by comparing the behavior of the light particles in Fig.7.8 and 7.9. It can be seen that negative and positive peaks occur for both Q^- and Q^+, respectively at approximately the same time in the period for all three boundary conditions. At first, this may seem counter-intuitive as the particles should either rise or fall depending on the direction of the vibration (i.e. if $Q^+ = 0$ then $Q^- < 0$ and if $Q^+ > 0$ then $Q^- = 0$). However, this observation should be taken as a cue to recall an important concept, namely, that given the presence of convection, particles do not simply travel in a rectilinear fashion as they would do in a quiescent fluid under the effect of vibrations. Rather, they interact with the carrier flow [1, 71]. In these studies, it has been shown that these connective bursts often lead to the formation of single or multiple competing rolls in the fluid, with parcels of fluid

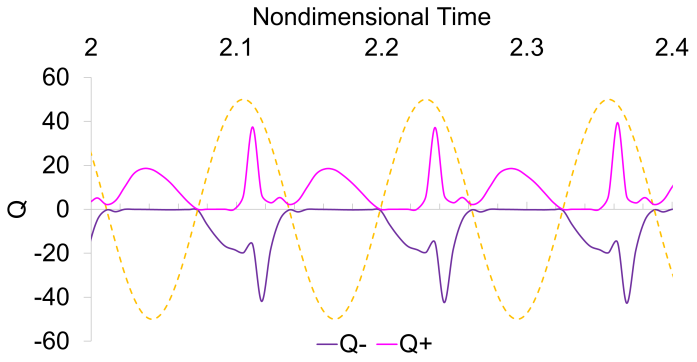

Figure 7.13: Evolution of Q^- and Q^+ over time for the case Pr=7, $Ra_\omega = 8.34 \times 10^4$, $\Omega = 50$, $\gamma = 1.68 \times 10^7$, $St = 1.25 \times 10^{-5}$ for the case where all side walls are adiabatic. The yellow dashed line represents the acceleration applied to the cavity for the given non-dimensional frequency $\Omega = 50$.

travelling in certain directions depending on their location in the cavity. When particles are added to these fluid systems, they are transported either up or down, depending on their location in the cavity, which explains why Q^- and Q^+ experience concurrent signal peaks (see Fig.7.13).

At this stage, the comparison of Figure Fig.7.8 and Fig.7.9,and the peaks experienced by Q^+ and Q^- can be made, leads to the straightforward identification of a set of general rules or predictive links by which the outcomes in terms of Q behaviour can be connected to the slope (ψ) of the acceleration $g(t)$ applied to the cavity for each particle density. These laws, summarized below, hold true for all three thermal boundary conditions.

For light particles ($\xi = 0.3$):

$$\begin{aligned}
&\text{For } \psi > 0 \text{ and } g(t) < 0, Q^- = 0 \text{ and } Q^+ > 0 \\
&\text{For } \psi > 0 \text{ and } g(t) > 0, Q^- < 0 \text{ and } Q^+ = 0 \\
&\text{For } \psi < 0 \text{ and } g(t) > 0, Q^- < 0 \text{ and } Q^+ > 0 \\
&\text{For } \psi < 0 \text{ and } g(t) < 0, Q^- = 0 \text{ and } Q^+ > 0
\end{aligned} \tag{7.3}$$

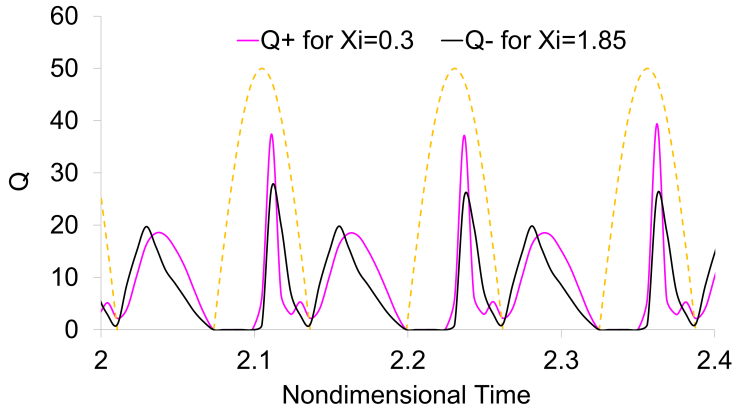

Figure 7.14: Evolution of Q^+ and Q^- for $\xi = 1.85$ (black) $\xi = 0.3$ (magenta) over time for the case Pr=7, $Ra_\omega = 8.34 \times 10^4$, $\Omega = 50$, $\gamma = 1.68 \times 10^7$, $St = 1.25 \times 10^{-5}$ for the case where all side walls are adiabatic. The yellow dashed line represents the acceleration applied to the cavity for the given non-dimensional frequency $\Omega = 50$.

For heavy particles ($\xi = 1.85$):

$$\begin{aligned} &\text{For } \psi > 0 \text{ and } g(t) < 0, Q^- > 0 \text{ and } Q^+ = 0 \\ &\text{For } \psi > 0 \text{ and } g(t) > 0, Q^- = 0 \text{ and } Q^+ > 0 \\ &\text{For } \psi < 0 \text{ and } g(t) > 0, Q^- < 0 \text{ and } Q^+ > 0 \\ &\text{For } \psi < 0 \text{ and } g(t) < 0, Q^- < 0 \text{ and } Q^+ > 0 \end{aligned} \tag{7.4}$$

Another key observation concerns the similarities appearing between the responses of Q^+ for $\xi = 0.3$ and Q^- for $\xi = 1.85$ (Fig.7.9 and Fig.7.10 respectively), and between Q^- for $\xi = 0.3$ and Q^+ for $\xi = 1.85$ (Fig.7.8 and Fig.7.11). An explanation/justification for this trend can be elaborated in its simplest form on the basis of the argument that the light and heavy particles are expected to behave in a quasi-polar opposite manner. This affinity is captured in Fig.7.14, where Q^+ for $\xi = 0.3$ and Q^- for $\xi = 1.85$ are superimposed for the case where all side walls are adiabatic. A similar agreement is found for the signals of Q^- for $\xi = 0.3$ and Q^+ for $\xi = 1.85$ (not shown).

On a separate note, it is also worth highlighting that although the trends for the different boundary conditions are relatively similar, some interesting differences can be spotted. Further inspection of Figs.7.8 to 7.11 is useful in this regard (in pink: fully

adiabatic side walls, in green: both side walls are perfectly conducting and the from and back walls are adiabatic and, in blue all side walls perfectly conducting). The first discrepancy concerns the case where the two side walls are conducting and the front and back are adiabatic. In such a case, there is little to no negative particle momentum (Q^-) when the heavy particles are considered for $\psi < 0$ and $g(t) > 0$. When recalling the similarities between Q^- for $\xi = 1.85$ and Q^+ for $\xi = 0.3$, the positive momentum for the case Q^+ for $\xi = 0.3$ for $\psi < 0$ and $g(t) > 0$, is also much lower than for the other two cases of differing thermal boundary conditions. The reason for such a behaviour resides in the fact that, as shown by previous work, Crewdson & Lappa [126], for this range of parameters and thermal boundary conditions, the flow is more stable than for the case where all walls are set to either adiabatic or conducting. Although the flow still undergoes a convective burst at a given point in the period, the patterning behaviour of the fluid during the resting configuration (i.e., when the fluid is quasi-stationary and the fluid velocity is close to zero), does not contain as many rolls as in the other cases. During this resting configuration, no toroidal rolls are visible as the structure simply reduces to a planar extension of the so-called 2D quadrupolar field.

A comparison is now made between the maximum absolute values of Q^- and Q^+ for each case. Starting with the negative particle momentum (Q-) (see Fig,7.15), for the case where light particles are considered ($\xi = 0.3$), it can be seen that all three boundary conditions return a similar maximum value of $|Q^-|$, whereas, for the heavy particles, the value of $|Q^-|$, is much higher for the case where all side walls are conducting.

Looking, at the positive particle momentum (Q^+, see Fig.7.16), the difference in maximum values of $|Q^+|$, are more pronounced, both when the particle density and the boundary conditions are changed. Particularly, the maximum negative momentum of the light particles is much lower than for the heavy particles for the cases where the side walls are conducting, and the front and back walls of the cavity are adiabatic and for the case where all side walls are conducting.

From this in-depth, quantitative analysis of the general behaviour of the particles dispersed in each of the three systems, some general conclusions can be drawn. Firstly, the particles structures are disturbed periodically and synchronously with respect to

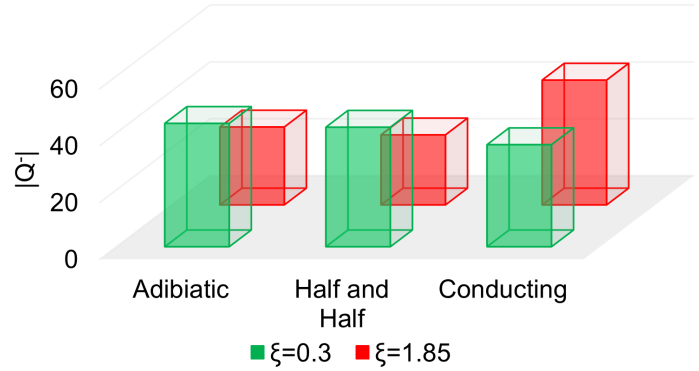

Figure 7.15: Maximum absolute values of Q^- for the case Pr=7, $Ra_\omega = 8.34 \times 10^4$, $\Omega = 50$, $\gamma = 1.68 \times 10^7$, $St = 1.25 \times 10^{-5}$ for all three boundary conditions.

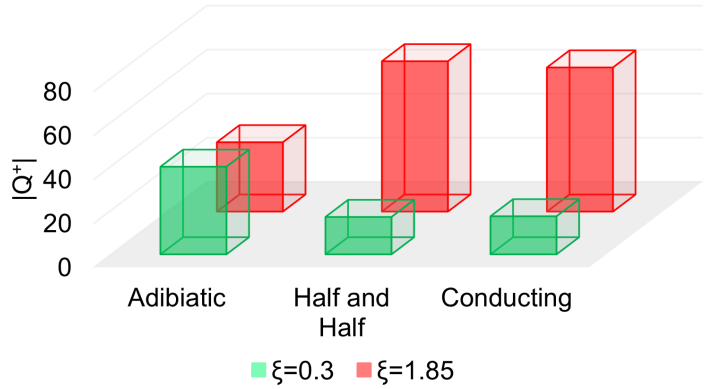

Figure 7.16: Maximum absolute values of Q^+ for the case Pr=7, $Ra_\omega = 8.34 \times 10^4$, $\Omega = 50$, $\gamma = 1.68 \times 10^7$, $St = 1.25 \times 10^{-5}$ for all three boundary conditions.

the forcing frequency applied to the system. The only exception is the hybrid ('half and half)' case, owing to the inherent stability of the fluid flow. Secondly, the overall momentum of the light particles and the heavy particles behaves similarly when the negative momentum of one is compared to the positive momentum of the other. This however does not translate to a similarity in maximum momentum amplitude. An interpretation of this specific aspect is not as straightforward as one would assume and

requires a detailed analysis of the particle spatio-temporal evolution and patterning behaviour, which is elaborated in the next section.

7.5.2 Temporal evolution of particle structures

Given the similarities in the system evolution (when different thermal boundary conditions are considered) described in the earlier section, without loss of generality here the treatment is limited for brevity to the case with conducting sidewalls. The first figure of the sequence (Fig.7.17) is instructive as it shows that in the time interval from $t = 0.640$ to $t = 0.690$, the particles distribution evolves from a scenario where it fully occupies the entire cavity space to one where the structure is compressed in the negative y direction, until a stage is attained where all particles lie on the bottom of the cavity. This compression occurs when the acceleration $g(t)$ is positive ($\psi < 0$). In this time frame, the velocity of the fluid is relatively small in the entire cavity (the aforementioned 'resting phase' of period). In the next 5 instances, from t=0.703 to t=0.754, the fluid transitions from an upwards motion ($\psi > 0$) to a downwards one where the slope of $g(t)$ becomes negative ($\psi < 0$). This change in the acceleration direction results in the particles detaching from the bottom wall and traveling upwards. In the snapshots pertaining to t=0.703 and t=0.716, the layer of particles travels up following this detachment, until the time t=0.728, where the layer is disrupted by the convective burst of the carrier fluid. During this convective burst, as demonstrated in the authors previous research [126], the fluid undergoes a series of complex textural transitions leading to a corresponding change in the particles distribution structure. Finally, at t =0.754 the fluid returns to its resting configuration and the same concept applies to the particles distribution.

Figure 7.17 is naturally complemented by Fig.7.18, where the fluid and system properties remain the same and the light particles are considered. In these circumstances, as expected, the particles behave in the opposite way with respect to the heavy case. The structure is compressed in the positive y direction when the slope of the acceleration $g(t)$ is positive ($\psi < 0$) and migrate in the negative y direction when the slope becomes negative. As an appreciable distinguishing mark, however, the distribution of

solid matter is not compressed along the wall as much as their heavy counterparts. This confirms that the particle density does play a role in the compressibility of the particle velocity field (at this stage it should also be recalled that the carrier flow underpinning the particle dynamics shown in Figs.7.17 and 7.18 is exactly the same and it is not affected by dispersed solid mass in the frame of a one-way coupling approach, which supports the straightforward conclusion that the visible differences relate only to the properties of the particles and their transport mechanisms).

To consolidate the idea that the convective burst and its related textural transitions ultimately dictate the resting configuration of the particles distribution, the next figure of the sequence (Fig.7.19) shows the change in the particle distribution and the related flow states associated with the convective burst.

Having completed a description of the particle patterning behaviour for a representative case, the next section is finally devoted to an assessment of the differences in structure morphologies obtained when the thermal boundary conditions are varied.

7.5.3 Morphological dependence of the PAS on imposed thermal boundary conditions

Selected examples of the 3D dynamics obtained with different thermal boundary conditions are collected in Figs. 7.20-7.28. In particular, one snapshot is reported for each case at the time after the convective burst occurs, i.e., when the 'frozen' configuration is entered. Starting with the thermal configuration where all the side walls are adiabatic, Fig.7.20 refers to the light particles case ($\xi = 0.3$).

By providing a good impression of the overall three-dimensional distribution of dispersed solid mass, this figure is instrumental in showing that the related morphology takes on a mushroom-like configuration, where two bulk structures are visible. The two lobes are almost perfectly symmetrical about the mid-plane of the x and the z axis and are separated by a region of clear (particle-free) fluid located at the mid plane of the x axis.

Additional insights follow naturally from a comparison of Fig.7.20 for $\xi = 0.3$ and Fig.7.21 for $\xi = 1.85$. The space configuration of the particle structures is similar.

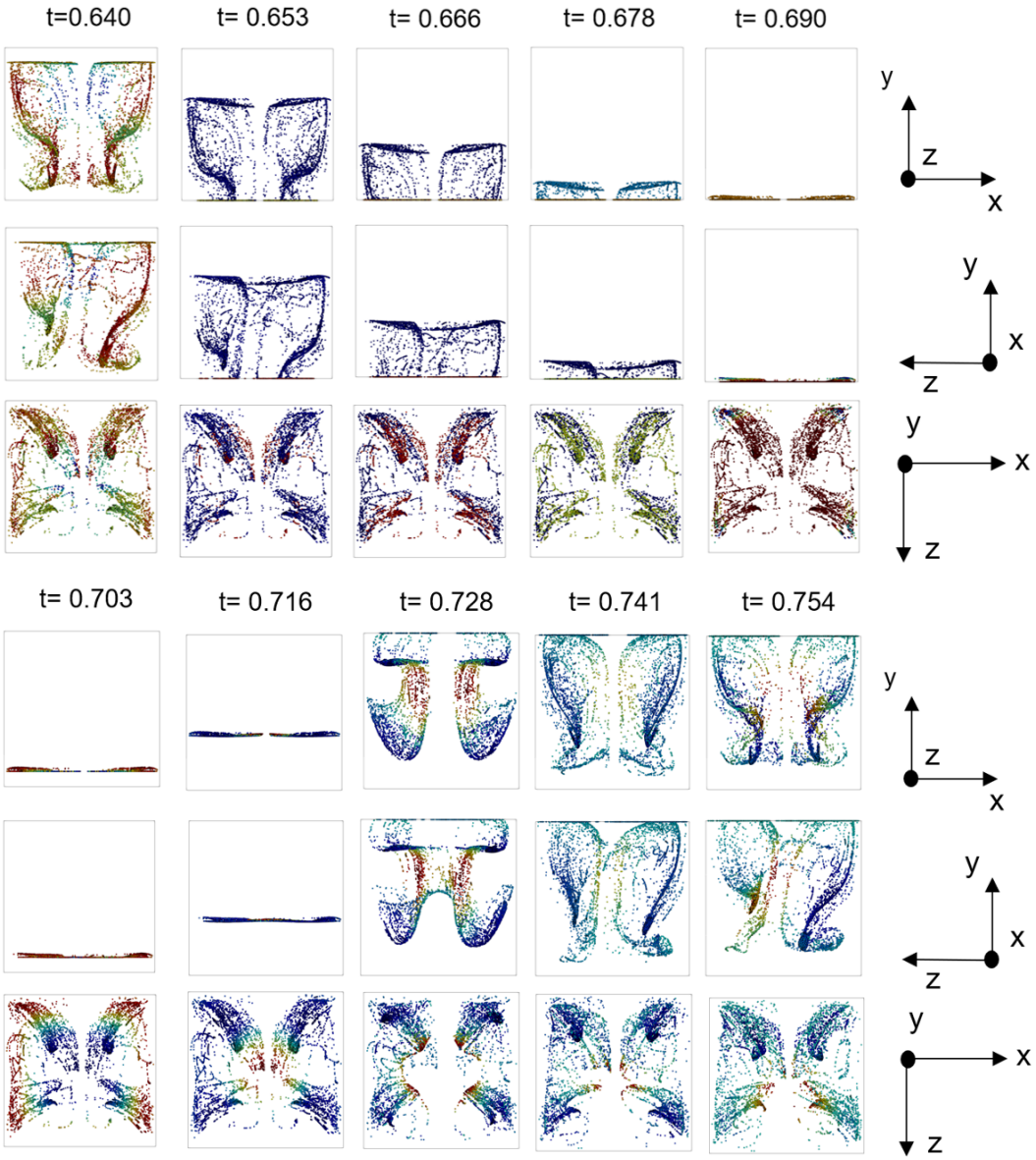

Figure 7.17: Temporal evolution of the particle accumulation structure (PAS) over one vibrational period for the case $Pr = 7$, $Ra_\omega = 8.34 \times 10^4$, $\Omega = 50$, $\gamma = 1.68 \times 10^7$, $St = 1.25 \times 10^{-5}$ where all walls are fully conducting and $\xi = 1.85$, where t is the non-dimensional time and the vibrational period is divided into 10 equally spaced snapshots. The blue colour indicates a low vertical velocity and the red colour a high vertical velocity.

However, in the latter case, the area occupied by the particles within the cavity is much larger and its shape is more defined or recognizable. For the convenience of the reader, a direct superposition of these particle formations is presented in Fig.7.22.

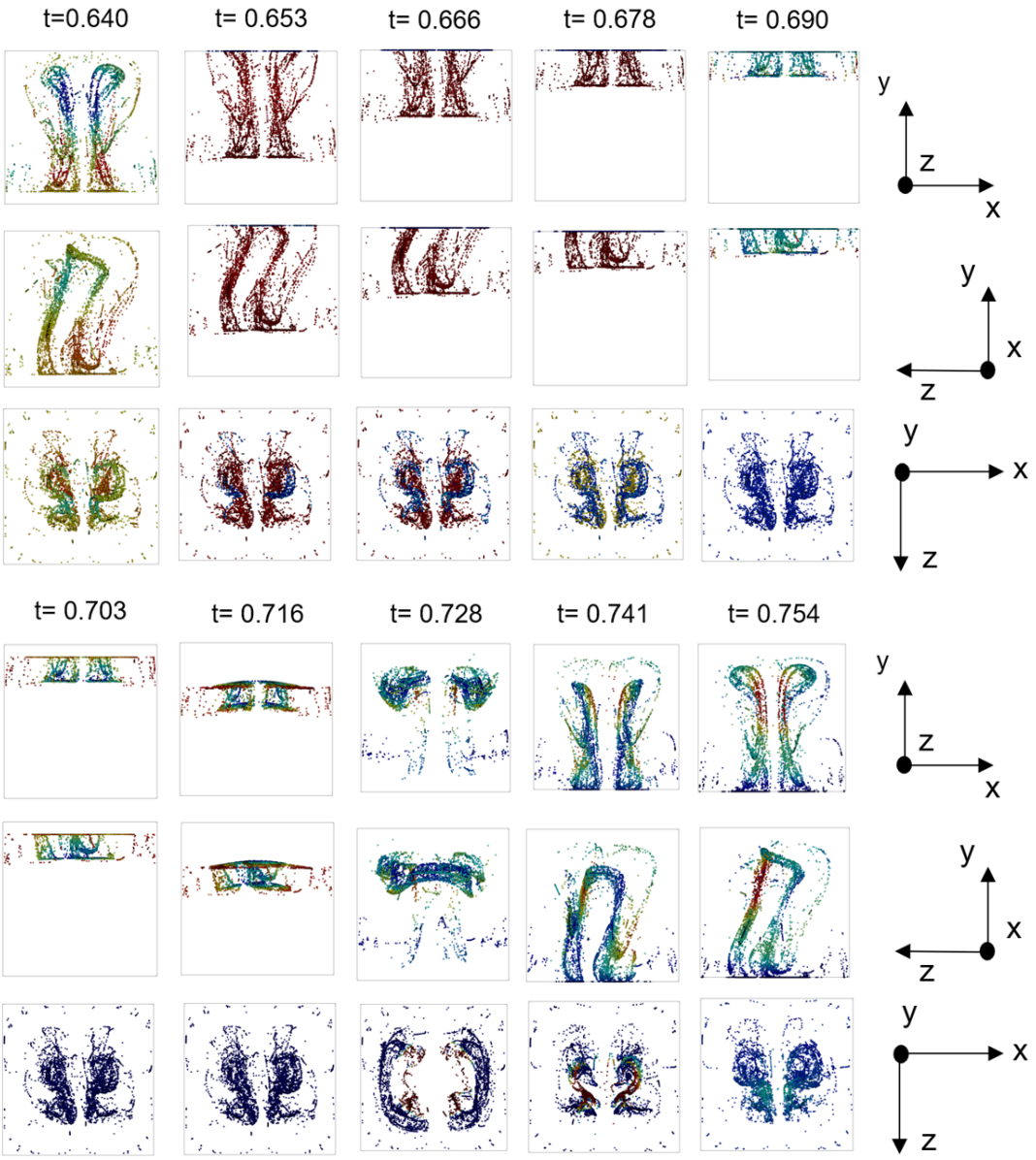

Figure 7.18: Temporal evolution of the particle accumulation structure (PAS) over one vibrational period for the case $Pr = 7$, $Ra_\omega = 8.34 \times 10^4$, $\Omega = 50$, $\gamma = 1.68 \times 10^7$, $St = 1.25 \times 10^{-5}$ where all walls are fully conducting and $\xi = 0.3$, where t is the non-dimensional time and the vibrational period is divided into 10 equally spaced snapshots. The blue colour indicates a low vertical velocity and the red colour a high vertical velocity (continued from Fig.7.17).

The next set of figures of the sequence illustrate the situation where two opposing side walls of the cavity are perfectly conducting, while the other two walls are adiabatic.

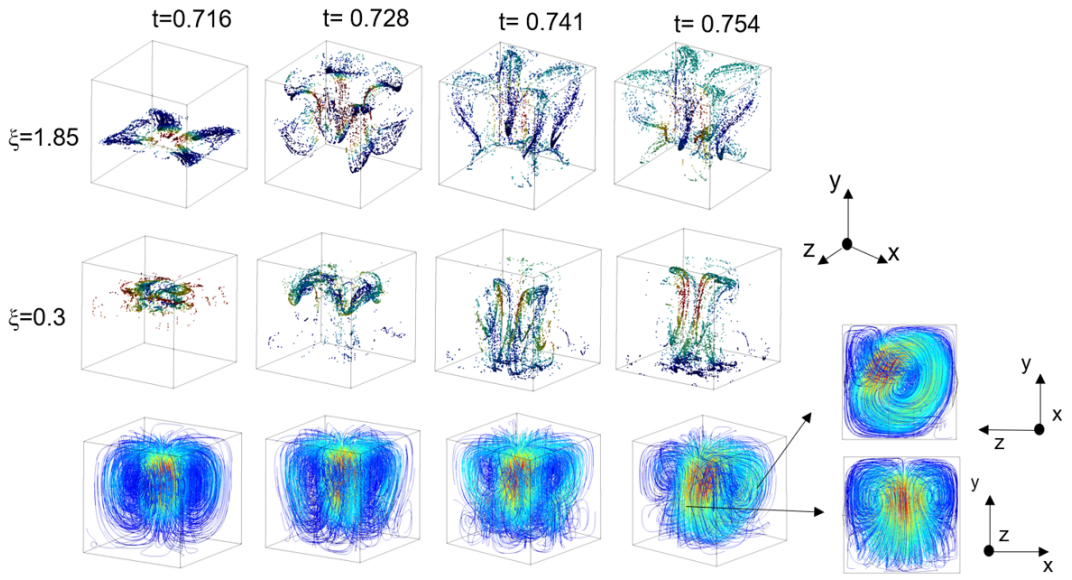

Figure 7.19: Temporal evolution of the particle accumulation structure (PAS) for both heavy ($\xi = 1.85$, top) and the light ($\xi = 0.3$, bottom) particles and the fluid structure (streamlines) during the convective burst for the case $Pr = 7$, $Ra_\omega = 8.34 \times 10^4$, $\Omega = 50$, $\gamma = 1.68 \times 10^7$, $St = 1.25 \times 10^{-5}$ where all walls are fully conducting, where t is the non-dimensional time. The blue colour indicates a low vertical velocity and the red colour a high vertical velocity.

In particular, Figs.7.23 and Fig.7.24 deal with the density ratios $\xi = 0.3$ and $\xi = 1.85$, respectively. Taken together (the reader being also referred to the direct cross-comparison implemented in Fig.7.25), these snapshots indicate that the formation in the heavy particle case is much more compact than the other. Both are much more symmetrical than those seen in the adiabatic wall case.

As a concluding step of such a logical sequence, a description of the corresponding dynamics for the configuration where all side walls are conducting is needed. Along these lines, Fig.7.26, shows the pattern for the light particles. Two lobes, symmetrical about the mid planes of the x and z axis, are visible and occupy the top section of the cavity where a concave morphology is observed on their undersides. Similarly to the case where all side walls are adiabatic, a slight asymmetry is visible about both mid planes of the x and z axis. This becomes evident when looking at the top view in Fig.7.26.

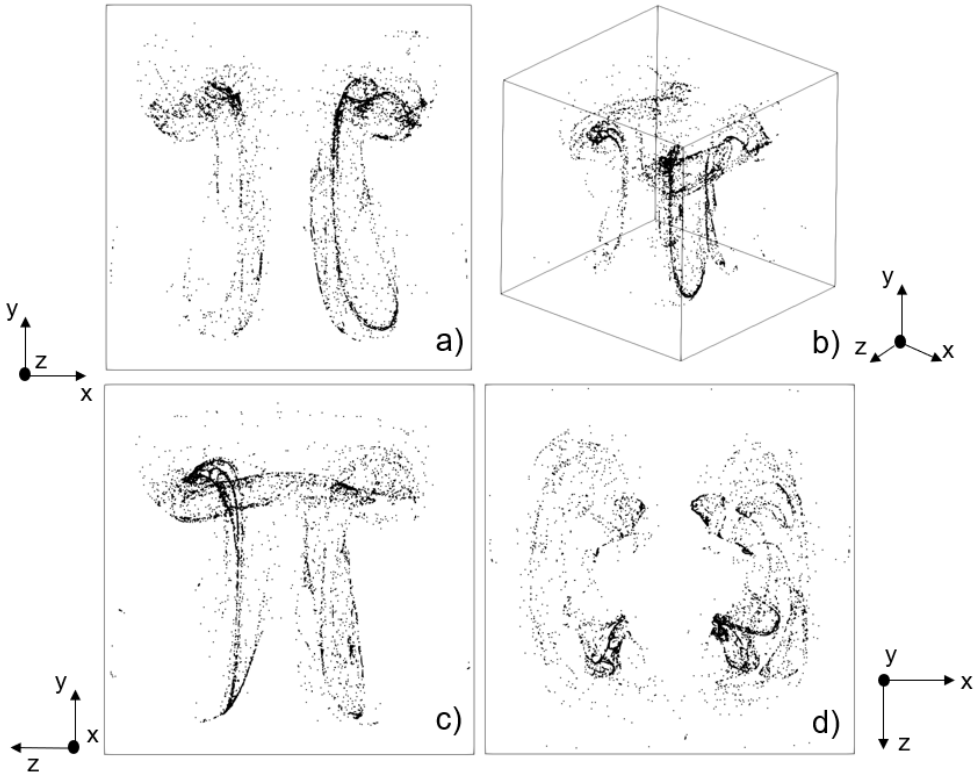

Figure 7.20: Particle morphology for the case of fully adiabatic side walls and $Pr = 7$, $Ra_\omega = 8.34 \times 10^4$, $\Omega = 50$, $\gamma = 1.68 \times 10^7$, $St = 1.25 \times 10^{-5}$ and $\xi = 0.3$ t=2.364.

To complement this scenario with additional relevant data, assessment of the formations visible in Fig. 7.22 against those revealed by Fig. 7.28 (dealing with the situations where walls are fully adiabatic and fully conductive respectively) leads to another key realization, namely, it provides evidence for the more symmetric nature of the particles distribution shown in red in Fig.7.28 (side view). When the light particles are considered (green symbols), the main dissimilarity concerns the extension of the formations in the -y direction. Indeed, for the case with the adiabatic walls, the aforementioned mushroom structure is visible, whereas for the companion situation where all walls are conducting, the fingerprint of the particle structure is its compact nature and the tendency of all particles to reside in the top half on the cavity.

A further understanding or meaningful classification of all these modes of particle clustering can be gained by distilling out their main features through a focused analysis of the 3D surfaces where the highest concentration of particles is attained (or, in

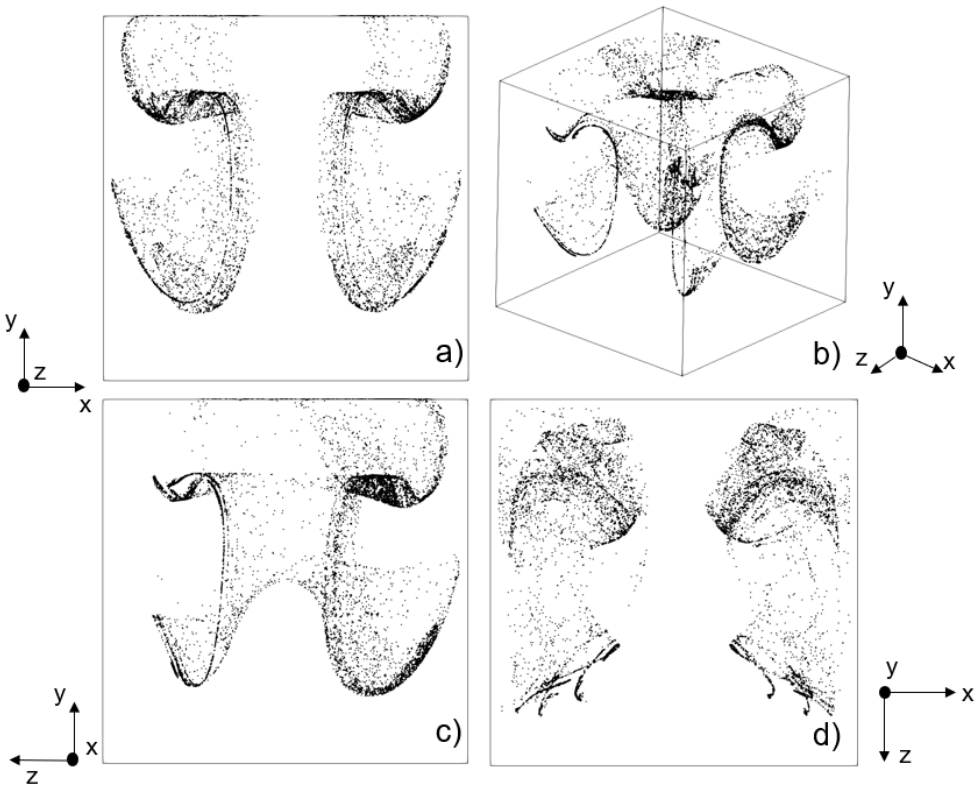

Figure 7.21: Particle morphology for the case of fully adiabatic side walls and $Pr = 7$, $Ra_\omega = 8.34 \times 10^4$, $\Omega = 50$, $\gamma = 1.68 \times 10^7$, $St = 1.25 \times 10^{-5}$ and $\xi = 1.85$ t=2.364.

an equivalent way, by considering the topology of the lines obtained by cutting such surfaces with specific planes). Such an attempt is implemented in Fig.7.29, where the topology of these lines is reported in the xy plane . Interestingly, for the heavy particles (left panel), a good degree of symmetry can be seen for all three variants of thermal boundary conditions, with the differences between the cases of the fully conducting and fully adiabatic walls being minimal (the distribution for the fully conducting case, however, being more compressed in the top section of the cavity). For the light particles, some breakdown in the symmetry become appreciable for the fully adiabatic and fully conducting walls. Regardless of the particle density, highly ordered symmetrical particles distributions emerge for the hybrid boundary thermal conditions (as also witnessed by Fig.7.23 to 7.25).

[htb!]

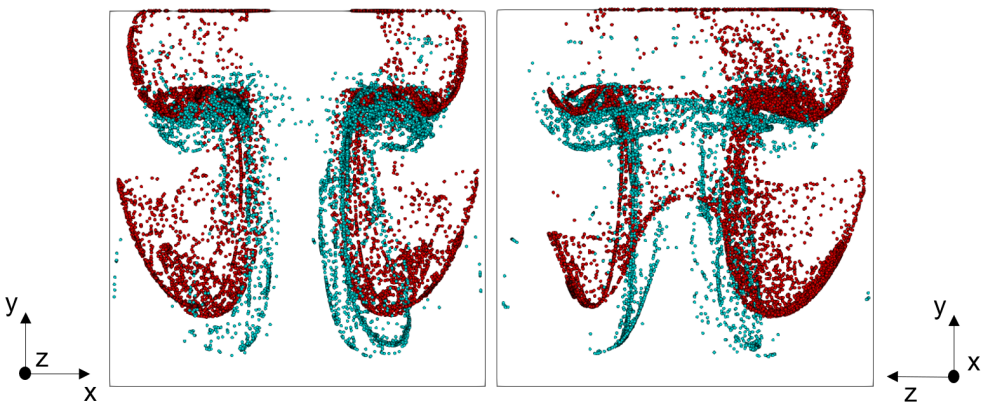

Figure 7.22: Superposition of the PAS for cases $\xi = 0.3$ (in blue) and $\xi = 1.85$ (in red) for the case of fully adiabatic side walls and $Pr = 7$, $Ra_\omega = 8.34 \times 10^4$, $\Omega = 50$, $\gamma = 1.68 \times 10^7$, $St = 1.25 \times 10^{-5}$ and $\xi = 1.85$ t=2.364.

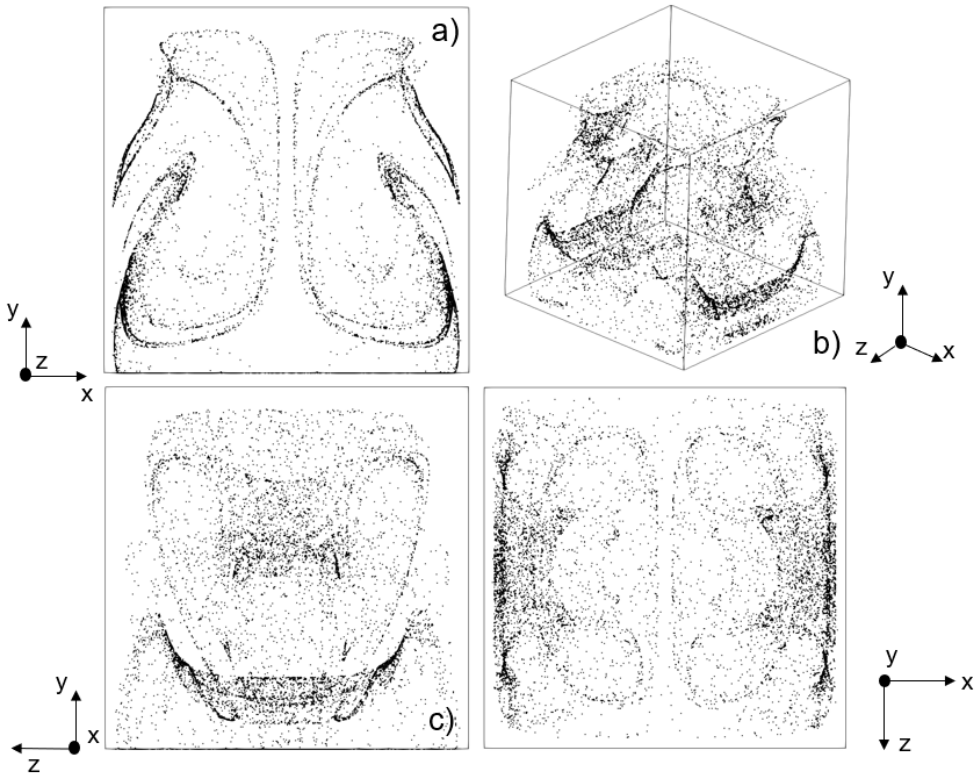

Figure 7.23: Particle morphology for the case of conducting side walls and adiabatic front and back walls and $Pr = 7$, $Ra_\omega = 8.34 \times 10^4$, $\Omega = 50$, $\gamma = 1.68 \times 10^7$, $St = 1.25 \times 10^{-5}$ and $\xi = 0.3$ at t=2.364.

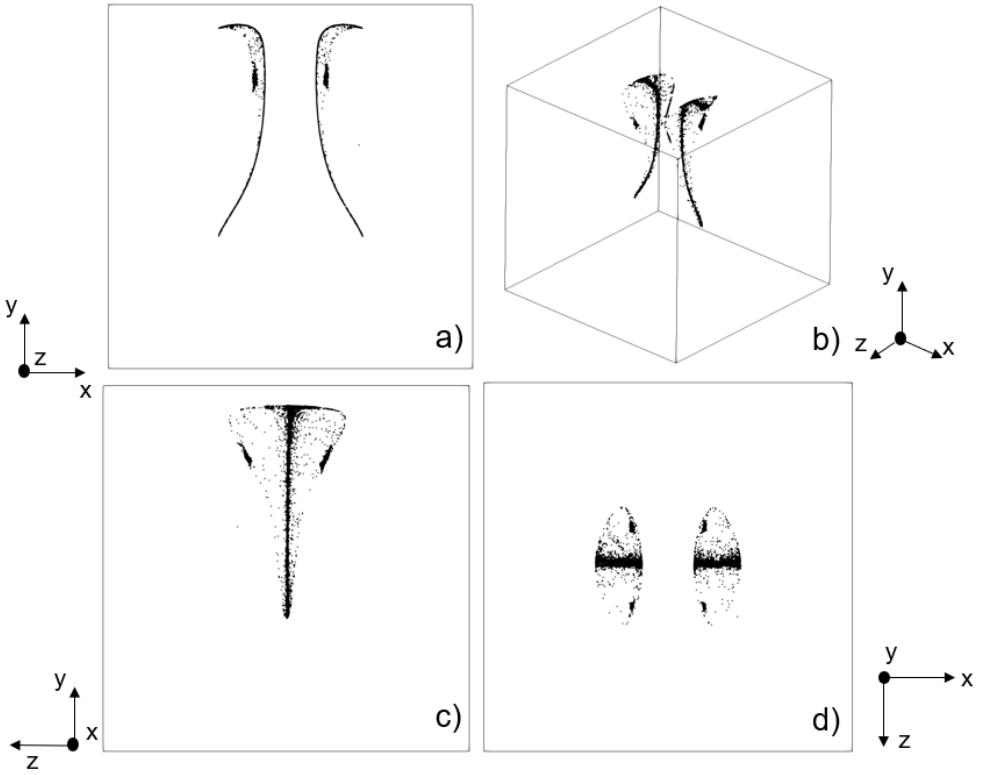

Figure 7.24: Particle morphology for the case of conducting side walls and adiabatic front and back walls and Pr=7 $Pr = 7$,, $Ra_\omega = 8.34 \times 10^4$, $\Omega = 50$, $\gamma = 1.68 \times 10^7$, $St = 1.25 \times 10^{-5}$ and $\xi = 1.85$ at t=2.364.

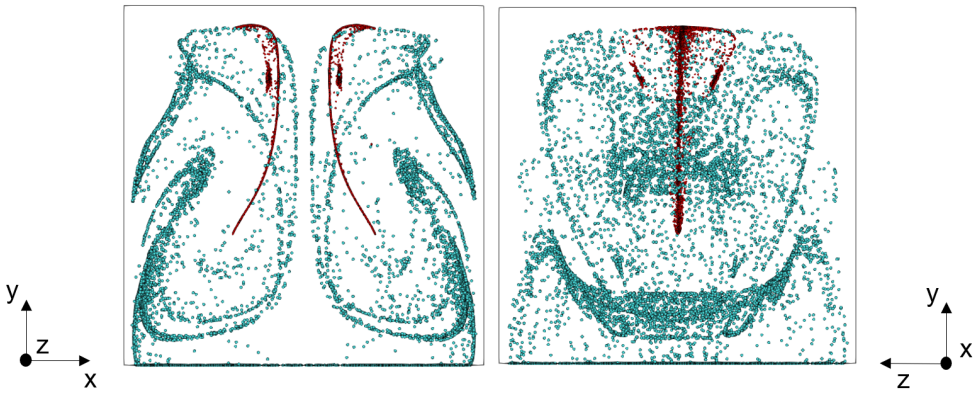

Figure 7.25: Superposition of the PAS for cases $\xi = 0.3$ (in blue) and $\xi = 1.85$ (in red) for the case of conducting side walls and adiabatic front and back walls and $Pr = 7$, $Ra_\omega = 8.34 \times 10^4$, $\Omega = 50$, $\gamma = 1.68 \times 10^7$, $St = 1.25 \times 10^{-5}$ at t=2.364.

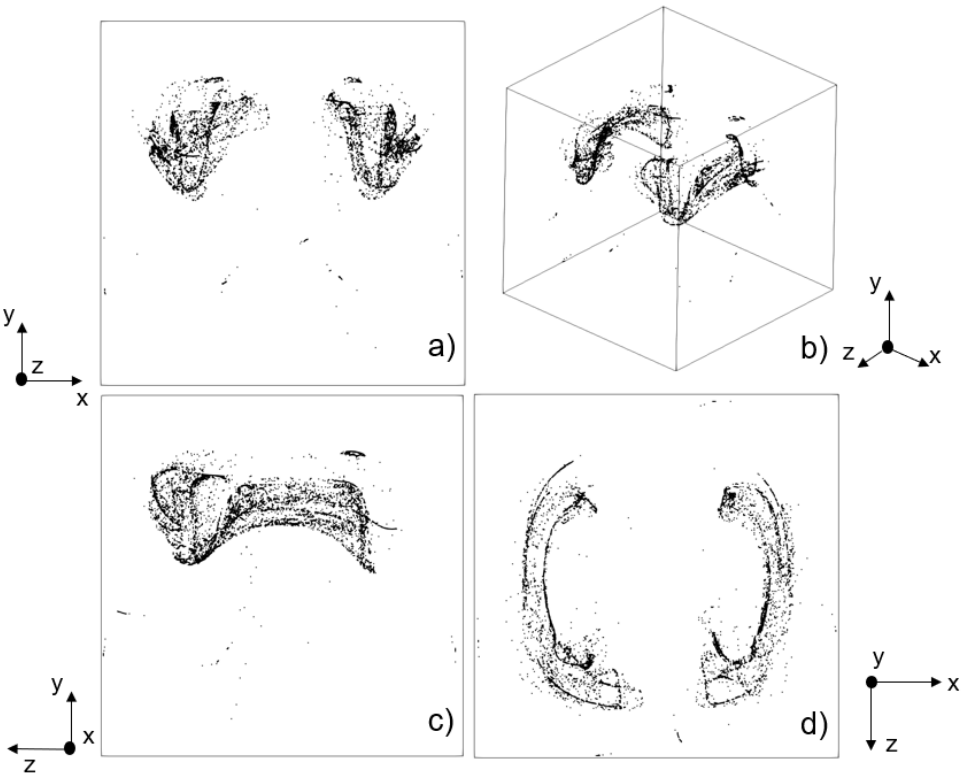

Figure 7.26: Particle morphology for the case of fully conducting side walls and $Pr = 7$, $Ra_\omega = 8.34 \times 10^4$, $\Omega = 50$, $\gamma = 1.68 \times 10^7$, $St = 1.25 \times 10^{-5}$ and $\xi = 0.3$ at t=2.364

Following up on the previous point, it is worth highlighting that, for the heavy particles, the ability of the distribution to protrude into the upper part of the cavity in the adiabatic wall case is due to a bulge in the structure (Fig.7.30, left panel). This patch is located near the top and in proximity to the back wall (z=0) of the cavity. For the fully conducting walls case, again the side view (Fig.7.30) reveals that the structure is slightly deformed at the rear section of the cavity, whereas for the hybrid case, symmetry is conserved within the particles distribution. Figures 7.29 and 7.30 are naturally complemented by Fig. 7.31, where the top views of the particles distribution are provided. Looking first at the pattern for$\xi = 1.85$, symmetry about the z axis at the mid x plane is achieved for all three boundary conditions. For $\xi = 0.3$, slight deviations from perfect symmetry can be noticed (except for the hybrid configuration, as already pointed out before).

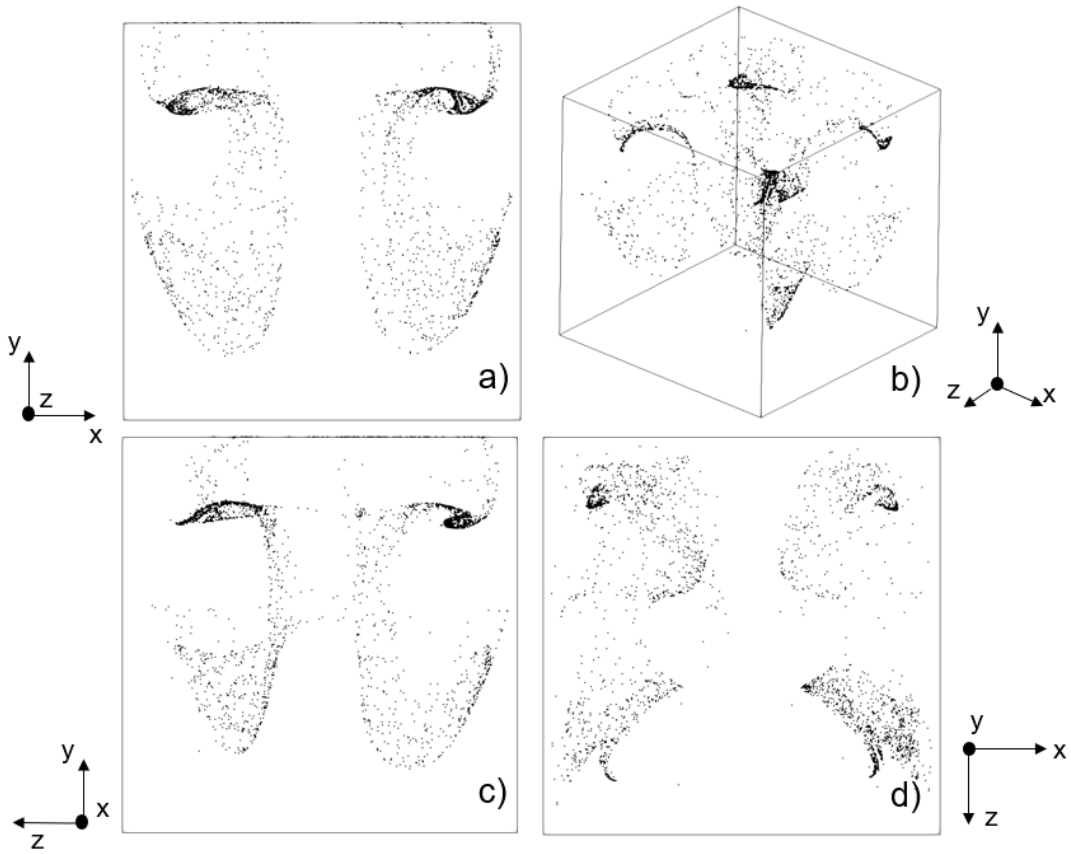

Figure 7.27: Particle morphology for the case of fully conducting side walls and $Pr = 7$, $Ra_\omega = 8.34 \times 10^4$, $\Omega = 50$, $\gamma = 1.68 \times 10^7$, $St = 1.25 \times 10^{-5}$ and $\xi = 1.85$ t=2.364

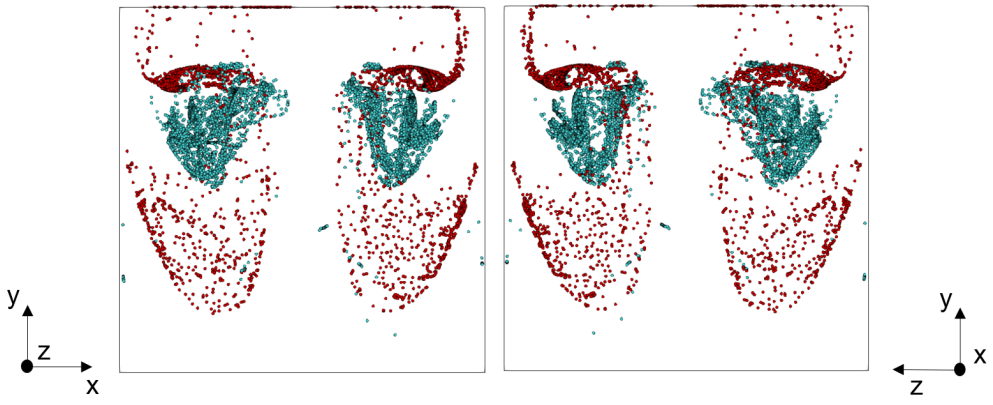

Figure 7.28: Superposition of the PAS for cases $\xi = 0.3$ (in blue) and $\xi = 1.85$ (in red) for the case of fully conducting walls and $Pr = 7$,, $Ra_\omega = 8.34 \times 10^4$, $\Omega = 50$, $\gamma = 1.68 \times 10^7$, $St = 1.25 \times 10^{-5}$ at t=2.364.

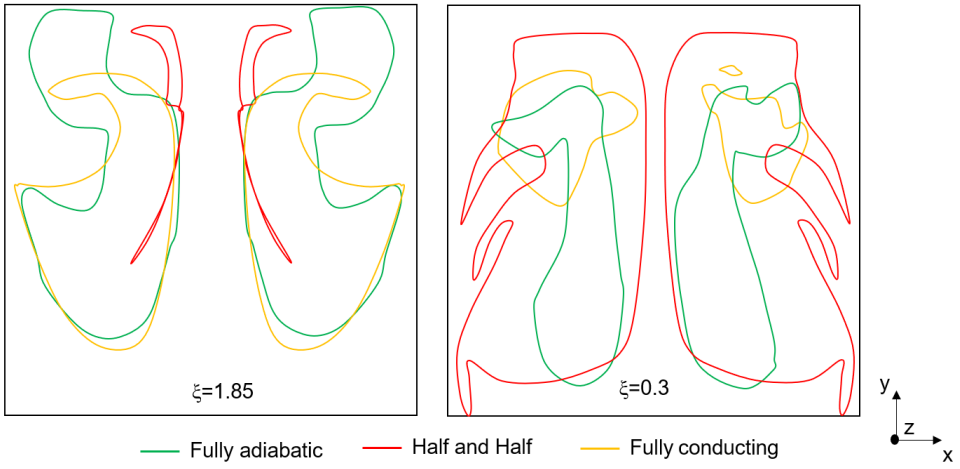

Figure 7.29: Superposition of the outline of the front view of the PAS for cases $\xi = 1.85$ (left) and $\xi = 0.3$ (right) for all three boundary conditions for the case $Pr = 7$, $Ra_\omega = 8.34 \times 10^4$, $\Omega = 50$, $\gamma = 1.68 \times 10^7$, $St = 1.25 \times 10^{-5}$ at t=2.364.

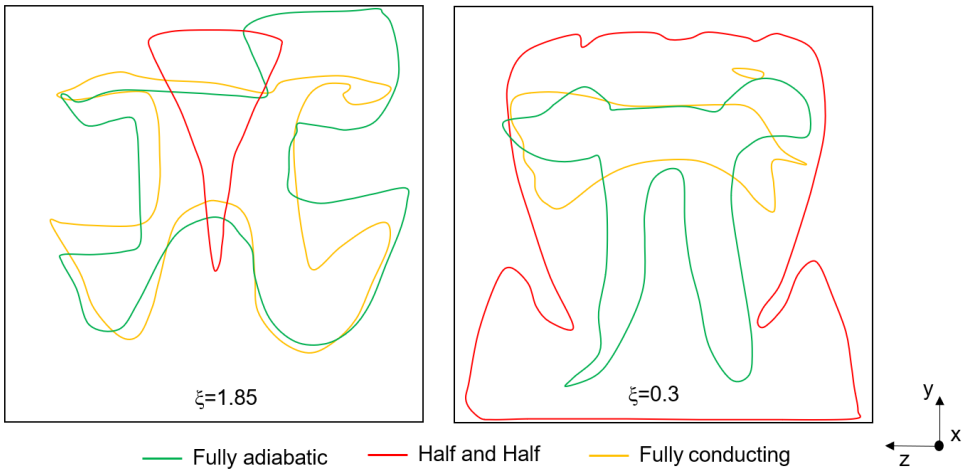

Figure 7.30: Superposition of the outline of the side view of the PAS for cases $\xi = 1.85$ (left) and $\xi = 0.3$ (right) for all three boundary conditions for the case $Pr = 7$, $Ra_\omega = 8.34 \times 10^4$, $\Omega = 50$, $\gamma = 1.68 \times 10^7$, $St = 1.25 \times 10^{-5}$ at t=2.364.

7.6 Conclusion

Through consideration of a situation as conceptually simple as that of a dilute distribution of solid finite-size (spherical) particles undergoing thermovibrational effects in a differentially heated cubic (three-dimensional) container, it has been shown that the

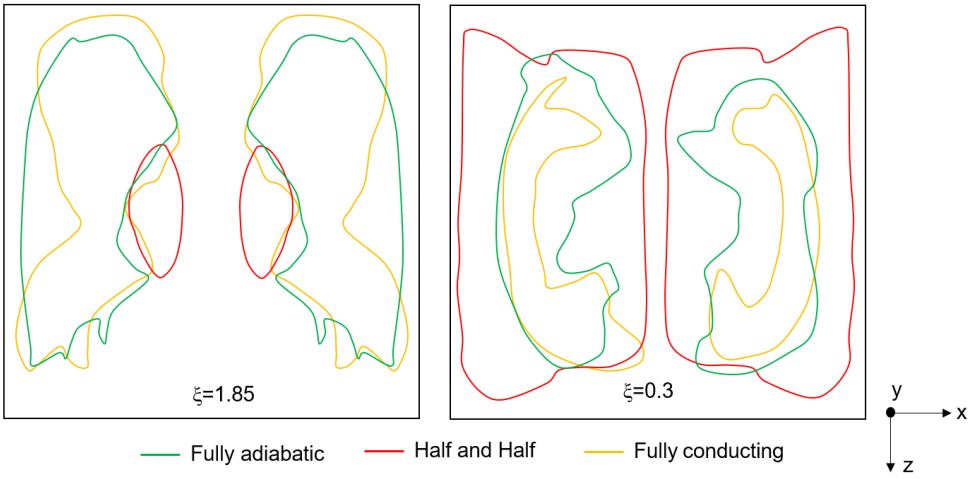

Figure 7.31: Superposition of the outline of the top view of the PAS for cases $\xi = 1.85$ (left) and $\xi = 0.3$ (right) for all three boundary conditions for the case $Pr = 7$, $Ra_\omega = 8.34 \times 10^4$, $\Omega = 50$, $\gamma = 1.68 \times 10^7$, $St = 1.25 \times 10^{-5}$ at t=2.364.

ability of this type of flow to support particle clustering phenomena is not an exclusive prerogative of systems where vibrations have a component acting in a direction perpendicular to the imposed (unidirectional) temperature gradient. Although the most common outcome of the configuration with vibrations perfectly parallel to the temperature gradient for relatively high values of the non-dimensional acceleration amplitude is a degenerate state in which all the dispersed solid mass accumulates in a perfectly planar surface that moves back and forth between the hot and cold sides of the cavity, specific conditions can be identified for which particles can be forced to demix from the liquid and give rise to structures with well-defined (non-trivial) morphological properties. These range from mushroom-like 3D surfaces to much more compact realizations depending on the particle-to-fluid density ratio and on the specific thermal boundary conditions implemented for the sidewalls of the enclosure. Such formations show up or exist as relatively stable entities during limited sub-intervals of the vibration period. First, the particles distribution is frozen in the cavity, then it is compressed to the bottom or top wall and then detaches when the cavity changes direction. As a convective burst occurs the 'flat' particles distribution is disrupted by the increase in the strength of the flow and then it regains its original 'frozen' configuration, thereby giving rise to an endless series of cycles where well-defined structures are continuously created and

destroyed. This confirms that the behavior of the particles distribution is synchronous and periodic (SY-P) in accordance with the regime associated with the carrier fluid. This transition of states is ubiquitous for all cases, irrespective of the thermal boundary conditions. Comparison with the companion category of particle attractors investigated by Lappa [1, 101, 132, 133], Lappa and Burel [71], Crewdson and Lappa [135] indicates that although these phenomena display some affinities in terms of driving forces or effects, notable dissimilarities exist. Both are driven by the joint action of thermovibrational convection and particle inertial effects. What sets the case with parallel vibrations apart from that with perpendicular ones resides essentially in the spatio-temporal nature of the phenomena and the specific relationships that is established between fluid motion and particle density-related effects. In the perpendicular case, particles clustering is a continuous process by which particles continuously demix from the fluid and accumulate along well-defined structures, which grow in time until an asymptotic state is attained in terms of shape and size. The related morphology depends essentially on the direction of vibrations with respect to the walls of the cubic cavity, possible shapes being paraboloids, conical surfaces, ellipsoids, cylinders, spheres etc. The related morphology can be considered 'stationary' in the sense that the final formations move back and forth along the direction of vibrations giving an external observer the illusion of a solid body being shaken inside the liquid. In the present case (parallel vibrations), no asymptotic state exists as the phenomena are intrinsically cyclic and the morphology of the emerging structures is dictated essentially by the thermal boundary conditions implemented along the sidewalls of the cavity. In place of the 'quadrics' structures typical of the perpendicular case, mushroom-like formations or more involved realizations are obtained. In both cases, particle accumulation is enabled by virtue of the compressible nature of the particle velocity field, however, while in the perpendicular case the accumulation of such compressibility effects results in the aforementioned stationary morphologies, in the parallel one it drives the emergence of asymmetries, which grow with time. In particular, the structures achieved when applying either fully adiabatic or fully conducting walls bare much resemblance to one another, this being especially true when the heavy particles are considered. In these cases, as a result of the above-

mentioned ongoing symmetry breaking process, a disruptive region can be identified at the top rear of the cavity. However, this process is greatly mitigated in the situation with the hybrid thermal boundary conditions. This boundary condition also allows for an appreciably different particle patterning behaviour, by which heavy particles tend to form compact structures at the centre of the cavity, whereas light particles display a more dispersed arrangement.

Possible practical uses aside, the present endeavour should be seen as another attempt to explore the physics of multi-phase (fluid-particle) systems evolving far from conditions corresponding to simple steady flow, other relevant examples of this line of inquiry for other types of thermal convection being the works by Yarin *et al.* [63], Solomon and Gollub [136], Park *et al.* [137], Jiang *et al.*[138] Xu *et al.* [139], Melnikov and Shevtsova [128], Gotoda *et al.* [129], Sakata *et al.* [130].

An exciting prospect for the future is the extension of the present analysis (the parallel vibrational case) to conditions for which the underlying fluid flow becomes turbulent, thereby bridging the gap with another important theme running in the literature, namely, that related to the dynamics of solid inertial particles in turbulent flow (Elghobashi and Truesdell, [140]; Maxey and Wang [141]; Fallon and Rogers [69]).

Chapter 8

Particle accumulation in non-uniformly heated cavities in vibrated liquids

This chapter is based on the following peer-reviewed publication:

Crewdson, G., Evans, M. and Lappa, M.,2022, "Two-dimensional solid particle attractors in non-uniformly heated vibrated fluid containers", *Chaos* 32, 103119, https://doi.org/10.1063/5.0104680..

The text in this chapter has been modified only when necessary in order to preserve the continuity and flow of this thesis.

8.1 Introduction

In the present work, this specific problem of multiphase thermovibrational convection is further explored by replacing the simple thermal boundary conditions considered in earlier studies with more complex ones. The main objective is a more in-depth analysis of the multiplicity problem when the aforementioned main simplifications at the basis of earlier studies, i.e., the unidirectional nature of the imposed thermal gradient, is removed. By doing so, a more complete characterization of this recently discovered class

of phenomena and of the related 'hidden mathematical order' is sought. Leaving aside for a while the purely theoretical implications that attach to such a purpose, the present work also aims to discern additional useful details, which in the future may lead to the definition of new vibration-based 'control' techniques for the contactless manipulation of particles dispersed in a fluid. The related technological implications would be of great value. Suffice it to say, that the properties of many composite/multiphase materials depend on the effective distribution of the related minority phase into a hosting matrix (the majority phase). Having the ability to control these would lead to significant improvements in many fields.

8.2 Mathematical model and boundary conditions

The problem is tackled under the constraint of two-dimensional (2D) flow. Such approximation is obviously chosen primarily for numerical convenience. It can be noted that in earlier works on this specific subject (Lappa 2014 [1]) where three-dimensional (3D) simulations were carried out for cubic cavities with thermal boundary conditions being kept 'unchanged' along the spanwise direction, the emerging particle structures were found to be the 'projection' in 3D of those found in 2D (i.e. cylindrical surfaces with axes parallel to the spanwise direction and cross-sectional shape identical to that obtained in the framework of 2D studies). As three-dimensional effects have been reported to be mild in those cases (a departure from the morphology found in 2D becoming evident only in proximity to the walls delimiting the container in a direction perpendicular to the spanwise direction), here 2D computations are intentionally used as a workhorse to investigate whether the multiplicity of particle attractee revealed by earlier studies can be somehow altered when the constraint of unidirectional temperature gradient through the fluid is removed (which makes the two-dimensional approximation acceptable in the context of the present investigation).

8.2.1 Archetypal configurations

Here, two new cases are considered, namely, (1) the situation where vibrations are perpendicular to the adiabatic walls of the square container and the temperature gradient effective through the fluid can change its sense through the cavity due to a non-uniform temperature distribution along the walls parallel to vibrations, case (1), and (2) a configuration where vibrations have an oblique direction and the corners of the cavity are thermally controlled in such a way that they have different temperatures if pertaining to the same wall, opposed corners having the same temperature, case (2). As evident in Fig.8.1, by assuming a reference system with origin in the left bottom corner of the cavity, the vibrations are set along the x axis in case (1) and along the direction $x = 1 - y$ in case (2).

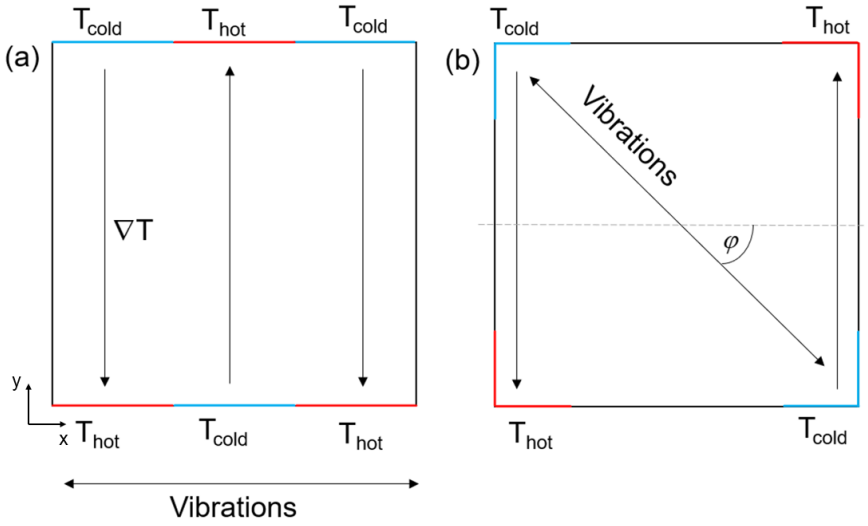

Figure 8.1: Sketch models of the two configurations considered in the present study, (a) case 1 and (b) case 2

8.2.2 Boundary conditions for the fluid phase

Initial conditions for the fluid can be represented for each cavity as follows:

Fig.8.1(a):

$$T = 1 - y \text{ and } u = v = 0 \text{ for } 0 \leq x \leq 1/3, 2/3 \leq x \leq 1,\ 0 \leq y \leq 1 \text{ for } t = 0 \qquad (8.1)$$

$$T = 1 - y \text{ and } u = v = 0 \text{ for } 1/3 \leq x \leq 2/3,\ 0 \leq y \leq 1,\ \text{for } t = 0 \tag{8.2}$$

Fig.8.1(b):

$$T = 1 - y \text{ and } u = v = 0 \text{ for } 0 \leq x \leq 1/4\, 0 \leq y \leq 1 \text{ for } t = 0 \tag{8.3}$$

$$T = y \text{ and } u = v = 0 \text{ for } 3/4 \leq x \leq 1\, 0 \leq y \leq 1 \text{ for } t = 0 \tag{8.4}$$

$$T = 1 - x \text{ and } u = v = 0 \text{ for } 0 \leq x \leq 1\, 0 \leq y \leq 1/4 \text{ for } t = 0 \tag{8.5}$$

$$T = x \text{ and } u = v = 0 \text{ for } 0 \leq x \leq 1\, 3/4 \leq y \leq 1 \text{ for } t = 0 \tag{8.6}$$

which describe a linear temperature profile running along the respective axis taking into consideration the direction in which the gradients are cast along with the condition that fluid is initially at rest (i.e., quiescent conditions). The boundary conditions for the solid walls read:

Fig.8.1(a):

$$\frac{\partial T}{\partial x} = 0 \text{ and } u = v = 0 \text{ for } x = 0, x = 1, 0 \leq y \leq 1 \text{ and } t \geq 0 \tag{8.7}$$

$$\begin{aligned} &T = 0 \text{ and } u = v = 0 \text{ for } 1/3 \leq x \leq 2/3 \text{ and } y = 0, \\ &0 \leq x \leq 1/3, 2/3 \leq x \leq 1, y = 1 \text{ and } t \geq 0 \end{aligned} \tag{8.8}$$

$$\begin{aligned} &T = 1 \text{ and } u = v = 0 \text{ for } 0 \leq x \leq 1/3, 2/3 \leq x \leq 1, \\ &y = 0, 1/3 \leq x \leq 2/3, y = 1 \text{ and } t \geq 0 \end{aligned} \tag{8.9}$$

Fig.8.1(b):

$$\begin{aligned} &\frac{\partial T}{\partial x} = 0 \text{ and } u = v = 0 \text{ for } x = 0, x = 1, 1/4 \leq y \leq 3/4 \\ &\text{and } 1/4 \leq x \leq 3/4, y = 0y = 1 \text{ and } t \geq 0 \end{aligned} \tag{8.10}$$

$$\begin{aligned} &T = 0 \text{ and } u = v = 0 \text{ for } 0 \leq x \leq 1/4, 3/4 \leq y \leq 1 \\ &\text{and } 3/4 \leq x \leq 1, 0 \leq y \leq 1/4 \text{ and } t \geq 0 \end{aligned} \tag{8.11}$$

$$T = 1 \text{ and } u = v = 0 \text{ for } 0 \leq x \leq 1/4, 0 \leq y \leq 1/4 \\ \text{and } 3/4 \leq x \leq 1, 3/4 \leq y \leq 1 \text{ and } t \geq 0 \tag{8.12}$$

8.2.3 Numerical solver

The numerical simulations included in this chapter have been produced by solving the balance equations presented in Chap. 3 in the framework of a finite volume method for incompressible flow. In particular, the computational platform ANSYS Fluent has been used. This computational platform relies on the well-known PISO algorithm (Pressure Implicit Split Operator) to ensure adequate pressure-velocity coupling. The details of this time marching procedure, where also expanded upon in Chap.3. The second order and the second order upwind spatial discretisation schemes are adopted to solve the pressure term and convective terms respectively, whilst the gradient is solved is using the Least Squares Call Based method. The second order implicit method is selected for the transient formulation.

8.3 Validation

Given the lack of results about thermovibrationally-driven particle-fluid mixtures in the literature, here the accuracy of the numerical solver has been assessed through consideration of a benchmark problem about particle self-organization in thermovibrational convection. In this two-dimensional benchmark solution, vibrations are set perpendicular to the direction of the temperature gradient (Hadley-flow-like configuration) and adiabatic conditions are considered at the side walls. The related non-dimensional parameters are summarized in Table 8.1. A mesh size of 90 $\times$ 90 has been used in this case.

The agreement found between the solver originally developed by Lappa (2014) [1] and the present one (ANSYS Fluent version 2020R2) has been verified by looking at both the x and y velocity components, signals being taken at three locations in the cavity P1, P2 and P3 where: P1 [0.25, 0.75], P2 [0.25, 0.5] and P3 [0.25, 0.25]. As quantitatively substantiated by Fig.8.2, almost no distinction can be made between the

Fluid Parameters	
Ra_ω	1.56×10^4
Ω	10^3
γ	1.50×10^6
Pr	8
Particle Parameters	
ξ	1.85
St	9.46×10^{-4}

Table 8.1: Fluid and particle parameters

results produced with ANSYS Fluent compared to those produced when employing the explicit in-house code by Lappa (2014) [1]. An additional level of validation obviously stems from comparison of the emerging particle structures in terms of patterning behaviour and size (Fig. 8.2). The minor differences in terms of lobe size visible in Fig. 8.3 can be ascribed to the different interpolation schemes used by Lappa (2014) [1] and ANSYS Fluent , while the "physics" underlying the considered phenomena is captured with a similar level of fidelity by both codes.

8.4 Grid refinement

The validation study presented in the previous section is here naturally complemented by a mesh refinement assessment conducted to verify that in addition to the "physics", also numerical aspect have been finely tuned. As described in previous chapters, the parameter known to influence the 'strength' of the convection is the Rayleigh number, in thermovibrational problems this role is played by the vibrational Rayleigh number. The higher the Rayleigh number, the more complex the flow response and therefore the more grid points are required to accurately capture the physics of the flow. As in this study the vibrational Rayleigh number is fixed to $Ra_\omega = 1.56 \times 10^4$, accordingly, the mesh refinement study is carried out assuming this specific value:

The outcomes of the grid refinement analysis are shown in Table 8.4. The x and y components of the velocity refer to a location P where the velocity magnitude of the flow is the highest (P [0.035, 0.08])

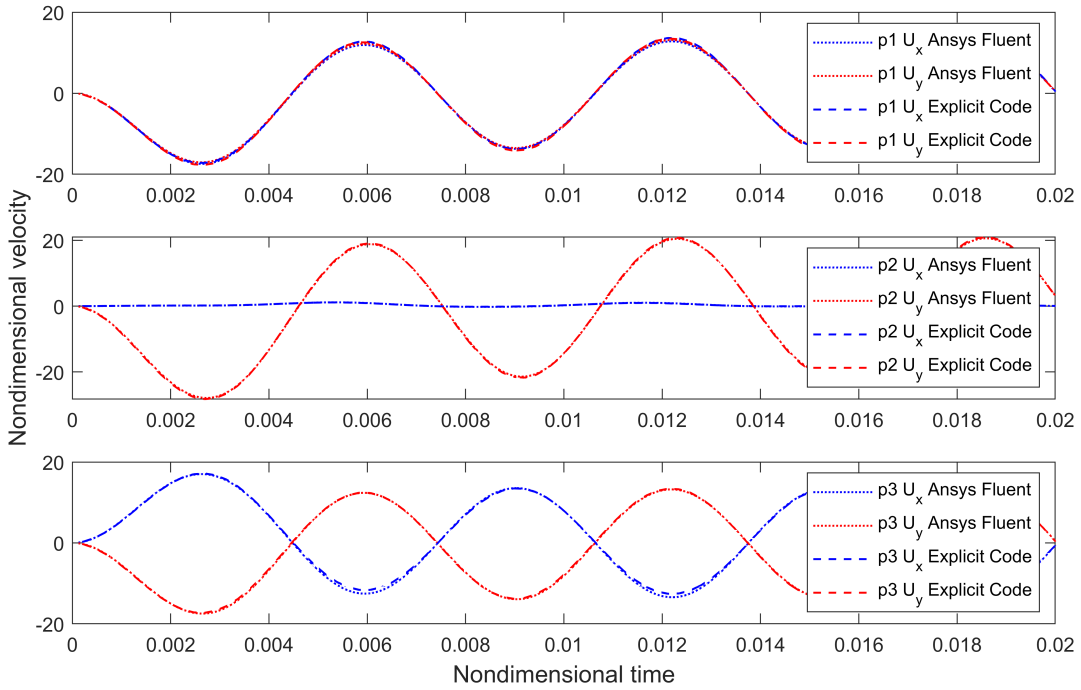

Figure 8.2: Horizontal (blue) and vertical (red) velocity components of the flow taken three locations in the cavity. The dotted lines represent the results obtained from ANSYS Fluent and dashed lines represented the results obtained from the in-house explicit code.

Fluid Parameters	
Ra_ω	1.56×10^4
Ω	10^3
γ	1.50×10^6
Pr	8

Table 8.2: Nondimensional Parameters set for mesh refinement study

8.5 Results

Variation of the temperature on the top and bottom walls

Following the approach, where the simplicity of the thermal boundary conditions considered in earlier studies is gradually taken over by more involved thermal configurations, first case (1) is examined (Fig.8.1 (a)), i.e. the vibrations are imposed along

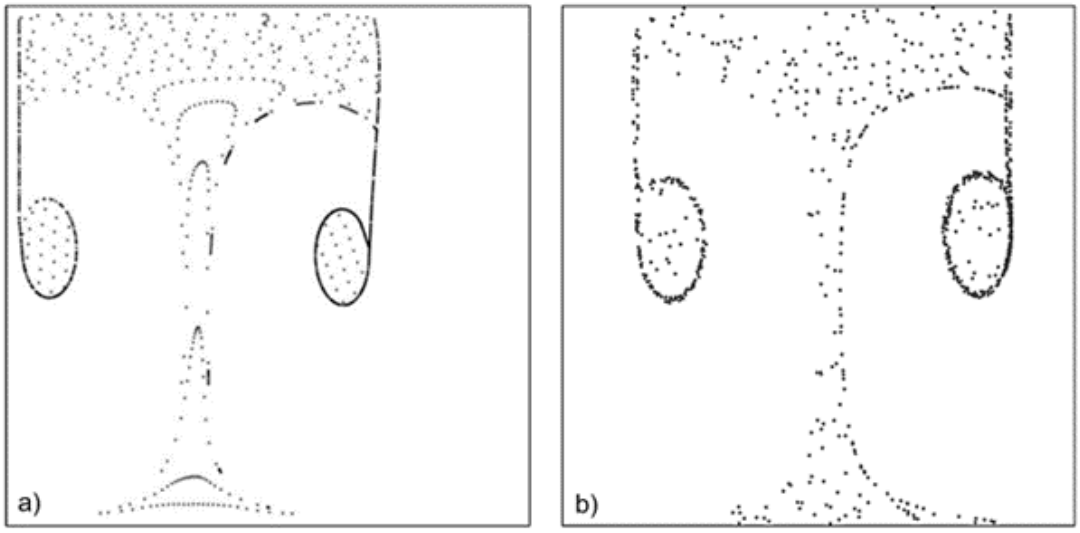

Figure 8.3: Snapshot of the tree-like patterning behaviour of the benchmark solution reported in Ref [1]. The results obtained by the in-house code (a) and ANSYS fluent (b) are shown on the left and right, respectively

System Properties	
Fluid (NaNO3) Density, ρ (kg/m3)	1904
Thermal Expansion Coefficient, β (1/K)	1.25×10^{-3}
Kinematic Viscosity, ν (m2/s)	1.27×10^{-6}
Specific Heat Capacity, Cp (J/kgK)	2892
Thermal Conductivity, k (w/mK)	0.87
Thermal Diffusivity, α (m2/s)	1.58×10^{-7}
Length of cavity, L (m)	0.01
δT (K)	0.01

Table 8.3: Dimensional Parameters set for mech refinement study

the x-direction and three alternating temperature gradients are set in the y-direction. The non-dimensional parameters (γ) and (St) are varied parametrically over a range of $\gamma = 1.5 \times 10^6$ to 6.5×10^7 and $St = 1.39 \times 10^{-5}$ to 8×10^{-4} respectively. The particle-to-fluid density ratio is fixed to $\xi = 1.85$. Under these vibrational and heating conditions, many structure types are observed, and the following nomenclature is coined here to adequately characterize them: the 'four loop' type, the 'central pillar accumulation', the '2 central structures' and the 'two side extensions'.

	$U_{x\,max}$	$U_{x\,min}$	$U_{y\,max}$	$U_{y\,min}$	$U_{x\,mean}$	$U_{y\,mean}$
45 divisions	1.326	-1.331	4.209	-4.207	-0.008	0.021
60 divisions	1.423	-1.427	4.081	-4.082	-0.008	0.019
% difference	7.35%	7.24%	3.02%	2.98%	1.57%	7.70%
75 divisions	1.504	-1.510	4.048	-4.047	-0.009	0.020
% difference	5.67%	5.77%	0.82%	0.86%	15.92%	4.58%
90 divisions	1.377	-1.382	4.125	-4.124	-0.008	0.020
% difference	8.43%	8.45%	1.89%	1.92%	12.59%	0.59%
105 divisions	1.377	-1.382	4.125	-4.124	-0.008	0.020
% difference	0.00%	0.00%	0.00%	0.00%	0.00%	0.00%

Table 8.4: Grid refinement study (based on case 1)

8.5.1 Pattern formation types (for case 1)

In this paragraph, a brief description of each structure is elaborated starting from the 'four-loop' type structure, depicted by the circle symbol (•) in Fig.8.4. This structure type has been found at three locations in the map,: at medium to high values of both (γ) and (St). Moreover, as a distinguishing mark with respect to other structures, symmetry has been found about the x-axis for y=0.5 and about the y-axis for a time dependent value x_t, where x_t is the point along the x-axis representing the location of the vertical centrelinecenterline of the structure. Four 'loops' can clearly be recognized, each tending towards a Cartesian oval (egg shape). From a practical (interpretative) standpoint, these ovals may be regarded as 'attractors' to which all particle trajectories tend, when a statistically relevant number of them are considered (further discussion of the concept of 'attractors' will be provided in the next section). The next structure attention is turned to is the 'central pillar accumulation', found at six instances, represented by the square symbol (■) in Fig.8.4. As qualitatively made evident by the insets in this figure, only one bulk structure emerges in this case, in contrast to the other three types where distinct accumulation loci are separated by the continuous phase (the clear fluid). The central pillar is formed primarily due to wall effects, by which the displacement of the cavity along the x-axis (i.e., the vibrations) causes the particles to accumulate along the vertical side wall and detach when the cavity is displaced in the opposite direction. These wall effects have been found to be a key

factor in influencing particle accumulation in thermovibrational problems when considering differentially heated cavities (Hadley flow type configuration) in both laminar [1] and turbulent conditions [135]. These wall effects however are not the only influential factor. Convection still plays a role as witnessed by the tendency of the structure to contract in an hourglass shape as time passes (where the smallest extension along x is visible at y=0.5). The next case of the sequence, i.e. the accumulation represented by the diamond symbol (⧫) in Fig.8.4, is the rarest of all structures. Indeed, only 2 instances have been detected (for the range of parameters considered here), denoted as '2 central structures'. This type exists in the region of medium values of γ and high values of St. This case bares much similarity to the (■) morphology; indeed, an even more pronounced constriction is visible at y=0.5. The particularity in this case is that the central column splits into two centralised structures, where a finite layer of clear fluid emerges through the centre of the overall aggregate. The perimeter of the structure is also more defined when compared to the central channel accumulation (■), where the structure is 'closed' near the top and bottom walls. Finally, the 'two side extensions' variant is considered, represented by a triangle symbol (▲) in Fig.8.4. The central structure visible here is very similar to the aforementioned central pillar represented by the square symbol (■). In this case, however, the pillar is adorned by two elongated ovals at the left and right sides. Having completed a description of the patterning behaviour, some general conclusions can be distilled out of this initial set of observations. Two global symmetrical trends emerge. Indeed, symmetry is observed about the x and y axis mid-planes in all cases (symmetry M1 and M3 according to Lappa [1]).

8.5.2 Trend analysis

This subsection is devoted to a quantitative assessment of the sensitivity of these structures to the problem parameters in their respective ranges of existence. In this regard, we start from the remark that while a decrease in the particle size (i.e., a decrease in St) is expected to lead to less compact structures, a higher vibrational amplitude γ should have the opposite effect [133]. It has also been demonstrated that under certain

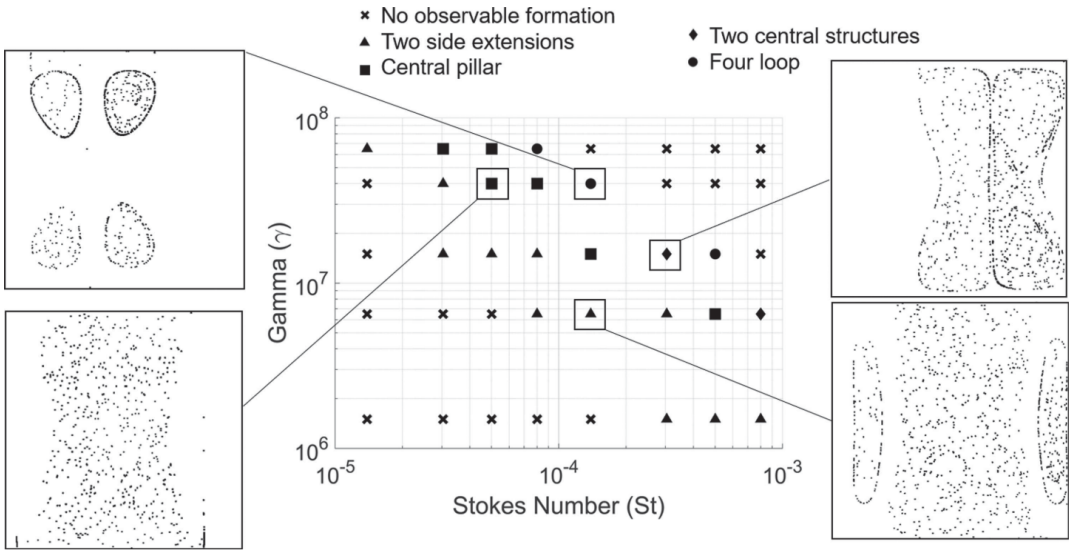

Figure 8.4: Map of structures for varying valued of (γ) and (St) for the case $Ra_\omega = 1.56 \times 10^4$, $\Omega = 2^3$, Pr=8, ξ=1.85.

conditions, the tendency toward more cohesive formations due to an increase in the value of γ may be offset by a decrease in St and vice versa. Notably, a similar scenario can be discerned in Fig.8.4, where diagonal trends in aggregate types are evident from the N-W to S-E regions of the map when γ decreases and St becomes larger. These observations are naturally complemented by the findings collected in Fig.8.5, where the "characteristic length" of the structure has been reported as a function of time for each particle accumulation type. Given the different morphologies and the intrinsic multiplicity of the different formation types, the characteristic length is defined as follows: "four-loop" type (Fig.8.5(a)), the maximum size of a sin- gle loop along the y direction; "two central structures" (Fig.8.5(b)), the maximum size of one of the two pillars along the x direction; "central pillar accumulation" (Fig.8.5(c)), the horizontal width of the "necked" region at half height of the cavity; and "two side extensions" (Fig.8.5(d)), the maximum size of the side loop along the y direction. In particular, in each panel of Fig.8.5, the evolution of two cases, differing in terms of γ and St, has been reported. The most interesting outcome of this figure resides in its ability to show that, in general, by compensating a decrease in St with an increase in γ, the final size of the structures (and the related formation time) can be kept unchanged. By contrast, as qualitatively

and quantitatively substantiated in Fig.8.4, significant changes (simultaneous increase or decrease) in both St and γ can cause the transition from one structure type to another.

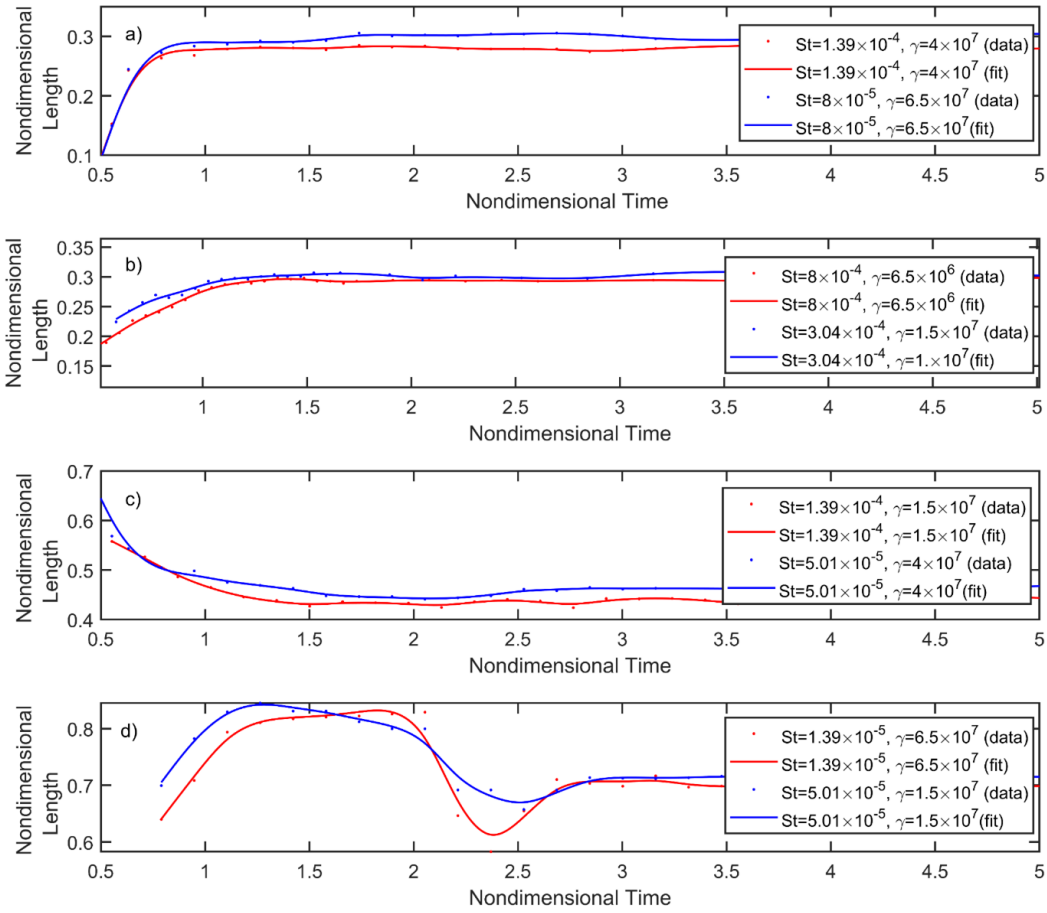

Figure 8.5: Non-dimensional structure length as a function of time : a),b),c) and d) correspond to types (•), (⧫) (■) and (▲) respectively.

8.5.3 Varying the vibrational frequency (Ω)

This subsection is devoted to the analysis of another influential parameter already identified in the frame of earlier studies where simpler more simple thermal boundary conditions where considered, i.e. the frequency of vibrations (Ω). This parameter was previously fixed to $\Omega = 2 \times 10^3$. In this section, three more (lower) values of Ω are considered for the two of the structure types: 'two side extensions' (▲, $\gamma = 1.5 \times 10^7$

and $St = 8.01 \times 10^{-5}$) and the 'four-loop' type structure (•, $\gamma = 4 \times 10^7$ and $St = 1.39 \times 10^{-4}$). The corresponding modifications in the two side extensions' variant (for $\Omega = 1.2 \times 10^3$, $\Omega = 1.3 \times 10^3$ and $\Omega = 1.5 \times 10^3$) are summarized in Fig.8.6. Interestingly, with an increase in the frequency of vibrations, the side ovals become more extended along the y-axis. The central pillar, however, remains undisturbed up until a value of $\Omega = 2 \times 10^3$, where two main lobes emerge resembling those pertaining to the 'two central structures' case. This reinforces the idea of a seamless transition between structure types.

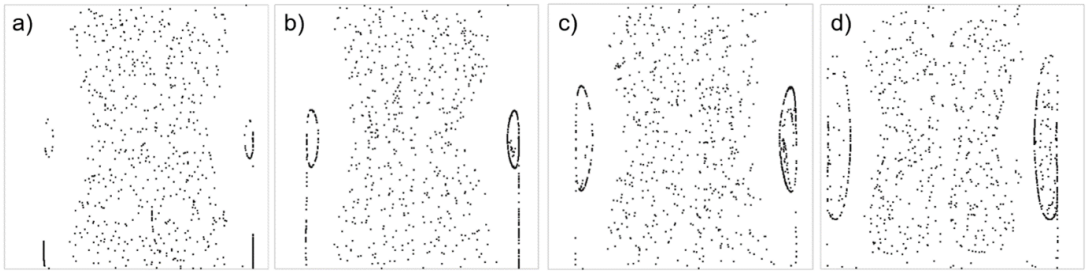

Figure 8.6: Particle structures for $Ra_\omega = 1.56 \times 10^4$ Pr = 8, $\gamma = 1.5 \times 10^7$, $St = 8.01 \times 10^{-5}$ and ξ=1.85, for varying values of angular vibration frequency Ω for (a) $\Omega = 1.2 \times 10^3$, (b) $\Omega = 1.3 \times 10^3$,(c) $\Omega = 1.5 \times 10^3$, and (d) $\Omega = 2 \times 10^3$ at nondimensional time t=3.2.

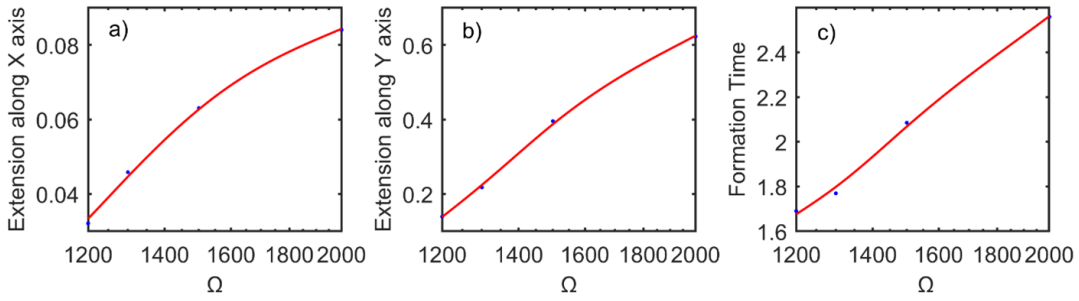

Figure 8.7: Structure extension length along x (a) and y (b) axes and formation time (c) for varying values of angular vibration frequency (Ω) for $Ra\omega = 1.56 \times 10^4$, Pr=8, $\gamma = 1.5 \times 10^7$, $St = 8 \times 10^{-5}$ and ξ=1.85.

The quantitative increase in extension along the y-axis is reported in Fig.8.7 (a) and (b). The structure formation time is also included in Fig.8.7 (c) for the sake of completeness. A rise of the formation time is observed when Ω is increased and these findings align with those by Lappa & Burel [71]. The analogous results for the 'four-

loop' type structure are depicted in Figs.8.8 and 8.9 (the range of values investigated here includes three additional values of Ω: $\Omega = 1.6\times10^3$, $\Omega = 1.7\times10^3$,$\Omega = 1.85\times10^3$).

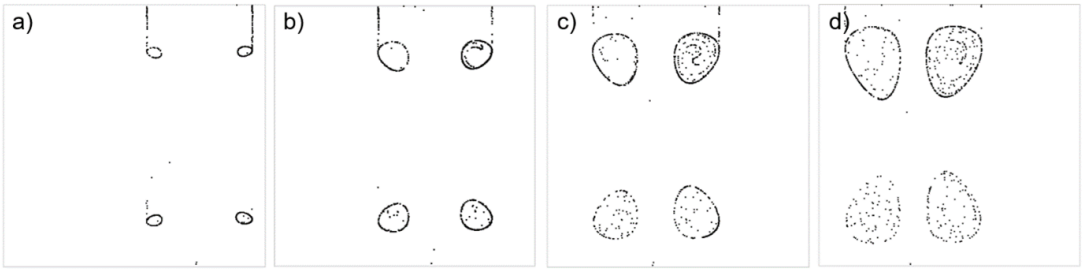

Figure 8.8: Particle structures for $Ra_\omega = 1.56\times10^4$ Pr=8, $\gamma = 4\times10^7$, $St = 1.39\times10^{-4}$ and $\xi = 1.85$, for varying values of angular vibration frequency Ω for (a) $\Omega = 1.6\times10^3$, (b) $\Omega = 1.7\times10^3$, (c) $\Omega = 1.85\times10^3$ and (d) $\Omega = 2\times10^3$). at nondimensional time t=3.2.

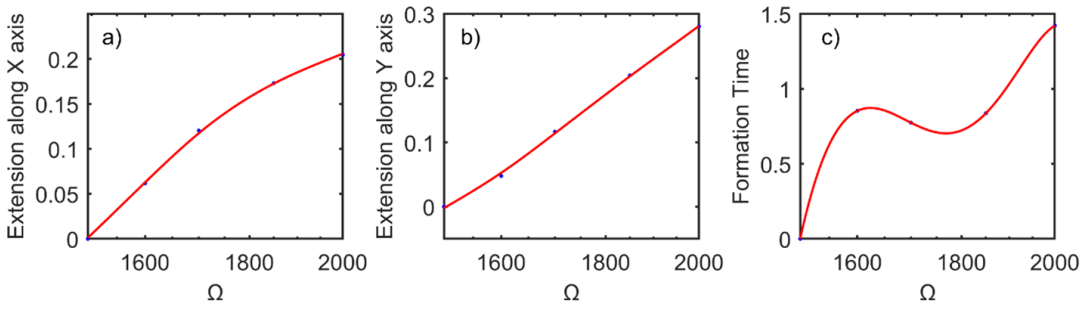

Figure 8.9: Structure extension length along x (a) and y (b) axes and formation time (c) for varying values of angular vibration frequency (Ω) for $Ra_\omega = 1.56\times10^4$ Pr=8, $\gamma = 4\times10^7$, $St = 1.39\times10^{-4}$ and $\xi = 1.85$.

A similar trend can be recognized in this case with a global increase in both the length of the x and y extensions of the rolls, together with a growth of the formational time when Ω becomes higher. All these results can be naturally combined with those pertaining to the 2D map shown in Fig.8.4. The outcomes of this exercise, by which the original 2D map is expanded through consideration of an additional degree of freedom (i.e. the vibrations angular frequency), are shown in Fig.8.10. The most important outcome of this 3D matrix of cases resides in its ability to provide a quick glimpse into the limitations of the range of parameters leading to particle accumulation.

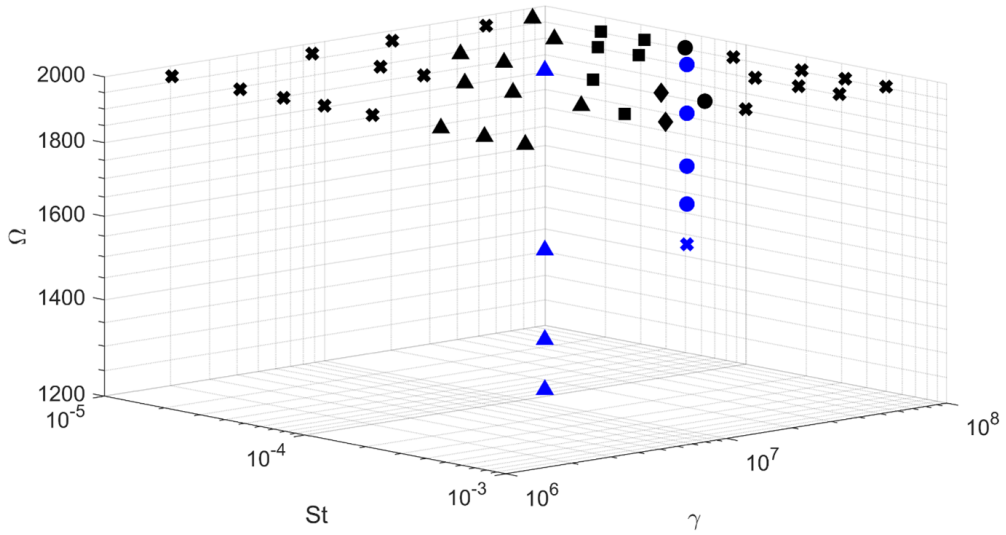

Figure 8.10: 3D Map of structures for varying values of γ, St and Ω for the case $Ra_\omega = 1.56 \times 10^4$, Pr=8.

8.5.4 Corner heated cavity (case 2)

In this section, the second archetypal configuration depicted in Fig.8.1 (b) is considered. In this case the N-O and S-E corners of the cavity are set to T_{cold} and the N-E and S-O corners to T_{hot}, leading to a symmetry about the x=y line, corresponding to the M2 and M3 symmetry groups [1]. As already described to a certain extent in the introduction, the direction of vibration is known to be an important influential factor in the behavior of thermovibrational systems [101]. Here, in particular, for consistency with the results presented for the companion case with non-inclined vibrations, the following case is assumed as a 'basic' configuration (to assess the changes induced by a variation in the vibration direction): $Ra_\omega = 1.56 \times 10^4$, $Pr = 8$, $\Omega = 2 \times 10^3$, $\gamma = 6.5 \times 10^6$, $St = 3.04 \times 10^{-4}$, $\xi = 1.85$ and $\phi = 0$. As shown in Fig.8.11, the emerging structure bares much resemblance to the 'two side extensions' variant, represented by the triangle symbol (▲) in Fig.8.4. However, some minor differences can be spotted. Firstly, the central pillar does not dispose of a contracted mid-section and appears to be of consistent width from $0 < y < 1$. Secondly, if one looks at the location from which the side loops originate, while for the case presented previously, the rolls originate from

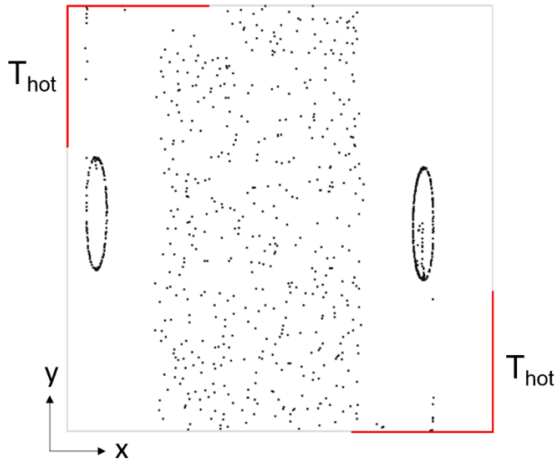

Figure 8.11: Final pattern formation for the case $Ra_\omega = 1.56\times10^4$, $Pr = 8$, $\Omega = 2\times10^3$, $\gamma = 6.5 \times 10^6$, $St = 3.04 \times 10^{-4}$, $\xi = 1.85$ and $\phi = 0$.

a stream of particles attached to the bottom wall (y=0, where the wall segments were set to T_{hot}), for the corner heated cavity, the side rolls originate from the heated wall sections, when these sections are located at opposite ends of the cavity.

The zoo of solutions produced when the inclination angle is varied is finally summarized in Fig.**??**(over the range $0 \leq \phi \leq 3\pi/4$). An obvious outcome is that when ϕ is changed from 0 to $\pi/2$, the entire pattern simply undergoes a complete 90 degrees rotation. For a relatively small departure from these limiting conditions (e.g. $\phi = \pi/12$ or $\pi/6$ and $5\pi/12$ or $\pi/3$, respectively), the central column begins to warp in the direction of the hot corners. Finally, a range of values of ϕ exists ($2\pi/9 \leq \phi \leq 3\pi/10$) where four distinct loops are formed. Owing to the symmetries embedded in the problem, the scenario for ϕ spanning other sub-ranges of the $0 \leq \phi \leq 2\pi$ interval can be inferred on the basis of similar arguments (see, e.g. the inset for $\phi = 3\pi/4$).

With these results in hand, a comparison can be made with the literature surrounding inclined vibrations in thermovibrational convection. To proceed in this way, reference can be made to previous work carried out by Lappa [101], where the classic case of a square cavity is considered and only one temperature gradient exists along the y axis, or $M = 1$ (M representing the number of inversions along the x axis). In this case, when π=0, the tree like structures emerges (see also the validation case shown in Fig.8.3). Upon varying the angle of vibration in a similar way to current method (as

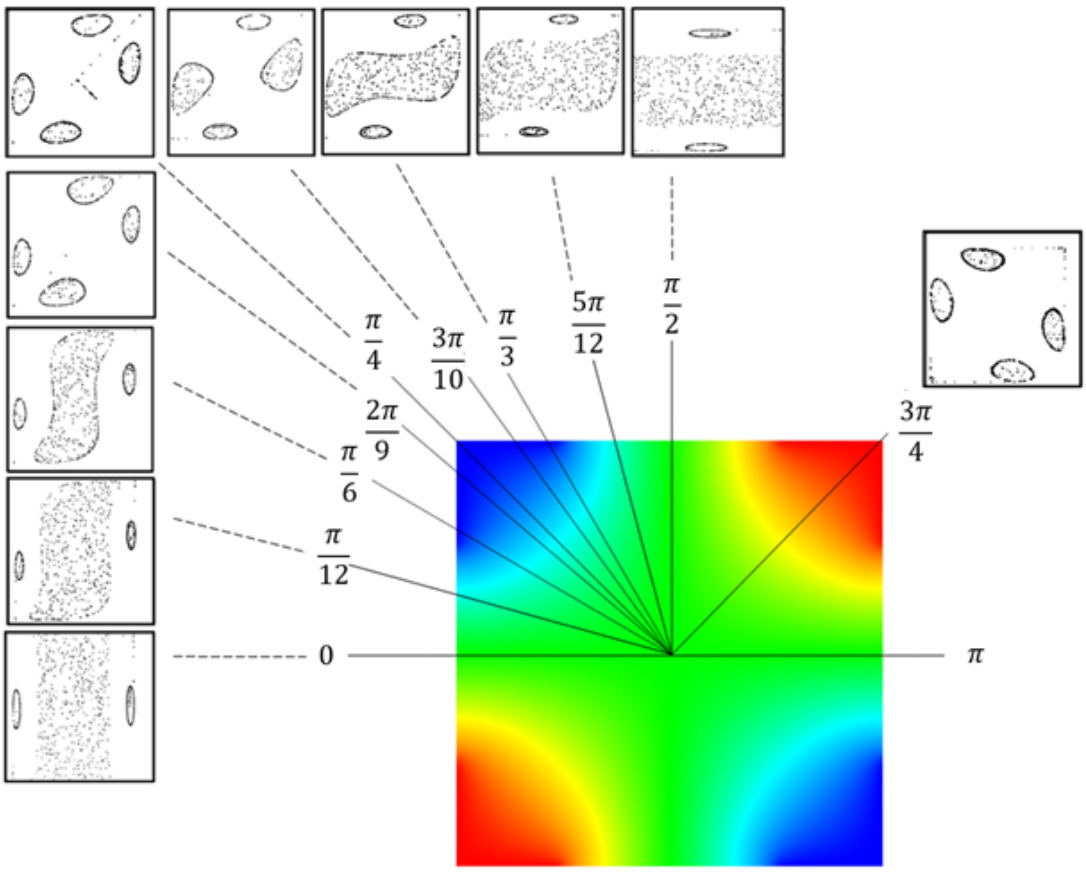

Figure 8.12: Variation of vibration angle (aligned with x-axis over $0 \leq \phi \leq 3\pi/4$) (nondimensional time t =3.2)

seen in Fig.8.12) a familiar behaviour is observed: the two rolls of the tree rotate synchronously with the angle of vibration and maintain symmetry about the axis parallel to this angle of vibration. In the case of Lappa however, the term 'symmetry' can be use lightly as the size of the two rolls become unequal. This is because the system is transitioning from a Hadley type configuration, where the onset of convection is achievable at low Rayleigh numbers, to the Rayleigh-Bénard type convection where the onset of convection occurs only when a critical value of the Rayleigh number is exceeded. Indeed for $\phi = \pi/2$ no convection occurs and therefore the particles are subject only to the 'wall effects' discussed previously. In the current simulations, no such transition from the Hadley flow to the Rayleigh-Bénard type flow is possible as the thermal boundary conditions and subsequent temperature field is symmetrical along the x=1-y axis.

8.6 Discussion

Placing the present results in a proper theoretical context requires a short excursus on the peculiar properties of this class of particle attractors and what has been understood until now in terms of underlying cause-and-effect relationships. In this regard, as already discussed to a certain extent in the introduction, it is worth recalling that the present work adds another piece to the puzzle related to the existence of particle attractors in vibrationally driven flow, which do not depend on particle interactions (whose first piece was placed by Lappa [1] with the discovery of a new class of self-induced particle aggregates in vibrated non-isothermal fluid-particle mixtures in the framework of a one-way coupling approach). By looking back at these previous works, some useful arguments can be drawn, which can help to interpret the present one and elaborate a more general 'view' of these phenomena and useful generalizations.

Compelling evidence has been provided (see, e.g. Lappa [1, 100]) that particle attractors are made possible by the interplay of inertial and thermovibrational effects as indirectly proven by the suppression of particle structures in the limit as the density of the particles becomes equal to that of the surrounding liquid or the thermovibrational effect is disabled (while still allowing non-iso dense particles to feel the acceleration pro-

duced by vibrations). Convincing arguments have also been elaborated about the direct relationship between the effective spatial shape of the 'attractors' (directly connected to the morphology of the particle structures emerging in the framework of one-way coupled numerical studies) and the relative direction of vibrations with respect to the boundary of the systems Lappa [1]. Indeed, It has been shown that, if the angle between vibrations and the walls of the system is changed while vibrations remain perpendicular to the imposed temperature gradient, a zoo of structures can be obtained. Subsequent studies such as that by Lappa [101] have shown that further changes in the morphology can be obtained by allowing vibrations to change their inclination with respect to the prevailing temperature gradient, which has led to the main conclusion that the effective physical realization in space of particle structures is dictated by the three-fold relationship between the direction of vibrations, that of the imposed (unidirectional) temperature gradient and the effective shape of the container physically hosting the fluid-particle mixture. While other works of relevance to this subject have shown that additional levels of complexity can be brought in by symmetry breaking effects emerging in the carrier flow itself in a 'spontaneous' way (i.e. due to a intrinsic bifurcation of this flow which would occur even in the absence of particles, Lappa and Burel [142] or produced as a result of the back influence of dispersed solid matter on such a flow, the major contribution of the present study can be found in its ability to show that the multiplicity of the attractors, i.e. the number of attracting loci coexisting in the physical space at the same time, can be somehow controlled by acting on the degree of thermal inhomogeneity of the fluid.

Through a generalization of a large number of results, it was previously concluded that this multiplicity N could not exceed a value $N = 2$ as the particle structures were always manifesting in couples or as a single large cohesive unit produced by the coalescence of two initially distinct aggregates.

Although conducted under the constraint of 2D flow, the present study has shown that even if the analysis is still limited to a case as simple as a square cavity, conditions can be identified for which several distinct formations (with $N > 2$) can co-exist within a single fluid domain (with intermediate regions of particle-free fluid clearly separating

them). In particular, by indicating with M the number of inversions in the temperature gradient effective through the fluid, the multiplicity for the first archetypal setting considered in the present work can be expressed as follows:

$$N \leq 2 + M \tag{8.13}$$

The significance of this inequality, which holds for a fixed value of ξ, Ra_ω, and Ω (ξ=1.85, $Ra_\omega = 1.56 \times 10^4$, and $\xi = 2 \times 10^3$, respectively, in the present work), can be further explained or elucidated as follows: by changing the amplitude of vibrations (γ) for a fixed size of particles (St) or, vice versa, changing the Stokes number for a fixed γ, topological changes can be induced in the emerging particle pattern, with the number of possible realization constrained to be less than or equal to 4.

For the second paradigm considered, i.e. the cavity shown in Fig.8.1 (case 2) (where M=2), and the vibrations can form an angle ϕ with the x axis), this relationship still holds provided a corrective factor is introduced to account for the inclination of the shaking direction, i.e:

$$N \cong 3 + \|sin(2\pi)\| \tag{8.14}$$

which indicates that the relative direction of vibrations can also affect the multiplicity parameter.

8.7 Conclusion

The problem related to the formation of particle accumulation structures in thermovibrationally driven systems still carries a number of interesting questions, some of a general nature, other more system specific. In the present work, a first attempt has been made to understand if and how behaviors and mechanisms known to be effective under unidirectional temperature gradients can be mapped into systems with non-uniformly heated boundaries. Emerging structures have been categorized into specific classes depending on their appearance in the physical space. After running a statistically representative number of numerical simulations, it has been demonstrated that a colorful spectrum of variants is possible, which differ in terms of topology, morphology

and number of attracting loci. For a fixed couple (ξ, Ra_ω), these accumulations exist through a multi-dimensional space of parameters (particle size (St), amplitude (γ), frequency (Ω) and angle (θ) of vibrations) as a result of the reverberation of physical processes driven by thermovibrational (convective) and inertial (particle-related) effects into a confined space. The major outcome of the present study is that such phenomena can also be "tuned" or "controlled' to a certain extent by acting on the degree of thermal inhomogeneity of the system. On increasing the number of inversions of the temperature gradient inside the fluid, the multiplicity of the emerging structures grows accordingly and transition among different realizations can be obtained on varying γ and/or St. Some correlations or relationships have been introduced in the attempt to model these behaviours. Although, these may be regarded as still incomplete realizations of a more complete theory that shall be formulated to predict the properties of particle formations in all situations and as a function of all the influential parameters, the present work should be considered as further step towards the complete characterization of the related dynamics. An interesting prospect for the future is the extension of this line of inquiry to the more general three-dimensional case for which the multiplicity of structures and the related response to changes in the system parameters and boundary conditions is expected to become even more intricate.

Chapter 9

Preliminary investigation into the accumulation of non-isodense particles in chaotic thermovibrational flow

This chapter is based on the following peer-reviewed publication:

Crewdson, G. and Lappa, M., 2022, "An Investigation into the Behavior of Non-Isodense Particles in Chaotic Thermovibrational Flow", *Fluid Dynamics & Materials Processing*, 18(3), 497-510, https://doi.org/10.32604/fdmp.2022.020248.

The text in this chapter has been modified only when necessary in order to preserve the continuity and flow of this thesis.

9.1 Introduction

From the literature review and Chap.7 and 8 it has been shown that many natural and industrial processes are known to depend on the delicate interplay of two or more phases. The mixing (or segregation) of the involved phases can depend on the type of

fluid motion associated with the considered problem. As many natural and industrial processes are intrinsically turbulent, a vast literature exists where such phenomena have been investigated in these circumstances. In particular, most existing studies have focused on the preferential clustering of either isodense or non-neutrally buoyant solid particles in the case of isotropic turbulence [68, 143] with the two-fold objective of describing the effect of turbulence on the dynamics of the discrete phase (including its sedimentation process) and elaborating strategies to modulate/attenuate turbulence [144–147]. In such analyses, particles have generally been observed to cluster and form irregular aggregates displaying fractal morphology.

More recently, other studies have been conducted considering turbulent natural (buoyancy) convection, which can no longer be considered isotropic. As an example of recent investigations for non-neutrally buoyant particles interacting with turbulence brought on by natural convection, it is worth citing Xu *et al.* [139], where the temperature gradient was set parallel to the gravity vector. In this work, (heavy) particles were observed to undergo accumulation into bands, with the strength of the bands depending on the inertial properties of the considered particles. For the companion problem represented by the Hadley flow, other authors, such as Gereltbyamba *et al.* [64], have found that the particle diameter can play a significant role in the resultant particle trajectories and their concentrations when relatively high value of the Rayleigh number are considered.

Despite these efforts and a few other relevant investigations [69, 140, 148], however, the problem related to particle behaviour in microgravity conditions has received less attention than the corresponding case dealing with particles in terrestrial flows. For these reasons, in the present chapter we concentrate on the preferential clustering of non-isodense finite-mass finite-size particles induced in microgravity conditions by turbulent thermovibrational flow. This may be regarded as a new line of inquiry standing at the intersection of the previously segregated fields about the (terrestrial) dynamics of inertial particles in isotropic turbulence and the behavior of such particles in laminar thermovibrational flows.

As seen in Chap.5 turbulent thermovibrational flow can be achieved when the amplitude of vibrations (or the related vibrational Rayleigh number) exceeds a given value and the fluid 'response' (in terms of induced velocity) becomes non-synchronous with the forcing of the system [38, 125].

9.2 Mesh refinement and numerical method

Similarly to the vast majority of the work presented in this thesis the simulations are carried out on OpenFOAM. It is worth recalling from Chap.5 that, for this type of grids and turbulent flows, requirements based on arguments related to the Kolmogorov length scale Eq.5.3.

Here, a maximum value of $Ra_\omega = 10^9$ is considered (along with Pr = 15), which according to this criterion would return a value of $N_{div} = 96$. As this, however, should be regarded only as a theoretical guideline, it has been deemed necessary to conduct a grid refinement study to verify the relevance of such a requirement. Fig.9.1 shows the power density spectrum (PDS) obtained when considering the velocity in the x-direction at the centre of the cavity. It can be seen that the slope of the spectrum in the low frequency range obeys the Kolmogrov law (-5/3) and is independent from the mesh size in terms of velocity amplitude and frequency distribution.

9.3 Results

The results presented in this section can be used to identify the salient factors contributing to the behavior of particles under the effect of vibrations and related turbulent fluid flow. They have been obtained by changing the influential parameters in a segregated manner in order to reveal the influence of each of them (namely, St and ξ accounting for the inertial effects, and γ and Ra_ω, accounting for the strength of vibrations and fluid motion induced accordingly). To reduce the (otherwise intractable) scale of the problem resulting from the consideration of so many parameters, without loss of generality, the vibrational frequency Ω has been fixed to $\Omega = 10^4$.

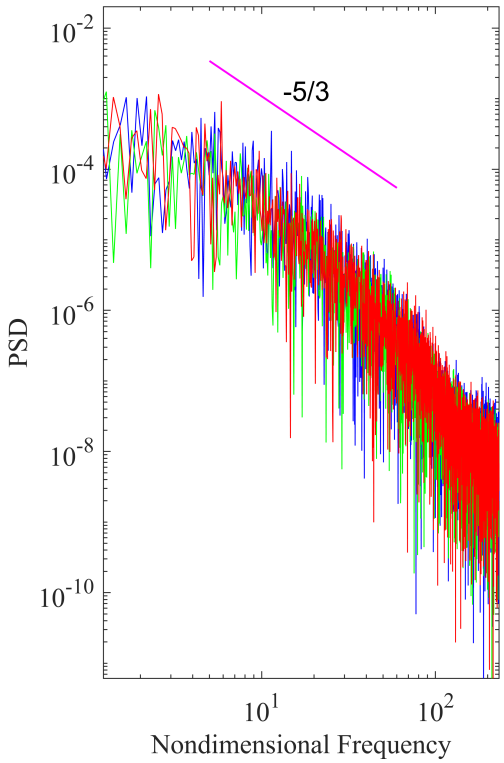

Figure 9.1: Power spectral density for grid sizes where blue represents a grid resolution of 60 by 60, green a resolution of 80 by 80 and finally red, a resolution of 96 by 96. The pink line shows the slope obeying the Kolmogrov law of -5/3

,

9.3.1 Formation mechanism

The accumulation of particles in turbulent flows comes primarily as a result of the inertial nature of the particles coupled with presence of eddies in the fluid. The investigation of Maxey *et al.* [143] into dispersed turbulent multiphase flow in the case of homogeneous, isotropic turbulence (for gas-particle and bubble-liquid mixtures), indeed, could show that the preferential concentration of bubbles/particles depends on the inertial properties of the dispersed phase and centrifugal effects. Preferential accumulation is typically observed in regions of strong vorticity for bubbles and regions of strong strain-rate for particles, meaning that for cases where the dispersed phase is less dense than the continuous phase (ξ <1) the particles will cluster in the centre of the

eddies/vortices and vice versa for the cases where the dispersed phase is denser than the continuous phase ($\xi > 1$).

The present results, however, reveal that, when subjected to vibrations, the displacement of the cavity gives rise to an external ('additional' with respect to the effects discussed before) force that influences the trajectory of the particles, whereby they are continuously pushed from one side of the cavity to another.

Notably, this causes the dispersed phase to accumulate periodically along the walls parallel to the y-axis (as the vibrations are imposed along the x-axis) and upon detachment from the wall, form filament type structures. As these filaments migrate periodically from wall to wall, they curve and bend around the eddies present in cavity (due to the chaotic nature of the flow). This delicate formation mechanism is illustrated in Fig.9.2 where two filaments can be seen appearing and disappearing in the space of one vibrational period.

9.3.2 Influence of vibrational amplitude on filament survival

The formation and survival of the small structures described in the previous section (simply referred to as 'filaments'), occurs approximately twice per period depending on the amplitude of the vibrations. Indeed, as b (the dimensional displacement of the cavity) is increased, the faster the particles accumulate on the opposite wall, hence reducing the filament survival time. This phenomenon is illustrated in Fig.9.3, where the dashed lines delimit one vibrational period. In particular, these results represent three archetypal cases where an increase in b results in a simultaneous increase in Ra_ω and γ. As qualitatively and quantitatively substantiated by this figure, for very high values of Ra_ω and γ, the filaments survive approximately a quarter of the total period duration, due to the fact they are quickly absorbed by the opposing wall.

This is also evident in Fig.9.4. When comparing columns 1 and 2 of this figure, the particles are pushed further way from the formation wall (indicated by the red arrow), following an increase in γ. However, for the same value of γ, and an increase in Ra_ω, the filaments become less defined and appear more dispersed in the cavity.

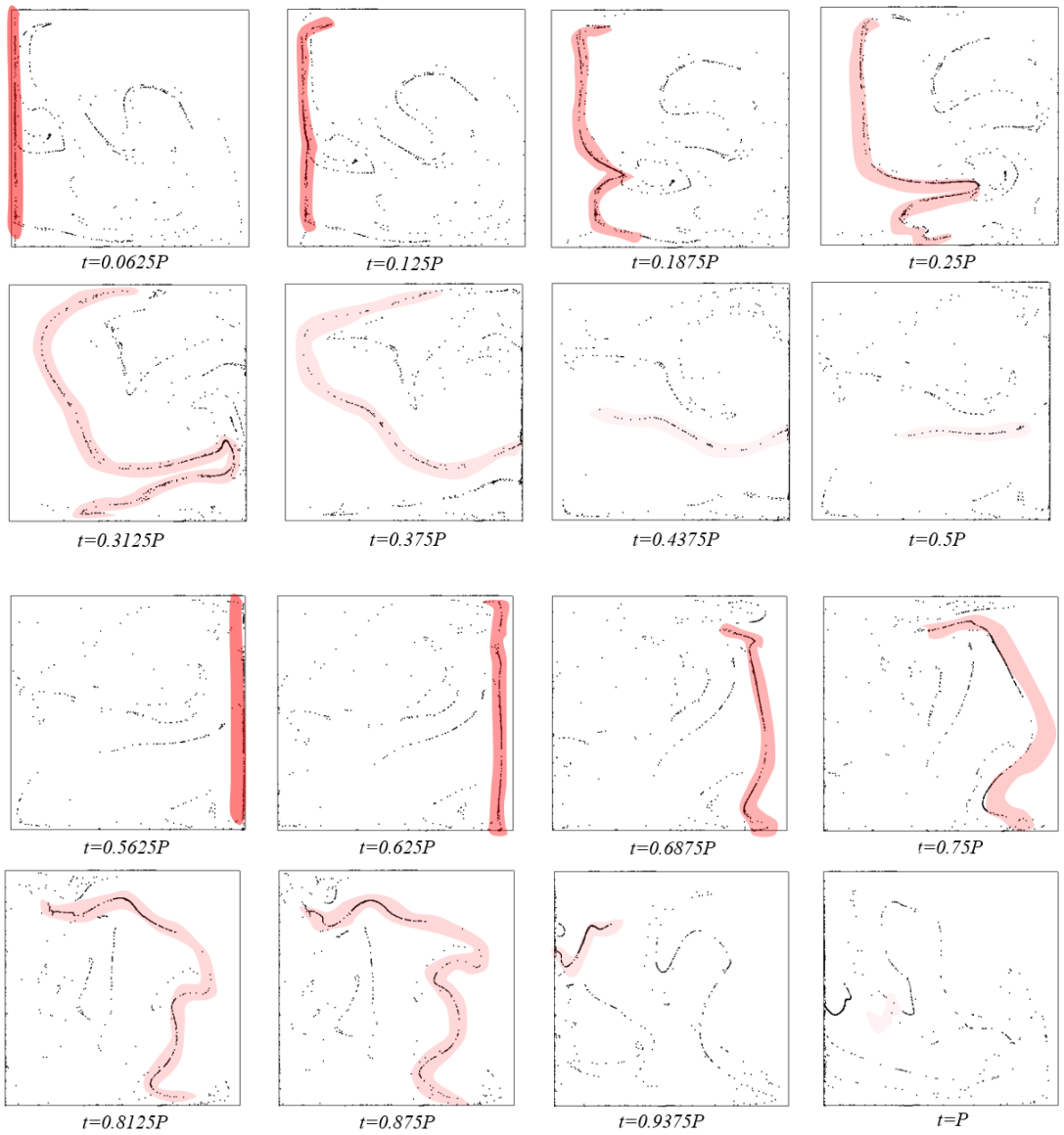

Figure 9.2: Sixteen equally spaced snapshots over one vibrational period P where P=$2\pi/\omega$, illustrating the formation mechanism on the filaments for $Ra_\omega = 1.00 \times 10^8$, $\gamma = 1.79 \times 10^8$, $\xi = 0.3$ and $St = 9.39 \times 10^{-4}$ ($\Omega = 10^4$)

9.3.3 Influence of the particle properties: ξ and St

The inertial properties of the particles can also influence greatly the formation (if any) of the structures. This is illustrated in Fig.9.5, where the particle accumulations resulting from two different densities are superimposed over each-other at the same

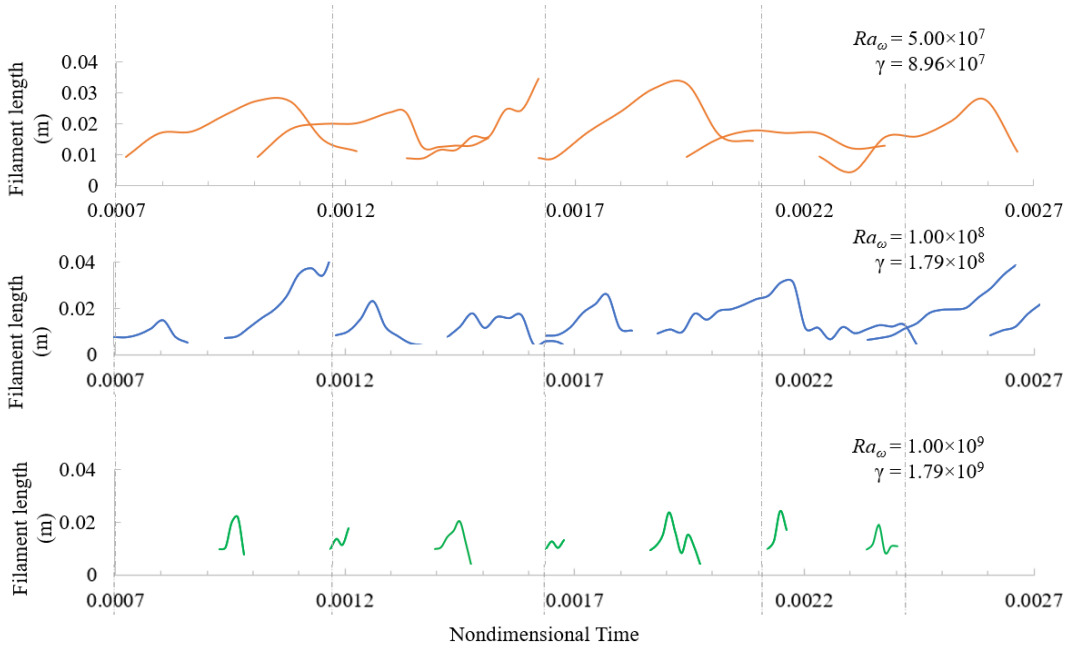

Figure 9.3: Filament length and survival time depending on Ra_ω and γ,for $\xi = 0.3$ and $St = 9.39 \times 10^{-4}$ ($\Omega = 10^4$)

instantaneous points in time. In particular, the light particles ($\xi = 0.3$) are represented in purple and the heavy particles ($\xi = 2$), in orange. Remarkably, it can be seen that the spaces occupied by the clouds formed for $\xi = 0.3$ and ξ =2, are for the most part complimentary to each other; moreover, the light particles are prone to form stronger filaments than the heavy particles.

Another important influential factor, already identified in the earlier study by Lappa [1] (where only laminar conditions were considered) is represented by the size of the particles, (the particle Stokes number St, from a non-dimensional standpoint). Along these lines, Figs.9.6 shows that a decrease in St, i.e., a decrease in particle size, can result in the inability of the dispersed phase to form any recognizable structure (under the specific considered operating conditions: Ra_ω and γ).

9.4 Conclusion

Towards the end of unifying the previously segregated fields represented by the study of particle behaviour in terrestrial turbulent flows and that concerned with the high-

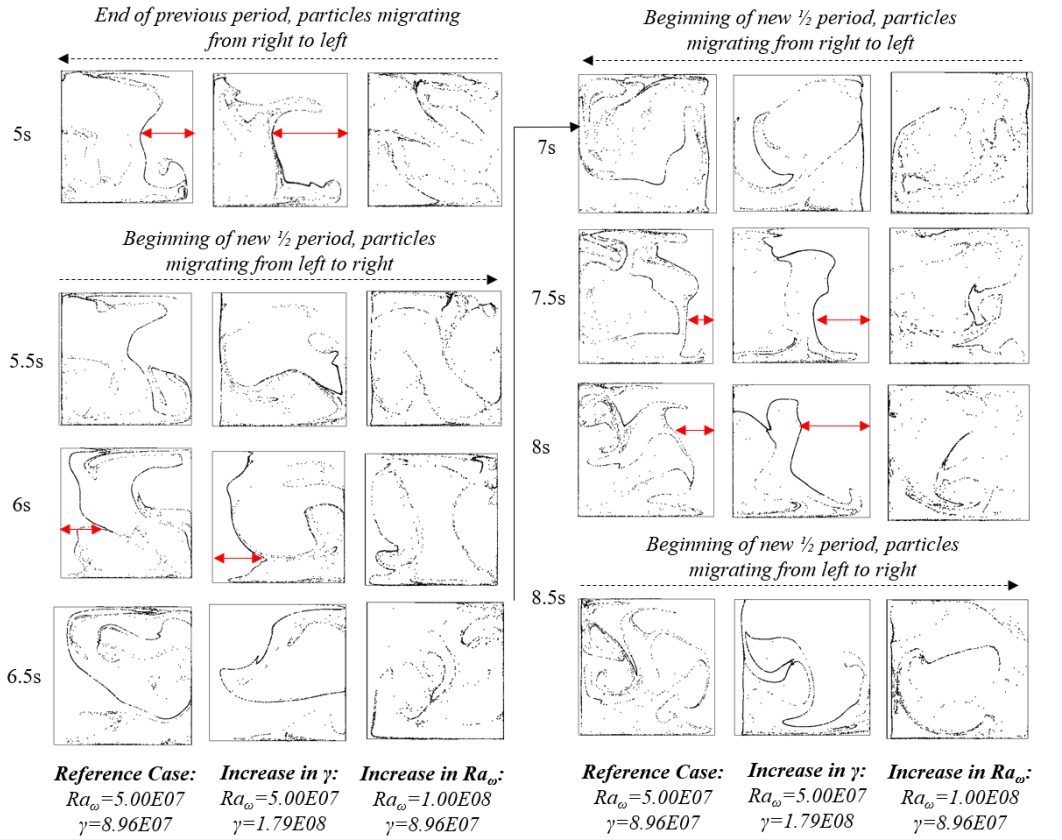

Figure 9.4: Isolated effects of Ra_ω and γ on filament behaviour for $\xi = 0.3$, $St = 9.39 \times 10^{-4}$ and $\Omega = 10^4$

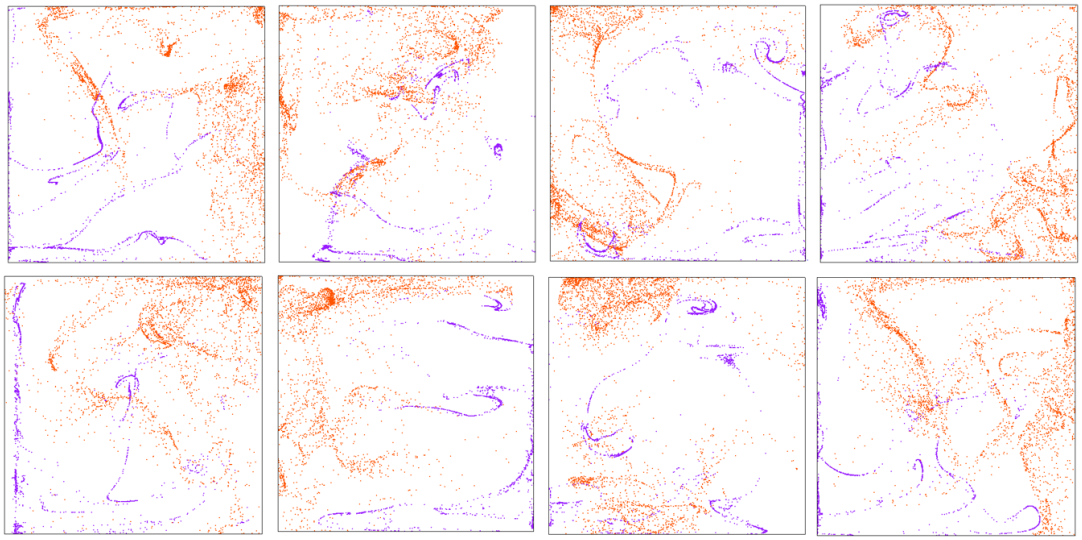

Figure 9.5: Eight snapshots equally spaced over two periods (2P) from left to right, top to bottom, where $Ra_\omega = 1.00 \times 10^8$, $\gamma = 1.79 \times 10^8$ and $St = 9.39 \times 10^{-4}$ ($\Omega = 10^4$). The light particles $\xi = 0.3$ are represented in purple and the heavy particles ($\xi = 2$), in orange

regular aggregates formed by particles interacting with laminar vibrational flow in microgravity conditions, particle dynamics have been investigated in conjunction with chaotic (turbulent) thermovibrational flow. It has been shown that circumstances still exist for which particles (initially uniformly distributed in the entire physical domain) de-mix from the fluid and form recognizable (well defined) structures. As opposed to the perfect morphology of clusters emerging in laminar flow, however, when thermovibrational flow is chaotic the topology of the structures is relatively irregular and time-dependent.

Nevertheless, precise trends and relationships can be established if specific problem 'statistics' are connected to the behaviour of the temporally evolving structures. As an example, a lack of filament formation due to a decrease in St can be offset by an increase in the amplitude of vibration acceleration γ; in turn, however, this may decrease the filament survival time due to a faster absorption rate of the filaments by the opposing wall. An exciting prospect for the future is to conduct an extensive analysis of these interdependences using the present relevant mathematical and numerical framework.

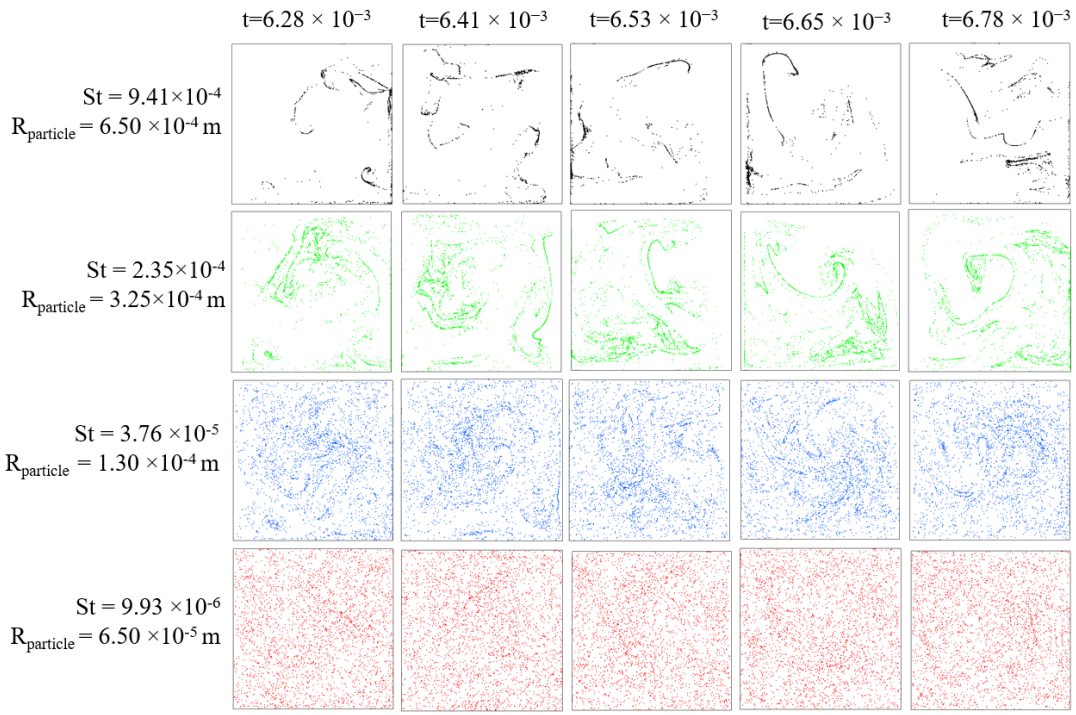

Figure 9.6: Snapshots of particle behaviour over one period (from left to right) for $St = 9.41 \times 10^{-4}$ (black), $St = 2.35 \times 10^{-4}$ (green), $St = 3.79 \times 10^{-5}$ (blue) and $St = 9.93 \times 10^{-5}$ (red) for the case, $Ra_\omega = 1.00 \times 10^8$, $\gamma = 1.79 \times 10^8$ and $\xi = 0.3$ at time $t = 6.28 \times 10^{-3}$, 6.41×10^{-3}, 6.53×10^{-3}, 6.65×10^{-3} and 6.78×10^{-3} for ($\Omega = 10^4$)

.

Part III

Conclusions

Chapter 10

Conclusions

Throughout this body of work, many notions surrounding and expanding upon thermovibrationally driven flows and particle accumulation in microgravity have been discussed. In this section, the research outcomes of the thesis are addressed. This is done by stating how each chapter has contributed towards answering the research questions posed in the introduction and how this work has made a novel and exciting contribution to knowledge.

10.1 Single phase thermovibrational flow (fluid only)

10.1.1 What thermovibrational effects can be achieved in a fluid, when the direction of the vibrations is changed (from Hadley type flow to RB type flow)?

It has been identified in the literature review that the behaviour of a thermovibrational system depends greatly on the direction of the temperature gradient in relation to that of the vibrations and that an extended range of parameters remains unexplored. Specifically, Chap.4, has provided answers to the following question: What thermovibrational effects can be achieved in a fluid when the direction of the temperature gradient is changed from Hadley type flow to RB type flow?

Indeed, only Hirata *et al.* [36] considered the pure thermovibrational flow in a square cavity assuming zero gravity and no inclination between vibrations and the temperature gradient. Chapter 4 has provided the scientific community with an RB

type thermovibrational study where parameters comparable to those employed for it's Hadley flow type (sister problem) are considered.

By increasing the strength of convection (Ra_ω) beyond the range considered by Hirata *et al.*[36] and exploring higher values of vibrational frequency (Ω), the first important contribution of this chapter is the identification of two new fluid states, namely: synchronous-periodic and synchronous non-periodic modes of convection, SY-P and SY-NP. The identification if these new modes leads also to new combinations of spatio-temporal patterning behaviours. In addition, contributions have been made by increasing the knowledge surrounding the related thermo-fluid dynamic disturbances (TFDs) and stabilisation phenomena of high Ra_ω RB type thermovibrational flows, using methods including the evaluation of heat transfer mechanisms (Nu) and examining the contributions of time averaged vs oscillatory flow components. From this, it has been found that the stabilisation of high frequency flows, identified by previous authors (Zenkovskaya and Simonenko [29], Geshuni *et al.* [30], Gresho and Sani [31], Biringen and Peltier [32] and Biringen and Danabasoglu [33]), also holds true for high values of Ra_ω. This is complimented by the confirmation that oscillatory disturbances prevail over time averaged ones, in agreement with the literature [46, 107]. Finally, this chapter has lead to the discovery of an optimum value of vibrational frequency (Ω=100), for which the TFD distortions are strongest for highly convective RB type thermovibrationally driven flows.

10.1.2 What thermovibrational effects can be achieved in a fluid, turbulent thermovibrational convection is considered?

Attention is turned now to the second research question identified following the review of the literature: What thermovibrational effects can be achieved in a fluid, turbulent convection is considered?

This question has be tackled in Chap.5, and treats specifically the case where Hadley type thermovibrational convection and high values of Gs and Ra_ω are considered. The aim of the study is to discern the influence of the vibrational frequency (Ω) on the magnitude and patterning behaviour of the time-averaged and instantaneous velocities,

to reveal the underlying textural transitions affecting the instantaneous flow field, and to decode the typical route of evolution towards chaos.

In this chapter, three transition mechanisms to chaos (upon an increase in Gs and Ra_ω) have been identified, including the Ruelle-Taken-Newhouse scenario [52], the Feigenbaum sequence [115] and finally the Manneville and Pomeau mechanism [55]. The occurrence of this transition mechanism has been shown to depend on the considered vibrational frequency (Ω). Indeed, it has been found that for high values of Ω, an increase in Gs and Ra_ω leads to the Ruelle-Takens scenario. This mechanism is the most commonly observed mechanism and has been identified in the many thermo-fluid related studies (the most poignant being the work of Lizée and Alexander [58]).

For intermediate frequencies however, a set of novel results has disrupted the notion that fluid systems obey the classical mechanism to chaos following the intuitive path of: steady $\rightarrow$ periodic $\rightarrow$ quasi-periodic $\rightarrow$ turbulent, as demonstrated by Paolucci and Chenworth [50], Goldhirsh [18] and Villermeaux [51]. Indeed for $\Omega = 10^3$, a *back transition* from chaos to laminar flow has been found. In addition, concurrent aspects of the Feigenbaum and Manneville and Pomeau mechanisms can be recognised, during the back transition and re-transition to chaos.

Although some fluid related studies have highlighted period-locking and resonance phenomena which results in a transition from chaotic to time-periodic states [56, 120–122], this behaviour has never before been achieved in the case of pure thermovibrational flow.

In addition to this novel contribution, the pattering behaviours and textural transitions observed in this study are of interest as the spatial arrangement (columnar structures) of fluid rolls (especially considering low values of Ω) of the time averaged flow has also not been reported before.

Finally, to conclude the research outcomes of this section, the remark can be made that TFD disturbances have been seen to obey the following law: when low frequencies are considered, the oscillatory disturbances prevail, whilst, when high frequencies are considered, time-averaged disturbances prevail. This is in agreement with the literature [46, 107], as was found in the previous section.

10.1.3 What thermovibrational effects can be achieved in a fluid various sets of thermal boundary conditions are applied to the system?

In Chap.6, a three-dimensional RB type thermovibrational system in considered. From the literature review and the additional information supplied in the chapter introduction, it is known that the thermal boundary conditions applied to a systems' solid boundaries can influence the response of a convective flow. This has been shown to apply to standard buoyancy (RB) convection as investigated by Pallarès [22, 23], Puigjaner [24, 25, 149] and Mizushima [19, 20]. However, a gap in knowledge exists when considering the effect of thermal boundary conditions on thermovibrational convection. The choice of adopting a 3D domain here is to enable a fair comparison to the spatio-temporal behaviours of systems studied in the existing literature and capture as realistic a situation possible.

The results of this chapter have bridged the gap in knowledge by providing evidence that thermal boundary conditions do in fact influence the response of the flow. Mainly, it has been found that the inclusion of perfectly conducting side walls (either or 2 or 4 walls) contributes to the stabilisation of the system. This is in agreement with the findings of the works cited above, in particular that of Mizushima [19] when considering standard RB convection.

For all cases, given the systems parameters considered in this study, the instantaneous response of the flow (i.e. the velocity at the centre of the cavity) is composed of a quasi-steady period and a convective burst. It has been shown here that different thermal boundary conditions yield similar velocity signals (i.e., the aforementioned temporal pattern is conserved), however, the specific patterning behaviours associate to each state depend heavily on the imposed conditions.

To this end, this chapter has identified new fundamental unique modes, as well as new combinations of modes complimenting those identified for standard RB convection ([22–25, 149]), notably the new mode S5a.

In addition the above mentioned findings, a complete description of the spatio-temporal behaviour if each case is provided as well as comprehensive maps illustrating the thermal response of the flow.

This chapter, therefore, provides a complete answer to the above question for the case of RB type thermovibrational convection.

10.2 Multiphase thermovibrational flow (with particles)

Having, in the previous section, laid out the contributions to knowledge made surrounding (single-phase) thermovibrational flow, the current section will concentrate on the research output concerning multiphase thermovibrational flow (with the addition of particles).

Chapters 7, 8 and 9 provide a set of answers to the following question:

- How do various thermovibrational effects modify the behaviour of particle accumulation structures in multiphase systems?

More specifically, each chapter answers a more detailed question, each relating to a different problem or system parameter.

10.2.1 What particles structures are enabled when 3D RB type convection is considered?

As previously explained, only the works of Lappa [101, 131, 132, 150] and Lappa & Burel [142] have considered the problem of multiphase thermovibrational flow. The adopted system configuration in these studies is the Hadley flow type configuration. The most natural next step in this case is to expand the knowledge surrounding multiphase thermovibrational flow to the case of RB type thermovibrational convection.

Equipped with a concrete understanding of single phase RB type thermovibrational convection, both from reviewing the literature and from the novel concepts ensuing from Chap.4 and Chap.6, an attempt is made in Chap. 7 to explore the possible particle structures enabled when an additional solid phase is added to the system.

Following this addition, particle structures emerge, however, the spatio-temporal characteristics observed differ greatly from those previously encountered by [1] and Lappa & Burel [142]. In the case of RB type thermovibrational convection (for the given set of established parameters), the particle structures are time dependent, in fact, they are periodic and synchronous (i.e., of regime type SY-P [125]) with the forcing frequency (Ω) of the system. This behaviour has, up until now, not yet been observed in the field of multiphase thermovibrational flow. These time-dependent particle structures, have found to be dependent on the system parameters including the strength of convection (Ra_ω), the vibrational frequency (Ω) and the fluid/ particle density ratio (ξ). Although additional degrees of freedom exist including the Prandtl number of the fluid (Pr), the vibrational amplitude (γ) and the Stokes number of the particles (St), investigating these effect would result in a significant amount of additional degrees of freedom and therefore their effects have not been considered here (although dedicated attention is paid to these in Chap.8 and Chap.9). Another notable distinction from the structures obtained when considering the Hadley type flow, is the morphology of these structures. In the classic case of the Hadley flow type (configuration investigated by Lappa [1]), the particle structures take the form of *quadrics*, where as, in the current configuration the structures form *mushroom* like structures, which display high level of symmetry about the centre line of the cavity (y axis).

In keeping with the theories put forward by Lappa (see above citations), it is clear that, despite the differences obtained both in temporal and morphological results for both the Hadley and RB type flows, that the particle structures are driven by the joint action of thermovibrational convection and the inertial properties of the particles.

10.2.2 What particles structures are enabled when 2D thermovibrational convection with non-uniformly heated cavities is considered?

Now that insights have been provided surrounding particle accumulation in RB type flows under various thermal boundary conditions, another possible line of enquiry may be pursued, this time returning to the case where the Hadley type configuration is con-

sidered. Chapter 8 investigates the effects of imposing non-uniform heating conditions on a 2D square cavity seeded with particles.

The novelty of this chapter lies in the identification of four types of particle structures when alternating vertical temperature gradient are applied: *the 2-side extensions, the central channel accumulation, the two central structures and the 4-roll configuration*. These appear depending on the specific combination of Ω, St, and ξ. An additional structure family is also enabled when, the corner heated case is considered and the angle of the vibrations is varied.

Another contribution to knowledge offered by this chapter is that the results of varying the inertial properties are not limited to the compacting effects of increasing the value of γ and the be offset of this effect produced by a decrease in St and vice versa [1, 134], and that indeed, entire new structure morphologies are possible when these parameters are varied, either independently or simultaneously.

Finally, a mathematical law is provided, linking the number of temperature inversions M and the multiplicity of the structures N.

This once again, as highlighted in the previous section, proves that the occurrence of particle accumulation phenomena depends on a delicate interplay of system (thermovibrational) parameters and inertial properties on the particles.

10.2.3 What particles structures are enabled when turbulent Hadley flow type 2D thermovibrational convection is considered?

The last chapter of this thesis investigates the complex problem of turbulent, multiphase thermovibrational flow. Thus far, through the existing literature and the work undertaken in this thesis, it has been shown that a large quantity of parameters govern the response of a *fluid-only* thermovibrational system and that an ever larger number of parameters need to be considered when investigating multiphase thermovibrational flow. Consolation is sought however, in the principal that, when laminar conditions are considered, general laws associated with the variation of specific parameters can be employed to predict the general behaviour of the particle structures.

In Chap.9, these general laws are largely (but as is demonstrated, not completely) inapplicable.

The chapter considered the Hadley type flow where Ra_ω is varied from $5 \times 10^7 < Ra_\omega < 5 \times 10^9$ and the vibrational amplitude is varied from $8.96 \times 10^7 < \gamma < 1.79 \times 10^9$.

It is shown that, contrary to the laminar case, no well defined structures are enabled, rather, filament type structures emerge. This is due to the collecting of the particles along the left and right side walls (perpendicular to the direction of vibration). Secondly, the genesis of these filaments has been shown to be periodic with the vibrational frequency (Ω). The survival time of the filament is evaluated (i.e., the time, after detachment from the wall, before the filament is broken up by turbulent fluid effects). The survival time has been found to depend on Ra_ω and the vibrational amplitude γ. An increase in Ra_ω resulted in a more turbulent flow as demonstrated in Chap.5, causing the vortices and eddies to *pull* the particle filaments apart, resulting in a reduced survival time. An increase in γ, appeared to have little effect on the structural integrity of the filaments, however it is shown that they detach from the cavity side wall much faster upon this increase in vibrational amplitude. Finally, a short investigation is carried out to inspect the behaviours of light particles vs dense particles (ξ) and small vs large particles (St). It can be seen that the spaces occupied by the particle clouds formed for $\xi = 0.3$ and $\xi = 2$, are for the most part complimentary to each other; moreover, the light particles are prone to form stronger filaments than the heavy particles. As for the influence of St a decrease in particle size, can result in the inability of the dispersed phase to form any recognizable structure, in line with the notions originally put forward by Lappa [1].

10.3 Further work

From this work it has been shown that endless possibilities and opportunities exist to control and manipulate small, solid, spherical particles in thermovibrational systems, when a dilute phase is considered. The mixing and de-mixing phenomena of the phases in the complex fluid uncovered in this work provide humans with an opportunity to

become less dependent on gravity to control the separation of phases and the development of new material processing techniques. Indeed, as we look to the (not so far away) future, space exploration missions such as Artemis (long duration crewed expedition to the moon and a future gateway to Mars), require cutting edge processes which will enable us to thrive and innovate in low gravity environments. More specifically, now that the underlying physics of multiphase thermovibrational flow are understood better than ever before for the case where dilute systems are considered, extensive work is required to understand how these systems behave when dense systems are considered. Indeed, many material processing techniques, separation and solidification processes that give rise to new material alloys, crystalline and metallurgic structures only occur when dense phases/slurries are considered. This is because the solid phase and its spatial arrangement in the fluid can improve the structural and conductive properties of the final product. An interesting line of enquiry would therefore be to evaluate both numerically and experimentally the characteristics and physical properties of dense thermovibrational systems in a range of reduced gravity environments. From a practical perspective and taking a second to acknowledge that this thesis is a result of peripheral work surrounding the T-PAOLA (PARTICLE VIBRATION) project, this work has provided the research community with a platform from which to base new space experiments akin to that of T-PAOLA in the field of both singlephase and multiphase thermovibrational flow.

Appendices

Appendix A

T-PAOLA experiment and related experimental activities

A.1 Experimental set-up and contribution to the experiment

The PARTICLE VIBRATION experiment relies on the utilization of ISS experimental hardware known as the Selectable Optical Diagnostics Instrument (SODI), originally designed to carry out physics experiments in the field of soft matter and fluids for a variety of conditions [151–158]. SODI was developed by an industrial consortium in the frame of a dedicated contract with the European Space Agency, and launched to the ISS in 2010.

Within SODI, the experimental setup for the PARTICLE VIBRATION project consists of four small cubic cells, each filled with a different fluid–solid particle mixture. Each cell is equipped with Peltier elements in order to establish a set temperature difference across the fluid (needed to generate thermovibrational convection in the presence of vibrations). The temperature gradient is set perpendicular to the shaking direction of vibration, where a Hadley type thermovibrational flow will emerge.

For the experiment to be successful, many aspects must be addressed such as the preparation of the experimental protocol and the related scripts to be sent to the SODI hardware in order to control the sequence of required temperature gradients, amplitudes and frequencies of the vibrations, preparation of the post-processing procedures,

calibration of the optical systems etc.. Two crucial aspects of the experiment to be prepared on ground however, are the fluid and the particles themselves. This section will provide an overview of the preparation of these two elements, critical to the success of the experiment.

A.2 Particle preparation

A total of four cells will be used in the experiment containing the following particle-fluid mixtures (see Table A.1). Only the size and density of the particles change while the carrier fluid is set to ethanol in all four cells. These cells are hosted in two arrays.

Table A.1: Particle characteristics for the PARTICLE VIBRATION project

Array no.	**Name**	**Diameter (μm)**	**Density ratio (ξ)**	**Material**
1	Light	75-90	0.18	Silver coated hollow glass
1	Extra heavy	75-90	3.50	Silver coated solid glass with 4% silver
2	Small heavy	53-63	2.84	Silver coated borosilicate solid glass
2	Heavy	75-90	1.65	Silver coated hollow glass

Fig.A.1 shows a microscopic view of the particles (in this case the light silver coated type). As can be seen the particles are perfectly spherical and uniform in size.

Much inspection work was carried out prior to the filling of the cells. This included, verifying that the particles were uniform in shape and size consistent with the characteristics of the particles simulated numerically. It was also important to inspect the particle samples for debris as any inconsistencies in the dispersed phase would be detrimental to the formation of the particle structures.

The number of particles to be inserted into the cells is critical. If the solid phase surpasses a volume fraction of α_d <0.001 the assumption of a dilute system will no longer be valid. Filling the cells with the appropriate number of particles therefore becomes an important task. A dummy cell was manufactured by QinetiQ (an industrial partner of the T-PAOLA project, responsible for the cell hardware), as to allow the science team to perform mock filling tests, here at the University of Strathclyde. The body of the dummy cell can be seen in Fig.A.2.

The light particles were particularly difficult to work with as they are made of very thin shells of hollow glass, making them susceptible to breakage. Due to their light

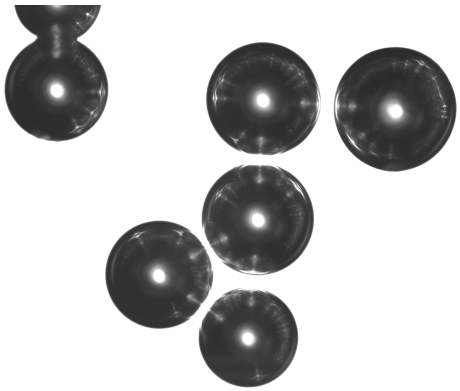

Figure A.1: Example of particle sample under microscope (d=85μm)

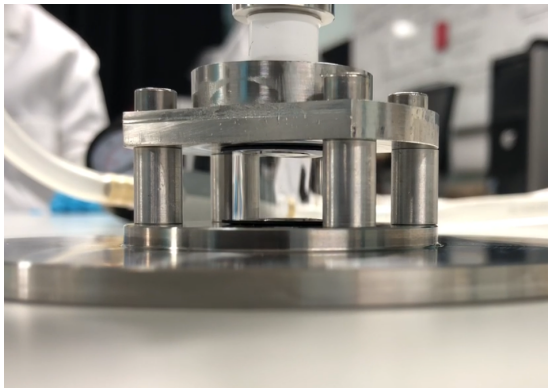

Figure A.2: Dummy filling cell

Figure A.3: Particles sitting at the entrance of the dummy filling cell

weight, they stuck to the walls at the entrance of the cell. This can be seen by taking a close look at Fig.A.3. The white specs show the individual particles seeded around the entrance of the cavity. In response to this problem, many iterations of filling methods

were tested. Perhaps the most obvious method would be to transport the particles through the opening with a carrier fluid. This however was not practical, as the surface tension effects prevented the drop of fluid from penetrating the small 1mm opening. Eventually, the science team identified that a smooth aluminium boat and funnel should be used to direct the particles to the small 1mm opening (see Fig.A.4). The smoothness of the aluminium facilitated the particles to easily detach from the boat and the funnel. The stubborn particles could be displaced from the aluminium tools by using a micro tip syringe which has the capability of generating a small air flow. This method resulted in a large percentage of the particles falling straight into the bottom of the cell and those that did not make it into the cell, accumulated locally close to the 1mm opening. The micro tip was again used to displace the final few particles into the cell itself. Fig.A.5 show the flight cell filled with light particles.

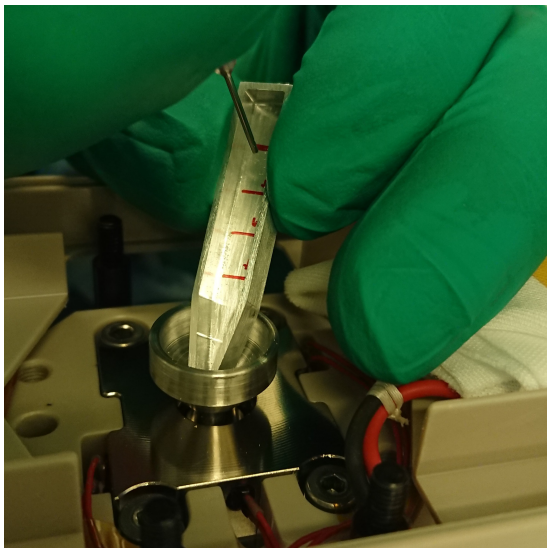

Figure A.4: Boat and funnel tools used during the flight cell filling

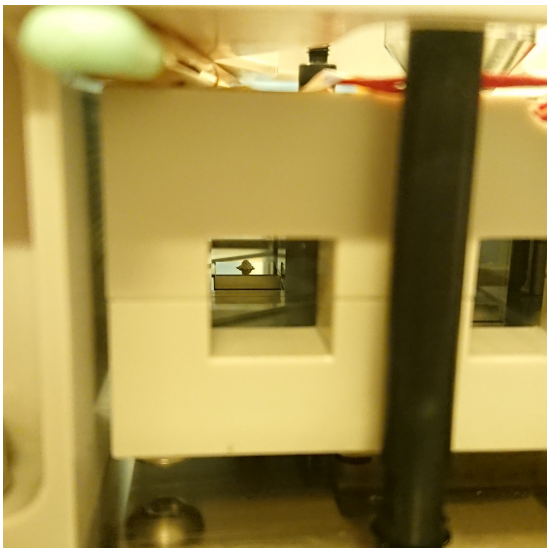

Figure A.5: Flight cell filled with the light particles

Using this technique the particles where filled at QinetiQ UK on the $7^{th} - 10^{th}$ of June 2022, in preparation for the experiment.

To adhere to the system requirement that the volume fraction (α_d) must be less than 0.001 to be considered a dilute phase, the number of particles was determined

via manual counting prior to the particles being inserted into the cells. The following (final) values of α_d where achieved:

Table A.2: Final number of particles and resultant particle volume fraction

Array no.	**Name**	**Number of particles**	**Volume fraction (α_d)**
1	Light	7,291	0.0021
1	Extra Heavy	2,679	0.0008
2	Small Heavy	5,260	0.0005
2	Heavy	3,690	0.0011

The reader may notice that the final volume fraction achieved for the light particles is over the prescribed limit of 0.001. The insertion of twice the amount of particles required is due to the fact that, during ground tests, when the light particles where inserted into the test cells (i.e. replicas of the flight cells) the light particles would become trapped in grooves present in the cell, grooves that are a bi-product of the manufacturing process employed to build the cells. This had not been an issue for past experiments carried out on SODI as these where "fluid only" experiments (or experiments where particles where only used for tracer purposes i.e., where the number of particles was not closely monitored). It was therefore anticipated that during the experiments, a large proportion of the particles would get stuck in these grooves. The team therefore prescribed a larger quantity of particles for the case of the light particles to compensate for this phenomenon.

A.3 Fluid preparation

The next important aspect in the preparation of the experiment, is the carrier fluid itself. The fluid considered here is pure ethanol (C_2H_5OH). During the experiment the fluid/particle mix will be placed under vacuum to ensure no air pockets are present in the cells. Under atmospheric conditions, all liquids (open to the air) contain so-called dissolved gases and include predominantly oxygen (O_2), nitrogen (N_2), and carbon dioxide (CO_2). These gasses are invisible to the naked eye, however, when the liquid is placed under vacuum, following Henry's law (which states that the quantity of dissolved gas in a liquid is proportional to its partial pressure above the liquid) [159], the gases

become less soluble resulting in bubbles of gas appearing in the cavity. To prevent this from happening during the experiment, a procedure known as freeze-pump-thaw was applied to the ethanol prior to the cell filling, in order to remove as much of the dissolved gases as possible.

The freeze pump thaw method was carried out using the following steps (the set up can be seen in Fig.A.6):

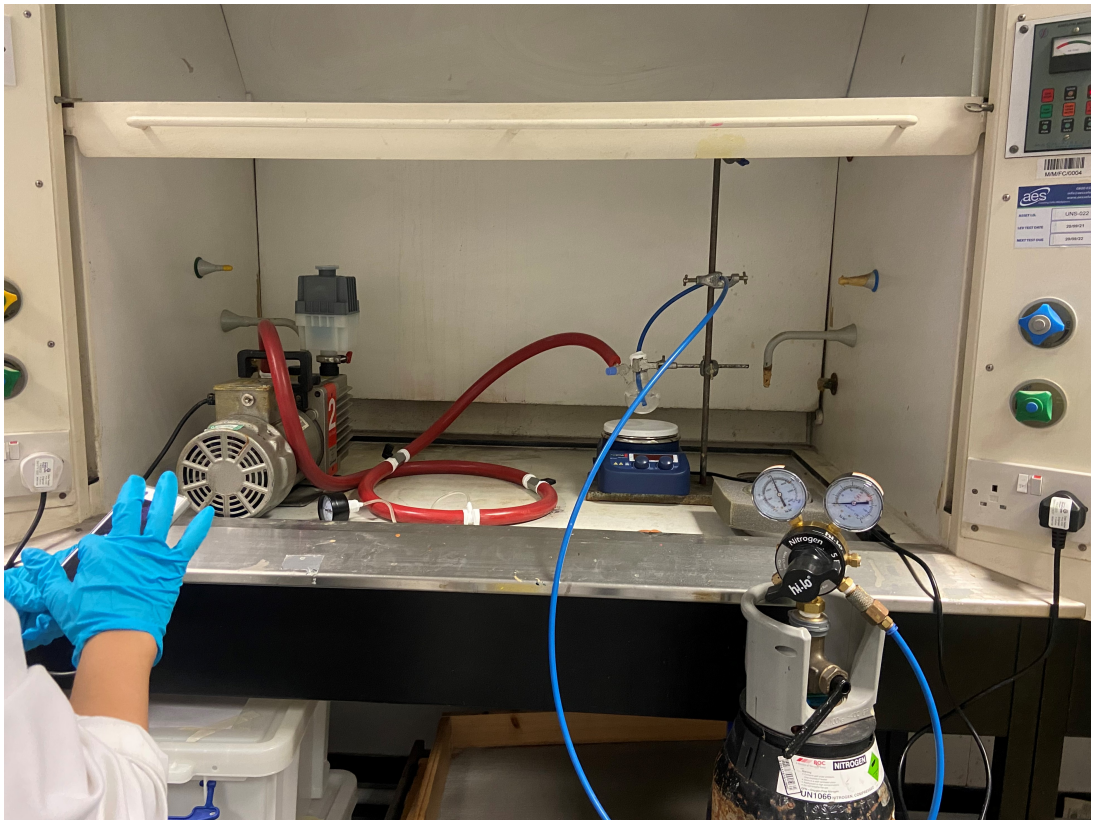

Figure A.6: Degassing set-up

- The ethanol is placed in a Schlenk flask (filled up to 50% of the volume of the flask).
- Nitrogen gas is bubbled through the ethanol to displace as much oxygen as possible from the liquid as to avoid the condensation of liquid oxygen during the freezing process (see Fig.A.7).
- The Schlenk flask is then frozen by lowering into a pool of liquid nitrogen.

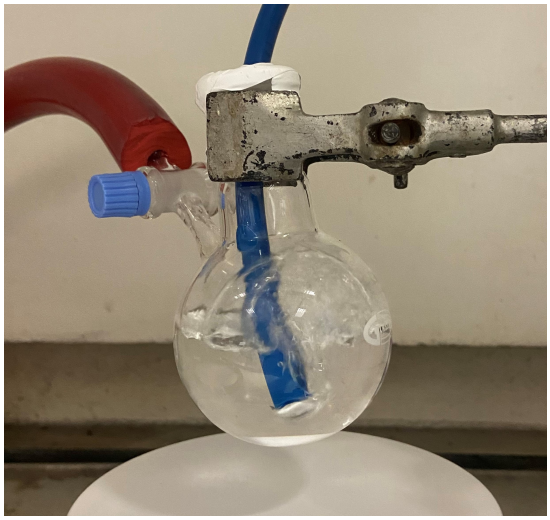

Figure A.7: Nitrogen gas being bubbled through the liquid ethanol

Figure A.8: Ethanol straight after the freezing cycle

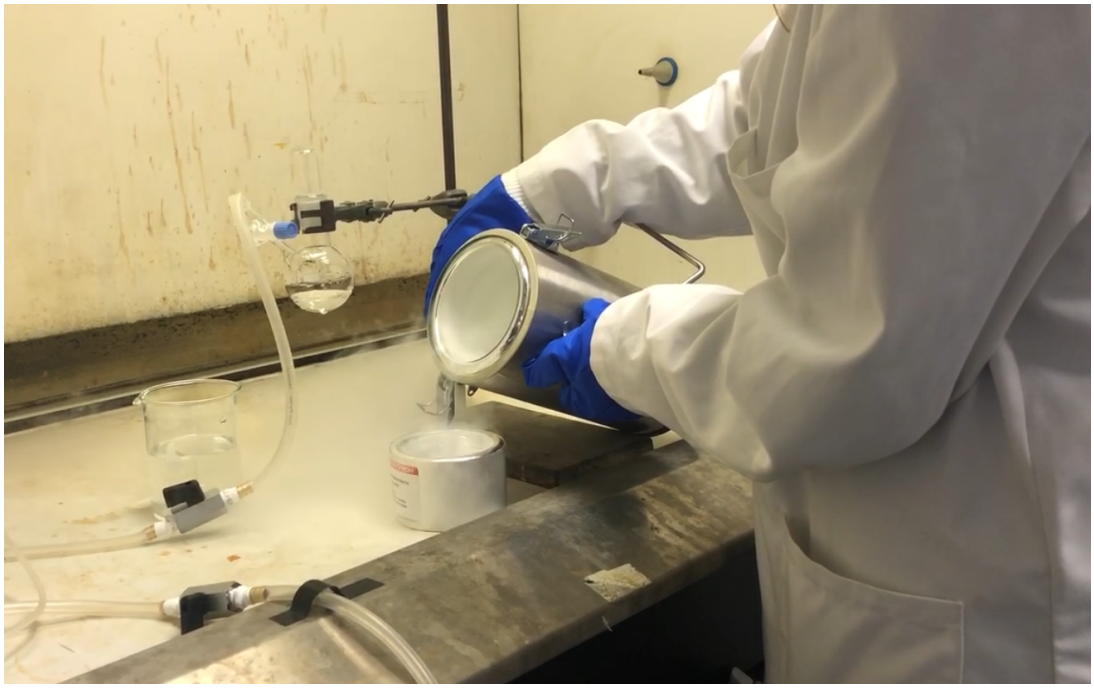

Figure A.9: Liquid nitrogen being poured into dewar for the freezing process

- When the ethanol is completely frozen, the Schlenk flask is removed form the liquid nitrogen and allowed to thaw whilst the head space of the flask is vacuumed (see Fig.A.8 for a snapshot of the frozen ethanol in the frozen Schlenk flask and Fig.A.9 for the filling/refilling of the pool of liquid nitrogen).

The above steps where carried out three times to remove as much of the dissolved gasses as possible. The ethanol was then placed into gas tight syringes. This procedure was carried out on the 6^{th} June 2022 and shipped to QinteiQ in time for the filling of the cells on the 8^{th}-10^{th} June 2022.

This section has described the experimental activities undertaken by the author in the T-PAOLA framework. These where instrumental in highlighting the sensitivity of the real fluid-particle systems being considered for the experiment and also aided in consolidating the theoretical knowledge acquired in the literature review surrounding particle/fluid properties.

Bibliography

[1] Lappa, M. "The patterning behaviour and accumulation of spherical particles in a vibrated non-isothermal liquid". In: *Physics of Fluids* 26.9 (2014). ISSN: 10897666. DOI: 10.1063/1.4893078. URL: http://dx.doi.org/10.1063/1.4893078 (cit. on pp. 5, 39, 40, 55, 58, 80, 147, 165, 168, 171, 172, 174, 176, 181, 184, 185, 194, 204–206).

[2] Lappa, M. "On the nature, formation and diversity of particulate coherent structures in microgravity conditions and their relevance to materials science and problems of astrophysical interest". In: *Geophysical \& Astrophysical Fluid Dynamics* 110.4 (July 2016), pp. 348–386. ISSN: 0309-1929. DOI: 10.1080/03091929.2016.1194410. URL: http://dx.doi.org/10.1080/03091929.2016.1194410%20http://www.tandfonline.com/doi/full/10.1080/03091929.2016.1194410 (cit. on p. 9).

[3] Savino, R. and Monti, R. "Buoyancy and surface-tension-driven convection in hanging-drop protein crystallizer". In: *Journal of Crystal Growth* (1996). ISSN: 00220248. DOI: 10.1016/0022-0248(96)00151-0 (cit. on p. 9).

[4] Alexander, J. I. D. et al. "g-Jitter effects on segregation during directional solidification of tin-bismuth in the MEPHISTO furnace facility". In: *Journal of Crystal Growth* 178.4 (1997), pp. 657–661. ISSN: 00220248. DOI: 10.1016/s0022-0248(97)00141-3 (cit. on pp. 9, 57).

[5] Fedoseyev, A. I. and Alexander, J. D. "Investigation of vibrational control of convective flows in Bridgman melt growth configurations". In: *Journal of Crystal Growth* 211.1-4 (Apr. 2000), pp. 34–42. ISSN: 00220248. DOI: 10.1016/S0022-

0248(99)00839-8. URL: https://linkinghub.elsevier.com/retrieve/pii/S0022024899008398 (cit. on p. 9).

[6] Feigelson, R. S. *Investigation of the Crystal Growth of Dielectric Materials by the Bridgman Technique Using Vibrational Control*. Vol. 6. December. National Aeronautics and Space Administration George C. Marshall Space Flight Center Marshall Space Flight Center, A1 35812, 2001. ISBN: 1200200535 (cit. on p. 9).

[7] Hadley, G. "VI. Concerning the cause of the general trade-winds". In: *Philosophical Transactions of the Royal Society of London* 39.437 (Dec. 1735), pp. 58–62. ISSN: 0261-0523. DOI: 10.1098/rstl.1735.0014. URL: https://royalsocietypublishing.org/doi/10.1098/rstl.1735.0014 (cit. on p. 10).

[8] Huang, J. and Mcelroy, M. B. "Contributions of the hadley and ferrel circulations to the energetics of the atmosphere over the past 32 years". In: *Journal of Climate* 27.7 (2014), pp. 2656–2666. ISSN: 08948755. DOI: 10.1175/JCLI-D-13-00538.1 (cit. on p. 11).

[9] Roux, B., Ben Hadid, H., and Laure, P. "Numerical simulation of oscillatory convection in semiconductor melts". In: *Journal of Crystal Growth* 1 (1989), pp. 201–226 (cit. on p. 12).

[10] Kuo, H. P. and Korpela, S. A. "Stability and finite amplitude natural convection in a shallow cavity with insulated top and bottom and heated from a side". In: *Physics of Fluids* 31.1 (1988), pp. 33–42. ISSN: 0031-9171. DOI: 10.1063/1.866574 (cit. on p. 12).

[11] De Vahl Davis, G. "Natural convection of air in a square cavity: A bench mark numerical solution". In: *International Journal for Numerical Methods in Fluids* 3.3 (May 1983), pp. 249–264. ISSN: 0271-2091. DOI: 10.1002/fld.1650030305. URL: https://onlinelibrary.wiley.com/doi/10.1002/fld.1650030305 (cit. on p. 13).

[12] De Vahl Davis, G. and Jones, I. P. "Natural convection in a square cavity: A comparison exercise". In: *International Journal for Numerical Methods in Fluids* 3.3 (May 1983), pp. 227–248. ISSN: 0271-2091. DOI: 10.1002/fld.1650030304.

URL: https://onlinelibrary.wiley.com/doi/10.1002/fld.1650030304 (cit. on p. 13).

[13] Chandrasekhar, S. *Hydrodynamic and hydromagnetic stability*. New York: Dover Publications, 1961. ISBN: 978-0-486-64071-6 (cit. on p. 14).

[14] Lappa, M. *Thermal Convection: Patterns, Evolution and Stability*. John Wiley \& Sons Ltd, 2010 (cit. on pp. 14, 79).

[15] Busse, F. H. "No Title". In: *Journal of Mathematics and Physics* 46 (1967), pp. 140–150 (cit. on p. 15).

[16] Busse, F. H. "Transition to time-dependent convection". In: 65 (1974) (cit. on p. 15).

[17] Davis, S. H. "Convection in a box: Linear theory". In: *Journal of Fluid Mechanics* 30.3 (1967), pp. 465–478. ISSN: 14697645. DOI: 10.1017/S0022112067001545 (cit. on pp. 15, 20).

[18] Goldhirsch, I., Pelz, R. B., and Orszag, S. A. "Numerical simulation of thermal convection in a two-dimensional finite box". In: *Journal of Fluid Mechanics* 199 (1989), pp. 1–28. ISSN: 14697645. DOI: 10.1017/S0022112089000273 (cit. on pp. 15, 33, 201).

[19] Mizushima, J. "Onset of the Thermal Convection in a Finite Two-Dimensional Box". In: *Journal of the Physical Society of Japan* 64.7 (July 1995), pp. 2420–2432. ISSN: 0031-9015. DOI: 10.1143/JPSJ.64.2420. URL: http://journals.jps.jp/doi/10.1143/JPSJ.64.2420 (cit. on pp. 16, 17, 19, 20, 76, 117, 202).

[20] Mizushima, J. and Adachi, T. "Sequential Transitions of the Thermal Convection in a Square Cavity". In: *Journal of the Physical Society of Japan* 66.1 (Jan. 1997), pp. 79–90. ISSN: 0031-9015. DOI: 10.1143/JPSJ.66.79. URL: http://journals.jps.jp/doi/10.1143/JPSJ.66.79 (cit. on pp. 16, 17, 117, 202).

[21] Mizushima, J. and Nakamura, T. "Onset of Three-Dimensional Thermal Convection in a Rectangular Parallelepiped Cavity". In: *Journal of the Physical Society of Japan* 72.2 (Feb. 2003), pp. 197–200. ISSN: 0031-9015. DOI: 10.1143/JPSJ.72.197. URL: http://journals.jps.jp/doi/10.1143/JPSJ.72.197 (cit. on pp. 17, 20).

[22] Pallares, J., Grau, F., and Giralt, F. "Flow transitions in laminar Rayleigh–Bénard convection in a cubical cavity at moderate Rayleigh numbers". In: *International Journal of Heat and Mass Transfer* 42.4 (Feb. 1999), pp. 753–769. ISSN: 00179310. DOI: 10.1016/S0017-9310(98)00192-6. URL: https://linkinghub.elsevier.com/retrieve/pii/S0017931098001926 (cit. on pp. 17, 18, 108, 117, 119, 120, 122, 127, 202).

[23] Pallares, J. et al. "Experimental laminar Rayleigh-Bénard convection in a cubical cavity at moderate Rayleigh and Prandtl numbers". In: *Experiments in Fluids* 31.2 (Aug. 2001), pp. 208–218. ISSN: 0723-4864. DOI: 10.1007/s003480100275. URL: http://link.springer.com/10.1007/s003480100275 (cit. on pp. 17, 18, 20, 108, 109, 119, 120, 122, 127, 202).

[24] Puigjaner, D. et al. "Stability analysis of the flow in a cubical cavity heated from below". In: *Physics of Fluids* 16.10 (Oct. 2004), pp. 3639–3655. ISSN: 1070-6631. DOI: 10.1063/1.1778031. URL: http://aip.scitation.org/doi/10.1063/1.1778031 (cit. on pp. 17, 18, 108, 118, 202).

[25] Puigjaner, D. et al. "Bifurcation analysis of multiple steady flow patterns for Rayleigh-Bénard convection in a cubical cavity at Pr=130". In: *Physical Review E* 73.4 (Apr. 2006), p. 046304. ISSN: 1539-3755. DOI: 10.1103/PhysRevE.73.046304. URL: https://link.aps.org/doi/10.1103/PhysRevE.73.046304 (cit. on pp. 17, 18, 108, 119, 202).

[26] Lappa, M. "On the Nature and Structure of Possible Three-dimensional Steady Flows in Closed and Open Parallelepipedic and Cubical Containers under Different Heating Conditions and Driving Forces ." In: *FDMP-Fluid Dynamics \&*

Materials Processing 1.1 (2005), pp. 1–20. DOI: 10.3970/fdmp.2005.001.001 (cit. on pp. 18, 108).

[27] Gelfgat, A. Y. "Different Modes of Rayleigh-Bénard Instability in Two- and Three-Dimensional Rectangular Enclosures". In: *Journal of Computational Physics* 156.2 (1999), pp. 300–324. ISSN: 00219991. DOI: 10.1006/jcph.1999.6363 (cit. on p. 18).

[28] Gershuni, G. Z. and Zhukhovitskii, E. M. *Convective stability of incompressible fluids*. Moscow: Nauka, 1976 (cit. on p. 19).

[29] Zenkovskaya, S. M. and Simonenko, I. B. "Effect of high frequency vibration on convective initiation". In: *Fluid Dynamics* (1966), pp. 35–37 (cit. on pp. 22, 27, 62, 200).

[30] Gershuni, G. Z., Zhukhovitskii, E. M., and Iurlov, I. S. "On Convective Stability in the presence of Periodially varying Parameter". In: *Journal of Applied Mathematics and Mechanics* 34.3 (1970), pp. 470–480 (cit. on pp. 22, 63, 200).

[31] Gresho, P. M. and Sani, R. L. "The effects of gravity modulation on the stability of a heated fluid layer". In: *Journal of Fluid Mechanics* 40.4 (1970), pp. 783–806. ISSN: 14697645. DOI: 10.1017/S0022112070000447 (cit. on pp. 22, 200).

[32] Biringen, S. and Peltier, L. J. "Numerical simulation of 3-D Bénard convection with gravitational modulation". In: *Physics of Fluids A* 2.5 (1990), pp. 754–764. ISSN: 08998213. DOI: 10.1063/1.857729 (cit. on pp. 22, 200).

[33] Biringen, S. and Danabasoglu, G. "Computation of convective flow with gravity modulation in rectangular cavities". In: *Journal of Thermophysics and Heat Transfer* 4.3 (1990), pp. 357–365. ISSN: 15336808. DOI: 10.2514/3.188 (cit. on pp. 22, 200).

[34] Gershuni, G. Z. and Zhukhovitskii, E. M. "Free thermal convection in a vibrational field under conditions of weightlessness". In: *Akademiia Nauk SSSR Doklady* 249.3 (1979), pp. 580–584 (cit. on pp. 23, 27, 29, 63).

[35] Gershuni, G. Z. and Zhukhovitskii, E. M. "Convective instability of a fluid in a vibration field under conditions of weightlessness". In: *Fluid Dynamics* 16.4 (1982), pp. 498–504. ISSN: 0015-4628. DOI: 10.1007/BF01094590. URL: http://link.springer.com/10.1007/BF01094590 (cit. on pp. 23, 24, 27, 29, 63, 77, 120).

[36] Hirata, K., Sasaki, T., and Tanigawa, H. "Vibrational effects on convection in a square cavity at zero gravity". In: *Journal of Fluid Mechanics* 445 (Oct. 2001), pp. 327–344. ISSN: 0022-1120. DOI: 10.1017/S0022112001005651. URL: https://www.cambridge.org/core/product/identifier/S0022112001005651/type/journal%7B%5C_%7Darticle (cit. on pp. 23, 26, 27, 58, 59, 62–64, 70, 113, 114, 147, 199, 200).

[37] Gershuni, G. Z., Zhukhovitskii, E. M., and Yurkov, Y. S. "Vibrational thermal convection in a rectangular cavity". In: *Fluid Dynamics* 17.4 (1983), pp. 565–569. ISSN: 0015-4628. DOI: 10.1007/BF01090025. URL: http://link.springer.com/10.1007/BF01090025 (cit. on pp. 24, 25).

[38] Crewdson, G. and Lappa, M. "Thermally-driven flows and turbulence in vibrated liquids". In: *International Journal of Thermofluids* 11 (Aug. 2021), p. 100102. ISSN: 26662027. DOI: 10.1016/j.ijft.2021.100102. URL: https://doi.org/10.1016/j.ijft.2021.100102%20https://linkinghub.elsevier.com/retrieve/pii/S2666202721000409 (cit. on pp. 26, 190).

[39] Simonenko, I. B. "A justification of the averaging method for a problem of convection in a field of rapidly oscillating forces and for other parabolic equations". In: *Mathematics of the USSR - Sbornik* 16.2 (1972), pp. 245–263. ISSN: 21695288. DOI: 10.1070/SM1972v016n02ABEH001424 (cit. on pp. 27, 62).

[40] Gershuni, G. Z. "Vibration-induced thermal convection in weightlessness". In: *Fluid Mech. – Sov. Res.* 15 (1986), pp. 63–84 (cit. on p. 27).

[41] Spradley, L., Bourgeois, S., and Lin, F. "Space processing convection evaluation-G-jitter convection of confined fluids in low gravity". In: *10th Thermophysics Conference*. 1975, p. 695 (cit. on p. 27).

[42] Kamotani, Y., Prasad, A., and Ostrach, S. "Thermal Convection in an Enclosure Due to Vibrations Aboard Spacecraft". In: *AIAA Journal* 19.4 (1981), pp. 511–516. ISSN: 00011452. DOI: 10.2514/3.50973 (cit. on p. 28).

[43] Nelson, E. S. *An examination of anticipated g-jitter on Space Station and its effects on material processes*. 1994 (cit. on p. 28).

[44] Dunbar, J. and Thomas, A. *Technical Paper The Microgravity Environment of the Space Shuttle Columbia Middeck During*. Tech. rep. NASA Technical Paper 3140, 1991 (cit. on pp. 28, 29).

[45] Monti, R. and Savino, R. "A new approach to g-level tolerability for fluid and material science experiments". In: *Acta Astronautica* 37 (Oct. 1995), pp. 313–331. ISSN: 00945765. DOI: 10.1016/0094-5765(95)00060-D. URL: https://linkinghub.elsevier.com/retrieve/pii/009457659500060D (cit. on p. 28).

[46] Monti, R. and Savino, R. "Influence of G-jitter on fluid physics experimentation on-board the international space station". In: *ESA Symposium Proceedings on 'Space Station Utilisation'*. 1996, pp. 215–224 (cit. on pp. 28, 102, 200, 201).

[47] Monti, R., Savino, R., and Lappa, M. "Microgravity sensitivity of typical fluid physics experiment". In: *the 17 th Microgravity Measurements Group Meeting, Cleveland, Ohio, 24-26 March 1998*. Vol. 23. July 1998, pp. 1–15 (cit. on pp. 29, 57, 64).

[48] Lorenz, E. "Deterministic Nonperiodic Flow". In: *Journal of Atmospheric Sciences* 20 (1963), p. 130 (cit. on p. 31).

[49] Grebogi, C., Ott, E., and Yorke, J. A. "Chaos, Strange Attractors, and Fractal Basin Boundaries in Nonlinear Dynamics". In: *Science* 238.4827 (Oct. 1987), pp. 632–638. ISSN: 0036-8075. DOI: 10.1126/science.238.4827.632. URL: https://www.science.org/doi/10.1126/science.238.4827.632 (cit. on p. 33).

[50] Paolucci, S. and Chenoweth, D. R. "Transition to chaos in a differentially heated vertical cavity". In: *Journal of Fluid Mechanics* 201 (Apr. 1989), pp. 379–410. ISSN: 0022-1120. DOI: 10.1017/S0022112089000984. URL: http://www.journa

ls.cambridge.org/abstract%7B%5C_%7DS0022112089000984 (cit. on pp. 33, 95, 201).

[51] Vilermaux. "Memory-Induced Low Frequency Oscillations in Closed Convection Boxes". In: *Physical Review Letters* 75.25 (1995), pp. 4618–4621 (cit. on pp. 33, 201).

[52] Ruelle, D. and Takens, F. "Nature of turbulence". In: *Commun. math. Phys* 20 (1971), pp. 167–192. DOI: 10.1007/978-94-007-7180-2_5 (cit. on pp. 34, 103, 105, 201).

[53] Takens, F. "Detecting strange attractors in turbulence Dynamical Systems and Turbulence, Warwick 1980". In: *Dynamical Systems and Turbulence* 898 (1981), pp. 366–381. URL: http://dx.doi.org/10.1007/bfb0091924 (cit. on pp. 34, 91, 95).

[54] Newhouse, S., Ruelle, D., and Takens, F. "Occurrence of strange Axiom A attractors near quasi periodic flows on Tm, m larger than 3". In: *Communications in Mathematical Physics* 64.1 (1978), pp. 35–40. ISSN: 00103616. DOI: 10.1007/BF01940759 (cit. on pp. 34, 103).

[55] Manneville, P. and Pomeau, Y. "Intermittency and the Lorenz model". In: *Physics Letters A* 75.1-2 (1979), pp. 1–2. ISSN: 03759601. DOI: 10.1016/0375-9601(79)90255-X (cit. on pp. 34, 201).

[56] Guzmán, A. M. and Amon, C. H. "Transition to chaos in converging-diverging channel flows: Ruelle-Takens-Newhouse scenario". In: *Physics of Fluids* 6.6 (1994), pp. 1994–2002. ISSN: 10706631. DOI: 10.1063/1.868206 (cit. on pp. 34, 95, 105, 201).

[57] Blondeaux, P. and Vittori, G. "A route to chaos in an oscillatory flow: Feigenbaum scenario". In: *Physics of Fluids A* 3.11 (1991), pp. 2492–2495. ISSN: 08998213. DOI: 10.1063/1.858191 (cit. on p. 34).

[58] Lizée, A. and Alexander, J. I. D. "Chaotic thermovibrational flow in a laterally heated cavity". In: *Physical Review E - Statistical Physics, Plasmas, Fluids, and*

Related Interdisciplinary Topics 56.4 (1997), pp. 4152–4156. ISSN: 1063651X. DOI: 10.1103/PhysRevE.56.4152 (cit. on pp. 35, 106, 201).

[59] Crowe, C. T. et al. *Multiphase Flows with Droplets and Particles*. 2nd. CRC Press, Aug. 2012. ISBN: 9780429106392. DOI: 10.1201/b11103. URL: http://www.nrcresearchpress.com/doi/10.1139/m75-269%20https://www.taylorfrancis.com/books/9781439840511 (cit. on pp. 36, 37, 52).

[60] Haller, G. and Sapsis, T. "Where do inertial particles go in fluid flows?" In: *Physica D: Nonlinear Phenomena* 237.5 (2008), pp. 573–583. ISSN: 01672789. DOI: 10.1016/j.physd.2007.09.027 (cit. on p. 37).

[61] Sapsis, T. and Haller, G. "Instabilities in the dynamics of neutrally buoyant particles". In: *Physics of Fluids* 20.1 (2008). ISSN: 10706631. DOI: 10.1063/1.2830328 (cit. on p. 37).

[62] Sapsis, T. and Haller, G. "Clustering criterion for inertial particles in two-dimensional time-periodic and three-dimensional steady flows". In: *Chaos* 20.1 (2010). ISSN: 10541500. DOI: 10.1063/1.3272711 (cit. on p. 37).

[63] Yarin, A. L. et al. "Distribution of particles suspended in convective flow in differentially heated cavity". In: *Physics of Fluids* 8.5 (1996), pp. 1130–1140. ISSN: 10706631. DOI: 10.1063/1.868913 (cit. on pp. 38, 166).

[64] Gereltbyamba, B. and Lee, C. "Behavior of settling inertial particles in a differentially heated cubic cavity at moderate Rayleigh number". In: *Journal of Mechanical Science and Technology* 32.7 (2018), pp. 3169–3182. ISSN: 1738494X. DOI: 10.1007/s12206-018-0620-z (cit. on pp. 38, 55, 189).

[65] Puragliesi, R. et al. "DNS of buoyancy-driven flows and lagrangian particle tracking in a square cavity at high rayleigh numbers". In: *International Journal of Heat and Fluid Flow* 32.5 (2011), pp. 915–931. ISSN: 0142727X. DOI: 10.1016/j.ijheatfluidflow.2011.06.007. URL: http://dx.doi.org/10.1016/j.ijheatfluidflow.2011.06.007 (cit. on p. 38).

[66] Patočka, V., Calzavarini, E., and Tosi, N. "Settling of inertial particles in turbulent Rayleigh-Bénard convection". In: *Physical Review Fluids* 5.11 (2020), pp. 1–36. ISSN: 2469990X. DOI: 10.1103/PhysRevFluids.5.114304. arXiv: 2005.05448 (cit. on p. 38).

[67] Maxey, M. R. "The gravitational settling of aerosol particles in homogeneous turbulence and random flow fields". In: *Journal of Fluid Mechanics* 174 (1987), pp. 441–465 (cit. on p. 38).

[68] Squires, K. D. and Eaton, J. K. "Preferential concentration of particles by turbulence". In: *Physics of Fluids A: Fluid Dynamics* 3.5 (May 1991), pp. 1169–1178. ISSN: 0899-8213. DOI: 10.1063/1.858045. URL: http://aip.scitation.org/doi/10.1063/1.858045 (cit. on pp. 38, 189).

[69] Fallon, T. and Rogers, C. B. "Turbulence-induced preferential concentration of solid particles in microgravity conditions". In: *Experiments in Fluids* 33.2 (2002), pp. 233–241. ISSN: 07234864. DOI: 10.1007/s00348-001-0394-3 (cit. on pp. 38, 166, 189).

[70] Lappa, M. "On the variety of particle accumulation structures under the effect of g-jitters". In: *Journal of Fluid Mechanics* 726 (2013), pp. 160–195. ISSN: 00221120. DOI: 10.1017/jfm.2013.203 (cit. on p. 40).

[71] Lappa, M. and Burel, T. "Symmetry breaking phenomena in thermovibrationally driven particle accumulation structures". In: *Physics of Fluids* 32.5 (2020). ISSN: 10897666. DOI: 10.1063/5.0007472. URL: https://doi.org/10.1063/5.0007472 (cit. on pp. 41, 58, 80, 105, 147, 165, 179).

[72] Harlow, F. H. and Welch, J. E. "Numerical calculation of time-dependent viscous incompressible flow of fluid with free surface". In: *Physics of Fluids* 8.12 (1965), pp. 2182–2189. ISSN: 10706631. DOI: 10.1063/1.1761178 (cit. on p. 50).

[73] Chorin, A. J. "Numerical Solution of the Navier-Stokes". In: *Mathematics of Computation* 22.104 (1968), pp. 745–762 (cit. on p. 50).

[74] Témam, R. "Sur l'approximation de la solution des équations de Navier-Stokes par la méthode des pas fractionnaires (II)". In: *Archive for Rational Mechanics and Analysis* 33.5 (1969), pp. 377–385. ISSN: 00039527. DOI: 10.1007/BF00247696 (cit. on p. 50).

[75] Biringen, S. and Cook, C. "ON PRESSURE BOUNDARY CONDITIONS FOR THE INCOMPRESSIBLE NAVIER-STOKES EQUATIONS USING NONSTAGGERED GRIDS". In: *Numerical Heat Transfer* 13.2 (Mar. 1988), pp. 241–252. ISSN: 0149-5720. DOI: 10.1080/10407788808910002. URL: http://www.tandfonline.com/doi/abs/10.1080/10407788808910002 (cit. on p. 50).

[76] Gresho, P. M. "Incompressible fluid dynamics: some fundamental issues". In: *Annual Review of Fluid Mech.* 23 (1991), pp. 413–435 (cit. on pp. 50, 51).

[77] Guermond, J. L. and Quartapelle, L. "On stability and convergence of projection methods based on pressure poisson equation". In: *International Journal for Numerical Methods in Fluids* 26.9 (1998), pp. 1039–1053. ISSN: 02712091. DOI: 10.1002/(SICI)1097-0363(19980515)26:9<1039::AID-FLD675>3.0.CO;2-U (cit. on p. 50).

[78] Guermond, J. L., Minev, P., and Shen, J. "An overview of projection methods for incompressible flows". In: *Computer Methods in Applied Mechanics and Engineering* 195.44-47 (2006), pp. 6011–6045. ISSN: 00457825. DOI: 10.1016/j.cma.2005.10.010 (cit. on p. 50).

[79] Ladyzhenskaya, O. A. *The mathematical theory of viscous incompressible flow*. Vol. 2. Gordon and Breach New York, 1969 (cit. on p. 51).

[80] Lappa, M. "Stratergies for parallelizing the three-dimensional Navier-Stokes equations on the Cray T3E: analysis of the thrmocapillary flow burifications". In: *Science and Supercomputing at CINECA* 11 (1997) (cit. on p. 51).

[81] Lappa, M. and Boaro, A. "Rayleigh-Bénard convection in viscoelastic liquid bridges". In: *Journal of Fluid Mechanics* (2020). ISSN: 14697645. DOI: 10.1017/jfm.2020.608 (cit. on p. 51).

[82] Issa, R. I. "Solution of the implicitly discretized fluid flow equations by operator-splitting." In: *Journal of Computational Physics* 62 (1985), pp. 40–65. ISSN: 15210634. DOI: 10.1080/10407782.2016.1173467 (cit. on p. 51).

[83] Rhie, C. M. and Chow, W. L. "Numerical study of the turbulent flow past an airfoil with trailing edge separation". In: *AIAA Journal* 21.11 (1983), pp. 1525–1532. ISSN: 00011452. DOI: 10.2514/3.8284 (cit. on p. 51).

[84] Zhang, Z. and Chen, Q. "Comparison of the Eulerian and Lagrangian methods for predicting particle transport in enclosed spaces". In: *Atmospheric Environment* 41.25 (2007), pp. 5236–5248. ISSN: 13522310. DOI: 10.1016/j.atmosenv.2006.05.086 (cit. on p. 52).

[85] Ostermeier, P. et al. "Comprehensive investigation and comparison of TFM, DenseDPM and CFD-DEM for dense fluidized beds". In: *Chemical Engineering Science* 196 (2019), pp. 291–309. ISSN: 00092509. DOI: 10.1016/j.ces.2018.11.007. URL: https://doi.org/10.1016/j.ces.2018.11.007 (cit. on p. 53).

[86] Maxey, M. R. and Riley, J. J. "Equation of motion for a small rigid sphere in a nonuniform flow". In: *Physics of Fluids* 26.4 (1983), pp. 883–889. ISSN: 10706631. DOI: 10.1063/1.864230 (cit. on p. 53).

[87] Babiano, A. et al. "Dynamics of a small neutrally buoyant sphere in a fluid and targeting in Hamiltonian systems". In: *Physical Review Letters* 84.25 (2000), pp. 5764–5767. ISSN: 00319007. DOI: 10.1103/PhysRevLett.84.5764 (cit. on p. 53).

[88] Faxén, H. *Der Widerstand gegen die Bewegung einer starren Kugel in einer zähen Flüssigkeit, die zwischen zwei parallelen ebenen Wänden eingeschlossen ist.* Jan. 1922. DOI: 10.1002/andp.19223731003. URL: https://doi.org/10.1002/andp.19223731003 (cit. on p. 54).

[89] Monti, R., Langbein, D., and Favier, J. J. "Influence of Residual Accelerations on Fluid Physics and Materials Science Experiments". In: *Fluid Sciences and Materials Science in Space: A European Perspective.* Ed. by H. U. Walter. Berlin, Heidelberg: Springer Berlin Heidelberg, 1987, pp. 637–680. ISBN: 978-3-

642-46613-7. DOI: 10.1007/978-3-642-46613-7_18. URL: https://doi.org/10.1007/978-3-642-46613-7%7B%5C_%7D18 (cit. on p. 57).

[90] Alexander, J. I. D. "Low-Gravity Experiment Sensitivity to Residual Acceleration: A Review". In: *Microgravity Sci. Technol* 3 (1990). ISSN: 0938-0108. arXiv: arXiv:1011.1669v3 (cit. on p. 57).

[91] Mialdun, A. et al. "Experimental Evidence of Thermal Vibrational Convection in a Nonuniformly Heated Fluid in a Reduced Gravity Environment". In: *Physical Review Letters* 101.8 (Aug. 2008), p. 084501. ISSN: 0031-9007. DOI: 10.1103/PhysRevLett.101.084501. URL: https://link.aps.org/doi/10.1103/PhysRevLett.101.084501 (cit. on p. 57).

[92] Mialdun, A. et al. "Experimental evidence of thermovibrational convection in reduced gravity". In: *Space Research Today* 171.C (2008), pp. 4–6. ISSN: 17529298. DOI: 10.1016/S1752-9298(08)80004-7 (cit. on p. 57).

[93] Melnikov, D. E. et al. "Thermovibrational Convection in Microgravity: Preparation of a Parabolic Flight Experiment". In: *Microgravity - Science and Technology* 20.1 (June 2008), pp. 29–39. ISSN: 0938-0108. DOI: 10.1007/s12217-008-9011-x. URL: http://link.springer.com/10.1007/s12217-008-9011-x (cit. on p. 58).

[94] Lyubimov, D. V. et al. "Influence of gravitational precipitation of solid particles on thermal buoyancy convection". In: *Advances in Space Research* 22.8 (1998), pp. 1267–1270. ISSN: 02731177. DOI: 10.1016/S0273-1177(98)00163-X (cit. on p. 58).

[95] Bouarab, S. et al. "Theoretical and numerical study on high frequency vibrational convection: Influence of the vibration direction on the flow structure". In: *Physics of Fluids* 31.4 (2019). ISSN: 10897666. DOI: 10.1063/1.5090264. URL: http://dx.doi.org/10.1063/1.5090264 (cit. on p. 58).

[96] Shevtsova, V. et al. "Experimental and theoretical study of vibration-induced thermal convection in low gravity". In: *Journal of Fluid Mechanics* 648 (2010), pp. 53–82. ISSN: 00221120. DOI: 10.1017/S0022112009993442 (cit. on p. 58).

[97] Shevtsova, V. et al. "Study of thermoconvective flows induced by vibrations in reduced gravity". In: *Acta Astronautica* 66.1-2 (2010), pp. 166–173. ISSN: 00945765. DOI: 10.1016/j.actaastro.2009.05.023. URL: http://dx.doi.org/10.1016/j.actaastro.2009.05.023 (cit. on p. 58).

[98] Vorobev, A. and Lyubimova, T. "Vibrational convection in a heterogeneous binary mixture. Part 1. Time-averaged equations". In: *Journal of Fluid Mechanics* 870 (2019), pp. 543–562. ISSN: 14697645. DOI: 10.1017/jfm.2019.282 (cit. on p. 58).

[99] Lappa, M. "Control of Convection Patterning and Intensity in Shallow Cavities by Harmonic Vibrations". In: *Microgravity Science and Technology* 28.1 (2016), pp. 29–39. ISSN: 18750494. DOI: 10.1007/s12217-015-9467-4 (cit. on p. 58).

[100] Lappa, M. "Numerical study into the morphology and formation mechanisms of three-dimensional particle structures in vibrated cylindrical cavities with various heating conditions". In: *Physical Review Fluids* 1.6 (Oct. 2016), p. 064203. ISSN: 2469-990X. DOI: 10.1103/PhysRevFluids.1.064203. URL: https://link.aps.org/doi/10.1103/PhysRevFluids.1.064203 (cit. on pp. 58, 139, 184).

[101] Lappa, M. "On the multiplicity and symmetry of particle attractors in confined non-isothermal fluids subjected to inclined vibrations". In: *International Journal of Multiphase Flow* 93 (July 2017), pp. 71–83. ISSN: 03019322. DOI: 10.1016/j.ijmultiphaseflow.2017.03.015. URL: https://linkinghub.elsevier.com/retrieve/pii/S0301932216307121 (cit. on pp. 58, 139, 165, 181, 182, 185, 203).

[102] Lappa, M. "On the formation and morphology of coherent particulate structures in non-isothermal enclosures subjected to rotating g-jitters". In: *Physics of Fluids* 31.7 (2019). ISSN: 10897666. DOI: 10.1063/1.5098438. URL: http://dx.doi.org/10.1063/1.5098438 (cit. on p. 58).

[103] Russo, G. and Napolitano, L. "Order of Magnitude Analysis of unsteady Marangoni and Buoyancy free convection". In: *35th Congress of the International Astronautical Federation*. 1984 (cit. on pp. 60, 82).

[104] Shishkina, O. et al. "Boundary layer structure in turbulent thermal convection and its consequences for the required numerical resolution". In: *New Journal of Physics* 12.7 (July 2010), p. 075022. ISSN: 1367-2630. DOI: 10.1088/1367-2630/12/7/075022. arXiv: 1109.6870. URL: https://iopscience.iop.org/article/10.1088/1367-2630/12/7/075022 (cit. on pp. 60, 82, 112).

[105] De, A. K., Eswaran, V., and Mishra, P. K. "Scalings of heat transport and energy spectra of turbulent Rayleigh-Bénard convection in a large-aspect-ratio box". In: *International Journal of Heat and Fluid Flow* 67 (2017), pp. 111–124. ISSN: 0142727X. DOI: 10.1016/j.ijheatfluidflow.2017.08.002. arXiv: 1708.02391 (cit. on p. 60).

[106] Lappa, M. "Some considerations about the symmetry and evolution of chaotic Rayleigh-Bénard convection: The flywheel mechanism and the "wind" of turbulence". In: *Comptes Rendus - Mecanique* 339.9 (2011), pp. 563–572. ISSN: 16310721. DOI: 10.1016/j.crme.2011.05.002. URL: http://dx.doi.org/10.1016/j.crme.2011.05.002 (cit. on p. 61).

[107] Savino, R. and Lappa, M. "Assessment of Thermovibrational Theory: Application to G -Jitter on the Space Station". In: *Journal of Spacecraft and Rockets* 40.2 (Mar. 2003), pp. 201–210. ISSN: 0022-4650. DOI: 10.2514/2.3954. URL: https://arc.aiaa.org/doi/10.2514/2.3954 (cit. on pp. 65–67, 79, 104, 200, 201).

[108] Birikh, R. V. et al. "Control of thermocapillary convection in a liquid bridge by high frequency vibrations". In: *Microgravity* 3 (1993), pp. 23–28 (cit. on p. 67).

[109] Hof, B., Lucas, P. G., and Mullin, T. "Flow state multiplicity in convection". In: *Physics of Fluids* 11.10 (1999), pp. 2815–2817. ISSN: 10706631. DOI: 10.1063/1.870178 (cit. on p. 76).

[110] Leong, S. S. "Numerical study of Rayleigh-Bénard convection in a cylinder". In: *Numerical Heat Transfer; Part A: Applications* 41.6-7 (2002), pp. 673–683. ISSN: 10407782. DOI: 10.1080/104077802317418287 (cit. on p. 76).

[111] Lappa, M. "On the Nature of Fluid-dynamics". In: *Understanding the Nature of Science; Lindholm, P., Ed.; Science, Evolution and Creationism, BISAC: SCI034000* (2019), pp. 1–64 (cit. on p. 76).

[112] Paolucci, S. "Direct numerical simulation of two-dimensional turbulent natural convection in an enclosed cavity". In: *Journal of Fluid Mechanics* 215 (1990), pp. 229–262. ISSN: 14697645. DOI: 10.1017/S0022112090002634 (cit. on p. 82).

[113] Farhangnia, S., Biringen, S., and Peltier, L. J. "Numerical simulation of two-dimensional buoyancy-driven turbulence in a tall rectanggular cavity". In: *International Journal for Numerical Methods in Fluids* 23.12 (Dec. 1996), pp. 1311–1326. ISSN: 0271-2091. DOI: 10.1002/(SICI)1097-0363(19961230)23:12<1311::AID-FLD447>3.0.CO;2-8. URL: https://arc.aiaa.org/doi/10.2514/6.1994-129%20https://onlinelibrary.wiley.com/doi/10.1002/(SICI)1097-0363(19961230)23:12%7B%5C%%7D3C1311::AID-FLD447%7B%5C%%7D3E3.0.CO;2-8 (cit. on p. 82).

[114] Ueno, I., Tanaka, S., and Kawamura, H. "Oscillatory and chaotic thermocapillary convection in a half-zone liquid bridge". In: *Physics of Fluids* 15.2 (2003), pp. 408–416. ISSN: 10706631. DOI: 10.1063/1.1531993 (cit. on p. 93).

[115] Feigenbaum, M. J. "Quantitative universality for a class of nonlinear transformations". In: *Journal of Statistical Physics* 19.1 (1978), pp. 25–52. ISSN: 00224715. DOI: 10.1007/BF01020332 (cit. on pp. 98, 104, 201).

[116] Boaro, A. and Lappa, M. "Multicellular states of viscoelastic thermovibrational convection in a square cavity". In: *Physics of Fluids* 33.3 (Mar. 2021), p. 033105. ISSN: 1070-6631. DOI: 10.1063/5.0041226. URL: https://aip.scitation.org/doi/10.1063/5.0041226 (cit. on pp. 99, 106).

[117] Monti, R. and Savino, R. "Microgravity experiment acceleration tolerability on space orbiting laboratories". In: *Journal of Spacecraft and Rockets* 33.5 (1996), pp. 707–716. ISSN: 00224650. DOI: 10.2514/3.26824 (cit. on p. 102).

[118] Pomeau, Y. and Manneville, P. "Intermittent transition to turbulence in dissipative dynamical systems". In: *Communications in Mathematical Physics* 74.2

(June 1980), pp. 189–197. ISSN: 0010-3616. DOI: 10.1007/BF01197757. URL: https://www.taylorfrancis.com/books/9780203734636%20http://link.springer.com/10.1007/BF01197757 (cit. on p. 104).

[119] Berge, P., Pomeau, Y., and Vidal, C. *Order Within Chaos*. Wiley, 1987 (cit. on p. 105).

[120] Farooq, A. and Homsy, G. M. "Streaming flows due to g-jitter-induced natural convection". In: *Journal of Fluid Mechanics* 271.2 (1994), pp. 351–378. ISSN: 14697645. DOI: 10.1017/S0022112094001801 (cit. on pp. 105, 201).

[121] Farooq, A. and Homsy, G. M. "Linear and nonlinear dynamics of a differentially heated slot under gravity modulation". In: *Journal of Fluid Mechanics* 313 (1996), pp. 1–38. ISSN: 00221120. DOI: 10.1017/S0022112096002108 (cit. on pp. 105, 201).

[122] Chen, W.-Y. and Chen, C. F. "Effect of gravity modulation on the onset of convection in a fluid and porous layer". In: *Journal of Fluid Mechanics* 395 (1997), pp. 327–344. ISSN: 00207225. DOI: 10.1016/s0020-7225(97)80002-x (cit. on pp. 106, 201).

[123] Kim, K. H., Hyun, J. M., and Kwak, H. S. "Buoyant convection in a side-heated cavity under gravity and oscillations". In: *International Journal of Heat and Mass Transfer* 44.4 (2001), pp. 857–861. ISSN: 00179310. DOI: 10.1016/S0017-9310(00)00142-3 (cit. on p. 106).

[124] Kim, S. K., Kim, S. Y., and Choi, Y. D. "Resonance of natural convection in a side heated enclosure with a mechanically oscillating bottom wall". In: *International Journal of Heat and Mass Transfer* 45.15 (July 2002), pp. 3155–3162. ISSN: 00179310. DOI: 10.1016/S0017-9310(02)00030-3. URL: https://linkinghub.elsevier.com/retrieve/pii/S0017931002000303 (cit. on p. 106).

[125] Crewdson, G. and Lappa, M. "The Zoo of Modes of Convection in Liquids Vibrated along the Direction of the Temperature Gradient". In: *Fluids* 6.1 (Jan. 2021), p. 30. ISSN: 2311-5521. DOI: 10.3390/fluids6010030. URL:

https://www.mdpi.com/2311-5521/6/1/30 (cit. on pp. 113, 114, 147, 190, 204).

[126] Crewdson, G. and Lappa, M. "Spatial and temporal evolution of three-dimensional thermovibrational convection in a cubic cavity with various thermal boundary conditions". In: *Physics of Fluids* 34.1 (2022), p. 014108. ISSN: 1070-6631. DOI: 10.1063/5.0078270 (cit. on pp. 138, 141, 144, 147, 150, 152).

[127] Capobianchi, P. and Lappa, M. "On the influence of gravity on particle accumulation structures in high aspect-ratio liquid bridges". In: *Journal of Fluid Mechanics* 908 (2020), pp. 1–30. ISSN: 14697645. DOI: 10.1017/jfm.2020.882 (cit. on pp. 55, 139).

[128] Melnikov, D. E. and Shevtsova, V. "Different types of Lagrangian coherent structures formed by solid particles in three-dimensional time-periodic flows". In: *European Physical Journal: Special Topics* 226.6 (2017), pp. 1239–1251. ISSN: 19516401. DOI: 10.1140/epjst/e2016-60191-x (cit. on pp. 139, 166).

[129] Gotoda, M. et al. "Experimental study of coherent structures of finite-size particles in thermocapillary liquid bridges". In: *Physical Review Fluids* 4.9 (2019), pp. 1–22. ISSN: 2469990X. DOI: 10.1103/PhysRevFluids.4.094301 (cit. on pp. 139, 166).

[130] Sakata, T. et al. " Coherent structures of m = 1 by low-Stokes-number particles suspended in a half-zone liquid bridge of high aspect ratio: Microgravity and terrestrial experiments ". In: *Physical Review Fluids* 7.1 (2022), pp. 1–25. DOI: 10.1103/physrevfluids.7.014005 (cit. on pp. 139, 166).

[131] Lappa, M. "Stationary solid particle attractors in standing waves". In: *Physics of Fluids* 26.1 (2014). ISSN: 10897666. DOI: 10.1063/1.4862780 (cit. on pp. 139, 203).

[132] Lappa, M. "Numerical study into the morphology and formation mechanisms of three-dimensional particle structures in vibrated cylindrical cavities with various heating conditions". In: *Physical Review Fluids* 1.6 (2016), pp. 1–25. ISSN: 2469-990X. DOI: 10.1103/physrevfluids.1.064203 (cit. on pp. 139, 165, 203).

[133] Lappa, M. "Characterization of two-way coupled thermovibrationally driven particle attractee". In: *Physics of Fluids* May (2022). ISSN: 1070-6631. DOI: 10.1063/5.0091520 (cit. on pp. 139, 165, 176).

[134] Lappa, M. "On the transport, segregation, and dispersion of heavy and light particles interacting with rising thermal plumes". In: *Physics of Fluids* 30.3 (2018). ISSN: 10897666. DOI: 10.1063/1.5013654. URL: http://dx.doi.org/10.1063/1.5013654 (cit. on pp. 140, 205).

[135] Crewdson, G. and Lappa, M. "An Investigation into the Behavior of Non-Isodense Particles in Chaotic Thermovibrational Flow". In: *Fluid Dynamics \& Materials Processing* 18.3 (2022), pp. 497–510. ISSN: 1555-2578. DOI: 10.32604/fdmp.2022.020248 (cit. on pp. 165, 176).

[136] Solomon, T. H. and Gollub, J. P. "Passive transport in steady Rayleigh–Bénard convection". In: *Physics of Fluids* 31.6 (1988), p. 1372. ISSN: 00319171. DOI: 10.1063/1.866729 (cit. on p. 166).

[137] Park, H. J., O'Keefe, K., and Richter, D. H. "Rayleigh-Bénard turbulence modified by two-way coupled inertial, nonisothermal particles". In: *Physical Review Fluids* 3.3 (2018), pp. 1–15. ISSN: 2469990X. DOI: 10.1103/PhysRevFluids.3.034307 (cit. on p. 166).

[138] Jiang, L., Calzavarini, E., and Sun, C. "Rotation of anisotropic particles in Rayleigh-Bénard turbulence". In: *Journal of Fluid Mechanics* 901 (2020). ISSN: 14697645. DOI: 10.1017/jfm.2020.539 (cit. on p. 166).

[139] Xu, A. et al. "Transport and deposition of dilute microparticles in turbulent thermal convection". In: *Physics of Fluids* 32.8 (Aug. 2020), p. 083301. ISSN: 1070-6631. DOI: 10.1063/5.0018804. URL: http://aip.scitation.org/doi/10.1063/5.0018804 (cit. on pp. 166, 189).

[140] Elghobashi, S. and Truesdell, G. C. "Direct simulation of particle dispersion in a decaying isotropic turbulence". In: *Journal of Fluid Mechanics* 242.January (Sept. 1992), pp. 655–700. ISSN: 0022-1120. DOI: 10.1017/S0022112092002532.

URL: https://www.cambridge.org/core/product/identifier/S0022112092002532/type/journal%7B%5C_%7Darticle (cit. on pp. 166, 189).

[141] Maxey, M. R. and Wang, L.-P. "Settling velocity and concentration distribution of heavy particles in homogeneous isotropic turbulence". In: *Journal of Fluid Mechanics* 256 (1993), pp. 27–68. URL: papers2://publication/uuid/DBB29E84-12AC-4308-B108-F1D2E725E18D (cit. on p. 166).

[142] Lappa, M. et al. "Particle Vibration, an instrument to study particle accumulation structures on board the International Space Station". In: *Microgravity Science and Technology* (2022) (cit. on pp. 185, 203, 204).

[143] Maxey, M. R. et al. "Simulations of dispersed turbulent multiphase flow". In: *Fluid Dynamics Research* 20.1-6 (1997), pp. 143–156. ISSN: 01695983. DOI: 10.1016/S0169-5983(96)00042-1 (cit. on pp. 189, 191).

[144] Elghobashi, S. and Truesdell, G. C. "On the two-way interaction between homogeneous turbulence and dispersed solid particles. I: Turbulence modification". In: *Physics of Fluids A* 5.7 (1992), pp. 1790–1801. ISSN: 08998213. DOI: 10.1063/1.858854 (cit. on p. 189).

[145] Bhatnagar, A. et al. "Heavy inertial particles in turbulent flows gain energy slowly but lose it rapidly". In: *Physical Review E* 97.3 (Mar. 2018), p. 033102. ISSN: 2470-0045. DOI: 10.1103/PhysRevE.97.033102. URL: https://link.aps.org/doi/10.1103/PhysRevE.97.033102 (cit. on p. 189).

[146] Ireland, P. J., Bragg, A. D., and Collins, L. R. "The effect of Reynolds number on inertial particle dynamics in isotropic turbulence. Part 2. Simulations with gravitational effects". In: *Journal of Fluid Mechanics* 796 (June 2016), pp. 659–711. ISSN: 0022-1120. DOI: 10.1017/jfm.2016.227. arXiv: 1507.07022. URL: https://www.cambridge.org/core/product/identifier/S0022112016002275/type/journal%7B%5C_%7Darticle (cit. on p. 189).

[147] Petersen, A. J., Baker, L., and Coletti, F. "Experimental study of inertial particles clustering and settling in homogeneous turbulence". In: *Journal of Fluid Mechanics* 864 (Apr. 2019), pp. 925–970. ISSN: 0022-1120. DOI: 10.1017/jfm.2

019.31. arXiv: 1812.04055. URL: https://www.cambridge.org/core/product/identifier/S0022112019000314/type/journal%7B%5C_%7Darticle (cit. on p. 189).

[148] Love, S. G., Pettit, D. R., and Messenger, S. R. "Particle aggregation in microgravity: Informal experiments on the International Space Station". In: *Meteoritics and Planetary Science* 49.5 (2014), pp. 732–739. ISSN: 10869379. DOI: 10.1111/maps.12286 (cit. on p. 189).

[149] Puigjaner, D. et al. "Bifurcation analysis of steady Rayleigh-Bénard convection in a cubical cavity with conducting sidewalls". In: *Journal of Fluid Mechanics* 598 (2008), pp. 393–427. ISSN: 00221120. DOI: 10.1017/S0022112007000080 (cit. on p. 202).

[150] Lappa, M. "Towards new contact-less techniques for the control of inertial particles dispersed in a fluid". In: *Twelve International Conference on Thermal Engineering: Theory and Applications*. 2019, pp. 5–7 (cit. on p. 203).

[151] Shevtsova, V. et al. "IVIDIL: on-board g-jitters and diffusion controlled phenomena". In: *Journal of Physics: Conference Series* 327.1 (Dec. 2011), p. 012031. ISSN: 1742-6596. DOI: 10.1088/1742-6596/327/1/012031. URL: https://iopscience.iop.org/article/10.1088/1742-6596/327/1/012031 (cit. on p. 210).

[152] Shevtsova, V. et al. "The IVIDIL experiment onboard the ISS: Thermodiffusion in the presence of controlled vibrations". In: *Comptes Rendus - Mecanique* 339.5 (2011), pp. 310–317. ISSN: 16310721. DOI: 10.1016/j.crme.2011.03.007. URL: http://dx.doi.org/10.1016/j.crme.2011.03.007 (cit. on p. 210).

[153] Lappa, M. *Rotating Thermal Flows in Natural and Industrial Processes*. Chichester, England: John Wiley \& Sons Ltd, 2012. ISBN: 9781119960799. DOI: 10.1002/9781118342411 (cit. on p. 210).

[154] Mazzoni, S. et al. "SODI-COLLOID: A combination of static and dynamic light scattering on board the International Space Station". In: *Review of Scientific*

Instruments 84.4 (2013). ISSN: 00346748. DOI: 10.1063/1.4801852 (cit. on p. 210).

[155] Mialdun, A. et al. "Analysis of the thermal performance of SODI instrument for DCMIX configuration". In: *Microgravity Science and Technology* 25.1 (2013), pp. 83–94. ISSN: 09380108. DOI: 10.1007/s12217-012-9337-2 (cit. on p. 210).

[156] Mialdun, A. et al. "Measurement of Soret coefficients in a ternary mixture of toluene-methanol-cyclohexane in convection-free environment". In: *Journal of Chemical Physics* 148.4 (2018). ISSN: 00219606. DOI: 10.1063/1.5017716. URL: http://dx.doi.org/10.1063/1.5017716 (cit. on p. 210).

[157] Triller, T. et al. "The Soret effect in ternary mixtures of water+ethanol+triethylene glycol of equal mass fractions: Ground and microgravity experiments". In: *European Physical Journal E* 42.3 (2019). ISSN: 1292895X. DOI: 10.1140/epje/i2019-11789-7 (cit. on p. 210).

[158] Schraml, M. et al. "The DCMIX project: Measurement of thermodiffusion processes in ternary mixtures on ground and in space". In: *Acta Astronautica* 160.April (2019), pp. 251–257. ISSN: 00945765. DOI: 10.1016/j.actaastro.2019.04.027. URL: https://doi.org/10.1016/j.actaastro.2019.04.027 (cit. on p. 210).

[159] William, H. "Experiments on the quantity of gases absorbed by water, at different temperatures, and under different pressures". In: *Phil. Trans. R. Soc.* 93 (1802), pp. 29–42 (cit. on p. 214).